Defect detection and condition assessment of adhesively-bonded joints using acoustic emission techniques.

CRAWFORD, A.R.

2021

Defect Detection and Condition Assessment of Adhesively-Bonded Joints Using Acoustic Emission Techniques

Author: Alasdair Ruairidh Crawford

Supervisors: Dr. Mohamad Ghazi Droubi & Dr. Nadimul Haque Faisal

August 2021

A thesis submitted in partial fulfilment of the requirements of the Robert Gordon University for the degree of Doctor of Philosophy

Acknowledgements

My sincere thanks go to:

- Dr. Ghazi Droubi and Dr. Nadimul Faisal for their supervision throughout this project.
- Dr. Anil Prathuru for his guidance when I first started this project and for many fruitful discussions since then.
- All of the admin. staff in the School of Engineering, particularly Dr. Rosslyn Shanks and Kirsty Stevenson.
- All of the technicians who have helped with my experiments and provided great advice. In particular thanks to Allan MacPherson for teaching me the 'correct' pronunciation of the term "PhD"...
- All of the many great friends I have made in my time at Robert Gordon University (RGU). You have made my time here so much more interesting, and I may have actually learnt more about international cuisine than I have about acoustic emission.
- Dr. Lev Roberts-Haritonov and the rest of the team at MMA Offshore for their support and flexibility throughout the final year of this project.
- My family for supporting me throughout the ups and downs of this project, especially Cara, my long suffering fiancee who has put up with my whingeing without killing me, yet...

Abstract

The aim of this study is to investigate the application of acoustic emission (AE) techniques to the defect-detection and monitoring of adhesively-bonded joints. Pencil Lead Breaks (PLBs) have been used as a simulated AE source to experimentally investigate the characteristics of AE wave-propagation in adhesively-bonded joints, and have been combined with Artificial Neural Networks (ANNs) to provide a novel method of defect detection and sizing. Modal AE analysis has been applied to destructive testing of adhesively-bonded specimens as a novel method to differentiate between fracture-modes. Dynamic Finite Element Analysis (FEA) has been utilised to simulate the AE generation and propagation to further investigate the findings of the experimental studies and to assess the applicability of the findings over a broader range of conditions than could be achieved experimentally.

PLB tests have been conducted on large ($500mm$ x $500mm$ x $1mm$) aluminium sheet specimens to identify the effects of an adhesive layer on AE wave-propagation. Three specimens were considered; a single sheet, two sheets placed together without adhesive, and an adhesively-bonded specimen. The simulated AE source is applied to the specimens at varying propagation-distances and orientations. The acquired signals are processed using wavelet-transforms to explore time-frequency features, and compared with modified group-velocity curves based on the Rayleigh-Lamb equations to allow identification of wave-modes and edge-reflections. The effects of propagation-distance and source orientation are investigated while comparison is made between the three specimens.

PLB tests were also used to investigate the effect of, and to detect and size void-type adhesive defects. Defect-free specimens were used for reference, and specimens with two different void sizes were tested. The PLB source was used to generate simulated AE which would propagate through the defect region and then be recorded with the AE system. Four configurations were tested to assess the effects of source-sensor propagation distance and source and sensor proximity to the defect. Typical AE parameters of peak amplitude, rise time, decay time, duration, number of counts and AE energy were investigated. Frequency analyses by Fast Fourier Transformation (FFT), partial powers and wavelet-transform (WT) were also implemented. Artificial-Neural-Networks (ANNs), using the raw Time-Domain signal as an input, were successfully trained and tested to differentiate between the specimen-types tested and to estimate the defect sizes.

AE-instrumented Double Cantilever-Beam (Mode-I fracture) and Lap-Shear (Mode-II fracture) tests were conducted on similar adhesively-bonded aluminium specimens. Linear source-location was used to identify the source-to-sensor propagation distance of each recorded hit, theoretical dispersion-curves were used to identify regions of the signal corresponding to the symmetric and asymmetric wave-modes, and peak wavelet-transform coefficients for the wave-modes were compared between the two fracture-modes and assessed as an indicator of fracture-mode. It was concluded that there is a relationship between the fracture-mode and the generated wave-modes, with Mode-II fracture typically generating a relatively greater symmetric wave-mode than Mode-I fracture.

Dynamic FEA was used to replicate both the PLB tests and the destructive tests, and to investigate the effects of a range of parameters which could not all be practically varied in experimental work. Adhesive Young's modulus (representative of different adhesive types), adhesive-layer thickness, and adhesive void size were varied in the simulated PLB tests. FEA was also used to investigate the effects of fracture-mode on the generated acoustic emissions in simulated mixed-mode-bending tests, conducted over a range of mode-mixities. The FEA results were found to

corroborate the results of the experimental work and support a relationship between fracture-mode and generated wave-modes. It was also identified that a variety of other parameters may also affect the wave-modes, and thus need to be considered to achieve effective use of modal-analysis to differentiate between fracture-modes.

CONTENTS

Nomenclature

A_0	Fundamental anti-symmetric Lamb mode
$A_{1,2,3...n}$	Higher order anti-symmetric Lamb modes
AE	Acoustic Emission
ASTM	American Society for Testing and Materials
CWT	Continuous Wavelet Transform
CFL	Courant-Friedrichs-Lewy (Stability Criteria)
c_l	Longitudinal wave velocity
c_p	Phase velocity
c_t	Shear wave velocity
DAQ	Data Acquisition Card
DCB	Double-Cantilever-Beam
FEA	Finite Element Analysis
FEM	Finite Element Method
FFT	Fast Fourier Transform
2D-FFT	Two-Dimensional Fast Fourier Transform
h	Half the sheet thickness
kHz	Kilo Hertz
LS	Lap-Shear
mm	Millimetres
MHz	Mega Hertz
MMB	Mixed-Mode-Bending
NDT	Non-Destructive Testing
NI	National Instruments
PLB	Pencil Lead Break
PSD	Power Spectral Density
PTFE	Polytetrafluoroethylene
S_0	Fundamental symmetric Lamb mode
$S_{1,2,3...n}$	Higher order symmetric Lamb modes
SCU	Signal Conditioning Unit
SEM	Scanning Electron Microscopy
SHM	Structural Health Monitoring
STFT	Short-Time Fourier Transform
WT	Wavelet Transform
g	Group-velocity
k	Wave number
ω	Angular frequency

Publications from this Thesis

Published:

1. Crawford, Alasdair, Mohamad Ghazi Droubi, and Nadimul Haque Faisal. "Analysis of acoustic emission propagation in metal-to-metal adhesively-bonded joints." Journal of Non-destructive Evaluation 37.2 2018: 33.

2. Crawford, Alasdair R., Mohamad Ghazi Droubi, and Nadimul Haque Faisal. "Modal acoustic emission analysis of mode-I and mode-II fracture of adhesively-bonded joints." presented at EWGAE 33rd European Conference on Acoustic Emission Testing, Senlis, France, Sept. 12-14, 2018.

Under preparation:

1. Crawford, Alasdair R., Mohamad Ghazi Droubi, and Nadimul Haque Faisal. "Detection and Sizing of Adhesive Defects by use of a Hsu-Nielsen Source". Currently under preparation for publication.

2. Crawford, Alasdair R., Mohamad Ghazi Droubi, and Nadimul Haque Faisal. "Acoustic Emission Characteristics of Adhesively-Bonded Specimens: An FEM Study". Currently under preparation for publication.

3. Crawford, Alasdair R., Mohamad Ghazi Droubi, and Nadimul Haque Faisal. "Finite Element Simulation of Acoustic Emission from Adhesive Bond Failure under Mixed-Mode Bending". Currently under preparation for publication.

Chapter 1

Research Context

Structural adhesives have rapidly gained popularity as a joining method in a variety of sectors, particularly the aerospace and renewable energy sectors, due to their various advantages over more traditional joining methods. They can however be subject to the introduction of a variety of defects, during both manufacture and service, which can ultimately lead to catastrophic failure. The safe use of adhesives in critical applications is therefore dependent on strict quality control, followed by regular inspection or monitoring of the adhesives' condition to ensure any degradation of the joint is detected early enough to prevent catastrophic failure.

Many techniques have been developed to identify the presence of defects in adhesively-bonded specimens. These techniques have included assorted ultrasonic scanning methods [1], guided Lamb waves [2, 3], acousto-ultrasonic methods, infrared-thermography [1] and radiography [4], and have had varying levels of success in identifying porosity, voids, disbonds and various interfacial defects and degradation. While, these methods have all been proven capable of identifying certain defects, and thus inferring the potential strength of a joint, or lack thereof, no method currently exists which can directly determine the bond strength of a joint [4]. This factor, combined with the potential for environmental degradation, occurring due to moisture ingress, chemical exposure, temperature or fatigue, can lead to a need for in-service testing or monitoring to ensure bond integrity [5, 6].

While many of the aforementioned techniques can be applied to structures in service, the need for access to the joints for inspection can be inconvenient, or in some cases even impossible due to the operating environment. For example, consider the blades of a wind turbine. These are typically constructed as either a "one-piece" design, in which a stiffening spar is adhesively bonded into a one-piece shell, or a two-piece design, in which the two halves of the blade are adhesively bonded together, along with internal shear webs, resulting in the use of as much as 400 kg of adhesive for a typical 42 m blade [7]. Inspection of these blades requires stopping the turbine, thus resulting in expensive downtime, and then typically the use of rope-access technicians descending the blade to carry out the inspection, a potentially dangerous operation which is reliant on suitable weather conditions. Likewise, adhesive joints used in the construction of aircraft will only be accessible during downtime once the plane has landed, meaning that for inspection the plane must be taken out of service. A technique that therefore lends itself to long-term monitoring of adhesive joints in service, is acoustic emission (AE) testing. AE sensors can be retro-fitted to an existing structure for temporary monitoring, or integrated into the structure during construction, and once fitted can be monitored remotely, removing, or significantly reducing, any subsequent need for direct access

to the joints. Due to the costs and added complexity of this approach, this is not a universal solution, but in scenarios where the costs of downtime and manual inspection will outweigh the cost of an AE system, or situations in which the consequences and costs of failure are high, AE can provide a suitable approach. As the technology matures, it can however be assumed that the cost of such systems is likely to fall, meaning that this will become an increasingly more viable approach in the future. Acoustic emission is not typically used to identify the presence of defects within a structure, but is capable of detecting their growth by detecting the propagation of elastic waves generated by the sudden re-distributions of stress which occur from defect growth. Using a suitably selected sensor array, AE can monitor a large area with a very small number of sensors, and can continuously monitor the condition of an entire structure, as opposed to scanning it region by region as is typical with most NDT methods.

Further understanding of the AE sources however forms only part of the challenge of AE testing of adhesive joints, as the process of wave-propagation from source to sensor also contributes significantly to the signal which is recorded. The presence of an adhesive layer along this propagation path will therefore contribute significantly to what is recorded, and thus needs to be well understood for quantitative AE testing to become a possibility. Previous works investigating AE testing of adhesives typically have not considered this aspect in great detail, but have highlighted its importance. In a study of Mode-I and -II fracture by Droubi et al. [8] it was observed that the frequency content of the acoustic emissions varied significantly as the crack-tip progressed towards the sensor. While the source of variation could not be confirmed in the study, it is believed to be due to the characteristics of the AE propagation due to the adhesive layer, as opposed to being a feature of the source. Some other studies, such as that by Prathuru [9] have considered the effects of bond quality on wave-propagation, and have even used AE-based techniques for the detection of defects. These studies have however been restricted to small coupon-type specimens, with little investigation of larger specimens as may exist in some industrial applications.

Significantly more work has been done regarding wave-propagation in adhesives using ultrasound methods rather than acoustic emission, such as the investigations by Heller et al. [2]. A lot of the findings of the ultrasonic investigations, particularly those focusing on Lamb wave propagation, can be applied to AE applications, but the studies typically focus on a significantly higher frequency-range than is used in AE. It is therefore felt to be important to carry out further investigation of wave-propagation in bonded specimens using typical AE sources and sensing equipment.

1.1 Research Methodology and Objectives

While there have been a variety of studies utilising closely-related techniques, such as ultrasound [2] or 3D laser-vibrometry [10], to the best of the author's knowledge, there has been little systematic investigation of the effects of adhesive bonding on the propagation of acoustic emission in large scale specimens. There have also been no studies conducted investigating the relationship between the fracture-mode of adhesive joints and the different Lamb wave modes generated by them. A series of Pencil-Lead-Break (PLB) [11] and fracture-based experiments and a variety of dynamic FEA simulations have therefore been conducted to develop a greater understanding of the effects of adhesive bond status on AE propagation and to assess the possibility of using modal AE analysis techniques to differentiate between fracture-modes in adhesively-bonded joints. An understanding of the effects of an adhesive layer on wave-propagation is critical for correct inter-

pretation of any AE data resulting from failure of an adhesive, or even for other unrelated sources, which result in propagation-path through an adhesive bond. It has been chosen to investigate the application of modal AE analysis to the study of adhesive fracture-modes, as the study of fracture-modes can be critical to the monitoring of adhesives due to the significant differences in load-bearing capabilities between the different modes. Modal analysis has shown great success in a variety of other applications, but has not previously been applied to the differentiation between adhesive fracture-modes. Dynamic finite element simulations were conducted to investigate both the effects of the adhesive-layer on wave-propagation and to investigate the effects of fracture-mode. The use of simulations allows for a much better controlled environment than experiments, allowing the effects of the parameters under investigation to be completely isolated for clearer analysis of their effects. Once a basic model has been implemented, simulations also provide an efficient way to investigate a range of variables which may not be possible or practical to investigate experimentally due to time or cost constraints. The main objectives of this project were therefore:

1. To develop an understanding of the effects of adhesive bond status on the propagation characteristics of acoustic emission in relatively large-scale test specimens by use of a standard PLB source. The findings of this part of the study were subsequently used to inform the design of experiments and analysis methods for the rest of this project.
2. To investigate the effects of bonding defects on AE propagation, and to develop AE-based methods of defect detection using a standard PLB source.
3. To experimentally investigate the relationship between the fracture-modes of adhesively-bonded joints and the generated acoustic emissions, specifically with respect to the Lamb wave modes generated. The primary aim of this being to investigate the potential application of Modal-AE analysis to differentiate between fracture-modes.
4. To develop a dynamic finite element model to investigate the effects of the parameters of adhesive layers on AE propagation. The use of the finite element approach, in addition to the experimental work, allows a greater degree of control of the test variables and provides an efficient way to investigate a large range of parameters.
5. To develop a dynamic finite element model to investigate the relationships between fracture-mode and acoustic emission through dynamic finite element analysis. The development of a finite element model will expand on the experimental findings and will again provide an efficient way to investigate a wide range of parameters in a much more controlled manner than is possible experimentally.

1.2 Contribution to Knowledge

The initial contribution to knowledge from this work lies in the systematic experimental study of AE propagation in relatively large scale adhesively-bonded specimens. The results of which were then used to provide confidence in the techniques in the following study of adhesive fracture. The study of wave-propagation in adhesively-bonded joints has demonstrated the effects of the adhesive layer on the wave-modes generated, the frequency content, amplitude, energy and other typical AE parameters. The results correlate well with those previously reported in studies utilising ultrasound techniques, but are unique in terms of the use of the AE equipment and the

accompanying focus on a lower frequency-range than is considered using ultrasound. The use of a PLB source to detect void-type adhesive defects is contributing to expanding on previous work conducted at Robert Gordon University, in which this method has been used to investigate other types of adhesive defects, as well as defects in other fields, such as weld defects. The introduction of basic artificial neural networks (ANNs) to this approach yields a significant improvement in terms of accuracy, and in terms of simplifying the interpretation of results.

The main novelty of this work lies in the application of modal acoustic emission analysis to the differentiation between fracture-modes of adhesively-bonded joints. Modal AE analysis is not believed to have previously been applied to the fracture of adhesively-bonded joints. In this study, through both experimental work and simulation, it is shown that the fracture-mode does significantly affect the wave-modes generated. It is however also seen that variation of other parameters has a similar effect on the wave-modes, and thus simple modal analysis alone does not provide a robust classifier of fracture-mode.

Further novelty lies in the FEA simulation of AE generation and propagation in adhesively-bonded joints. This is believed to be the first instance of the use of dynamic finite element analysis to simulate AE generation and propagation in adhesively-bonded joints. The use of this method has allowed controlled investigation of some of the parameters affecting wave-propagation, and has thus allowed the generalisability of previous experimental results to be investigated. The use of simulation has also allowed analysis of the true effects of fracture-mode to be investigated, with all other parameters remaining constant, a feat which is not typically possible with an experimental set-up due to the variation in real-world bond quality.

1.3 Thesis Outline

This thesis is structured in 7 chapters, a summary of their content is provided below:

1. Introduction

   This chapter introduces the general topic of acoustic emission testing of adhesively-bonded joints and summarises the current state of research in this area. It also outlines the objectives of this work and the novelty and contribution of the research.

2. Literature Review

   This chapter provides an introduction to, and critical review of, the current state-of-the-art in areas critical to this work. First, an overview of the advantages of, and problems faced in, adhesive bonding is given. This is followed by a review of acoustic emission, in terms of basic working theory and equipment and also current analysis techniques. A more detailed review of the application of acoustic emission techniques to investigation of adhesively-bonded joints is then given, highlighting the gaps in knowledge this thesis aims to fill. This is followed by a review of the relatively young and rapidly-developing field of finite element simulation of acoustic emission.

3. Pencil-Lead-Break based AE Tests

   This chapter describes a series of experiments using a pencil-lead-break source on various bonded, un-bonded and defective specimens to establish the effects of the bonded layer on AE propagation. This chapter includes details of the experimental set-up, signal processing, and analysis and discussion of the results obtained.

4. AE-Instrumented Destructive Tests

   This chapter contains details of experimental work conducted to investigate the potential use of modal AE analysis to differentiate between Mode-I (Crack-opening) and Mode-II (Shear) fracture. It includes the experimental set-up, signal-processing methodology and analysis and discussion of the results.

5. FEA of PLB Tests

   This chapter describes the finite element simulations of the pencil-lead-break tests. This includes the development of geometry, boundary conditions, meshing, simulation settings and post-processing methods which were utilised. It also includes validation of the model against theoretical and experimental results, and analysis and discussion of the results obtained.

6. FEA of Destructive Tests

   This chapter details dynamic finite element simulations of mixed-mode-bending tests developed to further investigate the differences in the wave-modes excited by different fracture-modes. It describes the development of geometry, boundary conditions, meshing, simulation settings and post-processing methods, and includes analysis and discussion of the results.

7. Conclusions

   This chapter summarises the most significant findings of the study, as detailed in the previous chapters. Recommendations for future work and for the application of this research are also provided.

Chapter 2

Literature Review

This chapter provides an overview of pertinent literature and background theory relating to the topics of adhesive-bonding, Acoustic Emission theory and application, and Dynamic Finite Element Analysis of Acoustic Emission. This chapter highlights gaps in the current knowledge and abilities in these fields, and introduces a number of concepts and techniques used throughout this project.

2.1 Adhesive-Bonding

Since the introduction of synthetic polymers in the early 1900s adhesives have increasingly become used in the place of more traditional mechanical fasteners, such as bolts and rivets. When used correctly they are capable of providing a preferable stress distribution across the area of a joint (not an entirely uniform stress distribution as sometimes stated), allowing greater joint stiffness and higher loading bearing. They also provide a number of other advantages such as being lighter than equivalent mechanical joints, having useful damping properties, offering good corrosion resistance and being suitable for joining dissimilar materials [12]. Due to these properties they are also increasingly being used in place of welding; in this context they are also advantageous as they can avoid heat-induced sensitisation, deformation or burn-through of the materials being joined. Due to their improved stress distribution, adhesives are the fastener of choice for composite materials which can be unsuitable for the high bearing stresses introduced by mechanical fasteners [12].

These advantages have led to adhesive bonding being used in many industries. In the aerospace industry it is used extensively for the bonding of skins to the underlying framework, but in some cases also for the joining of inner and outer frame members [13]. In space exploration, adhesives have been extensively used for the construction of composite panels, created by bonding metallic skins to honeycomb cores [14]. The rail industry uses adhesives extensively for internal finishing parts of train carriages, but as movement is being made towards lighter, more efficient trains, their use in more significant structural components, such as composite roof panels, is becoming more prominent [15]. The automotive industry uses adhesives for a variety of internal trim, but also for hem-flange bonding of panels such as doors and bonnets, a process in which one sheet of metal is folded over the edge of another, to join the two panels together while creating a strong and stiff edge. Another use in the automotive industry is anti-flutter bonding, in which adhesive is

applied between the inner and outer metal panels to prevent rattling [16]. The marine industry also uses adhesives extensively, particularly in the construction of small pleasure-craft and racing-yachts. Common applications being bonding of decks to hulls, bonding bulkheads to hulls, and the construction of composite honeycomb panels used in high-performance yachts [17]. The wind energy industry is also heavily reliant on adhesive bonding, with composite turbine blades often being made in two halves, which are then bonded together, or as a single outer shell, which then has internal stiffening beams bonded into it [7].

2.1.1 Adhesive Types

An ever-growing array of adhesives exists, with new formulations being constantly developed and tailored to suit specific applications. According to Papon [18], these can be broken down into three main families of adhesives, though with many more sub-categories within these. These three main families are; adhesives implemented via a physical process, pressure-sensitive adhesives, and adhesives implemented via chemical bonding.

Adhesives implemented by physical processes, refers to adhesives which change from a liquid-state to solid-state to form a bond by evaporation of the solvent component of the adhesive, water diffusion, or cooling. This includes water-based, solvent-based, dispersion-based and hot-melt adhesives. These types of adhesive are cheap and readily available, but of relatively low strength. They are used extensively for arts and crafts, furniture production, stationary, and medicine, but are generally not well suited for industrial use.

Pressure sensitive adhesives are visco-elastic solids which which can instantly adhere to a surface with the application of pressure [19]. These are typically silicone-, polyacrylate- or polydiene-based adhesives, which are generally supplied as self-adhesives for tapes, films or paper. These adhesives are typically very low strength and are non-permanent or semi-permanent, but offer the advantages of being fast and also of being repositionable [18]. Typical examples of their use are masking-tape, sticky-notes and sticking plasters.

Adhesives implemented by chemical reaction make up the majority of structural adhesives used in industrial applications, as well as high performance household adhesives. These adhesives work by the process of polymerisation, in which individual molecules join together to form a chain. This reaction can be initiated by the mixing of the adhesive with a catalyst (2-part adhesive), the reaction of the adhesive with elements in the environment such as oxygen or moisture, or the reaction of the adhesive with an external energy source such as heat, UV light or electromagnetic radiation [18]. Typical examples of these are 2-part Epoxies, Aminoplasts, Phenoplasts and Cyanoacrylates amongst others. These adhesives are available as liquids, pastes, aerosol sprays and also pre-impregnated tapes and sheets. When used correctly, these adhesives can offer very high-strength, permanent joints between a wide range of different materials.

2.1.2 Preparation, Application, and Curing of Adhesives

One-part adhesives, which react with the environment or with an energy source can be the simplest to work with, as a single layer of the adhesive can be applied straight from the container, without need for mixing. Two-part adhesives do however require mixing of the two parts prior to application. This step is critical, as the correct quantities of each part must be mixed to create a stoichiometric mixture, in which the reactants are correctly balanced for polymerisation [20].

Improper measurement of each part, or inadequate mixing of the parts can result in sections of unpolymerised adhesive, which has little to no strength. Two-part adhesives can be supplied with each part in a separate container, which for manual measurement and mixing means the components must be weighed to ensure the correct ratio before mixing manually with a spatula [21]. A better solution for manual mixing is the supply of both parts in a double-barrelled syringe, ensuring that the correct ratio of the parts can be easily acquired without having to weigh them. The two parts can then be mixed manually, or in some cases a mixing nozzle can be fitted to the syringe, so the adhesive can be applied directly to the adherends from the syringe, having already been mixed [22]. For more industrial applications in which large quantities of adhesives are being mixed, specialised mixing machines can be used. These vary in design based on the properties and quantity of the adhesive under preparation, but typically consist of a fixed mixing drum with some form of rotating mixing blade, agitator, or kneader. Centrifugal mixers in which the whole drum rotates in the opposite direction to the agitators also exist and are advantageous due to their fast mixing time. Vacuum mixing, the mixing of adhesives at below atmospheric pressure, is also used for certain applications. This has the advantage of de-aeration, which reduces the chance of voids or porosity within the adhesive, as well as being advantageous for certain adhesive formulations which may react in an undesirable manner with oxygen or with water present in the atmosphere. In some cases the measurement and mixing of the adhesives is done continuously using an integrated metering and mixing system, which significantly improves workflow when compared to the batch preparation of adhesives [22].

The most basic form of adhesive application is manual application, in which the adhesive is applied to the adherends using some form of spatula or spreading stick, or is extruded onto the adherends from the nozzle of a manual syringe or handgun-type applicator. This is cheap and simple, but the quality of the joint can be greatly affected by the skill of the personnel applying the adhesive. In larger-scale industrial applications, robotic applicators can be used to apply a bead, or spray a jet, of adhesive onto the adherends. Depending on the application, this can be done with either a fixed nozzle, which parts pass underneath on a conveyor, or with a nozzle mounted on a robot arm, allowing it to move in three dimensions. While the use of automated systems does not necessarily lead directly to a stronger joint, removing the element of human error allows joints to be made much more consistently, and therefore makes their behaviour much more predictable [22].

2.1.3 Adhesive Defects and Failures

While adhesive-bonding does offer many advantages and has been widely adopted across these industries, its use in safety-critical applications has been restricted by inadequate methods of non-destructive testing [4]. As discussed in the following sections there are a variety of potentially strength-reducing defects which may occur in bonds, only some of which can be readily detected with conventional NDT methods. The consequences of failure of an adhesive joint can vary greatly, depending on the application. In many cases it may just result in the minor inconvenience and cost of having to carry out repair work. At the other end of the spectrum is the Aloha Airlines Flight 243 incident, in which the debonding of a lap-joint in the crown skin of a Boeing 737-200 ultimately led to the explosive decompression of the planes cabin, resulting in the loss of one life, the severe injury of eight others, and the loss of the plane [13, 23].

As illustrated in Figure 2.1, there are a variety of defects which may occur within an adhesively-bonded joint which may result in reduced overall joint strength and ultimately lead to failure. The majority of these defects are introduced during the manufacture of the joint. Porosity can be in-

troduced by the entrapment of air or by the chemical reactions involved in the curing process of the adhesive. Some extent of porosity is present in most bond-lines and only becomes problematic when its presence is excessive or unexpected. Cracking of the adhesive may occur due to issues in the curing process, such as thermal shrinkage, or may alternatively occur due to overloading or fatigue during service. Poor cure of the adhesive can occur due to incorrect proportions of the adhesive components being mixed, improper mixing of these components or insufficient thermal exposure in thermally-activated adhesives. Voids may be introduced to a joint by air becoming trapped during the lay-up of the joint. This can be caused by insufficient or uneven spreading of the adhesive and also by relative movement between the adherends during cure. Surface unbonds are a type of void located between the adherend and adhesive which generally are the result of the adhesive being unevenly applied to only one adherend before the adherends are joined. A zero-volume unbond, or kissing bond, is an unbond in which the adhesive makes contact with the adherend, but does not fully adhere to it. This often results from inappropriate surface preparation or contamination. The result can vary from merely exhibiting reduced bond strength, to no bond strength at all. This is one of the most dangerous types of defects as it is hard to detect with standard non-destructive testing methods as there is no volume of void [4].

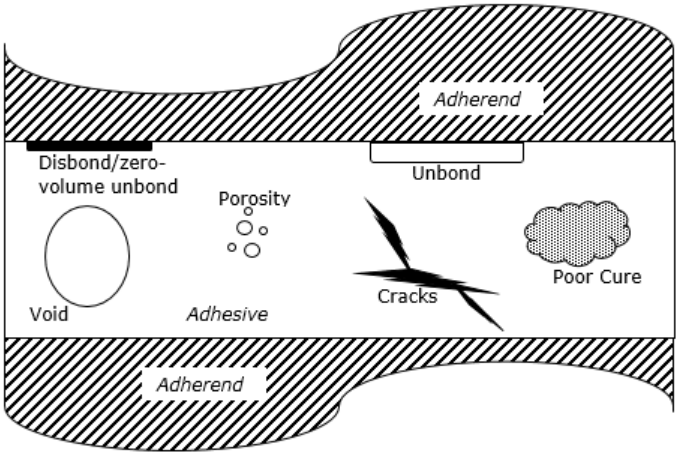

Figure 2.1: Potential bond-line defect types

The criticality of these defects is not only dependent on their severity, but also on their location and environmental conditions. Adhesive-bonds do not exhibit a uniform stress distribution, as is commonly assumed, but rather feature higher stresses around the edges than in the centre. This makes them highly tolerant of defects existing within the low stress central region of the joint, as has been demonstrated both theoretically and experimentally by a number of authors [4, 24, 25].

There are three main fracture-modes by which an adhesive joint can fail, which may occur individually or in combination, producing a mixed-mode failure. The main modes are illustrated in Figure 2.2. Mode-I is characterised by crack-opening, while modes -II and -III are both shearing modes, more specifically referred to as sliding, or in-plane shear, and tearing, or out-of-plane shear.

Joints are most commonly designed to be predominantly loaded in tensile shear, as this is how they are strongest. Peel and cleavage loads should be avoided wherever possible, as adhesive bonds are much more susceptible to failure under these loadings [26, 27]. While it should be minimised by suitable design, mixed-mode loading is however still a common occurrence for a variety of reasons. These can include other design constraints which prevent the joint from being oriented

in pure shear, varying loading orientations, deformation of the structure under load leading to variation in load orientation, manufacturing eccentricities, elastic mismatch of the adherends, thermal mismatch of the adherends and the adhesive, or the introduction of additional unplanned loadings, such as those from impact or collision [27]. Even a simple single-lap joint loaded in pure tension can be subject to some bending and the introduction of peel loads at the ends of the overlap due to the adherends being offset from each other.

The failure resulting from these loadings and the previously described defects can be described as adhesive, cohesive or adherend failure, or any combination of these. Adhesive failure is the separation of the adhesive from one or more of the adherends due to failure of the bonding between them. Cohesive failure is failure occurring within the adhesive itself, generally leaving a layer of adhesive stuck to both adherends. Adherend failure occurs when the adherend yields before the adhesive fails.

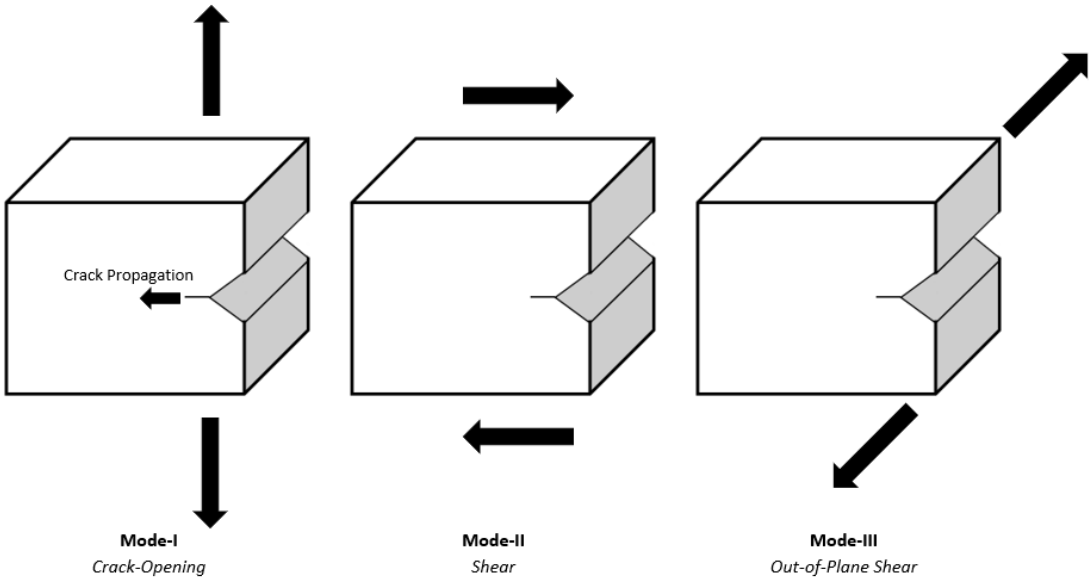

Figure 2.2: Fracture-modes

2.1.4 NDT of Adhesively-Bonded Joints

Quality assessment and condition monitoring of adhesive joints is faced with a number of challenges. First of all there is no non-destructive method which can directly assess strength of adhesion, this can only be done by destructive testing. There are a number of measurable variables which can be interpreted as an indication of strength, or lack thereof, but are not direct measurements of bond strength [4]. Methods such as ultrasound and X-ray have been well proven for identification of voids and cracks and can be used to assess the contact area of the bond, but they do not however assess the strength of the bond, so while they are valuable tools for identifying certain defects they are unable to give an overall picture of bond strength. Another limiting issue is the time taken by scanning methods such as ultrasound. In a large bonded structure, the scanning of the entire bonded area can be an extremely time consuming process. This becomes further complicated by access to the joint. In many practical situations access is only available to one

side of the joint being assessed, which limits the type of testing that can be carried out [4]. The inaccessibility of certain structures also provides a challenge to conventional inspection methods [28], although advances in robotics technology are improving this situation, with a variety of remote controlled and autonomous inspection robots having been developed, such as the six-legged, suction-cup footed, walker-robot developed by Herraiz et al. [29], or the suction-supported or magnet-supported tracked crawler robots built by International Climbing Machines [30]. These robots have been developed to climb structures such as wind turbine blades, aircraft fuselages or ships hulls, and can be equipped with cameras, ultrasound sensors and/or AE sensors, depending on the application.

Many techniques to assess adhesive-bond quality have been developed, with varying levels of success and differing merits in terms of accuracy and practicality. Various ultrasonic techniques, such as through-transmission, pulse-echo and pitch-and-catch systems are widely used throughout industry. While they are extremely effective in certain situations, they can be limited by aspects such as; requiring access to both sides of the bond (for through-transmission), the limited depth that can be inspected by single-sided approaches,the inability to detect certain defects such as zero-volume disbonds, and the necessity for sensor coupling by water jet or immersion bath, though this can be avoided by the use of air-coupled systems [31]. These techniques are also generally reliant on scanning of the entire area being inspected, an extremely time-consuming process for large areas, with areas of several square metres potentially taking over an hour to scan, depending on the desired resolution [4], though this can be improved by the use of Lamb-, or plate-waves, which can be used to inspect a path rather than just a point. Techniques such as radiography and infrared-thermography can inspect larger areas much faster, but radiography is largely insensitive to the presence of adhesive unless it is combined with a metallic filler, as the density of the adherends is generally much higher than that of the adhesive [32]. While infrared thermography provides a similar sensitivity to near-surface defects as ultrasonic pulse-echo techniques, it is less sensitive to deeper defects and is generally unsuitable for inspection of both thin layers and specimens made of highly conductive materials, such as metals [4]. A variety of other techniques including impedance, and sonic- and ultrasonic vibration based methods are also available and have their own advantages; the majority, however, are still restricted by the time-consuming requirement of scanning of the bond area. One technique which avoids this issue is acoustic emission.

2.2 Acoustic Emission

2.2.1 Introduction

Acoustic emission is the phenomena of transient elastic waves being generated by the sudden redistribution of stress within a material. The elastic waves will propagate through the material to the object's surface, where they can then be detected by sensors. Acoustic emission can be generated by a number of sources including; mechanical deformation, fracture, phase transformation, corrosion, friction and magnetic processes [33]. AE differs significantly from the majority of other NDT techniques in two respects. First of all, the signals detected by the AE system are generated by the object which is under examination, rather than being generated by the test equipment. Secondly, AE is the investigation of dynamic processes such as the development of defects within a specimen. AE testing is therefore not concerned with detecting the presence of defects in the manner which other NDT techniques tend to be, but is appropriate for monitoring the initiation and progression of defects. AE testing therefore requires some external stimulus such as a load

being applied to the object under investigation. This makes AE well suited to the monitoring of structures and systems which are in operation, as the working conditions can be enough to trigger the initiation or development of defects and therefore cause the generation of acoustic emissions. In other scenarios, a proof load can be applied to specimens specifically with the intent of generating AE; the loading at which the onset of AE occurs can then be used as an indicator of the specimens condition [34].

2.2.2 Advantages and Limitations

AE testing is generally not an alternative to other NDT methods, such as ultrasound, but is a complimentary method, as all of the available techniques have various strengths and weaknesses [34]. AE has the advantage of being able to cover large areas of a structure at once, and offers the opportunity to continuously, or semi-continuously, monitor the structure, with either permanently- or temporarily-installed sensors. AE is also ideal to use while equipment is in operation, particularly as, once installed, there is no requirement for an operator to be present [34]. This poses a significant advantage for situations in which an operator could not be present during operation, for example on the wings of a plane or the blades of a wind turbine. The ability to perform source-location is also a great advantage of the technique, as defects and damage can be located quickly without inspecting the entire structure. Additionally, as AE detects defect propagation, as opposed to detecting defect presence, there is no minimum physical defect size required for a defect to be detected [35]. The fact that AE only detects propagating defects can also be advantageous in the case of defect-tolerant structures, as it will allow defects which pose a threat to the structure to be identified, while other more harmless defects will be ignored. It is emphasised by Hart-Smith [13] that while adhesive bonding may offer an improved stress-distribution compared to other joining methods, that the stress distribution is not actually uniform, as is often wrongly stated, and thus not all defects or damage will actually cause a reduction in joint strength.

While AE has many advantages, it is not free of limitations. The fact that AE is currently a more qualitative than quantitative technique, and cannot directly detect the size of defects, means that its usefulness is limited when it comes to predicting the remaining lifespan of a structure, or the necessity for repair. It is therefore best used in conjunction with other techniques which are better suited to this aspect of NDT. The requirement for defects to be propagating for detection also poses a disadvantage for the technique, as it means that for AE to be used, damage must be caused to the structure, making it more of a semi-destructive testing technique than non-destructive.

2.2.3 Wave-Propagation

Waves propagating in an elastic medium can be represented by the general wave Equation 2.1, with the use of appropriate boundary conditions [36].

$$\frac{\partial^2 \emptyset}{\partial t^2} = c^2 \nabla^2 \emptyset \tag{2.1}$$

Where:

t : time

c : wave-velocity

∇^2 : Laplacian operator in cartesian coordinates = $\frac{\partial^2}{\partial x^2} + \frac{\partial^2}{\partial y^2} + \frac{\partial^2}{\partial z^2}$

$\emptyset$: Potential function, representing two plane waves propagating in positive and negative directions

For deformation occurring in a single direction, for example the x-direction, the general solution of the potential function is:

$$\emptyset = f(x - ct) + F(x + ct) \tag{2.2}$$

Where:

f : Function corresponding to wave travelling in +x direction

F : Function corresponding to wave travelling in -x direction

As previously stated, the boundary conditions determine how the elastic waves will actually propagate, and will determine the characteristics of any recorded AE signal. Within an infinite medium, or something that can be approximated as such (such as within the bulk of a large block specimen), waves will propagate as a combination of longitudinal and shear waves. Within an a medium bound by only one surface, such as close to the surface of a large block, the elastic waves will propagate as surface waves of either the Rayleigh or Love type. In a medium bound by two surfaces, such as a thin plate or sheet, waves will propagate in the symmetrical or asymmetrical Lamb-modes, also referred to as the extensional or flexural Lamb-modes.

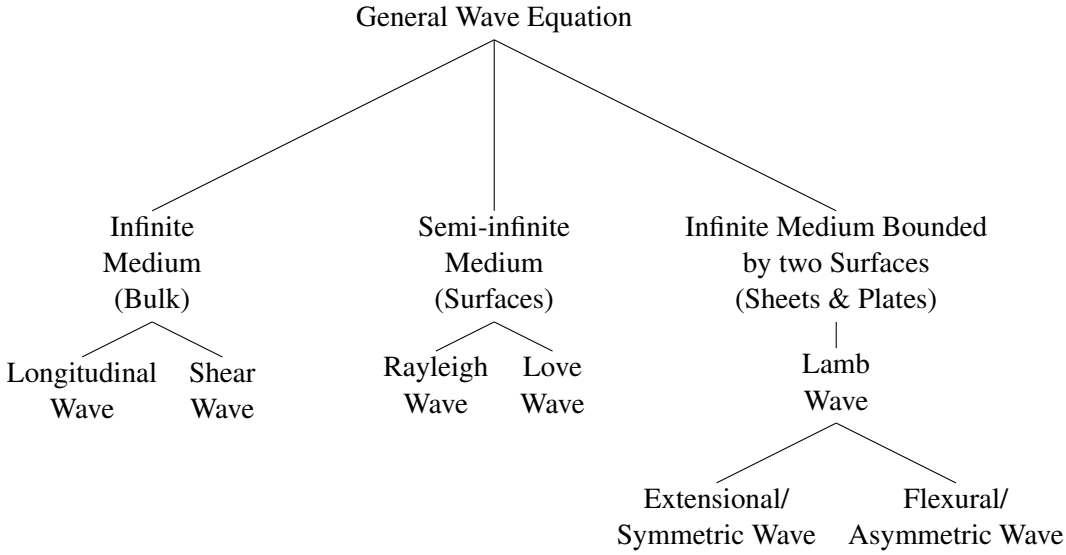

Figure 2.3: Wave-modes by media type

Within the bulk of a large specimen, AE waves consist of longitudinal and shear waves. In a Longitudinal wave, also know as a compression, dilation, pressure, or P-wave, localised compression and dilation of the material take place with the particle motion in line with the direction of wave-propagation, as shown in figure 2.4 [37–39]. Shear waves, also referred to as transverse, or S-waves, consist of particle motion perpendicular to the direction of wave-propagation, as per figure 2.5.

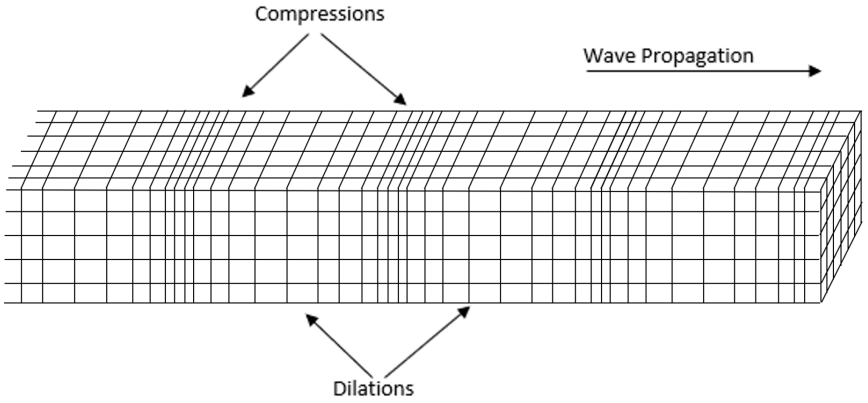

Figure 2.4: Longitudinal Wave

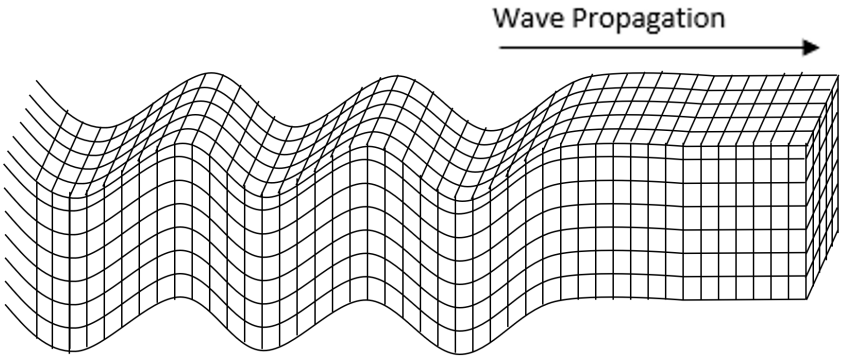

Figure 2.5: Shear Wave

The propagation velocities of both longitudinal and shear waves are independent of frequency, and are governed by the following expressions [37, 39]:

For Longitudinal waves:

$$c_1 = \sqrt{\frac{\lambda' + 2\mu}{\rho}} \tag{2.3}$$

For shear waves:

$$c_2 = \sqrt{\frac{\mu}{\rho}} \tag{2.4}$$

Where:

c_1 : Longitudinal wave-velocity

λ' : Lame's constant = $\frac{E_y}{(1+v)(1-2v)}$

μ : Rigidity Modulus = $\frac{E_y}{2(1+v)}$

E_y : Young's Modulus

v : Poisson's ratio

ρ : Density

The wavelength at a particular frequency can be calculated using the following equation [39]:

$$\lambda = \frac{c}{f} \tag{2.5}$$

Where:

λ : Wavelength

c : wave-velocity

f : Wave frequency

Surface waves are dominant in semi-infinite mediums, in which there is a single free surface located suitably far from other surfaces as to avoid interaction. These waves are commonly of interest in AE due to the sensors generally being surface mounted, rather than embedded within the bulk of a specimen. Two types of surface wave exist, the Rayleigh wave, and the Love wave. In a Rayleigh wave particles oscillate in an orbital manner, much like typical water waves, moving in the directions in and out of the surface, and along the surface in the direction of wave-propagation. In contrast to this, a Love wave consists of particle oscillation in the direction perpendicular to the direction of wave-propagation, similar to a shear wave [37].

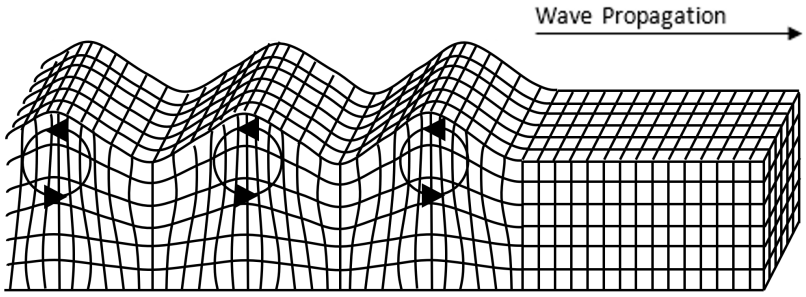

Figure 2.6: Rayleigh Wave

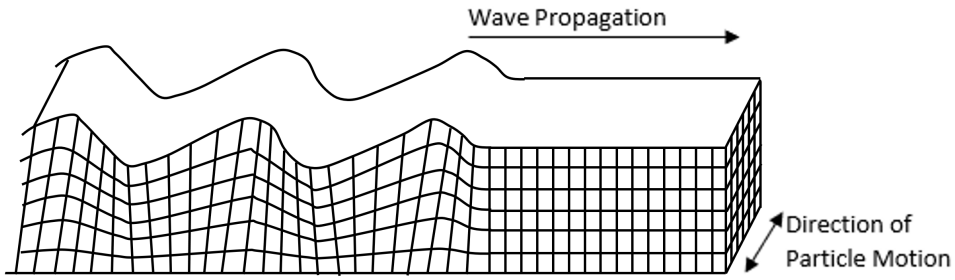

Figure 2.7: Love Wave

The propagation of surface waves is slower than that of bulk waves, and the velocity of a Rayleigh wave can be estimated as follows [39]:

$$c_r = 0.92c_2 \tag{2.6}$$

Within a thin sheet or plate, wave-propagation becomes more complex, due to the interaction of the waves on each of the surfaces. For relatively thick specimens, where the material is significantly thicker than the wavelength, separate Rayleigh waves can propagate on each surface. However, when the plate thickness is smaller than the wave-length, the interaction between the surfaces results in the generation of Lamb waves, also known as plate waves [38].

Two fundamental modes of Lamb wave exist, the Symmetric and the Asymmetric modes. These modes can be visualised as the Rayleigh waves on the opposing surfaces being in-phase with each other (Symmetric) resulting in an extensional wave, or out-of-phase (Asymmetric) resulting in a flexural wave.

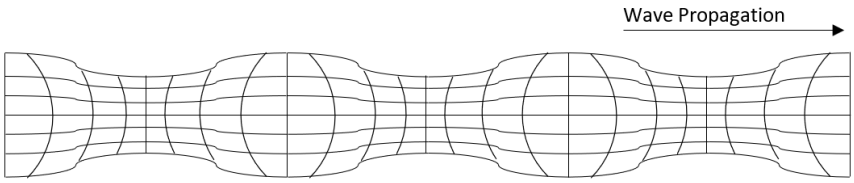

Figure 2.8: Symmetric Lamb Wave

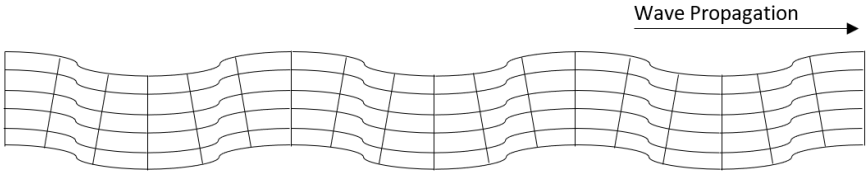

Figure 2.9: Asymmetric Lamb Wave

The Rayleigh-Lamb equations are given as Equations 2.7 and 2.8 below [40]:

$$Symmetric: \frac{\tan(qh)}{\tan(ph)} = \frac{4k^2pq}{(k^2-q^2)^2} \tag{2.7}$$

$$Asymmetric: \frac{\tan(qh)}{\tan(ph)} = \frac{(k^2-q^2)^2}{4k^2pq} \tag{2.8}$$

Where:

$p^2 = \frac{\omega^2}{c_l^2} - k^2$

$q^2 = \frac{\omega^2}{c_t^2} - k^2$

h : Half the sheet thickness

ω : Angular frequency

k : Wave number

c_l : Longitudinal wave-velocity

c_t : Shear wave-velocity

Phase velocity: $c_p = \frac{\omega}{k}$

Group-velocity: $g = \frac{\omega}{dk}$

Based on these equations, group-velocity curves, representing the variation in wave-propagation velocities with frequency, can be plotted, as shown in Figure 2.10.

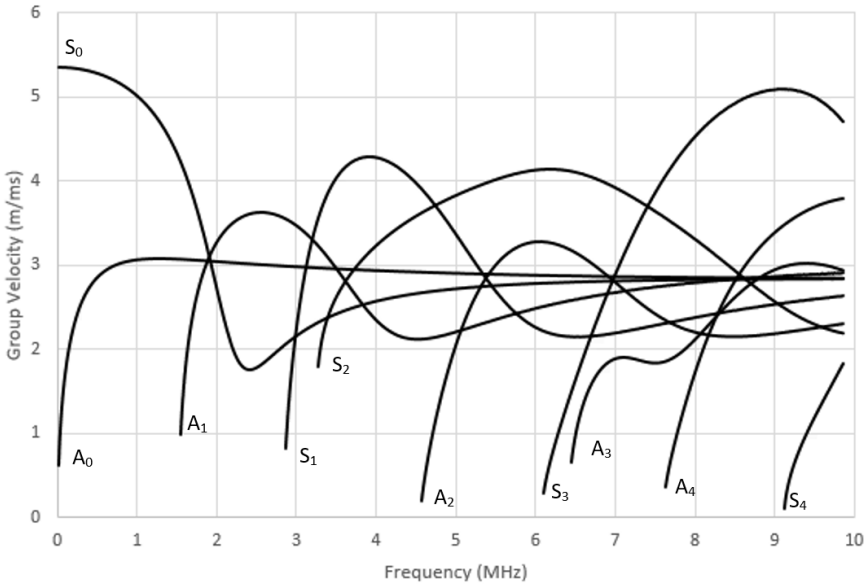

Figure 2.10: Group Dispersion-Curves for Symmetric and Asymmetric Type Lamb Waves (Example for 1 mm Aluminium Plate)

The velocity of a Lamb wave is frequency, mode and thickness dependent, thus resulting in rather complex behaviour for broadband signals, such as are typical in AE. A signal can contain multiple modes and frequencies, thus giving the signal a variety of arrival times at a sensor, and so requiring a more in-depth approach to signal processing. Which wave-modes are generated by a source is dependent on the source orientation and position, this will be discussed further in a subsequent section.

Propagating waves will, at some point, reach an interface between one material and another. At this point, the wave may be transmitted into the adjoining medium, reflected, or may propagate along the interface. Generally a combination of these mechanisms will occur. At interfaces between materials, or at changes in geometry, mode-conversion may also occur, in which waves will change from one type to another. For example, in a specimen consisting of a large block with a sheet attached to it, it is likely that Lamb-waves will form in the sheet section, but in the block section, only bulk and surface waves will propagate, so mode conversion will occur at the change in geometry. In the case of this project, mode conversion can occur at the interface between bonded and un-bonded sections of a specimen.

The reflection and refraction of the elastic waves is determined by the angle of incidence and the acoustic impedance (Z) of the two materials. Acoustic impedance is a material property that

can be calculated as follows [38]:

$$Z = \rho \times c \tag{2.9}$$

Where:

ρ : Material density

c : wave-velocity

The difference in acoustic impedance between the two materials can be used to approximate the proportion of energy which will be transmitted, and the proportion which will be reflected. For materials with impedances Z_1 and Z_2, the proportion of energy reflected E_r can be approximated by:

$$E_r = \frac{(Z_1 - Z_2)^2}{(Z_1 + Z_2)^2} \tag{2.10}$$

For materials of similar impedance, energy will be largely transmitted, while materials of greatly differing impedance will result in a high level of reflection.

2.2.4 Attenuation

While elastic waves can travel great distances under the correct conditions, their amplitude will reduce as the distance from the source increases. This phenomenon is called attenuation, and can be attributed to four main mechanisms; geometric attenuation, scattering/diffraction, material damping and dispersion.

Geometric attenuation is due to the spreading of a wave in space. In an infinite 3D space, the wave from a localised source will propagate outwards in a spherical pattern. Due to conservation of energy, the amount of energy contained within the wave remains constant. Thus as the radius of the wave-front increases, and the area over which the energy is spread increases, the concentration of energy at any given point on the wave-front must decrease. The wave amplitude (A) is therefore proportional to the inverse of the radius (r) of the wave-front $(A \propto 1/r)$. In a thin, sheet-type specimen, the geometric spreading can be approximated as being 2D, with the wave-front expanding as a cylinder of increasing radius, rather than a sphere. In this case the amplitude (A) will reduce proportionally to the square root of the inverse of the radius (r) of the wave-front $(A \propto \sqrt{1/r})$ [41, 42]. Attenuation in real-world structures is however more complex, due to the impact of reflections which can act to reduce the effective attenuation, in all but the largest of structures. In thin sheets or narrow rods, waves can cover significant distances with minimal attenuation, a feature which can be extremely useful when correctly exploited for techniques such as AE or certain types of ultrasound.

Scattering and diffraction contribute to attenuation in inhomogeneous media, where voids, cracks, inclusions and complex internal boundaries can re-direct the propagating wave on a localised scale. Scattering occurs in a similar manner to reflection at the edge of a specimen. When the wave reaches an internal interface with a material of a different acoustic impedance, such as a void, or an inclusion, a proportion of the wave will be reflected back, while the remainder of the wave will pass through the boundary into the secondary material. Diffraction of the elastic wave can also be caused by sharp-edged internal features, such as cracks. Both scattering and

diffraction can lead to increased attenuation within a specimen. Scattering and diffraction, along with edge-reflections, result in waves propagating in different directions, which can in turn result in interference, which can cause a further change in attenuation. Interference occurs when multiple waves interact. If the waves are in phase with each other, then the result is that of positive interference, and the wave amplitude will be greatly increased as the waves are essentially added together. While if the waves are out of phase, they can cause a significant reduction in amplitude, potentially cancelling each other out.

Material damping refers to the conversion of mechanical energy related to the wave motion to thermal energy. Hooke's law assumes stress and strain are proportional until yield, and in-phase, but this is only valid when the loading-rate is so slow that the deformation process may be considered static. With higher loading-rates however, the resultant deformation will lag behind the applied load. In the case of a cyclic loading the lag results in a hysteresis loop, as shown in Figure 2.11. The area between the loading and unloading curves represents the energy lost as heat.

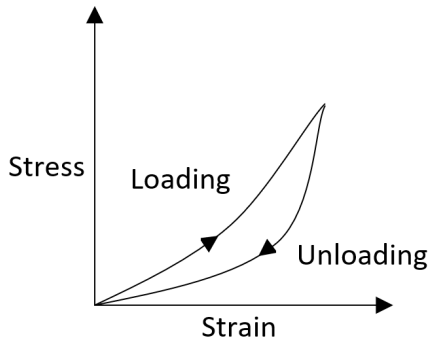

Figure 2.11: Hysteresis Loop

For materials with low damping, generally those typically considered to be linear-elastic, it is typical to quantify material damping using the dimensionless quantities of either Specific Damping Capacity (ψ) or Logarithmic Decrement (δ), measured by either cyclic loading or free-vibration respectively.

Specific damping capacity is defined as the ratio of energy lost per loading-cycle to maximum total strain energy [43]:

$$\psi = \frac{\delta W}{W} \tag{2.11}$$

Where:

δW : Energy dissipated in a cycle

W : Elastic energy stored when strain is at its maximum

When considering materials with significant visco-elastic properties, such as polymers, a more detailed approach is necessary, particularly if attempting to simulate the material behaviour.

Multiple different models of viscoelasticity exist, all of which can be represented in terms of springs and dashpot dampers, connected in series, parallel, or a combination of both series and parallel.

Behaviour of a simple linear elastic material with a stiffness E can be represented by a single linear elastic spring, as shown in Figure 2.12 and is governed by the constitutive Equation 2.12

[43]:

$$\varepsilon = \frac{1}{E}\sigma \tag{2.12}$$

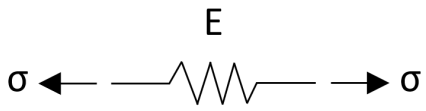

Figure 2.12: Linear Elastic Spring

In this case strain is instantaneous and directly proportional to the applied load. This model makes up the elastic part of a viscoelastic model. The viscous part of the model can be represented by a dashpot-style damper, as shown in Figure 2.13. The dashpot responds with a strain-rate proportional to the applied stress [43]:

$$\dot{\varepsilon} = \frac{1}{\eta}\sigma \tag{2.13}$$

Assuming zero initial strain, for an applied stress σ_0 the strain is given by [43]:

$$\varepsilon = \frac{\sigma_0}{\eta}t \tag{2.14}$$

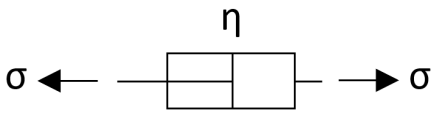

Figure 2.13: Linear Dashpot

For as long as the stress is applied, the strain will increase linearly. Upon unloading, the strain will remain constant, as illustrated in Figure 2.14.

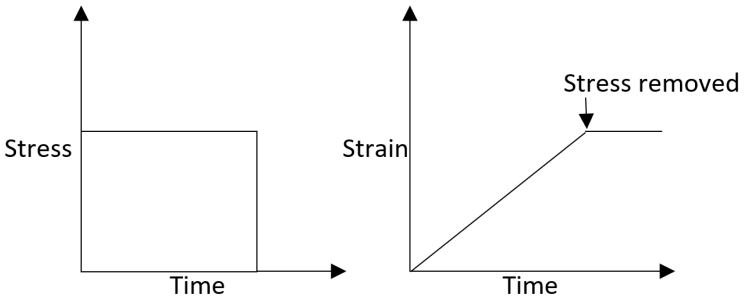

Figure 2.14: Linear Dashpot Response [43]

The Maxwell model for viscoelasticity places the viscous damper and linear elastic spring in series, as illustrated in Figure 2.15. For equilibrium, there must be uniform stress (σ_2) throughout both elements of the model, and the total strain will be comprised of strain in the spring element (ε_1) and strain in the dashpot element (ε_2). This yields the following three equations [43]:

$$\varepsilon_1 = \frac{1}{E}\sigma, \qquad \dot{\varepsilon}_1 = \frac{1}{\eta}\sigma, \qquad \varepsilon = \varepsilon_1 + \varepsilon_2 \tag{2.15}$$

which can be rearranged and combined to give the Maxwell Model:

$$\sigma + \frac{\eta}{E}\dot{\sigma} = \eta\dot{\varepsilon} \tag{2.16}$$

The response of the Maxwell model to instantaneous loading and unloading is illustrated in Figure 2.16. Upon application of load the spring element will be instantaneously strained, while the dashpot will take time, with strain increasing linearly until unloading occurs. Upon unloading, the spring will instantaneously recover, whereas there is no driving force for the dashpot to recover, and it will thus remain strained [43].

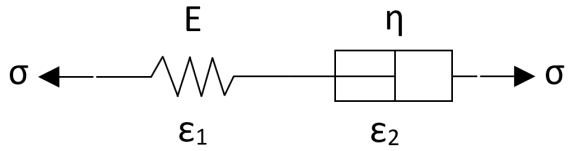

Figure 2.15: Maxwell Model

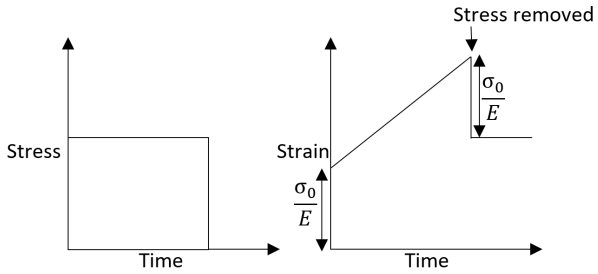

Figure 2.16: Maxwell Model Response

In contrast to the Maxwell model, the Kelvin-Voigt model places the spring and dashpot in parallel, ensuring uniform strain across the system. This yields the following three equations [43]:

$$\varepsilon = \frac{1}{E}\sigma_1, \qquad \dot{\varepsilon} = \frac{1}{\eta}\sigma_2, \qquad \sigma = \sigma_1 + \sigma_2 \tag{2.17}$$

Rearranging and combining then gives the Kelvin-Voigt Model:

$$\sigma = E\varepsilon + \eta\dot{\varepsilon} \tag{2.18}$$

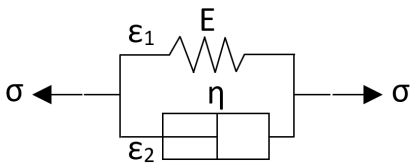

Figure 2.17: Kelvin-Voigt Model

The response of the Kelvin-Voigt model differs to the Maxwell, as on application of an instantaneous load, the motion of the spring is constrained by the movement of the dashpot, resulting in no instantaneous strain. The stress is initially taken by the dashpot, which therefore controls the initial strain-rate. As the dashpot starts to move and the spring extends, the contribution of the spring element increases until the entire load is taken by the spring and the strain reaches a maximum. This gives a curve with reducing strain-rate throughout the stroke, as opposed to the linear strain-rate of the Maxwell model. Upon unloading, the spring forces motion of the dashpot, returning the system to zero strain. As the initial return is governed by the spring, with an increasing contribution from the damper throughout the stroke, the relaxation of the Kelvin-Voigt model also follows a curve of decreasing strain-rate [43]. This response is illustrated in Figure 2.18

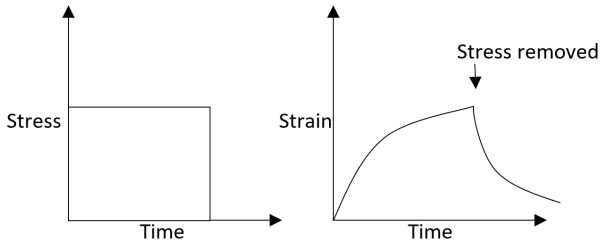

Figure 2.18: Kelvin-Voigt Response

To more accurately model the behaviour of real viscoelastic materials, these models can be combined into generalised models, which contain multiple Maxwell or Kelvin-Voigt units combined in either series or parallel. The Generalised Maxwell Model (Figure 2.19) consists of multiple Maxwell units connected in parallel with a spring and damper, while the Generalised Kelvin-Voigt model (Figure 2.20) consists of multiple Kelvin-Voigt units connected in series with a spring and damper [43].

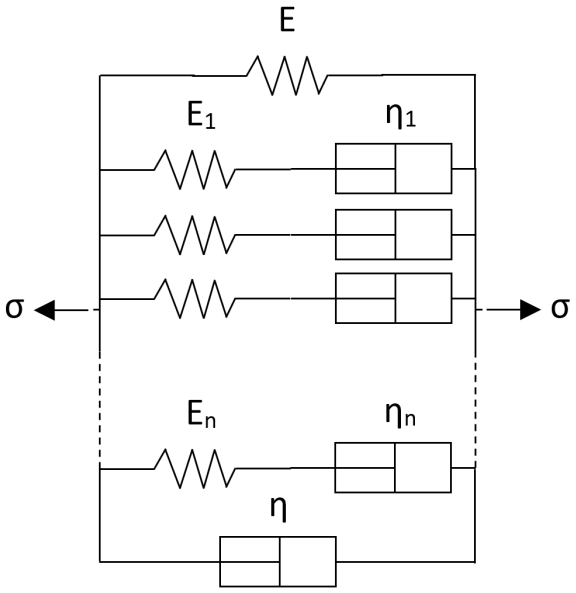

Figure 2.19: Generalised Maxwell Model

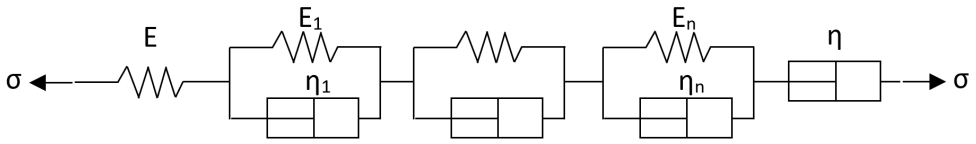

Figure 2.20: Generalised Kelvin Voigt Model

The Generalised Maxwell model is well suited to representing the behaviour of solids as the inclusion of the spring and damper in parallel result in no instantaneous strain, and does not result in residual stress upon unloading, whereas the generalised Kelvin-Voigt model is better suited to modelling a fluid-type response as the isolated spring and damper connected in series allows for instantaneous displacement and residual strain. Increasing the number of elements within a generalised model can greatly increase the accuracy with which it represents a material behaviour, but determining suitable parameters for such a model becomes incredibly challenging, and in many cases impractical [43].

Attenuation by dispersion occurs by the temporal and spacial separation of different wave-modes, and different frequency-components within a single wave-mode, due to their varying velocities [42]. Close to the source, the wave-modes will all ”overlap” resulting in a wave of high amplitude and energy. Further from the source, the faster waves will have moved ahead of the slower modes, eventually completely separating from them. The result being a signal of lower amplitude, but longer duration.

2.2.5 Time-Domain Analysis

Time-domain analysis forms a large part of traditional AE analysis. It is the simplest type of analysis in that parameters can be easily read or calculated from the raw AE signal as recorded. While more complex parameters and analysis methods now exist, time-domain parameters remain very useful and are widely used. The typical AE time-domain parameters are summarised below and are illustrated in Figure 2.21. An AE Hit, or Event, is a signal which exceeds a pre-set threshold value. Methodologies of setting the threshold level vary, though it is recommended to be 3dB to 4dB above the noise floor [44]. When a hit occurs, the signal, or certain parameters of it, will be saved and used for analysis. The accumulated number of hits or rate of hits can also be utilised in the testing of a structure. The signal duration is the time interval between the first and last threshold-crossings of a hit. The number of counts is the number of times within the duration that the signal exceeds the threshold. The Peak Amplitude is the peak voltage recorded within the hit. Amplitudes are typically expressed in decibel scale where 1V at the sensor is 0 dB AE, though they can also be expressed in terms of voltage. Rise-time is the time interval between the hit first exceeding the threshold-crossing and attaining its peak amplitude. Decay Time is the time interval between the hit attaining its peak amplitude and the last point at which the signal exceeds the threshold. Slight variations of the definition of AE energy exist depending on the equipment supplier but definitions are generally based on energy being the area under the rectified signal envelope, or in some cases the area under the rectified signal envelope but above the threshold [34]. Throughout this work the energy has been calculated independent of the signal threshold.

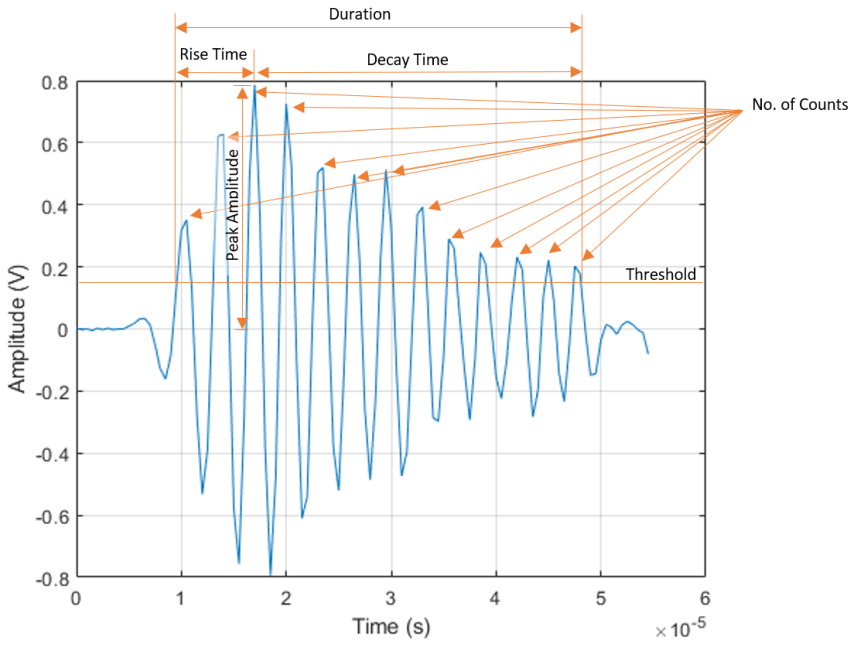

Figure 2.21: Time-Domain Parameters

2.2.6 Frequency-Domain Analysis

Frequency-domain analysis is widely used for differentiation between, and identification of, AE sources. A variety of frequency-based parameters exist, which each have various merits. Care should however be taken in the application of frequency-based techniques as the recorded frequency spectra will be affected greatly by the frequency response of the sensors and other acquisition equipment used, not just by the AE source being recorded [44].

A Fourier transform of the AE signal generates a frequency spectrum and is a good way to visualise the frequency content of a signal. Conducting a Fourier transform also allows features such peak-frequencies to be identified. Obtaining the the frequency spectrum can give a good overall image of the signal, but analysing and manipulating a frequency spectrum consisting of many data points can be cumbersome and computationally expensive. Other methods are therefore often used to summarise the frequency spectrum.

Partial powers act as a condensed frequency spectrum, by summarising the energy in a few key frequency bands. The typical process used to obtain partial powers is to filter the signal into a few different frequency bands, and then to calculate the energy in each of the filtered signals [44]. The frequency bands can be chosen either as regular intervals in the frequency-domain (often 100 kHz bands), or chosen to correspond to peaks identified from the frequency spectrum.

The peak-frequency is the frequency at which the frequency spectrum calculated by Fourier transform reaches its highest value [34, 44]. The simplicity of a single value to summarise the frequency content can be advantageous, however, for a lot of sensors the resonant-frequency of the sensor will dominate the signal, resulting in the same peak-frequency occurring for multiple different AE sources with different frequencies.

The frequency-centroid is the weighted mean of the frequency spectra, calculated from the Fourier-transform using the magnitudes of the frequencies as their weightings [34, 44]. This parameter summarises the frequency spectra into a single value without being dominated by the effects of a single peak and is thus capable of capturing subtle changes in the frequency spectra which may not be apparent in peak-frequency analysis.

The weighted peak-frequency is the root of the product of peak-frequency and frequency-centroid, thus combining the advantages of peak-frequency and frequency-centroid into a single parameter [44].

Frequency domain analysis has a variety of potential applications, but has been predominantly used to differentiate between different source-mechanisms, particularly in the failure of composites. Fourier transforms, partial powers, peak-, centroid-, and weighted-peak-frequencies were all successfully utilised by Njuhovic et al. to differentiate between the failure-modes of matrix-cracking, interface-failure, fibre-breakage and interphase-failure in metallised GFRP specimens subjected to tensile testing [45, 46]. Similarly, Kempf et al. utilised fourier-transforms, and a clustering method, based on weighted peak-frequency and partial-powers to differentiate between matrix-, interphase-, and fibre-failure in the fatigue testing of CFRP composite specimens [47]. Bak and Kalaichalvan also utilised peak-frequency to differentiate between adhesive-, fibre-tear-, and light fibre-tear-failure in adhesively bonded GFRP lap-joints [48]. An investigation of mode-I testing of metal-to-metal and metal-to-composite specimens by Droubi et al. also utilised frequency analysis in the form of partial powers, though in this case it was not used to differentiate between different failure modes, but used to illustrate the variation in frequency as the crack-front moved through the specimen, changing the source-to-sensor propagation distance [49].

2.2.7 Time-Frequency-Domain Analysis

Frequency-domain analysis is useful, but does not give the full picture of how the frequency varies throughout the duration of an AE event. Particularly in cases where dispersive wave types are dominant, the frequency content will vary significantly throughout the event's duration. A variety of approaches exist for conversion of time-domain data into time-frequency-domain. The Short-Time Fourier-Transform (ST-FT) method, also known as Short-Time Fast-Fourier-Transform (ST-FFT), captures variation in sinusoidal frequency content with time by conducting a Fourier transform of the signal over multiple short windows of the signal, thus generating a frequency spectra for each time-window. The use of a fixed time-window does however have the drawback of either poor frequency-resolution, if the chosen time window is too short, or poor time-resolution if the chosen window is too long. This issue can be avoided by the use of a continuous wavelet-transform instead of the Fourier transform. The wavelet-transform is based on comparison of the signal against a short wavelet function, which is scaled and time-shifted, instead of a sinusoidal function as is used in the Fourier transform. This approach allows the wavelet-transform to effectively use a longer window at lower frequencies and a shorter window at high frequencies, which ensures good frequency resolution at low frequency and good time-resolution at high frequency. While a fully-detailed description of the method is outside the scope of this project, a full description of the method applied to acoustic emission signals can be found in the work of Suzuki et al. [50]. Wavelet-transforms can theoretically be performed with a variety of different wavelets, including Gabor (also called Morlet), Meyer, Mexican Hat and Daubechies, but works in acoustic emission have typically used the Gabor-type wavelet as this provides the best combination of time and frequency resolution of all the available wavelets [51,52]. This is the wavelet-type used by the popular Vallen Wavelet software [53] used in this work, and also implemented in MATLAB. While the ST-FT and wavelet-transform have been the most widely used time-frequency transforms for AE so far, the Choi-Williams transform has also been used by some authors. The Choi-Williams transform provides higher time-frequency resolution than a wavelet-transform, but can be subject to the generation of parasitic interference in between the original frequency-components [54]. The Choi-Williams transform has been used most prolifically by Hamstad et al., for a variety of applications, including investigation of anisotropic attenuation of flexural wave-modes in carbon-fibre composites [55], the effects of fluid interaction with wave-propagation in multilayered vessels [56], and a comparison between the Choi-Williams Transform and Wavelet Transform for determination of group-velocities in aluminium sheets [57].

2.2.8 Modal Analysis

Modal AE analysis may be conducted through a variety of techniques, but is concerned with analysis of the different wave-modes propagating through the specimen. It can be used when dispersive wave-types such as Lamb waves exist, leading to separation of the wave-modes in the time- or time-frequency-domains, and is thus typically suitable for use in sheet-, plate-, bar-, pipe- or shell-type specimens, as opposed to bulk-type specimens. The general aim of modal analysis is to relate the wave-modes which are excited, or the relative proportions of the wave-modes excited, to features of the AE source.

The most basic method of modal analysis is peak-amplitude analysis of the time-domain signal, with peaks relating to the different wave-modes being identified by comparison with the theoretical velocities of the wave-modes. One of the most notable early examples of this is the work of Gorman, who investigated the effects of source-orientation on plate-wave propagation, by apply-

ing a PLB source to an aluminium plate at varying angles [58]. It was seen that the early part of the out-of-plane time-domain signal, corresponding to the extensional mode, reduced in amplitude with increasing source angle, while the later part of the signal, corresponding to the flexural mode, increased. To quantify this result, peak-amplitudes of the two modes were taken.

Modal analysis in the time-domain can be effective, but becomes difficult with higher numbers of wave-modes, overlapping wave-modes or the effects of features such as reflections which can make it impossible to separate the signals in the time-domain. The solution to this therefore lies in modal analysis in the time-frequency-domain. Modal analysis in the time-frequency-domain allows modes which overlap in the time-domain to be separated by frequency. In order to identify the wave-modes within the time-frequency-domain it is possible to overlay the theoretical Lamb wave dispersion-curves, providing theoretical arrival times for each wave-mode across the full frequency-range. This method is well illustrated in work by Hamstad et al. investigating the use of modal analysis to identify the effects of different source-types and source-depths using a dynamic finite element simulation [59]. The approach taken by Hamstad et al. to quantify their modal results was to identify regions of interest relating to each wave-mode, typically regions of the time-frequency-domain featuring a high level of activity. The peak values of the wavelet-transform coefficients were then taken from these regions, and the ratio of the coefficients used as an identifying feature.

Modal AE analysis has a large variety of potential applications. So far it has been applied to investigation of source orientation [58–60], source depth in simple plate and bar specimens [59,60] and in the complex geometry of a section of rail track [61]. It has also been used to great effect to differentiate between different failure modes of fibre-reinforced composites, with it being found that the in-plane nature of fibre-breakage causes a relatively large symmetric mode, while the out-of-plane nature of delamination results in a relatively large asymmetric mode [62, 63]. Modal analysis has also been used by Ebrahimkhanlou et al. to develop a single-sensor 2D source-location method, based on identifying the arrivals of not only the first symmetric and asymmetric waves, but also their reflections from the edges of the specimens [64, 65].

2.2.9 Source-Location

One distinct advantage of AE over other NDT techniques is the ability to accurately locate the position of damage occurring in real time, by using a network of sensors distributed across the object under investigation. A variety of methods for achieving source-location are available, and their suitability depends on the nature of the object under consideration, the required accuracy and the available equipment.

The simplest source-location method is zonal location. This utilises sensors spaced evenly across the object at relatively large distances apart (the distance possible will depend on the attenuation of the object). In this method, an AE hit may only be detected by one sensor and can therefore be assumed to come from within the zone surrounding that sensor. Alternatively, if the hit is detected at multiple sensors, it can be assigned to the zone surrounding the sensor registering the highest energy. This method is of low accuracy compared to others, but can be appropriate for large structures and in situations where accuracy is not highly critical. It has the advantages of requiring a low number of sensors for the area and also of requiring minimal prior data regarding the wave-propagation characteristics of the object under test.

Time Difference of Arrival (TDOA) methods provide significantly greater accuracy and can

assign hits to a point, rather than just a zone. TDOA relies on the use of multiple sensors, two for one-dimensional (linear) source-location or three for two-dimensional source-location. By using the known spacing between the sensors and the velocity of wave-propagation in the specimen, the difference between the arrival times at the different sensors can be used to calculate the source position. The equations for linear TDOA source location is given below [66]:

$$l_1 = \frac{1}{2}(t_1 - t_2).v = \frac{1}{2}\Delta t.v \tag{2.19}$$

$$l_2 = \frac{1}{2}l - l_1 = \frac{1}{2}(l - \Delta t.v) \tag{2.20}$$

Where:

l : The distance between the two sensors.

l_1 : The distance from the source to the midpoint between the two sensors.

l_2 : The distance from sensor 1 to the source.

$t_{1,2...}$: The arrival time of the signal at sensor 1, 2... etc.

v : The wave velocity.

TDOA methods rely on both accurate knowledge of the wave-velocity within the object under test, and accurate determination of arrival times, both of which can present issues. In the case of thin sheet or plate specimens, Lamb waves will develop, in which there may be multiple modes and also multiple frequency-components propagating at different velocities. The use of a simple threshold-crossing in the time-domain can therefore be insufficient if the frequency and wave-mode are not known with certainty. More advanced methods, such as that proposed by Hamstad et al. [67], utilise the wavelet-transform of the signal to identify the arrival times of a selected mode and frequency, and then use the appropriate corresponding wave-velocity to calculate the source-location. While this method is suitable for a large number of structure types it assumes a uniform propagation path and cannot account for features such as holes or changes in thickness, which can result in reflections of the signal or changes in velocity.

A more appropriate method for geometrically complex specimens is the delta-T method proposed by Baxter et al. [68], in which a simulated source, such as a Hsu-Nielsen source, is applied at multiple locations across the specimen to generate reference signals. The difference in arrival times between pairs of sensors for these reference signals can then be mapped, and the resolution of the map improved by linear interpolation between the tested points. During testing, the sources can be located by comparison of the recorded differences in arrival times with those of the reference signals. While the requirement for generation of a database of reference signals makes this method time-consuming and thus potentially unsuitable for particularly large specimens, it does have the advantages of requiring no prior assumption of the wave-propagation within the specimen and is therefore suitable for complex materials and geometries, and also, assuming the sensors are not moved between generation of the reference signals and testing, no knowledge of the sensor locations is required.

Another method which can be used to either reduce the number of sensors required, or to increase the accuracy of TDOA methods, is the use of Single-Sensor-Modal-Analysis-Location (SSMAL). As previously discussed, the zero-order symmetric and asymmetric components of a Lamb wave will propagate at different velocities. As demonstrated by Surgeon and Wevers [69],

and also by Holford and Carter [70], this can be utilised by using the difference in arrival times between the symmetric and asymmetric modes to calculate the propagation distance from source-to-sensor. This method does however rely on the propagation of both modes at suitable amplitudes for the determination of their arrival times, a situation which will not always arise, depending on the source.

Another method which utilises the principles of SSMAL is the previously mentioned single-sensor approach based on multimodal edge-reflections taken by Ebrahimkhanlou et al. [64, 65]. This method is proposed for use on isotropic sheet or plate specimens with suitable reflecting edges. The first stage of the method is to determine the direct source-to-sensor distance, using the principles of SSMAL, in this case the arrival times being taken from the continuous wavelet-transform of the signal. The arrival times of the subsequent edge-reflections are then utilised to determine the distance from the source to the edges of the specimen and to then triangulate the source-location.

2.3 Artificial Intelligence in AE Analysis

Rather than relying on classification based on a small handful of parameters to differentiate between source-types, -locations etc, there are now a great variety of computational techniques which allow analysis of vast quantities of data, and significantly reduce the necessity of human input for analysis. While there are a great number of techniques, and multiple variations and evolutions of each, for methods related to AE they can be broken into two main classifications: Untrained and Trained.

Untrained systems can be presented with input data from multiple different sources, with no information about which data correlates to each source. The system then aims to separate the data into groups or ”clusters” of similar data. The system therefore has to decide how many clusters are needed, how these clusters should be defined, and then which cluster the data belongs to. Once the data has been clustered, it is up to the user to find correlations between the clusters and the sources which they may represent. Trained systems, on the other hand, are supplied with input data which is already classified, for example results from multiple different known test types. The system is then ”trained” using this data, which is to say the system carries out an optimisation to find the best way to mathematically differentiate between the known data sets. The system can then use this optimised method to match any further data to one of the established classifications. Untrained methods have the advantage of no prior knowledge being necessary; they can be applied in situations in which the number of potential sources is entirely unknown and then used to help identify these sources. They do however present the issue that it is not always clear what the clusters created are actually related to, and it is down to the user to identify relationships between the clusters and the sources to which they may relate. Trained networks provide much more robust results, as it is known which phenomena each cluster relates to, but the generation of suitable training data can be both difficult to achieve and time-consuming.

For application to AE, the inputs for these methods can include typical AE parameters, such as amplitude, energy, duration, rise-time, peak frequency etc, but can also include the full signal, the frequency spectra or even the wavelet-transform coefficients of the signal.

The most widely used untrained method in AE is the K-means clustering method. The basic procedure is to consider the data points for each hit as existing within a multi-dimensional space, with as many dimensions as there are parameters being used to describe the hit. A number of initial

mean points are then identified, corresponding to the number of clusters to be formed; this can be achieved through a number of methods, but most simply the points can be randomly selected. Each hit is then assigned to the closest mean. The mean is then recalculated based on the values which have been assigned to it. This process is repeated until a converged solution is achieved in which each hit is part of a cluster. The number of clusters can either be determined by the user, based on the number of expected source mechanisms, or determined by mathematical optimisation, which may be based on factors such as variation within or between the clusters. K-means clustering has been successfully used in a large number of AE studies in different fields, including some studies of adhesive-bonding.

It was used by Prathuru [9] in the investigation of the application of in-plane and out-of plane PLB sources to adhesively-bonded specimens. Four parameters were used, peak amplitude, duration, and the ratios of energy and peak amplitude found in the low-frequency ($< 175\ kHz$) and high-frequency ($> 175\ kHz$) filtered signals. Use of these four parameters was found to provide robust classification of in-plane and out-of-plane sources.

Pashmforoush et al. [71] utilised a hybrid K-means genetic algorithm for differentiation between failure modes of core failure, adhesive-bond failure, matrix cracking and fibre-breakage, during Mode-I testing of composite sandwich panels. The approach taken in this case was to identify the potential failure modes prior to testing, and to establish the AE characteristics of each failure type in terms of amplitude and frequency spectra. Following the Mode-I tests, the hybrid K-means genetic algorithm was used for clustering. The hybrid method was utilised as it removes the dependency of the clusters on the initial estimate and prevents the algorithm from getting stuck in local minima. The clustering was based on the parameters of amplitude, energy and frequency. The number of appropriate classes was investigated using the Davies-Bouldin index, which indicated an optimum of four classes, thus corresponding to the number of potential failure mechanisms identified. The clusters were then assigned to the failure mechanisms based on the prior investigation of the characteristics of each of the failure modes. The prevalence of these failure modes in each specimen was then confirmed with SEM imagery. A great number of other studies have also applied similar methods for clustering of results from fibre-reinforced composites, typically focusing on input parameters of energy, amplitude, peak-frequency, duration and rise-time [72–75].

Destousse et al. utilised clustering to aid in analysis of bi-axial loading of scarf joints formed at a variety of angles [76]. In this case only two parameters were used, peak-frequency and amplitude, and the the number of classes was not pre-specified. A combination of the Davies-Bouldin index and silhouette coefficient were used to determine the optimum number of clusters, which was found to be four. At the time of publishing however, no explanation was provided for the differences between these clusters, although microscopy to further investigate the sources was claimed to be underway.

A large variety of methods now exist for trained systems to classify data, most of which are based on the principles of Artificial Neural Networks (ANNs), also known simply as "Neural Networks". A neural network consists of many small units called neurons, which are arranged into a number of layers, as illustrated in Figure 2.22. The first layer is the input layer, which contains the numerical inputs, and the final layer is the output layer. Neurons from one layer are connected to the neurons in the next layer through weighted connections, connections with a real-valued weight attached to them. In a fully connected network every neuron in one layer is connected to every neuron in the next layer, while in other more specialised architectures, only certain combinations of neurons will be connected. The values of the neurons in one layer are

multiplied by the values of their weighted connections. The bias values of the neurons in the next layer are then calculated by adding up these values for all of their connections. An activation function, such as the logistic function $y = 1/(1 + e^{(} - bias))$, is then used to transform the bias function into a value for the neuron, which can then be passed onto the next layer. This process is continued until the input values have been propagated through all of the layers to the output. For a neural network to provide the desired output from a certain set of inputs, the weights of the connections must be set correctly. The process of setting the weights is know as training the network, and is achieved using a back-propagation algorithm.

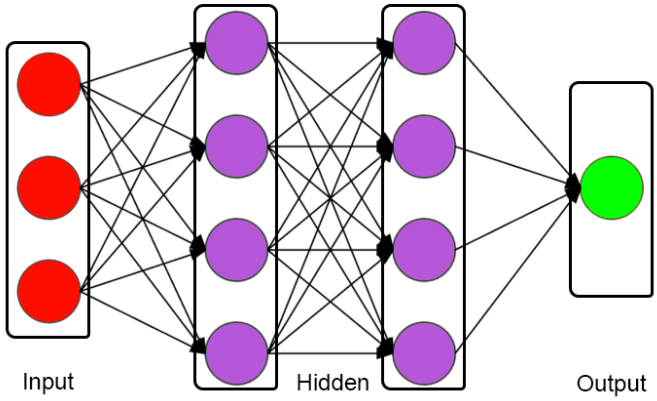

Figure 2.22: Example of a basic fully-connected ANN structure

Artificial neural networks have been used in a wide range of AE applications, including differentiation between failure modes in composites [77, 78], source-location [79, 80], detection of burn- and chatter-faults during grinding processes [81, 82], tool wear [83] and detection of partial discharge in electrical transformers [84].

Kumar et al. [78] tested two different network types, a Radial Basis Function Neural Network (RBFNN) and a Generalised Regression Neural Network (GRNN), to predict the final failure strength of sea-water aged GFRP specimens subject to three-point bending. 20 specimens were used in total, with 16 being used for training and 4 for testing. These were split equally between ageing periods of 4, 5, 6 and 7 months. The AE parameters used to train the networks were number of hits, cumulative counts, cumulative energy, cumulative absolute energy and cumulative signal strength. Analysis of the trained network identified that the network was best able to predict the final failure strength of a specimen during the period from 500 ms to 800 ms into the test, with final failure occurring in the range of 1400 ms to 1600 ms. To test the networks, the trained networks were used to analyse the acoustic emission from the 4 specimens not included in the training data-set. It was found that within the time region of 500 ms to 800 ms, the networks could predict the final failure strengths with an error of only 0.5% - 7.2% for the RBFNN type and 0.5% - 4.4% for the GRNN type.

Kalafat and Sause [79] have presented a source localisation method based on the Delta-T method, but utilising a neural network with the aim of increased accuracy. The experimental setup used consisted of a cylindrical CFRP pressure vessel with a metallic lining, which was tested both while empty and whilst filled with water. Seven AE sensors were mounted on the pressure vessel. A PLB source and a piezoelectric pulser were both used as input sources to cover a wide range of input frequencies. These were both applied at 444 different points which were marked out on the vessel. The time difference of arrival between all of the sensor pairs was used as the

input for the neural network, with the source x and y coordinates as the target output. 111 of the 444 source locations were used to train the network, while the other 333 were used to test it's accuracy. Comparison with locations determined using the classical Delta-T method, using the same test data, showed the neural network based approach to improve source location accuracy by up to a factor of 6, with the significantly better performance being most prominent in the region directly in between two sensors, where the time difference of arrival is at its lowest.

Caprino et al [80] have also experimented with the use of neural networks to aid in source location, but with a rather different approach. This study focuses on source location in an anisotropic unidirectional carbon fibre plate. The test setup is fairly typical, with a square 280 mm x 280 mm CFRP plate, with three sensors located near the edges, and a PLB being used as a source. As in the work described above by Kalafat and Sause [79], the input to the network is the time difference of arrival between the sensors, and the target outputs are the coordinates of the source location. In this case however, the network is not trained with experimental data. A small series of PLB tests were done to derive an expression for variation in wave velocity with regard to propagation direction. This was then used to calculate the theoretical time difference of arrival at the sensors for 2500 randomly selected locations on the plate. These theoretical values were then used as a training data-set for the neural network. The system was then tested with experimental data from 14 randomly selected locations and was found to perform well, with a mean error of only 2.18 mm. While this approach has been proven to be effective, it is questionable what the advantage is compared to traditional TDOA methods, as it is still dependent on the accurate determination of the wave velocity in multiple directions, while systems trained with experimental data have no reliance on this and are therefore able to cope with complex geometry and variable wave velocities throughout the specimen.

Kwak and Ha [82] have used a neural network combining inputs from an AE sensor and a power-meter connected to a grinder to detect and differentiate between burning and chatter vibration during the grinding process. The network utilises the static and dynamic power parameters from the power meter, and peak RMS amplitude and Peak Frequency from the AE sensor as inputs. The simple feed-forward network with two hidden layers was trained using a dataset of 12 sample signals. When tested using different signal samples, the network identified the faults correctly with an accuracy of around 95%.

Assessment of machine tool wear by AE has also been achieved by Jemielniak et al [83]. Various AE parameters were tested as inputs for the system, along with feed speed, cutting speed and cutting forces, which were measured using other sensors. The parameters which were found to be most useful, and which were used as inputs to the network were the average RMS value of the signal, and the burst rate, defined as the number of times the RMS value exceeds a preset threshold in a given time-frame. These parameters were utilised as inputs to a feed-forward network, with a single output of crater size, a parameter which is directly indicative of tool wear.

A somewhat different approach has been taken by Boczar et al [84] in their investigation of recognising partial discharges in electrical insulation systems of power transformers. In this case, instead of using a small number of parameters which summarise the AE signal, such as peak values or mean values, the approach has been taken of using a much larger input vector. Two different inputs have been tested, the first being the power spectral density, and the second being the Short Time Fourier Transform (STFT), with the STFT being rearranged into a single vector with an arbitrary order, instead of a 2D matrix arranged by frequency and time. A feed forward network with a single hidden layer of sigmoid neurons was used. Sensitivity studies were carried out to investigate the effects of the input vector size, with the length of the PSD being varied from 16 to

1024, and the time interval for the STFT varied from 0.05 ms to 1.95 ms, and also to determine the most appropriate number of neurons in the hidden layer. Based on a compromise between accuracy and efficiency (training time), the two final networks produced utilised a PSD length of 128 or an STFT created with a time interval of 0.4 ms as the input, and used a hidden layer comprising of 45 neurons. Both of these networks were found to be able to classify the partial discharges into 8 categories with an accuracy exceeding 95%.

It can be seen from the brief descriptions of the works above, that not only do neural networks have a lot of potential in AE, in terms of the practical applications for which they may be useful, but also there is a vast scope for experimentation, in terms of network architecture and the ways that AE data and features can be utilised as inputs.

2.4 Application of AE to Adhesive-Bonds

The application of AE to adhesively-bonded joints has been explored by a variety of researchers, with varying levels of insight gained from its use. A selection of these works are described in the following section and are summarised in Tables 2.1 and 2.2.

Table 2.1: Literature on Application of Acoustic Emission to Adhesive-Bonds

Adhesive	**Adherend**	**Test**	**Variables**	**Analysis techniques**	**Ref.**
Epoxy FM300-2M	Graphite-Epoxy composite	DCB, ENF, single-lap-tension	Fracture-mode	Peak-frequency, pattern-recognition	[85]
Epoxy FM300	Composite	Single-lap-shear	Void-size, Adhesive-thickness, aging	Acousto-ultrasonic-parameter	[86]
Polyurethane-SikaForce 7851	GFRP	Double-lap-shear	Adhesive thickness	Cumulative energy	[87]
Epoxy	CFRP	DCB	Temperature	Cumulative energy, source-location, clustering	[88]
JGN-T	CFRP/Steel	Uniaxial-tension	-	Cumulative energy	[89]
Terokal 5045	CFRP, GFRP	Single-lap-shear creep	Temperature, moisture	Cumulative counts	[90]
Epoxy-Araldite LY556	GFRP	Repair-patch -Tension	Repair-patch type	Cumulative counts	[91]
Epoxy	GFRP	DCB, MMB	Fracture-mode	Amplitude	[92]

Table 2.2: Literature on Application of Acoustic Emission to Adhesive-Bonds (contd.)

Epoxy	GFRP	Single-lap-shear, Double-lap-shear	Adhesive-thickness, failure-mode	Amplitude, duration, peak-frequency, cumulative counts, source-location	[48, 93, 94]
Loctite 638	18NiCrMo3 steel	Conical-torsion	Defect-density	Cumulative counts	[95, 96]
Redux 775, BSL 308	Aluminium alloy	Single-lap-shear	Adhesive-type, adhesive-thickness	Cumulative energy	[97]
Loctite AA326 Loctite EA3430	Aluminium alloy, CFRP	DCB, 3-ENF	Fracture-mode, adhesive-type, defect-density	AE amplitude, partial powers	[8]
Loctite AA326 Loctite EA3430	Aluminium alloy	MMB	Mode-mixity, adhesive-type, defect-density	AE energy	[98]
Epoxy ER331,	Aluminium alloy	Single-lap-shear	Surface treatment	PCA, k-means clustering, cumulative counts	[99]
Epoxy EPG 2601	CFRP	DCB ENF ECT	Fracture-mode	Amplitude	[100]
Epoxy SR150	GFRP-polyethylene-foam-sandwich	DCB	Failure-mode	PCA, K-means clustering, cumulative counts	[71]
Loctite 326, Loctite 3430	Aluminium alloy	PLB, 4-Point-Bend, Indentation, Single-Lap-Shear	Fracture-mode, Defect density, Adhesive thickness, Adhesive type	WT, modal analysis, AE energy, PCA, k-means clustering	[9]
Araldite 2021, Sikasil SG500	Aluminium alloy	DCB	Adhesive type	TDOA source-location, FEA	[101]
Araldite LY 1564	GFRP	DCB, 3-ENF	Fracture-mode	AE Amplitude, cumulative counts, cumulative energy	[102]

The earliest and most basic use of AE for adhesives has been its use as an indicator of the onset of failure during destructive tests. A large number of studies have used AE-instrumented destructive tests of adhesively-bonded specimens, and have utilised either amplitude, energy (per hit), cumulative-energy or cumulative counts to identify the initiation and progression of failure [8, 71, 87–93, 95–103]. All of these studies have observed that the onset of acoustic emission correlates well with the load-displacement curves acquired in destructive tests. Typically a low level of AE activity will slightly precede the drop in load which occurs due to failure, and a high level of AE activity will be observed during the failure. These types of relationship can be seen in Figure 2.23. This basic relationship allows AE to be used to successfully detect damage occurring in an adhesive-bond, and in some cases, to pre-empt total failure of the specimen. This type of basic study however does not yield the full depth of results that more detailed AE analysis can provide. More detailed analysis has been utilised not just to identify damage, but to locate it, to differentiate between different failure modes, different fracture-modes and to estimate the final failure load. Investigations have also looked at the effects of varying adhesive and adherend materials, thicknesses and loadings on AE generation.

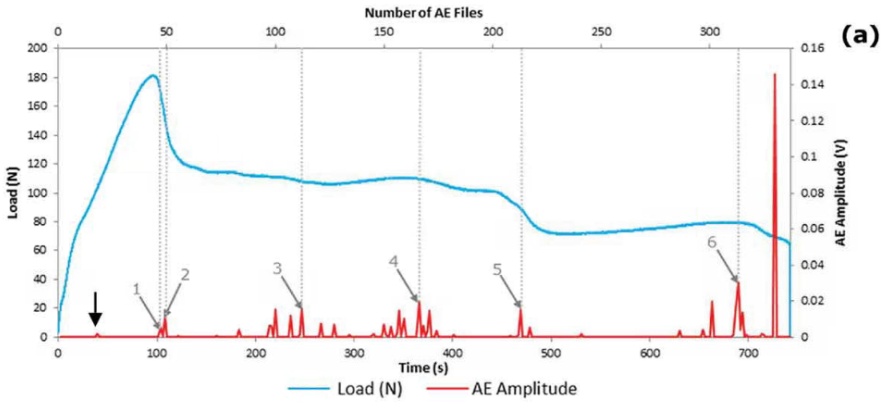

Figure 2.23: AE amplitude and loading curve for a DCB test performed by Droubi et al. [8]

The earliest use of AE with adhesives is believed to be by Curtis in 1975 [97]. In this study lap-shear tests were conducted on specimens bonded with a brittle Redux 775 adhesive and a more ductile BSL 308. The bond strength was varied by varying the thickness of the Redux 775 adhesive, whose strength was noted to be approximately inversely proportional to its thickness. Cumulative AE energy was investigated as the main parameter of interest, and it was found that in both adhesives, weaker bonds produced a greater cumulative energy during failure. It was proposed that, for the Redux 775 adhesive, the cumulative AE energy at fracture (per unit glue-line volume) was inversely proportional to the lap-shear strength raised to the power n, where n was less than 6, but this required further analysis to be more clearly defined.

The idea of relating cumulative AE enery to final failure-load was also pursued more recently by Croccolo and Cuppini [95,96], who applied a similar method of utilising cumulative AE activity to predict the final releasing moment of an adhesively-bonded conical torsion-test specimen. As opposed to cumulative energy, cumulative counts of AE were utilised. Testing specimens with various bond qualities, modified by oiling parts of the adhesive-bond surfaces, revealed that the gradient of cumulative counts vs applied load corresponded to the treatment of the surfaces, and therefore to the overall bond strength. It was therefore proposed that a methodology of applying a low load (25% of the predicted releasing moment), and recording the cumulative AE counts, could be used to estimate the defective bond area and the total strength of the joint.

Droubi et al. [98] investigated the Mode-I and -II failure of bonded metal-to-metal and metal-to-composite specimens through use of AE-instrumented double-cantilever-beam (DCB) and three-point end-notch-flexure (ENF) tests. Both a ductile and a brittle adhesive were investigated with varying levels of bond quality, introduced by use of polytetrafluoroethylene (PTFE) spray to reduce the effective bond area. As well as noting correspondence between AE activity and features in the load-curves, it was also recognised - during both calibration tests using a PLB and during debonding - that there was an increase in both AE amplitude and in the proportion of higher-frequency spectral content as the source moved closer to the sensor. Analysis was conducted by Fast Fourier Transform (FFT) and by energy content after band-pass filtering into low-, medium- and high-frequency-ranges, and therefore considered the entire hit, including the multiple edge-reflections likely in small specimens.

Liu et al. [102] have also investigated Mode-I and -II failure of adhesive joints using DCB and ENF tests, but in this case using composite adherends. Very basic AE analysis of cumulative counts, energy and amplitude was combined with SEM imagery. It was shown that the Mode-I tests produced a lower number of hits overall, but a higher number of high-amplitude hits than the Mode-II tests. SEM imagery was used to identify adhesion failure, cohesive failure and fibre-breakage. It was suggested that the low-amplitude hits corresponded to micro-cracking, while the high-amplitude hits corresponded to fibre-failure, but no attempt was made to directly relate AE parameters to adhesive or cohesive failure.

Mode-I fracture was also investigated with a double-cantilever-beam test by Manterola et al. [101] who focused on the use of TDOA source-location in DCB specimens prepared with both rigid adhesives and flexible adhesives. Comparison of the AE location with the visually observed crack-front revealed good correlation in the specimens prepared with rigid adhesives. However, when the flexible adhesive was used, the AE locations progressed at the same rate as the visual crack, but AE locations were in the region of 25 mm ahead of the visual crack-tip. Static FEA, using a bilinear cohesive-zone-model, was used for comparison of the fracture-process zones (FPZ). It was demonstrated that the flexible adhesive yielded a far greater FPZ than the brittle adhesive. It was therefore concluded that the AE events originated from the leading edge of the FPZ, rather than from the visible crack-front as may have ben previously assumed.

One of the features of adhesive-joint failure investigated most successfully using AE is the failure mode. In metallic specimens, this tends to be differentiation between debonding between the adherend and adhesive, and cracking of the adhesive itself. In composite specimens the number of potential failure mechanisms increases significantly, with fibre-breakage, fibre-pullout, fibre-tear and matrix cracking potentially occurring on top of the two previously mentioned modes.

Bak and Kalaichelvan have conducted a number of studies [48,93,94] in which they have managed to differentiate between failure mechanisms of fibre-tear, light fibre-tear and adhesive failure by analysis of the peak frequencies of each hit during lap-shear testing of glass-fibre composite and pure resin single- and double-lap-joint specimens. Comparison of the AE peak frequencies with scanning electron microscope images allowed identification of correspondence between the failure-mechanisms and peak-frequencies. The use of a second sensor also allowed for linear source-location of each hit for further validation of the failure-mechanisms. It was found that peak-frequencies of $< 100\ kHz$ corresponded to adhesive failure, 100 kHz to 200 kHz corresponded to light fibre-tear failure and $> 200\ kHz$ corresponded to fibre-tear failure. While this method appears successful in the small specimens tested (25.4 mm square bond area), where the source-sensor distance experiences minimal variation, the results presented by Droubi et al. [98] indicate that changes in source-sensor separation may lead to changes in spectral content, and

thus in the failure-mechanism recognised. For application of this method to larger bond areas the effects of propagation distance may need to be accounted for to ensure reliability of results.

Galy et al. [99] have also successfully differentiated between failure-mechanisms of aluminium and epoxy lap-shear specimens. By use of the k-means clustering method, with inputs of temporal features including amplitude, energy, duration and rise-time, it was possible to attribute AE hits to either debonding between the adhesive and adherends, or cracking of the adhesive. As with most of the works relating to AE testing of adhesive-bonds, the bonded area of the specimens used was of a standard size for a lap-shear test (25 12.5 mm), resulting in minimal variation in propagation distance. As in Bak and Kalaichelvan [48], the application of this method to larger specimens - in which propagation distances will vary more significantly - should be approached cautiously as the dispersion of AE waves with increasing propagation-distance may lead to reduced amplitude and energy, and variation in duration and rise-time, while edge-reflections will also play a more complex role in affecting these factors, dependent on the geometry.

Pashmforoush et al. [71] also utilised a k-means clustering scheme to differentiate between core-failure, adhesive-debonding, matrix-cracking and fibre-breakage in a Mode-I delamination test of a composite sandwich structure. In this case, the clustering was done using a hybrid k-means-genetic algorithm, which provides a more robust clustering method than pure k-means and is less likely to suffer from becoming stuck in local minima when attempting to establish the correct number of clusters. The input to the k-means-genetic algorithm was derived from a principal components analysis of frequency, amplitude and energy. Clusters were defined through the k-means algorithm, and then attributed to their associated failure mechanisms by comparison with experimental data from tests in which the failure mechanisms were isolated. The results of the AE study were then validated with scanning electron microscopy of the damaged areas, which allowed the failure mechanisms to be observed. Out of the parameters included in the clustering method, it was observed that frequency provided the best discrimination between the failure modes, with dominant frequency-ranges of 35 kHz to 65 kHz, 100 kHz to 130 kHz, 170 kHz to 250 kHz and 350 kHz to 450 kHz corresponding to core-failure, adhesive-bond failure, matrix cracking and fibre-breakage respectively.

Differentiation between fracture-modes (Mode-I = crack-opening and Mode-II = shear) has also been achieved by acoustic emission through various methods. Dzenis and Saunders conducted AE instrumented Mode-I, -II and mixed mode DCB, ENF and Lap-shear tests. It was observed that in typical parametric AE analysis, the different tests yielded very similar results, with hits having a similar amplitude and similar frequency spectra. However, using the Vallen software VisualClass it was possible to differentiate the signals using statistical pattern recognition. VisualClass normalises the waveform, and then breaks it into smaller time-windows. The FFT of each of those time-windows is then taken, resulting in a spectrum of a number of data-points. These values, along with the normalisation factors, are then used as features. Visual-class then selects the features of highest discrimination quality, based on a set of training data. In this case the results from the DCB and ENF tests were used as the training data. It was found that by use of this approach the pure Mode-I and -II signals could be fully separated in feature-feature space. Using the same discriminating features to analyse the results of the lap-shear test resulted in a data cluster which overlapped significantly with the Mode-II results, which is as should be expected considering that a lap-shear test is predominantly a Mode-II test. This approach of utilising statistical pattern recognition has proven to be extremely powerful and able to succeed where parametric analysis fails, and has demonstrated that there is a significant difference in the signals acquired from Mode-I and Mode-II fracture. It does not however shed any light onto what the

actual differences between these signals are.

Prathuru [9] takes a rather different approach to differentiating between Mode-I and Mode-II type hits during four-point flexure and lap-shear testing. PLB tests are carried out on both the face (in-plane) and the end (out-of-plane) of various bonded specimens. It is proposed that Mode-I fracture will correspond to an out-of-plane source, while Mode-II fracture will correspond better to an in-plane source. K-means clustering is then used to differentiate between the signals and to identify the parameters that give greatest discrimination between the two source orientations. The parameter identified as having the greatest potential for discrimination being the ratio between energy in the high ($> 175\ kHz$) and low ($< 175\ kHz$) frequency bands. This clustering method was then applied to the data from a four-point-bending test and a lap-shear test. It was found that both tests produced both Mode-I and -II type signals, but were dominated by the Mode-II type. As four-point-bending and lap-shear tests are both predominantly Mode-II tests, this is the expected result. While this attempt to differentiate between fracture-modes appears to be successful, it is difficult to assess the true validity of this method as Mode-I dominant fracture tests were not carried out. It could therefore be the case that adhesive failure of any type corresponds better to the in-plane PLB than the out-of-plane PLB, due to the differences in source material (graphite vs adhesive material) and source-type and location (surface monopole vs buried dipole).

2.5 Finite Element Simulation of Acoustic Emission

Numerical modelling and simulation of acoustic emission can provide a greater understanding of the underlying physics, and provides the ability to quickly and cost-effectively investigate the effects of multiple different parameters affecting the generation, propagation and detection of AE, in an environment free from the sources of error and variation typically present in an experimental set-up. Numerical modelling of AE does however have the disadvantage of being incredibly computationally expensive, due to the requirements for a well refined mesh, and for a high number of small time-steps, thus requiring significant RAM, memory for large volumes of temporary files, and a suitably fast processor. With the continued rapid development of the computer industry, these disadvantages are however likely to become significantly less of a challenge in future. While there is no substitute for real-world experimental data for studies of different AE sources, FE simulations are superior to experimental results in terms of exact knowledge of their source-location, size, magnitude and orientation. The option to record the absolute surface displacement or velocity without the significant effects of the sensor type used (although this can be introduced in a totally controlled manner if desired); the lack of noise and the ability to include or exclude reflections as is deemed appropriate [59]. AE propagation is relatively well understood and draws on knowledge established in the field of ultrasonics, as well as work conducted in seismology. The processes involved in the generation of AE sources is however far less well documented, as is the detection of AE signals. A variety of methods of varying complexity have been implemented by previous authors to simulate AE generation and detection. This section will give an overview of some of the key literature in this field, as summarised in Table 2.3, giving particular emphasis to the simulation methodology and set-up, as opposed to the results gained.

Table 2.3: Literature on Finite Element Simulation of Acoustic Emission

Parameter Investigated	**Source**	**Sensor**	**2D/3D**	**Software**	**Ref.**
Rise-time, source-width, stress-distribution and sensor diameter	Surface force, linear rise and time-dependent	Surface area	2D Axi.	NIST Boulder	[104]
Source size, rise-time and mesh resolution effects on 1” steel plate	Surface force, time-dependent	Point, high-pass filtered	3D	NIST Boulder	[105]
PLB source modelled on isotropic and anisotropic sheet specimens	Surface force, linear ramp	Point	2D Axi. 3D	NIST Boulder	[106]
Edge-reflections in aluminium plate specimens, in- and out-of-plane sources	Surface force	Point, high-pass filtered	3D	NIST Boulder	[107]
Modal analysis of source-type, -depth, propagation distance and source-location on aluminium plates	Cosine-bell buried dipole, surface monopole,	Point, high-pass filtered	3D	NIST Boulder	[59], [67]
Modal analysis of source rise time in thin plates	Cosine-bell buried dipole	Point, high-pass filtered	2D Axi.	NIST Boulder	[108]
Matrix-cracking, fibre-breakage and fibre-matrix interface -failure in CFRP.	Buried cross-shape multi-material crack source	WD-type surface sensor	3D	COMSOL	[109]
Inhomogeneous source materials to represent resin or fibre-failure	Buried dipole Time dependent	Point	3D	COMSOL	[110]
Dipole source characteristics	Buried dipole time dependent	Point	2d Axi.	COMSOL	[111]
Detailed modelling of PLB source fracture	Pencil lead fracture	Point	2D	COMSOL	[112]
Effects of holes, rivets and delaminations in CFRP sheet	Buried dipole, linear ramp	Point, high-pass filtered	3D	COMSOL	[113]
Investigation of anisotropic attenuation behaviour of CFRP	Cosine-bell force	Point	3D	ABAQUS	[55]
Lamb-mode interaction with macroscopic CFRP defects	Buried dipole	-	3D	COMSOL	[114]
Lamb-mode propagation in isotropic/anisotropic layered hybrid composite	Buried dipole	-	3D	COMSOL	[115]
Fibre-failure and matrix cracking	CZM crack-propagation	Multi-physics sensor and pre-amp	3D	COMSOL	[116]
Modal analysis of buried dipole source angles in PVC rod	Cosine-bell buried dipole	Point	3D	NIST Boulder	[117]
Modal analysis investigating source depth and direction	Buried dipoles, linear rise-time	Point, surface with transfer function	3D	ABAQUS	[60]
Source-location of PLB on anisotropic honeycomb sandwich structure	Time-varying force	Point	3D	ABAQUS	[118]
Lamb wave generation by PLB on aluminium sheet	Cosine-bell surface force	Point	2D	ANSYS	[119]

Early works by Hamstad, Gary, Prosser and OGallagher [104–106] investigated the FE modelling of out-of-plane and in-plane PLBs on aluminium and steel plate specimens, initially utilising a simplified axisymmetric 2D finite element code developed by Blake and Bond [120], before moving to a 3D model. These studies aimed to validate the FE models by comparison with experimental data for the PLB tests and also by comparison with Mindlin plate theory. Particular attention was given to the effects of mesh size, source size, source rise-time and source-type. In these cases the source models used were, for the majority of tests, a uniformly-distributed time-varying force with a maximum value of 1 N applied over the contact area of the PLB source. A force of constant intensity and increasing application-area was also trialled and found to create a similar result. As the actual source from a PLB results from the removal of load as the lead breaks, as opposed to the deformation as the lead is applied, the results obtained were 180° out of phase with experimental results, but otherwise accurate. Mesh sizes were varied from 0.6 mm to 0.023 mm, and time steps chosen to be between 0.082 μs and 0.0033 μs as to satisfy the CFL stability condition, which requires the time steps to be shorter than the time taken for the highest velocity wave to cross an element. These studies successfully demonstrated good correlation between between experimental, theoretical and FE results and demonstrated the potential of FE simulations of AE. It was observed that to generate AE in the typical detectable range of over 100 kHz, source times must be of the order of 10 μs or less. Attempts to determine the effect of source size were somewhat limited by the mesh refinement which could be achieved with the minimal random access memory of the early computers which were being used. It was however observed that a source diameter of 0.528 mm or 1.1 mm provided good time-resolution in the generated Rayleigh waves, while a 4.23 mm diameter source gave poor results, leading the authors to conclude that a source diameter of less than 3 mm should provide a sufficiently accurate result. The sensor was modelled in these studies as a disc on the surface of the specimen, with the electrical output of the sensor being assumed to be directly proportional to the average surface displacement over the area of this disc. Comparisons were made between sensor diameters of 2 mm, 3.18 mm, 6.35 mm, 12.7 mm and 25.4 mm, with the two smallest sensors reportedly producing near identical results to the displacement profile of a single point at the sensor's centre, while the 6.35 mm sensor still produced relatively accurate, but observably different, results, and the two larger sensors suffered from significant distortion as the sensor diameter became comparable to the wavelength. The outputs from these simulated sensors were filtered to a suitable frequency band for AE using a simple 50 kHz [105] or 100 kHz [104] high-pass filter. No further attempts were made to model the effects of sensor coupling, frequency response or the effects of the data acquisition system on the signal. These initial simulations were only run for the first 150 μs of the signal, and thus included the initial S_0 and A_0 or Rayleigh waves, but did not include the effects of edge-reflections.

Further work by the same group in 1999 [107] introduced 3D simulations of in-plane and out-of-plane PLB tests conducted on aluminium plates, with source- and sensor-configurations designed to induce both normal- and oblique-incidence edge-reflections. The same 3D modelling set-up was used as in previous works, with a time-varying normal force with a maximum value of 1 N applied a 0.3 mm diameter area on the specimen surface. The FE results were compared with experimental results acquired using an absolutely calibrated sensor with a flat frequency response from 20 kHz to 1 MHz. Post-processing of signals to allow direct comparison consisted of inverting the signal (to account for the source being 180° out of phase) and filtering both experimental and FE signals with 50 kHz to 1 MHz or 100 kHz to 1 MHz band-pass filter. The upper and lower limits were selected due to the limited response of the sensor above 1MHz and below 20 kHz. The 100 kHz limit was then used to remove the low velocity A_0 mode which obscured S_0 reflections

during investigation of in-plane sources. This study found excellent correlation between the experimental and FE results and demonstrated that 3D FE simulations were capable of accurately predicting edge-reflections.

The modelling of buried monopole and dipole sources, which are more representative of the majority of AE sources than a force applied to an external surface, was also introduced by Hamstad et al. in 1999 [121]. Using the same axisymmetric model as in their previous studies, this study investigated the effects of source sizes and mesh sizing as well as demonstrating the ability to model buried monopole and dipole sources in steel plates. The monopole source was created using a single vertical body force located at the midplane of the plate. The dipole was created with two simultaneously-opposing body-forces separated by a small distance. In both cases the force was applied over a small but finite area, thus meaning that the forces were not technically point sources, but were small enough to be considered as such. The forces were applied as cosine-bell-type step functions with a rise-time of 0.5 μs. Due to the difficulty in experimentally validating the results of the simulation they were compared with the analytical solutions of Scruby et al. [122], Pao et al. [123] and Hsu [124]. The FE solutions showed good agreement with the analytical solutions, thus validating this method of modelling buried AE sources. The investigation of source size and mesh size concluded that the ratio between the minimum wavelength of interest and the source size must be at least two, while the ratio between wavelength and mesh size must be at least fifteen for adequate results to be obtained.

This work was followed up by a two-part article by Hamstad, OGallagher and Gary, which investigated the application of wavelet-transforms to a database of AE signals generated by FEA. The first article [59] focused on source identification, while the second [67] investigated the application to source-location. The first investigation utilised 4.7 mm thick aluminium specimens with lateral dimensions of 1000 mm by 1000 mm and 480 mm by 25.4 mm, giving the potential to investigate a case analogous to an infinite specimen (edge-reflections can be easily excluded) and a small coupon-type specimen. The study considered three types of buried point source; a 1 N magnitude in-plane dipole aligned with the direction of propagation towards the sensors, a 1 N magnitude out-of-plane dipole, and a source designed to represent crack initiation. The crack initiation source consisted of three dipoles, the largest being a 1 N dipole aligned in the propagation direction towards the sensors, and dipoles in the other two directions having magnitudes of 0.52 N. The dipoles were each composed of a central cell with the cells either side being subject to opposing body forces. As in previous works, the sources forces varied with a cosine-bell-type step function, with a rise-time of 1.5 μs. The mesh consisted of uniform three-dimensional elements of 0.313 mm and time steps of 0.045 μs were used during the simulation. Out-of-plane displacement of points located 60 mm, 120 mm and 180 mm from the source were taken as the recorded AE signal, thus obtaining a perfect signal, neglecting the aperture effects of sensor size or any effects of sensor coupling. To make the simulated results more directly comparable with experimentally acquired AE signals the results were re-sampled to a step size of 0.1 μs (sampling frequency 10 MHz) and filtered with a 40 kHz high-pass filter. As previously discussed in Section 2.2.8. This set-up was used to investigate the signals occurring from the three different source-types located at seven different source depths, varying from the surface to the mid-plane, and demonstrated the ability to differentiate between source-types at constant depth, or source depths for a constant source by using ratios of the WT magnitudes of the A_0 and S_0 modes. In the second part of this article the same database of simulated AE wave-forms is then used to investigate the use of wavelet-transforms for source-location.

Hamstad [108] also presented an investigation of Lamb-modes as a function of source rise-

time, using the same axisymmetric model with a cosine-bell dipole source, as validated in previous studies. It was demonstrated over a range of source-depths and propagation distances that the rise-time of the source, which was varied from 0.5 μs to 15 μs, affects the Lamb-modes present in the generated signal. It was observed that only the fundamental A_0 and S_0 wave-modes were present for all rise-times, while the higher order A_1 and S_1 modes, which occur at higher frequency, were only apparent in the case of lower source rise-times

Sause and Horn [109, 110] used FE modelling in COMSOL Multiphysics® to simulate AE in anisotropic CFRP plates resulting from fibre-breakage, matrix-cracking and fibre-matrix interface failure. In contrast to the majority of previous works in which attempts have been made to approximate a point source, in this study a new source model was developed based on the microscopic source geometry and micro-mechanical properties of the resin and fibres. The source model utilised consists of a model fibre with a cross-section of 10 m x 10 m and a length of 30 m, embedded in a resin cube, with an edge length of 100 m, all embedded at the centre of the anisotropic CFRP plate. To simulate displacement of the crack surfaces, a cross-shaped cut-out is introduced at the centre of the resin cube, butting onto the fibre.

The motive for this being the ability to enable quasi-independent displacement of the crack surfaces in the x, y or z direction without the requirement to re-mesh the model for each crack orientation, thus allowing direct comparison between sources without influence of the mesh. Fibre-breakage was simulated by x-direction (in-plane) displacement of the surface of the cross at the end of the model fibre. Matrix cracking is simulated in both the x- and z-directions, with the displacements being applied to the surfaces of the cross accordingly. For simulation of pure matrix-cracking, the material properties of the model fibre were set to that of the resin, although the mesh remained unchanged. Fibre-matrix interface failure was modelled as a z-axis displacement (perpendicular to the crack) with an additional x-axis displacement along the axis of the fibre, due to relaxation of the fibres as they break contact with the matrix. A displacement of 100 μm was widely used throughout the study, though the effects of displacement were also investigated, with displacements of 10 μm, 30 μm and 50 μm also being tested for matrix cracking. The rise-time of the source was also varied from 50 μs to 1000 μs, with a value of 100 μs being widely used throughout the article. After the total displacement was reached the crack surfaces were then free to vibrate purely due to the elastic nature of the material and were not constrained or forced. It was demonstrated that while the source rise-time did slightly affect the observed frequency content of the signal, the material properties as well as the source orientation and depth dominated the frequency response and not the source rise-time. In this study, the simulated sensor response was generated by integrating the out-of-plane surface velocity over the sensor area, which was made up of an external ring-type element and a circular central element, representing the piezo-electric element configuration of the WD-type sensor used for the experimental validation of this work. The use of surface velocity, as opposed to displacement as used in most previous works, results from the work of Ono et al. [125] who demonstrated that the response of this particular sensor, amongst others, was proportional to velocity, and not displacement or acceleration which certain other sensors' responses are proportional to. Results were presented in terms of velocity and attempts were not made to convert the signal into voltage for direct comparison with experimentally obtained data.

Sause and Horn [113] also used FE simulations conducted in COMSOL Multiphysics ® to investigate the influence of internal discontinuities on ultrasonic signal propagation in unidirectional CFRP. Four 400 mm x 400 mm x 1 mm unidirectional CFRP plates (reduced to 200 mm x 200 mm by use of two symmetry planes) were modelled, including; a featureless reference plate, one

containing a hole, another containing a rivet and another featuring a delamination. A buried dipole source, oriented in the x-direction (in-plane), and located slightly offset from the mid-plane, was used to simultaneously induce both A_0 and S_0 mode Lamb waves. The source was applied as a linear-ramp function with a rise-time of 1 μs and with a maximum force of 3 N. A tetrahedral mesh of 1 mm maximum edge size was used, with refinement down to a minimum edge size of 5 μm around the features. Time steps of 100 ns were used and results were computed for the first 100 μs. The results analysed were the out-of-plane displacement of points located 100 mm from the source at angles of 0°, 45 ° and 90 °; in this study the effects of any sensor characteristics were not included. The simulated results were analysed in the time-frequency-domain by comparison of the wave-modes observed in the Choi-Williams distribution, identified by overlaying theoretically-calculated dispersion-curves. Typical AE parameters of peak amplitude, energy, peak frequency, frequency centroid, partial powers and arrival times of the A_0 and S_0 modes were also calculated. It was demonstrated that all of the discontinuities had significant effects on the detected signals, particularly in the cases of the hole and the rivet, which resulted in mode conversion and generation of secondary A_0 and S_0 waves. It was discussed that the most significant result is that inclusions such as bolts, rivets or holes can act as virtual AE sources due to the mode conversion altering the arrival times of the wave-modes, especially as the conversion of the fast-propagating S_0 mode into a secondary A_0 mode can result in an A_0 mode which arrives significantly before the original A_0 mode should arrive, giving the impression of an AE source which is significantly closer to the sensor than it actually is. It was however concluded that while there was a significant deviation from the reference case of over 70% in some AE parameters, the majority of parameters ($>$75%) exhibited deviation of $<$ 10%, which is well within the typical distribution for experimental AE data, and therefore it should still be possible to differentiate between AE sources in the presence of inclusions. A further study by Sause [114] utilised a very similar model set-up to investigate the effects of inter-ply delamination, inter-fibre cracks and fibre-breakage within a CFRP plate. These defects were included in the model as cuts of various lengths, depths and orientations. Inter-fibre cracks were modelled as 0.25 μm cuts in the fibre-axis direction, while fibre-breakage was modelled with 100 μm cuts perpendicular to the fibre direction and inter-ply delamination was modelled as a 50 μm cut parallel to the fibre-axis direction. A tetrahedral mesh with maximum edge size of 1 mm was utilised, with refinement down to a minimum of 5 μm in narrow regions. It was concluded from this study that all of the defects examined significantly impact the wave-propagation and the recorded AE parameters.

Sause, Hamstad and Horn have also used 3D FE analysis, conducted in COMSOL Multiphysics ®, to investigate AE propagation in multi-layered specimens, featuring isotropic and anisotropic layers [115]. The study considered both a flat sheet and a pressure vessel. The material properties, thicknesses, thickness ratios and stacking sequences were all varied, and modal analysis was conducted using a Choi-Williams type time-frequency transformation, with the results being compared to analytical solutions. The model set-up utilised quarter-symmetry to reduce computational time, and the source used was an out-of-plane buried dipole, with a linear temporal dependency, a maximum force of 3 N and a rise-time of 1 μs. The element-size used was 1 mm, and the time-steps were 100 ns A notable feature of this study is the use of a low-reflecting boundary condition. This boundary condition attempts to represent an adjacent medium with identical impedance, thus avoiding edge-reflections. This provides a extremely computationally efficient alternative to modelling a significantly larger specimen. It is however noted that the result of utilising this boundary condition is not perfect, with the S_0 mode being suppressed by over 95.8%, while the A_0 mode was only suppressed by 45.7% in the worst case. The plate size was therefore chosen to be large enough to avoid any significant effect of the remaining reflections at the sen-

sor positions. While this may not be a perfect solution, it is significantly better than attempting to model an excessively large specimen just to avoid edge reflection effects. In terms of results, this study concluded that the model utilised was capable of calculating Lamb-modes in hybrid isotropic and anisotropic composites and that for the materials studied, the Lamb wave propagation can occur as a motion of the complete multi-layered plate, which can be superimposed by guided waves propagating within the individual layers.

Sause also conducted an investigation into the modelling of PLBs as an AE source [112]. Prior attempts at modelling PLB sources have been limited to forces being applied as a step, linear-ramp or cosine-bell function, with a suitable peak force and rise-time. In this investigation however, a 2D model was created of the pencil and lead itself acting on an aluminium block. Contact conditions were created between the pencil lead and the collet of the pencil, allowing the pencil lead to fracture at a given load, and between the lead and the block, allowing the lead to move away from the block after fracture. A variety of loads, lead angles and materials were modelled and validated against experimental results. Comparisons were made between the detailed contact model, linear-ramp, and cosine-bell functions, in terms of both transferred load and surface displacement at a propagation distance of 40 mm. It was found that both the analytical functions provide a very good approximation of the PLB behaviour observed in the detailed model, with the cosine-bell function providing the closest approximation. It was therefore recommended that, for the sake of computational efficiency, cosine-bell functions should be used to model PLB sources in future works.

The merits of various source models were also investigated by Hora et al [111], who used COMSOL Multiphysics ® to create a 2D axisymmetric model of a steel cylinder and investigated a variety of concentrated force (monopole) and dipole source configurations, and compared the FEM results with those derived analytically. The source geometry for both dipole and monopole sources was varied between a point, a circular area and a cylindrical volume. In the case of the dipole source, the arm-length of the dipole was also varied. Additionally the time-dependency of the source force was varied. In this case the source force was not of the step, linear ramp or cosine-bell varieties seen previously, but was of the form $f_0(t) = ate^{-bt}$, featuring a steep rise and a more gradual decay.

The model utilised a mapped-quad mesh, with an element-size of 0.5 mm x 0.5 mm, chosen on the principle of having six elements per wavelength for the shortest wavelength under examination. The time-steps utilised are 0.01 μs from 0 μs to 8 μs. It is concluded that for the concentrated-force type source, the circular geometry provides the best correlation with the analytical solution, while for the dipole source, the cylindrical source with the minimum arm length (1 mm) provides the best match for the analytical solution.

Burks and Hamstad [55] investigated the attenuation behaviour of unidirectional carbon-fibre composite plate, utilising a 3D quarter-symmetry model constructed in ABAQUS. The model consisted of a 1.14 mm thick anisotropic linear-elastic plate, meshed with hexahedral elements of 0.5 mm x 0.5 mm x 0.1905 mm. The source utilised was a concentrated 1N force, applied with a cosine-bell time-dependency with a rise-time of 1 μs. Stiffness-proportional Rayleigh damping was introduced to the model in order to match the attenuation of the model at a given frequency to that which was recorded experimentally. The out-of-plane displacements of points located across the specimen were examined as the AE signals. Both numerical and experimental signals were band-pass filtered between 40 kHz and 1500 kHz to allow better comparison. It was found that the model did effectively capture the anisotropic attenuation behaviour around the frequency to which the damping parameters were tuned, $\pm$ 10 kHz. Across the full frequency-

range however, the attenuation was found to be accurate only in the 90° direction, and not in the 0° direction. Recommendations for further work included two potential solutions; either the use of an anisotropic stiffness-proportional Rayleigh vector, which would still not have the ability to capture the attenuation of different modes correctly, or to attempt to model the visco-elasticity of the materials, which would require significant experimental work to accurately determine the suitable viscoelastic parameters over the frequency-range of interest.

Further work by Sause and Richler [116] pioneered the modelling of cracks as AE sources, utilising a cohesive-zone-element approach to model the localised material degradation and crack-opening. The source model developed utilises three simulation steps. The first step is a static simulation, in which the specimen is loaded incrementally to a high enough stress to initiate fracture at a predesignated crack-path. In the second step the initial values are inherited from the solution of the first step, but a transient simulation is performed. The boundary conditions at the predesignated crack are chosen to allow crack-opening as per a cohesive-zone law. The duration of the second step is chosen to be sufficient to allow crack propagation to come to a rest. The propagation of the crack excites AE waves in the specimen. The third step inherits its initial values from the final time-step of the second step, and boundary conditions are chosen to allow free movement of the newly-formed crack surfaces. The duration of the third step is chosen to be suitable to allow wave-propagation throughout the specimen. A tetrahedral mesh was used, featuring a maximum edge size of 1 mm at the edges of the specimens and multiple levels of refinement down to an edge length of 0.4 μm at the crack. This source model was applied to both carbon fibre-breakage and to crack-growth in epoxy resin. For each of these a different initial time-step was chosen to account for the different wave-velocities within the materials. A time-step of 0.01 ns was used for the fibre-breakage and 0.1 ns for the epoxy during the period of crack-growth. A coarser time-step of 10 ns is then used for the subsequent wave-propagation. The total crack lengths for the specimens were 7 μm and 800 μm for the fibre-breakage and matrix-cracking respectively. The multi-physics capabilities of COMSOL Multiphysics ® were utilised to include an explicit model of the piezoelectric sensor, giving a voltage output, as opposed to a displacement or velocity seen in most other works. The circuit simulation capabilities of COMSOL Multiphysics ® were then used to include the effects of the cables, resistors and capacitors of the sensing circuit. The preamplifier and DAQ are not included explicitly in the model, but their affects are approximated by the band-pass filtering of the acquired voltage signal. Comparisons were made between the developed Cohesive Zone Model (CZM) source, a simple dipole point-source with a cosine-bell force application, and an "extended" source model, in which the same cosine-bell force is applied over the full fracture-surface. It was found that in terms of amplitude and frequency content, all source models were in relatively good agreement for the small fracture length of the fibre-breakage. For the matrix-cracking however, the dipole and the CZM sources remained in close agreement, but the extended source overestimated the signal amplitude by a factor of four, and featured a significantly different frequency distribution. This study represents one of the most detailed approaches taken to the modelling of acoustic emission thus far, and is likely to set the precedent for future AE simulations. It is however extremely computationally expensive compared to other approaches. It also requires significantly more knowledge of the material properties than other approaches, in particular the inclusion of the cohesive-zone model requires accurate determination of the fracture properties of the material, which are not widely available in literature for many materials and are therefore likely to require significant experimental work to be conducted in order to prepare an accurate simulation.

The majority of AE simulations have focused on wave-propagation in sheet- or plate-type specimens, with little work having been done on other geometries. One study which has consid-

ered other geometry was conducted by Hamstad [117], and considered wave-propagation in an 8.5 mm diameter Polyvinyl chloride (PVC) rod. The study utilised dipole sources, oriented axially, radially and tangentially, as well as a combination of three mutually perpendicular dipoles. The model was meshed with a swept quadrilateral mesh with a maximum size of 0.2 mm. A source rise-time of 2 μs was used with a cosine-bell time-dependency. The time steps utilised in the simulation were 0.0429 μs. Point-type sensors measuring out-of-plane displacement were used. The recorded signals were re-sampled 0.1 μs time-steps for analysis. A high-pass filter of 6 kHz was used to account for the frequency-limitations of a real wide-band AE sensor, and a low-pass filter of 100 kHz was also used to approximate the material damping of high-frequency content. While this approach may be significantly less accurate than the inclusion of Rayleigh damping, or full modelling of the material visco-elasticity, it is a very efficient way for the simulation results to be matched to appropriate experimental results with no impact on computation time and with no knowledge of the material properties beyond the readily-available density and Young's moduli. The FE results were compared with theoretical dispersion-curves for the longitudinal and flexural wave-modes of the rod in the time-frequency-domain, allowing one longitudinal and two flexural modes to be identified. It was found that both the dipole orientation and the offset from the axis affected the relative amplitudes of each of the wave-modes.

Le Gall et al. [60] have conducted a thorough study of FE simulation of AE in ABAQUS, considering a variety of sources, specimen-geometries and sensor types. The geometries utilised are dog-bone type aluminium test specimens, 200 mm long and 3.7 mm thick, with widths of 3 mm, 16 mm and 80 mm at the neck. For validation of the model against experimental results, a PLB is modelled on the surface as a monopole point source, with a time-dependency as determined by Sause [112]. For investigation of the effects of specimen geometry on the propagating wave-modes a chirp signal was applied to the specimen as a point force. The chirp signal is not representative of any typical AE source, but excites all frequencies up to 1.2 MHz relatively equally. The use of such a source allows the effects of the specimen geometry to be investigated over a wide frequency-band, rather than the results being a product of the source as much as the geometry. Attempts were also made to model typical AE sources; fracture-opening mode was simulated with a set of three perpendicular buried dipoles, with the dipole force in the x-direction (crack-surface opening displacement direction) being twice that of the y- and z-directions. In-plane shear was also modelled, using a pair of perpendicular buried dipoles, of equal and opposite amplitude, expanding in the x-direction and contracting in the y-direction. The dipole sources featured linear-ramp type time-dependencies, with rise-times of 0.1 μs, 1 μs and 10 μs being investigated. In order to include material damping, Rayleigh damping is included in the model in a similar manner as that used by Burks and Hamstad [55]. The simulations utilised a typical element-size of 400 μm and a time-step of 1.35 $e^{-7}s$. Sensing in the model is accomplished by point sensors measuring out-of-plane velocity. It is noted that the use of point sensors does not accurately model the aperture effect of a real sensor's physical size. The frequency response of the sensor is however included in the post-processing routine conducted in MATLAB, with frequency responses for both R15 and μ80 sensors being used. It was demonstrated in this study that varying the width of the specimen has a significant impact on the wave-propagation, with wide specimens exhibiting Lamb-modes, while narrower specimens exhibited bar-modes, and in the smallest specimens the edge-reflections made interpretation of the wave-modes very difficult. The FE simulated PLB source was validated against experimental results and showed good correlation. The other AE sources were not compared with experimental results, but the effects of varying the source parameters were investigated using modal analysis in the wavenumber-frequency-domain using a 2D Fourier Transform. It was demonstrated that variations in both the source-type and

source rise-time could be clearly detected by the 2DFT, in terms of the modes excited and the frequency-ranges excited.

FE simulation of AE was utilised by Sikdar in the development of a source-location scheme for hexagonal-honeycomb-type composite sandwich panels, consisting of a face material and a core material bonded with an epoxy layer [118]. ABAQUS was used to simulate a PLB source applied to a 3-layer panel of anisotropic materials. The source was applied as a time-varying force as described by Sause [112], and the specimen was meshed with a quadrilateral mesh, with an edge size of 0.5 mm; further details of the model set-up were not published however. The results presented from the FE model were also rather limited, with a single time-domain signal being compared to one acquired experimentally and showing relatively good correlation.

Ghouri et al. also utilised FE modelling of AE propagation in a study of linear source-location [119]. In this study, however, the specimen was a single layer of $3mm$ thick aluminium alloy. A 2D plain-strain simulation, conducted in ANSYS, modelled the application of a PLB source as a cosine-bell force applied to the surface of the specimen. The model utilised a 2.2 mm mesh, and a step size of 0.001 μs. Results presented in both time- and time-frequency-domain clearly illustrate the generation of an A_0 wave-mode which showed good correspondence with the theoretical dispersion-curves.

In summary, the use of finite element simulation of acoustic emission is still a relatively new and rapidly-developing field, but has shown significant promise as an efficient way to investigate a number of parameters which are difficult to control experimentally. Work thus far has focused primarily on the modelling of either isotropic materials, typically aluminium, or homogeneous representations of anisotropic materials. While a small number of multi-layer models of composites have been developed, no literature has been found on the modelling of AE in adhesive-bonds. PLB sources have been modelled extensively, and various models of crack-type sources have been proposed, but all those found so far have considered cracking within a homogeneous material, rather than considering the separation of two materials, as is the case for adhesive failure.

The modelling of wave-propagation is relatively well developed, although there is currently a lack of readily-available data for the visco-elastic properties of materials, which limits the ability to accurately model the frequency-dependent attenuation of certain materials.

The modelling of sources and sensors, however, still has a lot of scope for development. The cohesive-zone-model of a crack source implemented by Sause [116] is probably the most detailed model of an AE source developed thus far, but could still be further developed. Such detailed models do however require significantly more knowledge of the material properties than other approaches and are far more computationally expensive. It is therefore understandable that simple dipole sources have become the norm for many studies. Which approach is more appropriate will be dependent on the aim of the study, but in cases where the effects of specimen geometry are of greatest concern, such as for source-location projects, a simple dipole source is likely to be sufficient. If, however, the source mechanism itself is of greatest concern, then detailed source models, such as that proposed by Sause, are likely to offer the way forwards.

Similarly, in terms of sensor simulation, the full multi-physics simulation by Sause provides the most accurate model seen thus far, but is again computationally expensive and requires significantly more knowledge of the material properties and the sensor construction. Simple point-probes recording out-of-plane displacement or velocity can be appropriate for efficient determination of wave-modes, arrival times etc., even if they do not accurately capture the aperture effects of the sensor size, nor the frequency-response of the sensor or recording equipment. A happy medium

may, in some cases, be found by the use of an area sensor, as opposed to a point, to account for the aperture effects, and by post-processing of the signal by filtering to give a better representation of the frequency response of the sensor and the recording equipment.

2.6 Summary

This literature review has demonstrated that a significant amount of work has been conducted with regard to application of acoustic emission to the field of adhesive-bonding, and has shown that the technique has great potential in this field. It has, however, highlighted a variety of areas in this work which could be expanded on, and additional techniques which could be utilised. The majority of previous works, particularly early works, have relied on simple analysis methods such as number or rate of AE hits as an indicator of joint health, which, while effective, does not make use of the wealth of data which is contained within each hit. Some of the more recent studies have utilised more detailed approaches for the analysis of each hit, using methods such as source-location and analysis of time-domain and frequency-domain parameters, as well as the use of basic artificial intelligence and statistical pattern-recognition tools. The majority of works thus far have been limited to small laboratory-scale specimens and have therefore not given much consideration to the signal propagation within the specimens and to the impact that the adhesive-bond may have on this. Detailed investigation of AE propagation in large-scale specimens therefore presents a research opportunity which may be critical if the methods used in previous laboratory experiments are to be scaled up for potential large-scale industrial uses. Additionally, some work has been carried out to investigate the effects of adhesive-bonding defects on AE propagation, and the use of AE with a simulated source, such as a PLB, as a method of defect detection. This work, however, is in its infancy and would benefit from investigation of a greater range of defect- and specimen- types, as well as further assessment of appropriate analysis methods. A variety of works have conducted fracture tests using different fracture-modes, and have analysed the overall trends throughout the tests in terms of onset of AE, and rate of hits, with these studies typically comparing these features with the load and displacement plots for the tests. These works have, however, not typically used techniques such as modal AE analysis to delve deeper into the data contained within each hit. As modal AE analysis has been well proven in other applications, such as for differentiation between failure-modes in composites, it stands to reason that its application to the failure of adhesive-bonds may also be worth investigation. Dynamic Finite Element Analysis of AE is a rapidly developing field which has already been demonstrated to have significant value. As yet, little work has been conducted with regards to modelling AE occurring from, or propagating through, adhesive joints. There is therefore, significant scope for novel work in this field.

Chapter 3

Pencil-Lead-Break-based AE Tests

This chapter describes a series of practical experiments conducted using a PLB source to assess the wave propagation in a variety of specimens. The chapter covers the materials, instrumentation, procedure and signal-processing techniques used and illustrates, presents and discusses the results obtained.

3.1 Introduction

The first stage of this study was to investigate the effects of the presence of an adhesive layer on AE propagation in aluminium sheet specimens. While the ultimate aim of acoustic emission is to identify, locate and classify a source, understanding of the propagation phase of acoustic emission is a vital building block towards being able to achieve this, as the recorded signals are a product of the source, the propagation medium and the sensing system.

While previous works, such as those by Heller et al. [2], have investigated the propagation of Lamb waves in bonded specimens using other methods, such as laser-ultrasound, it was felt to be important to conduct tests using an AE system to establish the applicability of these findings over the significantly lower frequency-range used in AE. It was therefore decided to investigate AE propagation utilising a standard PLB as a repeatable simulated source, with signals being recorded using an AE system.

It is noted that this isn't true acoustic emission, as the source is an external source being applied to the specimen, rather than the source resulting from the failure of the specimen itself. This technique is truly more similar to acousto-ultrasonics. The technique does however provide a relatively repeatable broadband source which allows the signal propagation and detection to be investigated in a systematic manner which would not be possible when considering true acoustic emission arising from failure of the adhesive bond, as bond failure is too variable and unpredictable.

Previous works using a PLB AE source for investigation of adhesively-bonded joints, namely works by Prathuru [9] and Droubi et al. [8,98] have yielded some interesting observations, but have been limited to small (120 mm x 50 mm) coupon-type specimens, in which the propagation distance is minimal, and signals are highly convoluted by the inclusion of multiple edge-reflections, making it difficult to investigate features such as the wave-modes generated. It was therefore decided to focus on significantly larger specimens, in which larger propagation distances could be investigated and edge-reflections are identifiable and can be analysed or isolated at will.

Following the investigation of bonded and un-bonded specimens, it was decided to extend the study to include specimens featuring defects, specifically void-type defects. The aim of this part of the study being two-fold. Firstly to assess the effects of defects contained within the propagation path on the recorded signals. Secondly, to assess the potential of the use of a simulated AE source (PLB) as a potential method for detection and classification of void-type defects, as has previously been demonstrated by Prathuru [9] for detection of kissing-type debonds in adhesively-bonded specimens, and by Droubi et al. [49] for detection and classification of welding defects.

3.2 Materials

3.2.1 Defect-Free Tests

The essential experimental approach was to carry out a systematic investigation of AE propagation in aluminium sheet specimens, that investigation spanning over a single sheet, two identical sheets placed on top of each other without adhesive (un-bonded double-layer), and an adhesively-bonded specimen, consisting of two aluminium sheets, bonded together with an epoxy adhesive layer. 1050A H14 aluminium substrate sheets of average thickness 1 mm (Grampian Steel Services, UK) were cut into sections of 500 $mm\times$ 500 mm. For the adhesively-bonded specimen, the adherends were first abraded by hand with P400-grade abrasive paper then rinsed with acetone and cleaned using Loctite®SF 7063, giving a mean surface roughness (Ra), before bonding, of 1.18 μm, tested using a Taylor Hobson Surtronic 3+ surface roughness tester at ten randomly selected locations on each specimen. Following the process of surface preparation, the LOCTITE EA 9461 adhesive (a typical thixotropic two-part epoxy, chosen for its ease of application and room-temperature curing) was applied uniformly to the entire surface of a single sheet using a clean aluminium spreading stick. The opposite sheet was carefully placed on top and a flat plate with weights, totalling 180 N, was placed on top of the specimen to create a uniform load. The specimen was left to cure for over 72 hours (as per manufacturer recommendation) to achieve full strength before being handled. Average room temperature and relative humidity during curing were approximately 19°c and 41%, respectively. The mean cured adhesive thickness (calculated from 40 thickness measurements taken around the edges of the specimen using a micrometer) is 0.2 mm, with a standard deviation of 0.01 mm.

3.2.2 Void-Type-Defect Tests

The experimental approach was to use defect-free control specimens as a reference, and to conduct a comparative study of multiple AE parameters with specimens featuring two different sizes of deliberately-induced defects within the adhesive layer, allowing the effects of defect presence and defect size on AE propagation to be evaluated. Three specimens of each type were prepared and tested to ensure reliability of results and to minimise the effects of any defects introduced accidentally. Each specimen was prepared from two 500 $mm\times$ 250 mm layers of 1 mm thick 1050A H14 aluminium sheet. This smaller size, compared to the defect-free tests, was chosen for convenience and ease of manufacture. The aluminium adherends were prepared by rinsing with acetone, manual abrasion with P400-grade abrasive paper, followed by a further acetone rinse and cleaning with Loctite®SF7063. Average surface roughness before bonding was found to be 1.17 μm, tested using a Taylor Hobson Surtronic 3+ surface roughness tester at ten randomly selected locations on each specimen. The specimens were bonded using Loctite®EA 9461 adhesive, a typical

commercially-available thixotropic two-part epoxy chosen for its ease of application and room-temperature curing. The adhesive was manually applied to a single adherend for each specimen using a clean aluminium spreading stick. Small aluminium shims, 0.5 mm thick and approximately 2 $mm\times$ 2 mm, were placed throughout the adhesive. This approach allows more control of the bond-line thickness than was possible in the previous tests as the minimum thickness of the adhesive is limited to the thickness of the shims (assuming minimal bending of the adherends). For the defect-free control specimens the adhesive was spread over the entire 500 $mm\times$ 250 mm area of the adherend. To induce the void-type-defects, however, no adhesive was applied to the defect area. The defect areas were located at the centre of the specimens and measured 10 $mm\times$ 10 mm and 40 $mm\times$ 40 mm. While the defects are referred to by these sizes throughout this study, it is fully expected that the actual sizes of the defects will be slightly reduced by spreading of the adhesive as the second adherend is applied. After adhesive application, the second adherends were carefully aligned and placed onto the adhesive layer, and a large steel plate and a series of weights totalling 10 kg were then placed on top to maintain pressure during curing. Specimens were left to cure for over 72 hours (as per manufacturer recommendations) at approximately 19°c and 41% humidity before testing was conducted.

3.3 AE Instrumentation

An in-house-built four-channel AE system was used throughout this study. The system consisted of AE sensors, preamplifiers, a signal conditioning unit (SCU), shielded connector-block and a desktop PC with a data acquisition card (DAQ).

The sensors used throughout this study were Physical Acoustic Corporation Micro-80D differential sensors. These are high sensitivity and high bandwidth sensors with good resistance to background noise, due to the elimination of common-mode noise by the differential design. The sensors feature a stated operating frequency-range of 175-900 kHz and have a good response within this range, but will operate well below this range, albeit with reduced sensitivity. The two sensors used in this study exhibit peak frequencies at 307.62 kHz and 322.27 kHz. The calibration certificates for these sensors are included as Appendix A Sensor Calibration Certificates.

The sensors are connected to Physical Acoustics Corporation 2/4/6 switch-selectable-gain single-ended differential preamplifiers. These preamplifiers feature adjustable gain of either 20 dB, 40 dB or 60 dB and feature a 20 kHz high-pass filter. The signal conditioning unit (SCU) is an in-house-built four-channel system, which allows selection of a further -12 dB, 0 dB, +6 dB or +12 dB gain. The shielded connector-block used, which acts as the link between the SCU and DAQ, is a National Instruments BNC-2120. The data acquisition card in the desktop PC is a National Instruments PCI-6115, capable of recording at a rate of 10MS/s.

In these experiments a sampling rate of 2.5 MHz was used. This was chosen to be more than double the maximum frequency of interest (1 MHz) thus ensuring that the Nyquist sampling criteria [126] was satisfied and the signal would not be subject to aliasing. A trigger level of 0.2 V was used, and for each hit 100,000 samples were recorded.

The system is controlled using NI LabVIEW virtual instruments (VIs). Two different VIs were used in this project. One uses a threshold-crossing on one of the input channels to trigger recording of data, and will record a predefined number of data-points and save the data as a .bin file. This VI was used for all tests conducted using a simulated source. Recording in the second VI is manually started and stopped and is used to record continuously. This VI saves output files

in the National Instruments .TDMS format.

For the calibration tests, and for the investigations of AE propagation, a simulated source was used. The simulated source chosen was a PLB, also known as a Hsu-Nielsen source [127]. This standardised source involves breaking the lead of a mechanical pencil against the surface of the specimen being tested. It is a commonly-used calibration technique as it produces a strong broadband signal with good repeatability while being simple and low cost. As per ASTM E 976-99 [11], a 2-3 mm length of 2H grade lead was broken to create the source. To improve repeatability of the angle at which the source was applied, an in-house 3D printed guide-ring was fitted to the pencil. While the PLB source does feature relatively good repeatability, there is some variation. To account for this, a minimum of 10 breaks were conducted for each test, to ensure that variation seen in the results could be attributed to the parameters under investigation, and not to random variation of the source.

3.4 Experimental Procedure

3.4.1 Defect-Free Tests

For all experiments carried out in this study, the AE sensor was positioned on the face of the specimen in its centre, and AE was recorded with the simulated source placed along the centre-line at 50 mm, 100 mm, 150 mm and 200 mm away from the specimen centre as shown in Figure 3.1. To assess the effects of source orientation, the simulated AE source was also applied to the edges of the specimens at 250 mm from the sensor, as shown in Figure 3.1. The source applied to the edge of the specimens was applied at the mid-depth of the specimen in the case of the single sheet. On the un-bonded double-layer specimen, it was applied to the mid-depth of the upper sheet. For the bonded specimen, the source was applied at the mid-depth of the upper adherend and on the adhesive layer at the mid-depth of the entire specimen. To ensure repeatability, five pencil lead breaks were recorded at each of the positions as per Figure 3.1.

3.4.2 Void-Type-Defect Tests

In order to assess the effect of source-to-sensor distance, and the effects of source and sensor proximity to the defect, four different source and sensor configurations were investigated, as illustrated in Figure 3.2. In Configuration A, the source and sensor are located on the centreline 50 mm apart, evenly spaced either side of the central defect. Configuration B is similar, but with an increased source-sensor distance of 100 mm. In Configuration C, the sensor is mounted at the centre of the defect, with the source located on the centreline 50 mm away. In Configuration D, the source is located at the centre of the defect, while the sensor is mounted 50 mm away on the centreline.

This approach was taken as a previous study by Prathuru [9] indicated that similar PLB tests conducted on specimens with kissing-type bond defects were most sensitive to the defects when the source or sensor were located directly above the defect. It would however be more efficient to be able to inspect a path which may include a defect somewhere along its length. In terms of inspection efficiency, the longer the path that can be inspected, the better. although it is expected that sensitivity to defects will reduce as the path length is increased, hence the choice to test two different configurations with the source and sensor either side of the defect, but with different source-sensor distances. For each configuration of each specimen, the sensor was mounted,

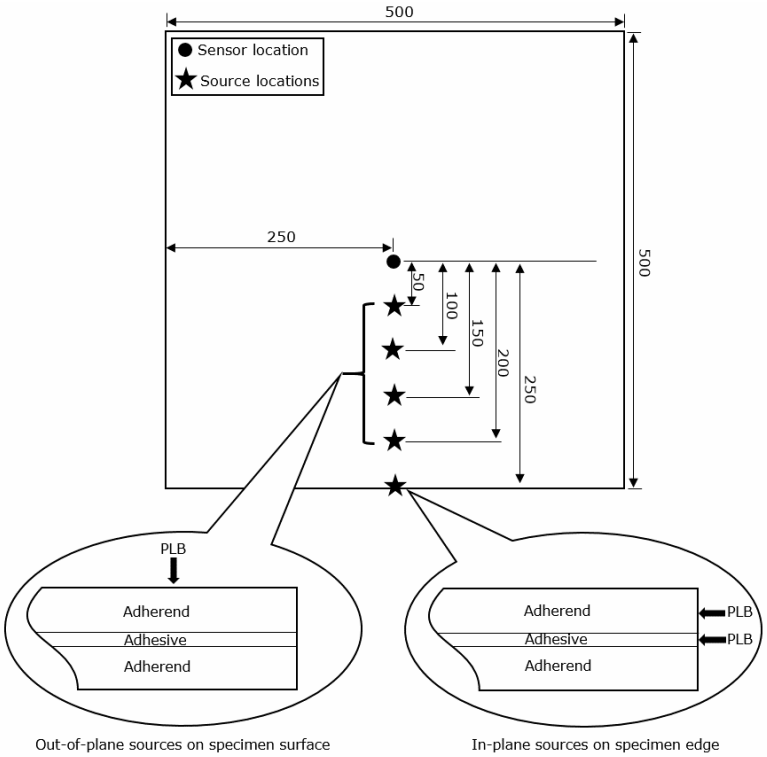

Figure 3.1: Source and sensor locations used for all specimens. PLB applied on sheet surface to create an out-of-plane source at 50mm, 100 mm, 150 mm and 200 mm from the sensor. PLB applied to edge of the sheet (and edge of the adhesive for the adhesively-bonded specimen) to create an in-plane source 250 mm from the sensor. All dimensions in millimetres.

removed and remounted three times to account for any potential variation in the quality of the sensor's coupling. Analysis of variance (based on signal energy) showed sensor mounting to be statistically insignificant in these tests, with a P-Value of 0.748 (P ¡ 0.05 for significance). For each of these three fittings the PLB source was applied ten times to account for variation in the source. The results presented in the rest of this chapter for each configuration of each specimen are therefore the average of a total of 90 repeats, resulting from three specimens of each type, three mountings of the sensor on each specimen and ten applications of the source for each mounting. 1080 PLBs were conducted in total.

3.5 AE Signal-Processing Techniques

3.5.1 Wavelet-Transforms

In the analysis of thin sheets, it is particularly important to be able to conduct analysis in both time- and frequency-domains. The dispersive nature of Lamb- or Plate-waves results in the propagation of multiple wave-modes with different frequency components travelling at different velocities. Combined with the effects of edge-reflections this makes in-depth analysis in either time or frequency-domain alone extremely challenging, particularly where components may overlap and edge-reflections may occur prior to the arrival of slower-travelling components of the ini-

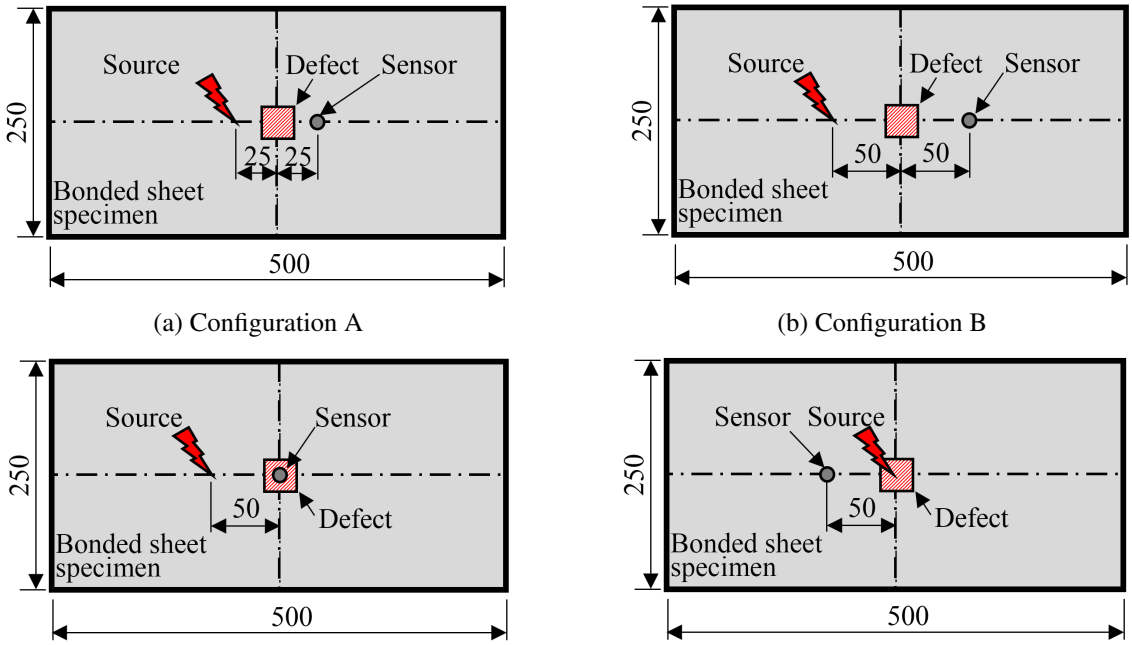

(a) Configuration A

(b) Configuration B

(c) Configuration C

(d) Configuration D

Figure 3.2: Source, Sensor and Defect configurations

tial wave. To allow analysis of the recorded AE waveforms in both time and frequency-domains the wavelet-transform (WT) has been utilised. In this study wavelet-transforms were initially implemented using open-access AGU-Vallen Wavelet software (ver. R2015.0430.6), though the use of MATLAB (ver. 7.9.0.529 (R2009b)) was later found to be preferable. This was due to a more efficient workflow, using only a single software, and also due to the added flexibility and the ability to include multiple dispersion-curves with different propagation-distances, representing edge-reflections. The wavelet used was a Gabor-type wavelet as this is known to provide the best combination of time and frequency resolution of any available wavelet as the product of its standard deviations in both time and frequency-domains are minimised [51].

3.5.2 Lamb wave Dispersion-Curves

To allow identification of the different Lamb wave modes and edge-reflections present within the acquired wavelet-transforms, the theoretical arrival times of these different features have been calculated from the group-velocity curves based on the Rayleigh-Lamb equations. In this study, this process of generating group-velocity curves has been carried out using initially the open-access Vallen Dispersion software (ver. R2015.0430.6) [128], and additionally using a modified version of the MATLAB app ElasticMatrix [129]. Vallen Dispersion is an easy-to-use standalone programme, but is limited to generating dispersion-curves for single-layered specimens. The ElasticMatrix MATLAB app is less user-friendly, but does support generation of dispersion-curves for multi-layered specimens, which is advantageous for the study of bonded specimens. The app requires the user to specify the materials and thicknesses of each layer in the specimen. It contains a library of standard materials which can be utilised, and also features the option to add or modify materials, specifying their density, and compression- and shear-wave velocities.

The group-velocity curves for the five lowest-order wave-modes of a 1 mm thick aluminium sheet are shown below in Figure 3.3. For this thickness of specimen, only the zero-order symmetric (S_0) and anti-symmetric (A_0) modes exist at frequencies under 1 MHz, meaning that for frequencies generally considered in AE there will be only two wave-modes propagating and therefore higher-order modes need not be considered, simplifying any analysis. At these relatively low frequencies, the group velocities of the two modes are significantly different; given suitable propagation distance, the arrivals of these modes should therefore appear well separated in the time-domain.

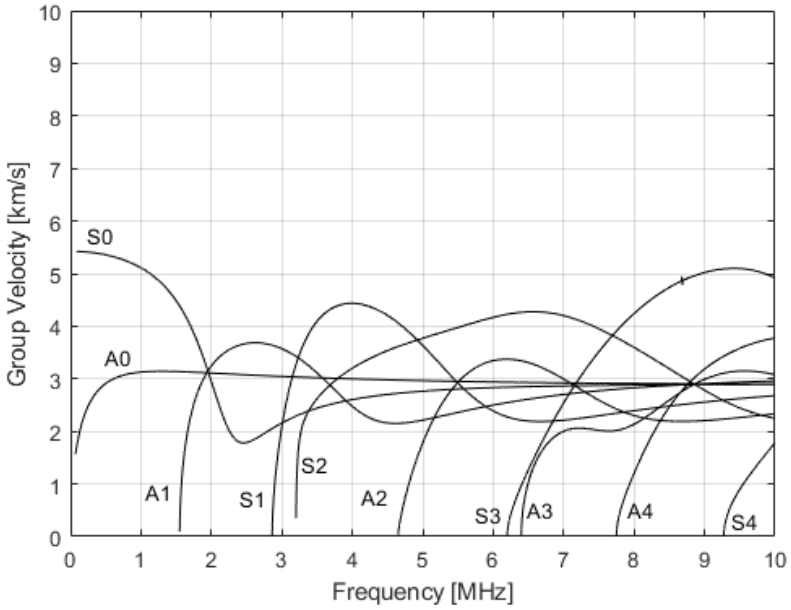

Figure 3.3: Group-velocity curves for a 1 mm aluminium sheet. $A_{0\rightarrow4}$ represent the four lowest-order anti-symmetric waves and $S_{0\rightarrow4}$ represent the four lowest-order symmetric waves.

To allow comparison of the group-velocity curves with the WT coefficient plots, the velocities at each frequency are converted to arrival times based on the known propagation distance for each test. This technique has previously been successfully demonstrated by Hamstad et al. [59] [67] [57], considering AE wave-propagation from in-plane and out-of-plane sources in large aluminium plate specimens, as well as having been applied to analysis of the more complex geometry of a section of rail track by Zhang et al. [61]. As a PLB source is being used in this study, the exact application time is unknown and cannot be used to align the theoretical dispersion-curves with the recorded signal. The curves have therefore been aligned with the acquired time- and time-frequency-domain plots in MATLAB, by aligning the earliest arriving group-velocity component with the first threshold crossing of the recorded time-domain signal. Throughout this work, unless otherwise stated, the dispersion-curves used are those calculated for a single adherend, rather than for the entire multi-layer specimen. This is based on the findings of previous works by Seifried et al. [3] and Heller et al. [2], whose studies have suggested that while the presence of additional layers may generate additional wave-modes with different dispersion characteristics, those which are recorded on the surface of the adherend can be reasonably approximated by the dispersion-curves of that single adherend. Further justification of this is provided in Sections 3.8.1 and 3.6.1.

3.5.3 Edge-Reflections

Both fundamental symmetric (S_0) and anti-symmetric A_0 mode Lamb waves are subject to multiple reflections from the edges of the specimens, and reflections will continue to occur until the waves have been fully attenuated. Due to the relatively large size of the specimens tested, the high energy A_0 reflections generally appear well separated from the initial waves in the time-domain, allowing separation and identification of these waves. The higher-velocity (S_0) reflections do however still overlap with the initial A_0 mode in the 100 mm, 150 mm and 200 mm configurations, due to the source proximity to the edge of the specimen. Identification of the reflections and their propagation paths provides a clearer understanding of the features appearing in the WT coefficient plots. Group-velocity curves have been converted to arrival times based on propagation distance for the first three reflections, as was done for the initial S_0 and A_0 waves. The propagation paths and distances used for the reflections, as shown in Figure 3.4, are: the near-edge-reflections (labelled R1 in following figures), from the source to the closest edge and back to the sensor all along the centre-line of the specimen, the side-edge-reflections (labelled R2 in following figures), from the source to the side edges of the specimens at an angle and then reflecting back to the sensor at the corresponding angle, and the far-edge-reflections (labelled R3 in following figures), from the source to the furthest edge and back to the sensor all along the centre-line of the specimen. Due to the symmetry of the test set-up, reflections from both side edges occur simultaneously. By overlaying the converted group-velocity curves on the WT plots, high-energy regions can be attributed to certain reflections. This is illustrated in Figure 3.5. This method of identifying reflections has been successfully extended to identify more than three reflections, but, for the sake of brevity only the first three are presented.

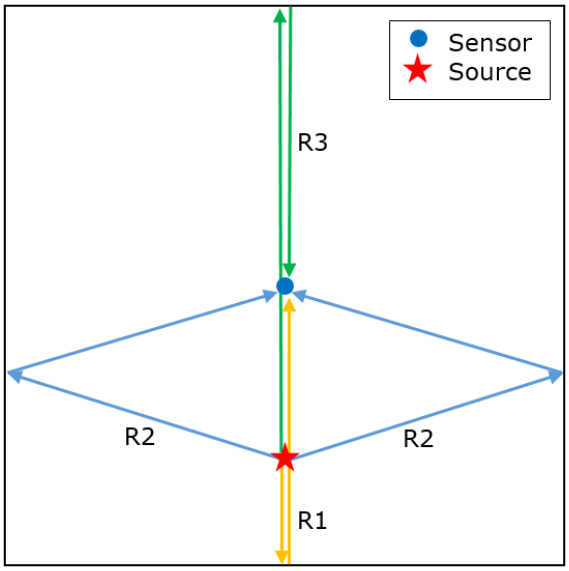

Figure 3.4: Predicted wave-propagation paths from source to sensor by means of edge-reflections: (R1) Near-edge-reflections, (R2) Side-edge-reflections, (R3) Far-edge-reflections

3.5.4 Wavelet-Transform Example

Figure 3.5 illustrates an example of the techniques previously described. The lower window of the figure shows the original time-domain signal recorded from the sensor. The upper window presents a contour plot of the wavelet-transform coefficients. The red, high-energy, regions of the WT plot can be seen to correspond with high-amplitude regions of the time-domain signal, while the lower-energy regions correspond to lower-amplitude regions. The group-velocity curves overlaid on the upper plot represent the theoretical arrival times of the initial zero-order wave-modes (shown in red), the reflections from the near edge (yellow), side edges (blue) and furthest edge (green). The alignment of the modified group-velocity curves based on the first threshold crossing of the time-domain signal is shown to be effective, as the curves are seen to align well with high-energy regions of the WT coefficient plot. In the time-frequency-domain, and with the aid of the overlaid curves, it is possible to assess the contributions of each wave-mode and each reflection to the overall signal in a way which is not possible from analysis in the time-domain alone.

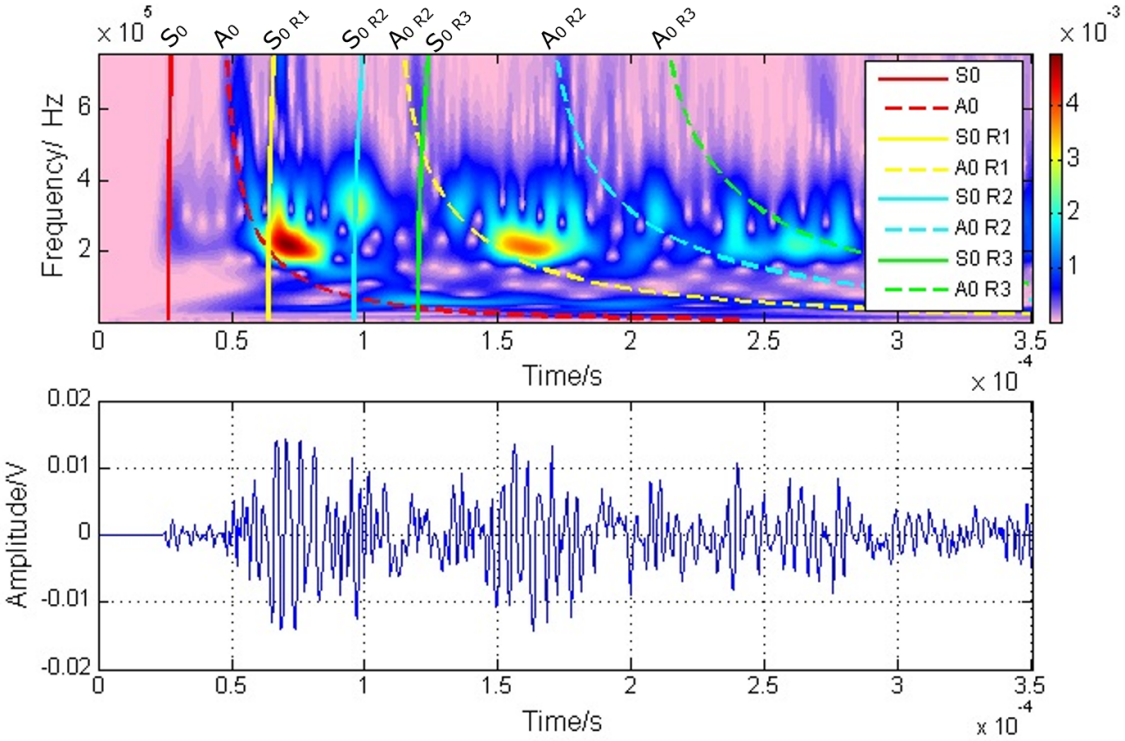

Figure 3.5: Top: Example WT coefficient plot with overlaid group-velocity curves corresponding to initial S_0 and A_0 waves and their subsequent edge-reflections. Bottom: Original time-domain signal. Example shown for single-sheet specimen with out-of-plane source and 150 mm propagation distance.

3.5.4.1 Artificial-Neural-Network Pattern-Recognition

In order to differentiate between the different specimen types and to estimate the defect sizes in the void-containing specimens, artificial-neural-networks have been utilised. Artificial neural net-

works use a set of training data in which each data-set has been manually labelled as corresponding to a certain category, in this case the categories of No Defect, 10 mm Void and 40 mm Void. The ANN uses the training data and labels to learn how to categorise the data or to estimate an output based on the data-set. A full explanation of ANNs is beyond the scope of this article, but a very basic explanation is included in Chapter 2, and further, more detailed, explanation is given by Shanmuganathan and Samarasinghe [130] amongst others.

Multiple different combinations of parameters could be utilised as inputs to the neural networks, however, after some experimentation, the initial portion of the raw AE time-domain signal (as described below) was found to provide the best results. Other approaches, based on the time-frequency-domain, provided results which came close in terms of accuracy, but were far more computationally expensive, while other attempts based on typical AE parameters, or on the frequency content, provided results of significantly lower accuracy.

A continuous series of 1000 data points (400 μs) was extracted from the time-domain signal, starting from just before the first threshold crossing, as shown in Figure 3.6. The limit of 1000 data points was chosen as this section includes the arrivals of the initial S_0 and A_0 wave-forms and the initial edge-reflections, as previously described. It does however exclude a large number of low-amplitude edge-reflections which occur later in the signal. Using a lower number of data-points to exclude the initial edge-reflections may be beneficial in cases where defects are located randomly on the specimens, and where the source and sensor positions vary significantly. In this case, however, as the defects are all in the same location and the source and sensor positions are consistent between defect types, inclusion of these reflections was found to be beneficial over using a lower number of data-points.

To perform the classification, a two-layer feed-forward network with ten sigmoid hidden neurons and softmax output neurons was implemented in MATLAB using the Neural Network Pattern Recognition app. A feed forward network is the most basic type of network architecture, in which data is passed sequentially from input to output through all of the layers, without the inclusion of any feedback loops. The sigmoid neurons in the hidden layers will output a value between 0 and 1, based on the input, and the weights and biases, of the neuron. They act similarly to a simple threshold or step function, in which inputs below the threshold result in a zero output, and inputs above the threshold result in an output of one, but the use of a sigmoid function instead of a sudden step results in a more gradual change in output which is typically better representative of most data-sets [131]. The softmax output neurons are used to normalise the network output into a probability distribution over the output classes. To do this, it applies the exponential function to it's input, and then normalises it by dividing by the sum of the exponentials of all of the inputs to that layer [132]. The result being that each output class (No defect, 10mm defect, 40mm defect) is assigned a probability between 0 and 1, with the probabilities of all the classes adding up to a total of 1. A diagram of this network, generated in MATLAB, is included as Figure 3.7. The network was trained using scaled conjugate gradient backpropagation.

To estimate the defect size, the Neural Network Fitting Tool was utilised to create another two-layer feed-forward network with ten sigmoid hidden neurons and linear output neurons. In this case the linear output neurons do not generate a probability of occurrence for a number of predefined classes like the softmax neurons do, but instead the output is simply the weighted sum of its inputs, plus a bias term, resulting in the output of potentially any real number [133]. As will later be discussed, this can result in outputs that are not physically possible, such as in this case negatively-valued defect-sizes, which require some form of correction. This network was trained using the Levenberg-Marquardt backpropagation algorithm. A diagram of this network is included

as Figure 3.8.

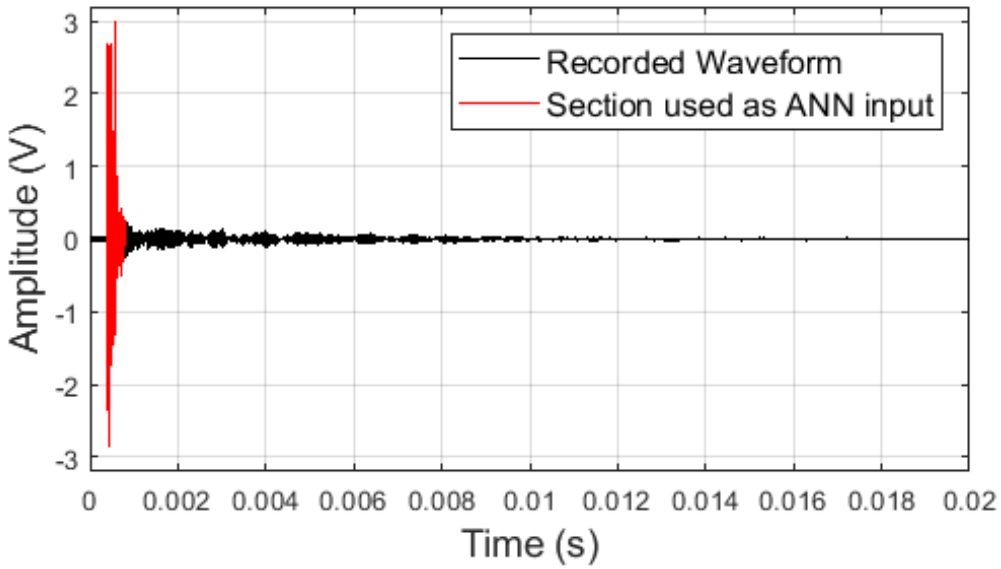

Figure 3.6: Example of the section of waveform recorded from a PLB used for an input to the ANN

For both the classification and the defect-size estimation, the 1080 samples, composed of data from 3 defect sizes, 3 specimens of each defect size, 4 source-sensor configurations, 3 sensor mountings and 10 applications of the source, were randomly divided to give 70% of the data for training of the network, 15% for validation and 15% for testing. This means that 70% of the samples are used to initially set and optimise the weights of the connections during the training of the network. The 15% used for validation can be used to test the network and to make further small adjustments to its parameters, while the final 15% for testing are used to give an un-biased (test data has not been previously used in training or validation) measure of the network's effectiveness. This approach ensures the generalisability of the network, and ensures that the network is not only valid for the PLBs included in the training data-set.

As this is very early preliminary work in the use of ANNs for PLB-based detection and sizing of adhesive defects, the system has only been tested on defect-types, defect-sizes, and source-sensor configurations which have been included in the training data, to simply establish whether the concept is viable. For the method to be truly useful, it will need to be able to detect defects of different types and sizes from those included in the training data. Due to the constraints of this project, testing of this type to find the limitations of the system has not been conducted, and remains a key part of future work if this method is to progress any further.

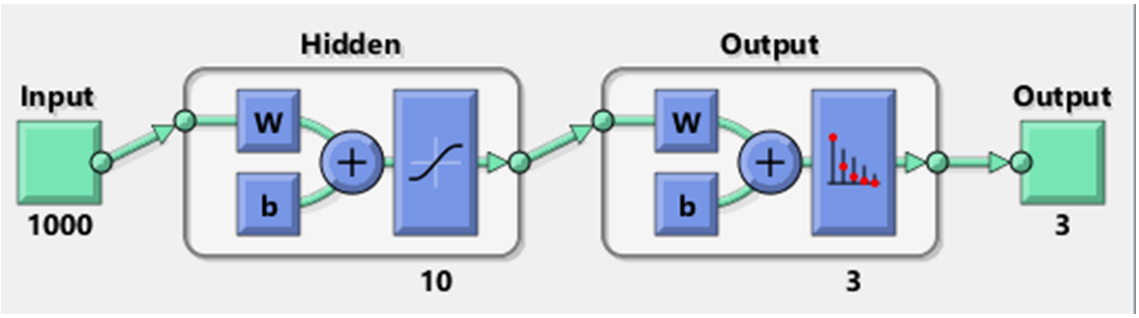

Figure 3.7: Defect-classification network diagram

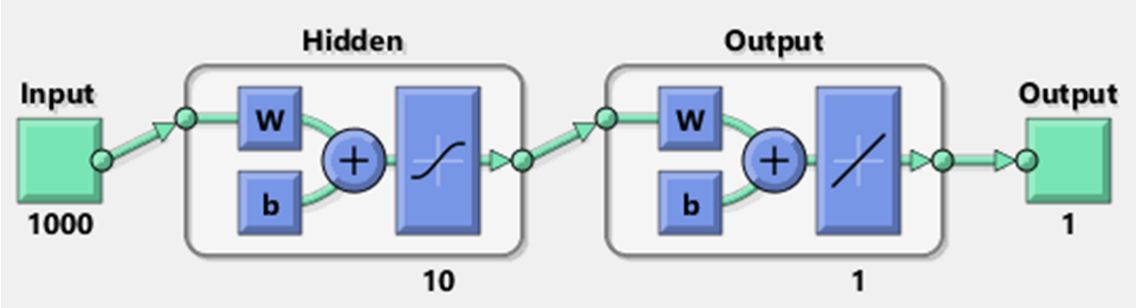

Figure 3.8: Defect-size-estimation network diagram

3.6 Results of Defect-Free Simulated-Source Tests

3.6.1 Modal Analysis

It was found that all specimens tested show good correspondence between high-energy regions of the WT-coefficient plots and the modified group-velocity curves generated for a single 1 mm sheet. The theoretical dispersion-curves for both a single sheet and for a bonded specimen were both calculated and are shown in Figure 3.9. Comparison of these dispersion-curves reveals that the number of modes which will theoretically exist over the frequency-range of interest in a bonded specimen is higher than in a single specimen, with four modes existing as opposed to just the fundamental symmetric and asymmetric modes. It can however be seen that these modes are very close to those for a single sheet. There are two modes which closely represent the A_0 mode. The first is a dispersive mode which approximately follows the A_0 mode, but has a slightly higher velocity below 200 kHz, and slightly higher at frequencies above this. The second is a non-dispersive mode which propagates at the same velocity as the A_0 mode at 300 kHz (close to the peak frequency of the sensors used in this work). This mode follows close to the A_0 mode at higher frequencies where the A_0 mode is less dispersive, but diverges from it at low frequency. There are two highly-dispersive modes which come close to the S_0 mode of the single sheet. The first closely follows the the S_0 mode at low-frequency and then diverges, while the other mode appears at very low velocity at around 450 kHz and then begins to converge with the S_0 mode with increasing frequency.

Based on this comparison of the theoretical dispersion-curves it can be seen that the fundamental dispersion-curves of the adherend do generally provide a good approximation of the dispersion characteristics of a bonded specimen. The accuracy of this approximation is however dependent

on the mode and frequency under consideration. The A_0 mode provides a good approximation over the entire frequency-range, while the S_0 mode provides a close approximation at lower frequencies (<400 kHz), with a less accurate approximation at higher frequencies. In this case the peak-frequency of the sensors, and therefore the majority of the recorded signal, is centred in the 200 kHz to 400 kHz region, in which the approximation of the dispersion remains relatively accurate for both modes. This is reflected in by the fit of the single sheet dispersion-curves to the experimental results.

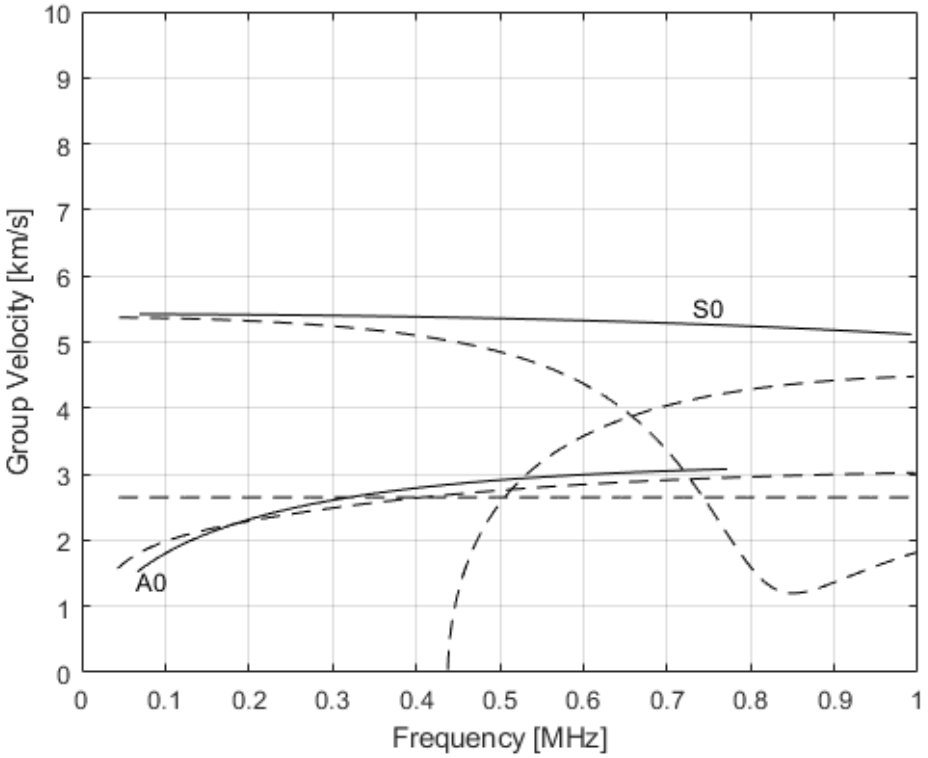

Figure 3.9: Theoretical dispersion-curves for a single $1mm$ aluminium sheet (Solid lines), and for a bonded specimen with $1mm$ aluminium adherends and $0.2mm$ thick epoxy adhesive-bondline (Dashed lines).

Figures 3.10 to 3.12 show the WT coefficient plots and modified group-velocity curves for an out-of-plane source applied at propagation distances of 50 mm, 100 mm, 150 mm and 200 mm on the single-sheet, un-bonded double-layer and bonded specimens. All specimen types exhibit the same basic features in the time-frequency-domain. A low-amplitude peak with frequency content between 200 kHz and 400 kHz signals the arrival of the initial S_0 wave, this is followed by the A_0 wave, which contains three prominent regions. The first appears in the high-frequency region above 400 kHz and is of short duration. The second region corresponding to the A_0 wave occurs in the 200 kHz to 400 kHz region, around the peak frequency of the sensor, and continues for a significantly longer duration than the first region. The third region occurs at low-frequency, under 100 kHz, and is of relatively long duration. These high-energy regions corresponding to both S_0 and A_0 waves recur throughout the signal as the waves are reflected by each of the edges. Increasing propagation distance leads to increasing the effects of dispersion, and thus also the separation between A_0 and S_0 waves. Moving the source further from the sensor is also seen to

affect the arrival times of the reflections, as the propagation distance for a near-edge reflection is reduced, while the propagation distances for side-edge and far-edge-reflections is increased. At a propagation distance of 200 mm the S_0 reflection from the near-edge arrives before the A_0 component of the initial wave.

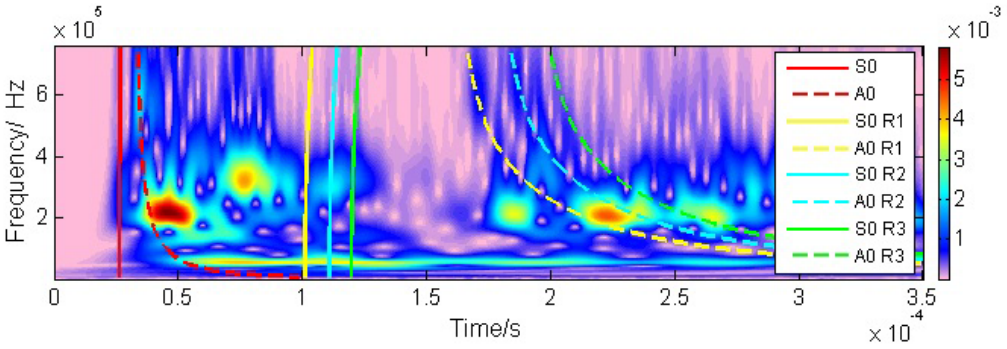

(a)

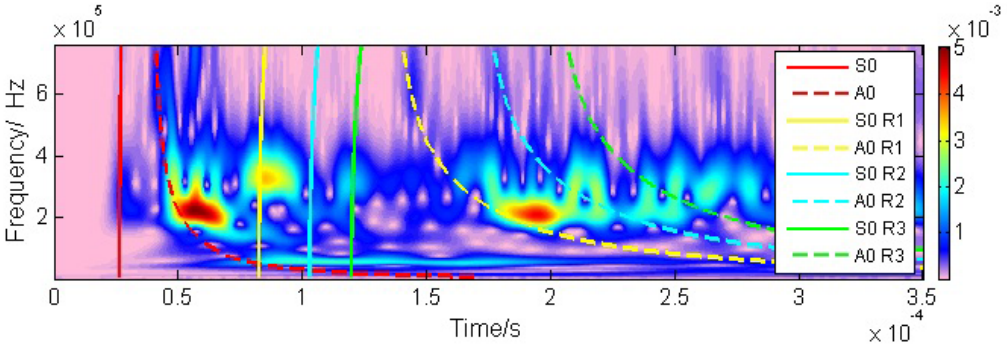

(b)

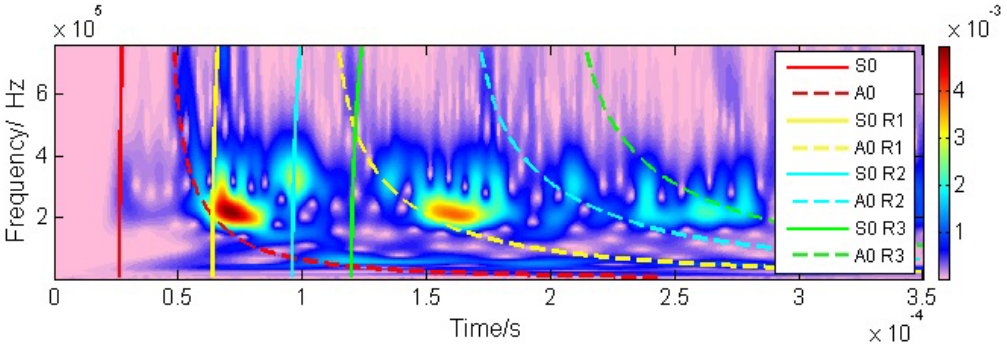

(c)

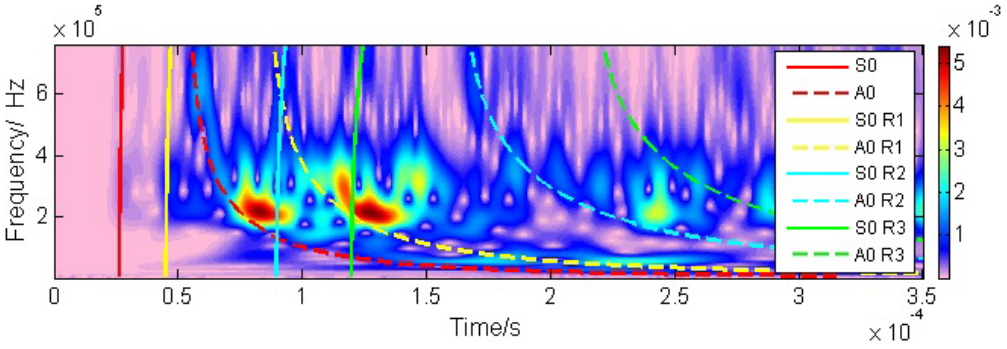

(d)

Figure 3.10: Example WT coefficient plots and modified group-velocity curves for an out-of-plane source applied to the single aluminium sheet specimen with source-sensor propagation distances of (a) 50 mm, (b) 100 mm, (c) 150 mm and (d) 200 mm.

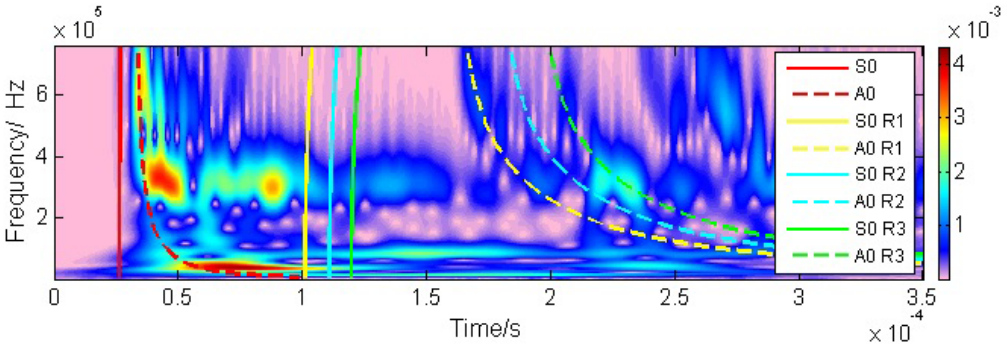

(a)

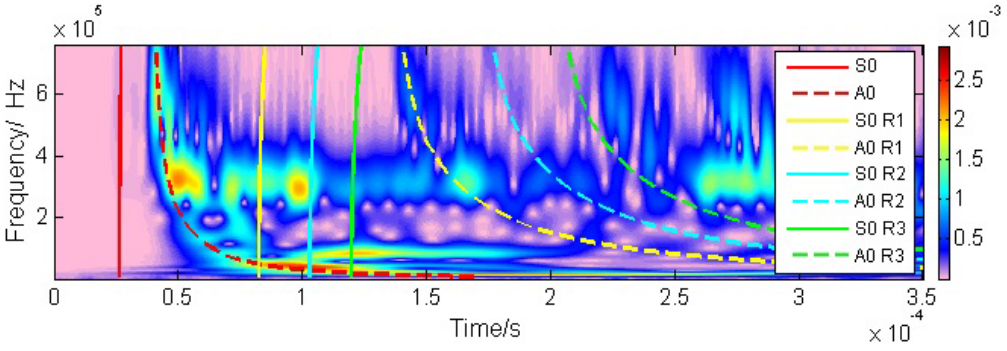

(b)

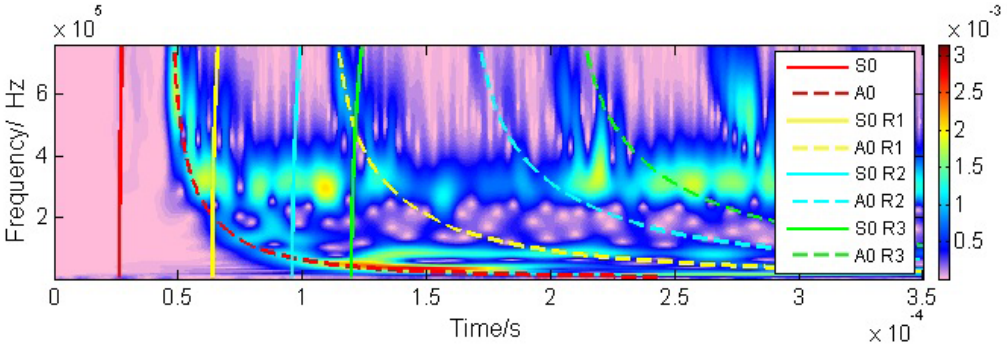

(c)

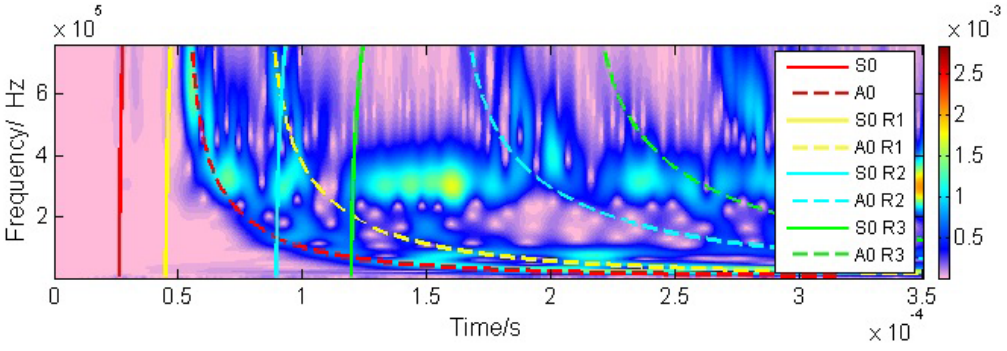

(d)

Figure 3.11: Example WT coefficient plots and modified group-velocity curves for an out-of-plane source applied to the un-bonded double-layer aluminium sheet specimen with source-sensor propagation distances of (a) 50 mm, (b) 100 mm, (c) 150 mm and (d) 200 mm.

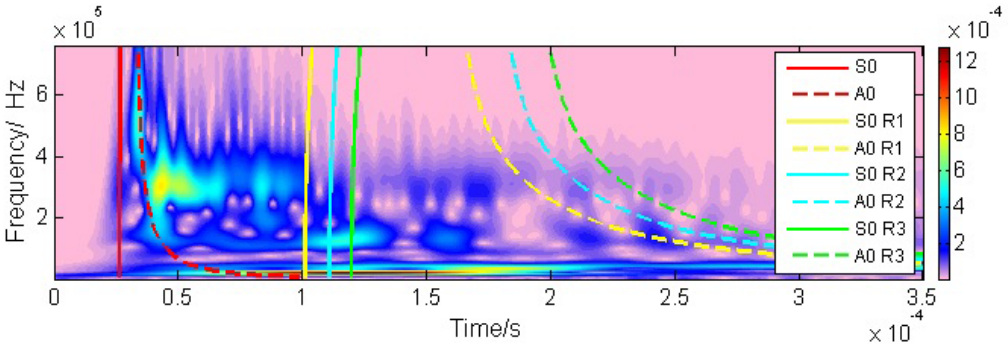

(a)

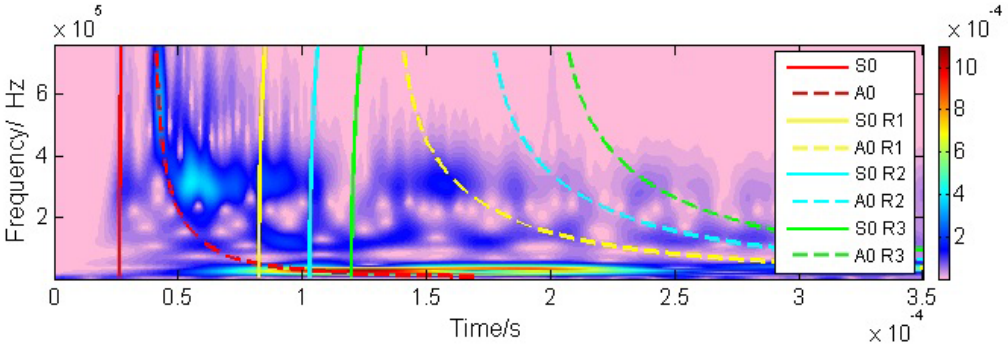

(b)

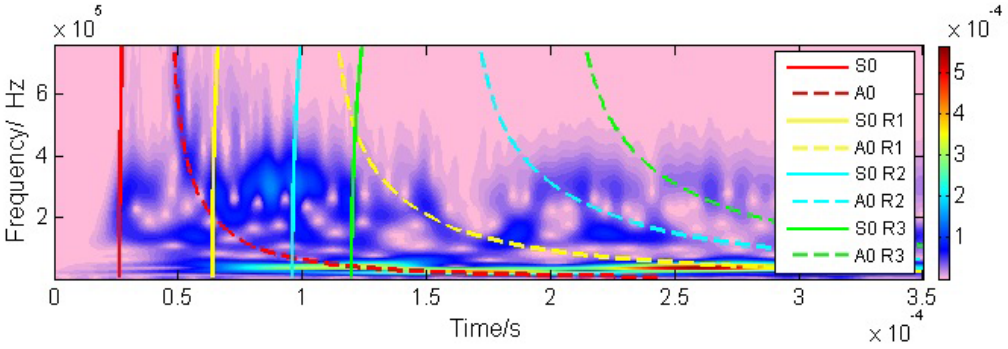

(c)

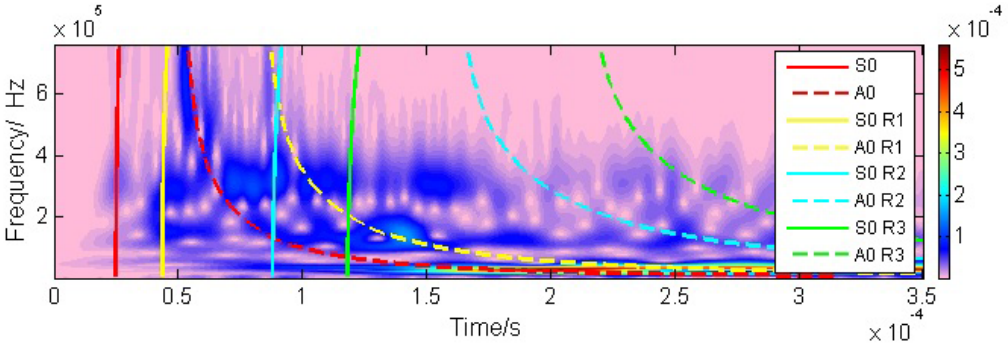

(d)

Figure 3.12: Example WT coefficient plots and modified group-velocity curves for an out-of-plane source applied to the bonded aluminium sheet specimen with source-sensor propagation distances of (a) 50 mm, (b) 100 mm, (c) 150 mm and (d) 200 mm.

3.6.2 Attenuation

Due to the increased specimen volume, leading to geometric attenuation, and the inclusion of a visco-elastic adhesive material, leading to increased material damping, the attenuation in the bonded specimen is found to be significantly higher than in the single or double layer aluminium specimens.

Comparing the energy over the whole signal duration, made up mainly of edge-reflections, results in the attenuation shown in Figure 3.13a. All specimens do exhibit attenuation over the propagation distances tested, but due to the high proportion of the signal made up of edge-reflections, the level of attenuation is minimal. There is however a significant difference between the specimens. The unbonded double-layer specimen exhibits AE energy reading in the region of 20% to 31% of the single sheet, while the bonded specimen produces AE energy in the region of only 0.96% to 6.93% of that recorded on the single-layer specimen. Focusing solely on the direct waves, rather than reflections, by investigating a time-window of only 150 μs, shows the effects of attenuation much more clearly. Figure 3.13b shows the AE energy recorded in these shorter time-windows. In this case the attenuation can be seen to follow the pattern of logarithmic decay which is typically associated with attenuation. It can also be seen that the rate of attenuation is far higher in the adhesively-bonded specimen than in the unbonded specimens, with the energy recorded in the bonded specimen varying from 71.4% of that recorded in the single sheet at 50 mm, down to only 5.87% at 200 mm from the source. This can be attributed to both the increased specimen volume, increasing the geometric attenuation, and the high level of material damping introduced by the viscoelastic adhesive layer. The unbonded double-layer specimen actually produced a slightly higher mean energy at 50 mm from the source, 3% higher than the single sheet, but exhibited a more rapid decay, down to only 55% at 200 mm from the sensor. The behaviour of the un-bonded specimen has potential to be quite complex, as the specimens will not be in perfect contact over their entire surface areas due to imperfections in the sheets, and additionally the contact status at any given point may change with time as the specimens vibrate. It can however be concluded that, over areas in which the sheets are in contact, the matching impedance of the two sheets will result in a higher level of energy transmission from one sheet to another than would occur from the single sheet to the cardboard and tissue paper on which the specimens were placed. The level of geometric attenuation in the un-bonded double-layer specimen will thus be higher than that of the single specimen, contributing to the reduced energy levels seen in the un-bonded specimen in Figures 3.13a and 3.13b.

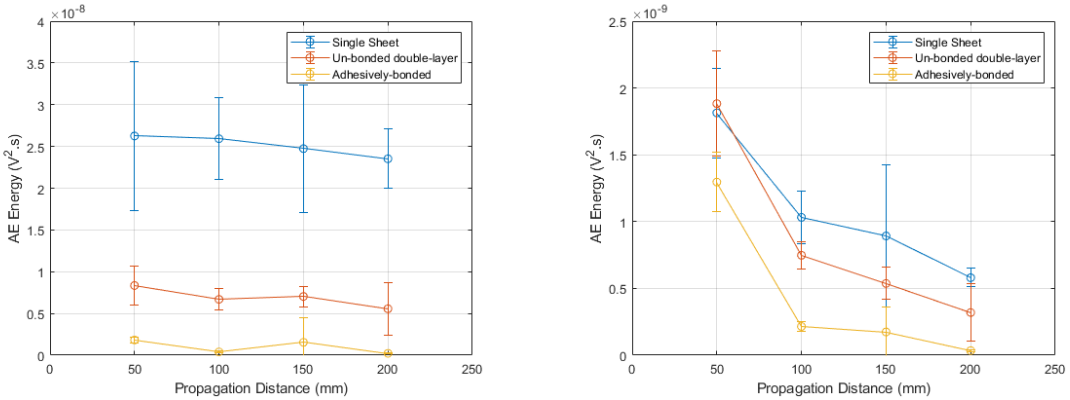

(a) (b)

Figure 3.13: Attenuation of AE energy with increasing propagation distance for a single aluminium sheet specimen, un-bonded double-layer aluminium specimen (no adhesive) and adhesively-bonded specimen. (a) Energy over full time-domain. (b) Energy over 150 μs time window. (Plot shows mean and standard deviation).

3.6.3 Frequency-Domain Analysis

While all three specimens exhibit similar Lamb wave behaviour, there are significant differences in the spectral content of the recorded signals and in the changes to this content resulting from variation in propagation distance. Figure 3.14 shows power spectral density (PSD) plots, illustrating the frequency peaks for the full-length of the signals recorded on the three specimens at the varying propagation distances. For ease of comparison, the plots are normalised by division of all PSD values by the peak value in each data-set. While the recorded frequency content is largely determined by the frequency-response of the sensor, which has a number of local peaks, the differences between specimens is significant; the single sheet exhibits content in frequency-bands centred around approximately 50 kHz, 210 kHz and 320 kHz, with the peak frequencies being in the 210 kHz region. The un-bonded double-layer specimen also features significant content under 100 kHz, though does not feature a peak at 210 kHz but has a single prominent peak at around 320 kHz. Low-amplitude content in the 400 kHz to 600 kHz region is also visible. The bonded specimen features a narrow peak centred at around 50 kHz with minimal content visible across the rest of the spectrum. As the source remains constant across all specimens, the change in peak frequencies between specimens is because of the bond condition of the specimen that the AE waves are propagating through, and not the nature of the source. This factor must therefore be considered if a peak-frequency-based analysis method is to be utilised to differentiate between failure mechanisms, as the propagation path will affect the mechanism detected. From the PSD plots, it can be seen that there is no significant change in peak frequency resulting from variation in propagation distance. To provide greater comparison of the overall spectral content, rather than just the peaks, partial-power characteristics have been investigated, with the percentage of total signal energy contained in each of the four main frequency bands identified being calculated. The selected frequency bands are 0 kHz to 100 kHz, 100 kHz to 250 kHz, 250 kHz to 375 kHz and $>$ 375 kHz. Signal energy was calculated as the integral of the square of the signal over the entire record: $E = \int_0^t V^2 dt$ [134]. Figure 3.15 illustrates the proportion of energy contained within each frequency band and its variation with propagation distance. As in the PSD plots, there is a clear difference between specimens, with the highest percentages of energy being contained

in the bands covering the peak frequencies previously discussed. In this case, however, variation with propagation distance can also be identified. In the single and un-bonded double-layer specimens, the variation is minimal, and increasing or decreasing trends are inconsistent, apart from a slight decrease in the low-frequency band. The bonded specimen, however, exhibits a significant and consistent increase in low-frequency content and a decrease in all higher-frequency content with increasing propagation distance. It can therefore be seen that while the peak frequencies remain consistent across the source-sensor distances tested, the spectral content does experience a significant change in the bonded specimen as the adhesive attenuates high-frequency components of the signal. While the two previously-described methods provide insight into the variation in spectral content regarding source-sensor distance, it should be remembered that most of the signal analysed comprises of edge-reflections, each of which has a different propagation distance, and therefore potentially different spectral content, from the initial wave. It can be seen from the WT coefficient plots for the bonded specimen (Figure 3.12) that, even at the shortest source-sensor distance, the edge-reflections contain very little high-frequency content due to the attenuation over their additional propagation distance. As the changes in source-sensor distance are minimal, compared to the propagation distances of the reflections, the effects of varying source-sensor distance are somewhat masked when the entire signal is analysed. Complete isolation of the initial wave in either time- or time-frequency-domain is limited by the overlapping of edge-reflections with low-velocity components of the initial wave, as can be seen in the WT coefficient plots. Therefore, to demonstrate the effect of propagation distance on the spectral content of the initial wave, a similar approach to that taken by Zhang et al. [61] has been utilised, and the peak WT coefficient in the low- ($<$100 kHz) and mid- (200 kHz to 400 kHz) frequency regions corresponding to the arrival of the initial A_0 wave have been extracted. The ratio between these peak WT coefficients has then been used to define the changes with propagation distance and between specimens. This ratio is defined below as Equation 3.1:

$$Ratio = \frac{WTPeak_{Lowfreq.}}{WTPeak_{Midfreq.}} \tag{3.1}$$

Figure 3.16 illustrates the change in this ratio of low- to mid-frequency content with increasing propagation distance for the three specimens tested. The single-sheet specimen exhibits a very minor decrease in ratio, implying that the low-frequency component becomes less prominent over distance. There is slight variation in the ratio for the un-bonded double-layer, though there is no distinguishable increasing or decreasing trend. The low-frequency peak value is consistently slightly higher than the mid-frequency peak value. The bonded specimen features a similar ratio to the un-bonded specimen at a propagation distance of only 50 mm, though increases exponentially with increasing propagation distance, indicating that within the initial wave the mid- to high-frequency components are being attenuated significantly more than low-frequency components as the wave propagates. In summary, the three methods of frequency analysis utilised indicate significant variation in spectral content between the single, the un-bonded and the bonded specimens despite use of the same source. The presence of an the second aluminium sheet in the unbonded specimen causes a slight increase in the high-frequency content recorded, while the presence of an adhesive layer in the bonded specimen causes attenuation of mid- to high-frequency components, resulting in a dramatic drop in peak frequency. The effect of propagation distance is seen to have minimal effect on the frequency content of the single and un-bonded specimens, while the attenuation introduced by the adhesive results in a significant variation in spectral content with varying propagation distance in the bonded specimen. The increased volume of the bonded specimen should result in an overall increase in geometric attenuation across all frequencies, due to

spreading of the wavefront, while the selective attenuation of the mid- to high-frequency content is believed to be due to the viscoelastic nature of the adhesive.

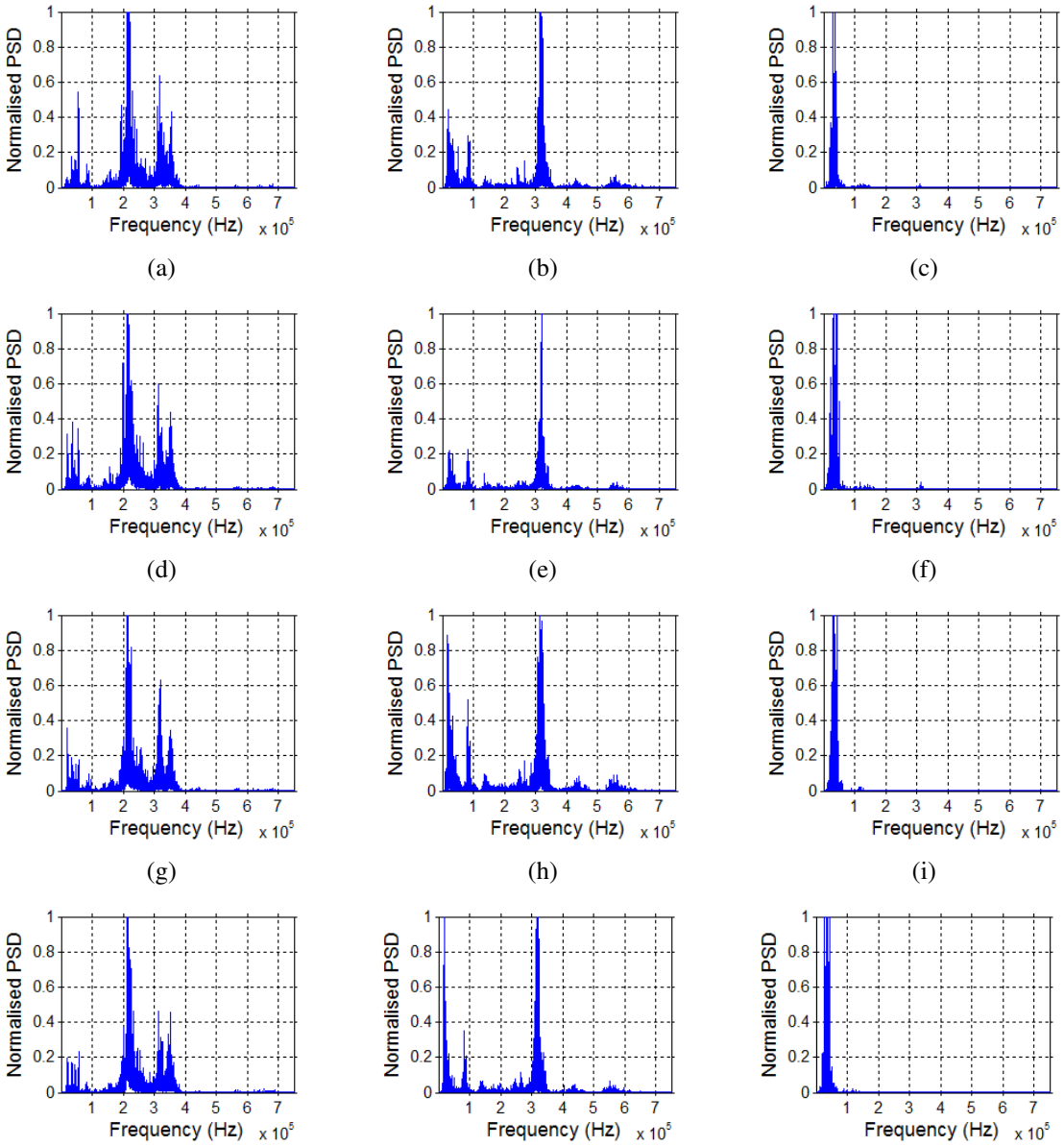

Figure 3.14: Normalised Power Spectral Density plots indicating spectral content of the entire recorded signals for an out-of-plane source on a single-sheet specimen (1st column), an un-bonded double-layer specimen (no adhesive) (2nd column) and an adhesively-bonded specimen (3rd column), at propagation distances of 50 mm (1st row), 100 mm (2nd row), 150 mm (3rd row) and 200 mm (4th row).

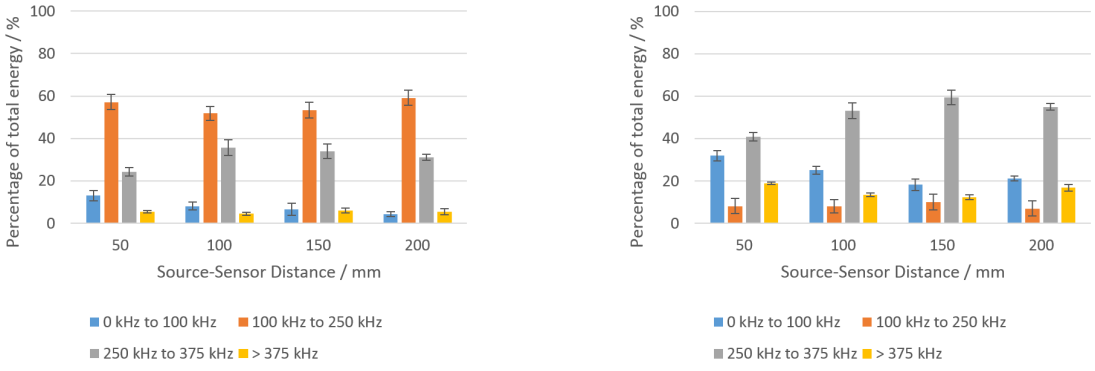

(a) (b)

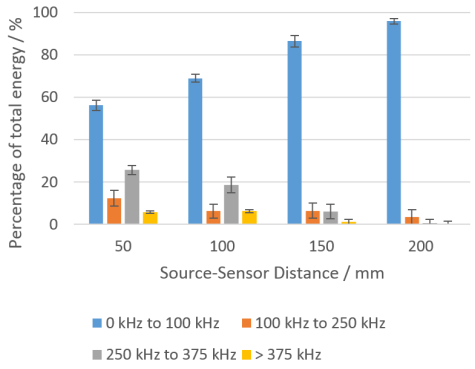

(c)

Figure 3.15: Mean percentage of AE energy in key frequency bands at varying source-sensor distances for; (a) single-sheet specimen, (b) un-bonded double-layer specimen (no adhesive) and (c) adhesively-bonded specimen. (Error bars show standard deviation).

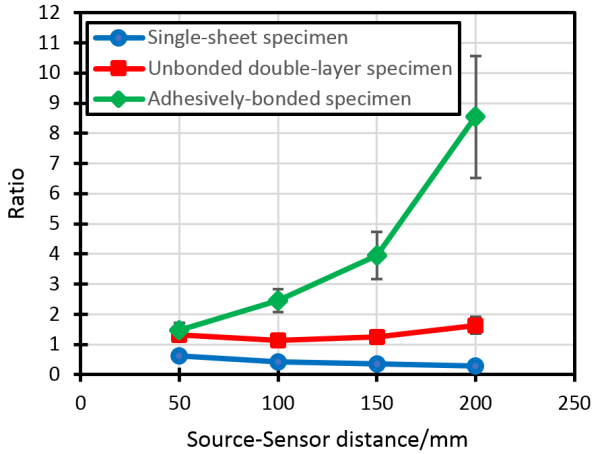

Figure 3.16: Mean WT coefficient peak ratio between low ($<100\ kHz$) and mid (200 kHz to 400 kHz) regions of initial A_0 wave with increasing source-sensor distance for the single-sheet, un-bonded double-layer (no adhesive) and adhesively-bonded specimens. Error bars show standard deviation.

3.6.4 Effects of Source-Orientation

The resultant WT coefficient plots from application of an in-plane source on the edge of the specimens (as shown in Figure 3.1) are shown in Figure 3.17. These differ greatly from those acquired with an out-of-plane source as the S_0 mode becomes more significant. In the single-sheet specimen, the high-energy regions all exist within the 200 kHz to 400 kHz region and are seen to correspond to the S_0 mode and its multiple reflections. There is little content which can be positively identified as corresponding to the A_0 mode. As in the tests using an out-of-plane source, the un-bonded double-layer specimen exhibits much greater high-frequency content above 400 kHz. The S_0 mode, and subsequent reflections, can be identified as occurring across the frequency-range of approximately 200 kHz to 750 kHz. Unlike in the single-sheet specimen, the initial A_0 wave in the unbonded specimen can also be clearly identified, although its reflections are less clearly defined. Compared to the single sheet, the un-bonded double-layer specimen also exhibits a much higher amplitude low-frequency component corresponding to the A_0 mode. For both source depths tested, the bonded specimen exhibits a clear initial S_0 wave, present across the mid-frequency band of 200 kHz to 400 kHz. The reflections of this mode however are not as clearly defined as in the other specimens. As was found in the previously discussed tests, the adhesively-bonded specimen appears to quickly attenuate any high-frequency content. This results in there being no significant content above 400 kHz, and the reflections present in the other specimens being attenuated significantly before arrival at the sensor. The peak WT coefficient occurs in the low-frequency region below 100 kHz, which appears to correspond approximately to the A_0 mode. It is however noted that the arrival of this low-frequency component is slightly earlier than predicted by the group-velocity curves. Overall, both source depths tested on the bonded specimen provide very similar results. In general, the in-plane source results in a significant increase in the proportion of energy propagating in the S_0 mode, when compared to an out-of-plane source. This result is to be expected, based on the previous demonstrations of this characteristic such as those by Gorman [58] and Hamstad et al. [67]. From these studies, it is also to be expected that sources located at the mid-depth of the specimen will excite the purest S_0 mode, while offset from the mid-depth will introduce a greater flexural A_0 component. The source was applied at the mid-depth of the single-sheet specimen as accurately as was possible for the source-type used. The resulting WT coefficient plots are seen to exhibit a clear S_0 wave and its subsequent reflections, with little clear evidence of any significant A_0 mode, providing a perfect example of the expected behaviour. The un-bonded double-layer specimen, on which the source was applied at the mid-depth of the upper adherend, shows a greatly increased S_0 component but still exhibits a well-defined A_0 mode. In the bonded specimen, it was expected that there may be an observable difference between the two source-locations; based on the finding that individual Lamb waves are propagating in each layer, the source applied to the mid-plane of the adherend should create the purest S_0 mode, while the source applied to the adhesive is offset from the plane in which the recorded waves are propagating, and should thus create an increased A_0 component. Applying the previously-used method of creating a ratio between peak WT coefficients gives a clear differentiation between the specimens. In this case the peaks were taken from the mid-frequency (200 kHz to 400 kHz) region of the S_0 wave and the low-frequency ($<$100 kHz) region of the A_0 wave. The ratio between the peaks is calculated as per Equation 3.2 below:

$$Ratio = \frac{WTPeak_{A_0 Low freq.}}{WTPeak_{S_0 Low freq.}} \tag{3.2}$$

The resulting ratios, presented in Figure 3.18, show the single sheet provides the lowest ratio,

with a mean of 0.2, indicating that the S_0 mode is clearly dominant. The low-frequency A_0 peak is however still the highest in the un-bonded double-layer specimen with a ratio of 1.4. Both source depths on the bonded specimen yield similar results showing dominance of the low-frequency A_0 component, with ratios of 1.9 and 2.1 for the source applied to the adherend and adhesive respectively. The difference between the two source depths cannot however be considered significant due to the variation in ratio within each of these tests. The minimal difference between source-locations may be in part due to the low total thickness of the specimens, resulting in minimal offset from the central plane regardless of source-location on the edge. For comparison, the plates considered by Hamstad et al. [59] were 4.7 mm thick and a maximum offset from the central plane of 1.88 mm was considered. In the case of the experiments detailed in this chapter, however, the offset from the centre of the adhesive was only 0.6 mm. While the change in ratio between A_0 and S_0 peaks can be largely attributed to the wave-modes excited in the specimens, the attenuation of high-frequency content in the adhesively-bonded specimen will also contribute towards the relative dominance of the low-frequency A_0 component by attenuation of the mid- to high-frequency S_0 waves. Ultimately, as was seen for an out-of-plane source, the addition of a second adherend and of an adhesive layer does not change the propagation modes of AE from a simulated in-plane source, with the recorded waveforms showing good correspondence to the theoretical dispersion-curves of a single adherend. The adhesive layer is again seen to introduce greater attenuation, particularly of higher frequency components, and most noticeably in reflections where the propagation distance is greatest.

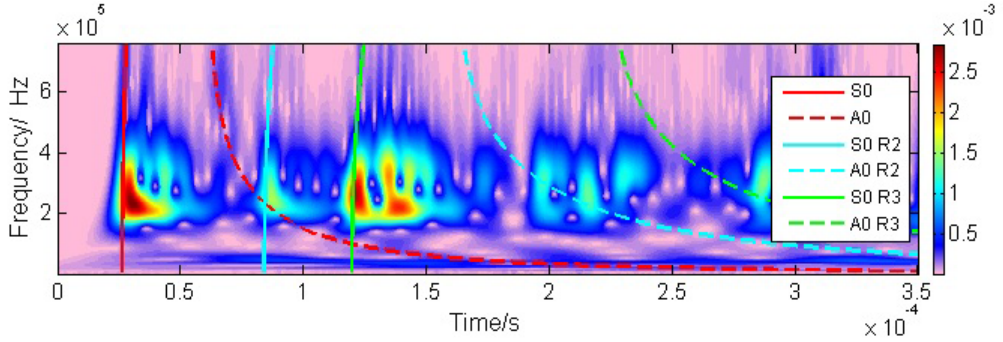

(a)

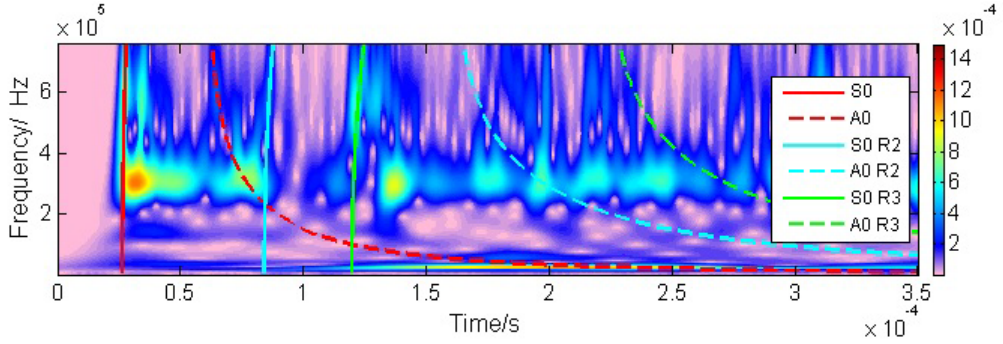

(b)

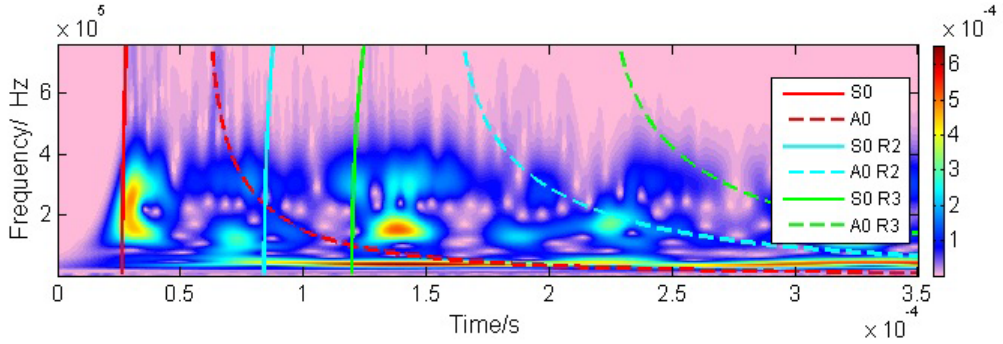

(c)

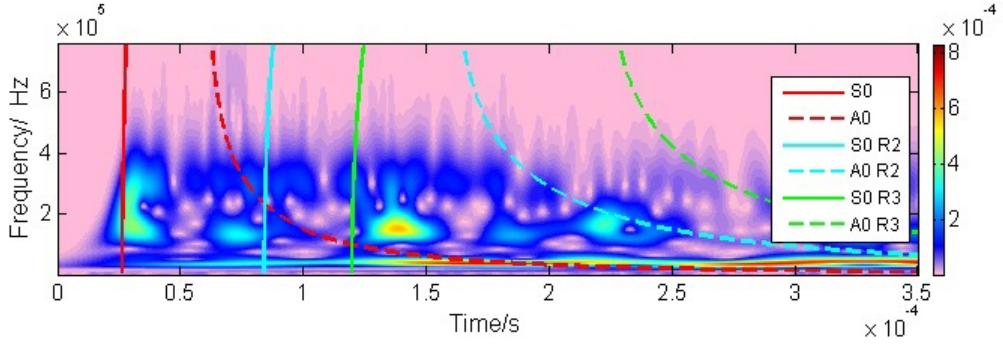

(d)

Figure 3.17: Example WT coefficient plots and modified group-velocity curves for an in-plane source applied at a source-sensor distance of 250 mm to the edge of (a) the single-sheet specimen, (b) the un-bonded double-layer specimen, (c) the upper adherend of the adhesively-bonded specimen and (d) the adhesive layer of the adhesively-bonded specimen.

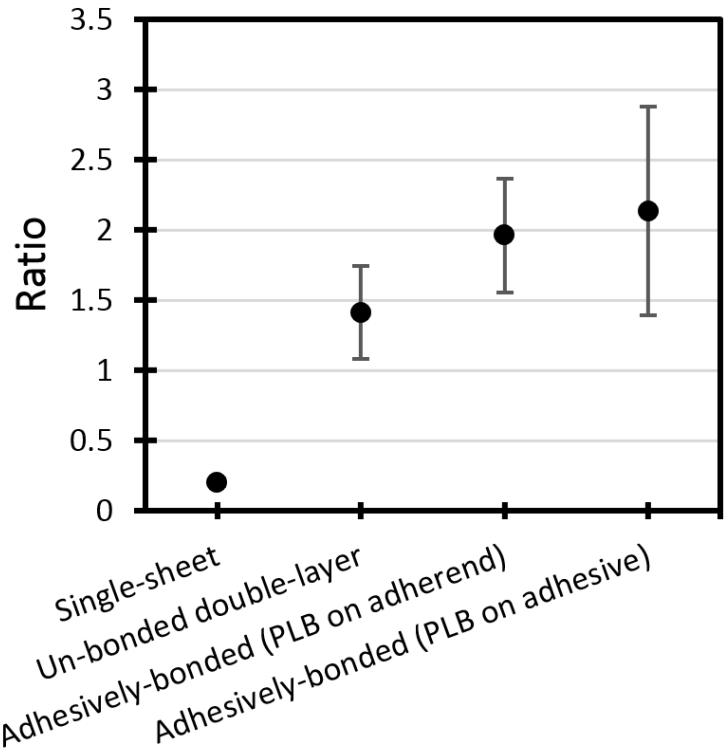

Figure 3.18: Mean WT coefficient peak ratios (Peak A_0/Peak S_0) for an in-plane source located 250 mm from the sensor. Error bars show standard deviation.

3.7 Results of Simulated-Source Tests featuring Voids

3.7.1 Time-Domain Analysis

Figure 3.19 illustrates the mean results and standard deviations of the time-domain features for all experiments carried out. Peak amplitude shows a marked increase with increasing defect size in Configuration A, which features the shortest propagation distance across the defect; however, for different source-sensor configurations this is not as clear. The defect-free specimen features a lower peak amplitude than the 40 mm defect specimen in all cases, however the 10 mm defect specimens results are seen to fluctuate from lowest to highest, depending on the configuration. Energy is seen to increase with increasing defect size for all configurations. The variation is most significant in Configuration A, in which differentiation between defects is clear, whereas in other configurations there is significant overlap between the defect sizes due to variation within the tests for each defect size, arising from variation of the source, the sensor coupling, and the three different specimens of each type which were used. Rise-time also generally increases with increasing defect size, however in configurations B and C, the 10 mm defects have a lower mean rise-time than the defect-free specimens. There is significant variation of the rise-time within each test and significant overlap between defect sizes, making rise-time of little use for differentiation between defects. Decay time and duration show very similar results as the rise-time is essentially negligible in comparison to the decay time. Both of these parameters show an increase with increasing defect size, with the exception of Configuration B, in which there is negligible difference in the mean values between the 10 mm and 40 mm defects. Number of counts is also seen to generally increase

with increasing defect size, however for configurations A, B and D, there is negligible difference in the means between no defect and the 10 mm defect, with significant differences between all defect sizes only existing for Configuration C.

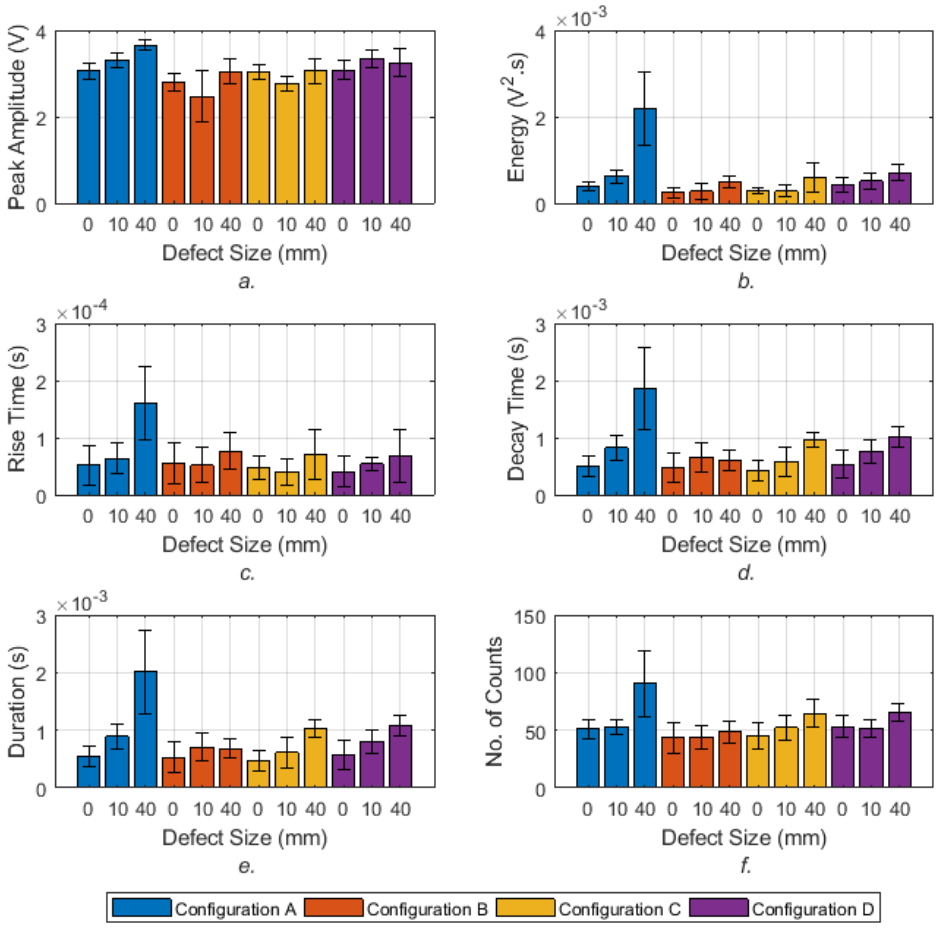

Figure 3.19: Mean and std. deviation of time-domain parameters for all tested specimens and configurations: (a) Peak amplitude, (b) AE energy, (c) Rise-time, (d) Decay time, (e) Duration, (f) Number of counts.

It has been demonstrated in previous works [135] that the presence of an adhesive layer significantly increases signal attenuation. It can therefore be assumed that the general increase in all of these parameters, with increasing defect size, could be attributed to the lower attenuation throughout the defect region where there is no adhesive. While all of these parameters are demonstrated to be affected by the presence of different-sized defects, there is significant variation within each of the tests due to variation of the source application, the sensor coupling and the variation between the individual specimens of each type. This variation within each defect type will make it difficult to use any of these parameters as a reliable single method for defect classification. It should also be noted that mode-conversion will occur at the edges of the voids. Throughout the void regions the wave-modes propagating through each adherend will be those of a single adherend, while in the rest of the specimen, the multi-layer-modes will exist. As shown in Section 3.6.1, these modes are very similar, with the single-adherend modes providing a good approximation of the multi-

layer-modes across the majority of the frequency range, so the direct effects of mode-conversion on the recorded signal will be minimal.

The optimum threshold values to separate the three defect types were calculated for each AE parameter and each configuration, and also for each AE parameter when including all configurations. This was done using a MATLAB script which iteratively optimised the threshold values which could be used to separate the defects into their correct size. For example, for configuration A, categorising any signal with a duration of under $500\mu s$ as "No defect", any signal with a duration between $500ms$ and $1000ms$ as a 10 mm defect, and any signals with a duration of over $1000ms$ as corresponding to a 40 mm defect. The optimum threshold value in each case being the value which resulted in the highest number of defects being correctly identified. The percentage of defects which could be correctly classified by using each of the parameter was calculated and the results are presented in Table 3.1. It can be seen that Configuration A provides the best differentiation between defects for all parameters, while Configuration B provides the worst. This can be readily explained by the relationship between the source-sensor distance and the defect size. In Configuration A, the propagation length is half that in Configuration B, and thus the defect makes up a much larger proportion of the signals' propagation path, meaning that any difference in signal propagation will be much more significant. Likewise this explains why Configuration A provides better results than configurations C and D, as although the propagation distances are the same, only half of the defect is included within the direct propagation path. Configurations C and D provide similar levels of accuracy, although D, in which the source is on the defect, provides marginally better results in most cases than C, in which the sensor is on the defect. When investigating one configuration at a time, Energy provides the best differentiation with an accuracy of 88.89% in Configuration A, while Decay Time and Duration also provide accuracy of over 80%. This accuracy drops significantly, however, for other configurations, meaning that the abilities of such a technique would be significantly limited if the exact location of a defect was not known, as would be the case in practical scenarios. When considering all configurations together, to identify thresholds that can separate results from any configurations, the accuracy is further reduced, with the best accuracy of 51.2% being achieved using the signal Duration. It can therefore be concluded that while the time-domain parameters can be severely affected by the presence of defects, their use does not provide a robust method for differentiating between defects.

Table 3.1: Maximum percentage classification accuracy using single AE features

AE Feature	Config. A	Config. B	Config. C	Config. D	All
Peak Amp.	72.22%	47.78%	44.07%	50.74%	38.61%
Energy	88.89%	51.48%	50.00%	54.81%	42.22%
Rise-time	76.30%	46.67%	43.70%	58.15%	49.44%
Decay Time	80.37%	47.04%	67.41%	67.04%	48.89%
Duration	86.67%	47.78%	65.93%	70.74%	51.20%
Counts	57.04%	40.00%	53.70%	53.33%	49.63%

Figure 3.20 shows the mean of the normalised power spectral density for each specimen type and configuration. PSD for each test has been normalised by division by its maximum value. The plots shown are the mean of these values for all 90 tests completed on each specimen type. Figure 3.21 illustrates the results of partial powers analysis and Figure 3.22 illustrates the effect of defect size and configuration on the frequency centroid. For all tests the content lies in the range from 20 kHz (the cutoff of the high-pass filter in the preamplifier) to around 400 kHz. The overall peak frequencies vary between specimens, but local peaks exist consistently in the regions of 25 kHz

to 35 kHz, 200 kHz to 260 kHz and around 310 kHz, the peak frequency of the sensor used. It can be seen from the PSD, partial powers and frequency centroid plots that there is a general shift towards low frequency (< 100 kHz) content with increasing defect size, and a relative decrease in higher frequency content, particularly in the 200 kHz to 300 kHz range.

As demonstrated on the large defect-free specimens, the presence of an adhesive layer contributes significant attenuation, particularly to higher frequency content, and it could thus be expected that the presence of an adhesive-free void would lead to decreased attenuation of the high frequency components and therefore a shift towards higher frequency content with increasing defect size. This effect however, seems to be negligible compared to other interactions between the propagating waves and the defects. Increased low frequency content with increasing void size has also been previously observed by Tanary [86], in work utilising acousto-ultrasonics. While there is a general trend in the data, there is significant variation within each data-set and some inconsistencies, leading to overlap between the results for each defect size, despite the large difference in defect sizes. It is therefore concluded that while the frequency-domain is clearly affected by the presence of voids, typical AE frequency-domain parameters will not provide reliable discrimination between known defect sizes or allow prediction of arbitrary defect sizes.

Figure 3.23 shows the mean wavelet-transform plots for each specimen type tested in Configuration A, further configurations have been excluded for brevity. dispersion-curves corresponding to the S_0 and A_0 wave-modes and their subsequent edge-reflections have been overlaid on the plots to aid in identification of the sources of high-energy regions within the plots. It can be seen that all three specimen types produce very similar-looking signals in the time-frequency-domain, which are difficult to distinguish between visually. The results from configurations B, C and D were also essentially indistinguishable, aside from the variations in arrival times due to the differing propagation distances. While discrimination between defects was not possible visually, subtle differences could be detected using an ANN, as discussed in the following section.

As would be expected with the application of an out-of-plane source, the majority of the signal energy is carried in the dispersive A_0 mode [58]. An initial high-energy region occurs between 200 kHz and 400 kHz, centred around the peak frequency of the sensor, and a secondary region occurs in the low frequency-range below 100 kHz, arriving slightly later. Edge-reflections occur simultaneously from the top and bottom edges of the specimens due to symmetry, and left and right edge-reflections also occur simultaneously due to having the same propagation distance. These reflections are seen to have been significantly attenuated compared to the initial waves due to their increased propagation distance. The high-frequency band present in the initial waves narrows towards the sensor's peak frequency in the reflections, as well as significantly reducing in amplitude. The low-frequency region is present in the reflections, with the top and bottom edge-reflections featuring frequency content under 100 kHz, while in the left and right edge-reflections this reduces to mainly content under 50 kHz.

It can be concluded that the majority of the significant data in the recorded AE signal stems from the initial A_0 wave passing directly through the defect, while the edge-reflections, which avoid the defects, have only a minor contribution to the signal. It can therefore be assumed that for other larger sheet specimens, with similar-sized defects, the performance of this technique would be similar. It can however be assumed that performance on significantly smaller specimens would be reduced, due to the lower attenuation and earlier arrival of the reflections which are unaffected by the defect.

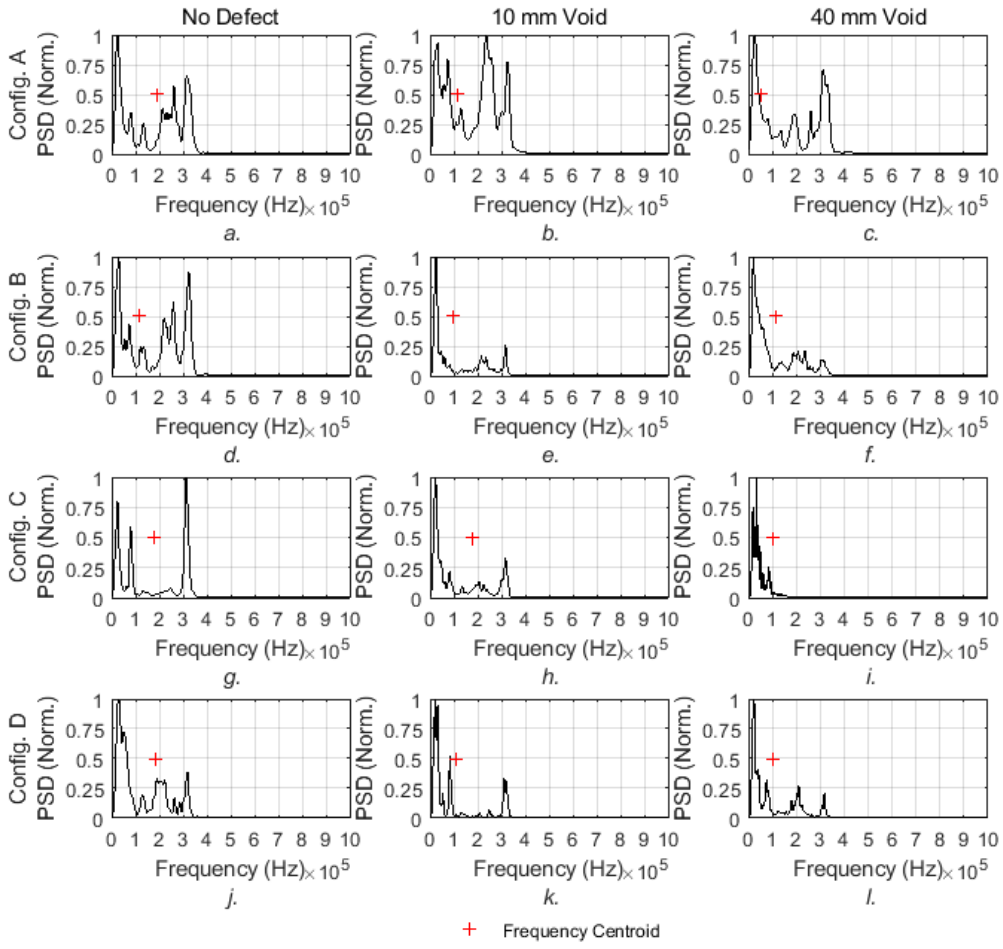

Figure 3.20: Mean normalised power spectral density and mean frequency centroids for all specimens and configurations.

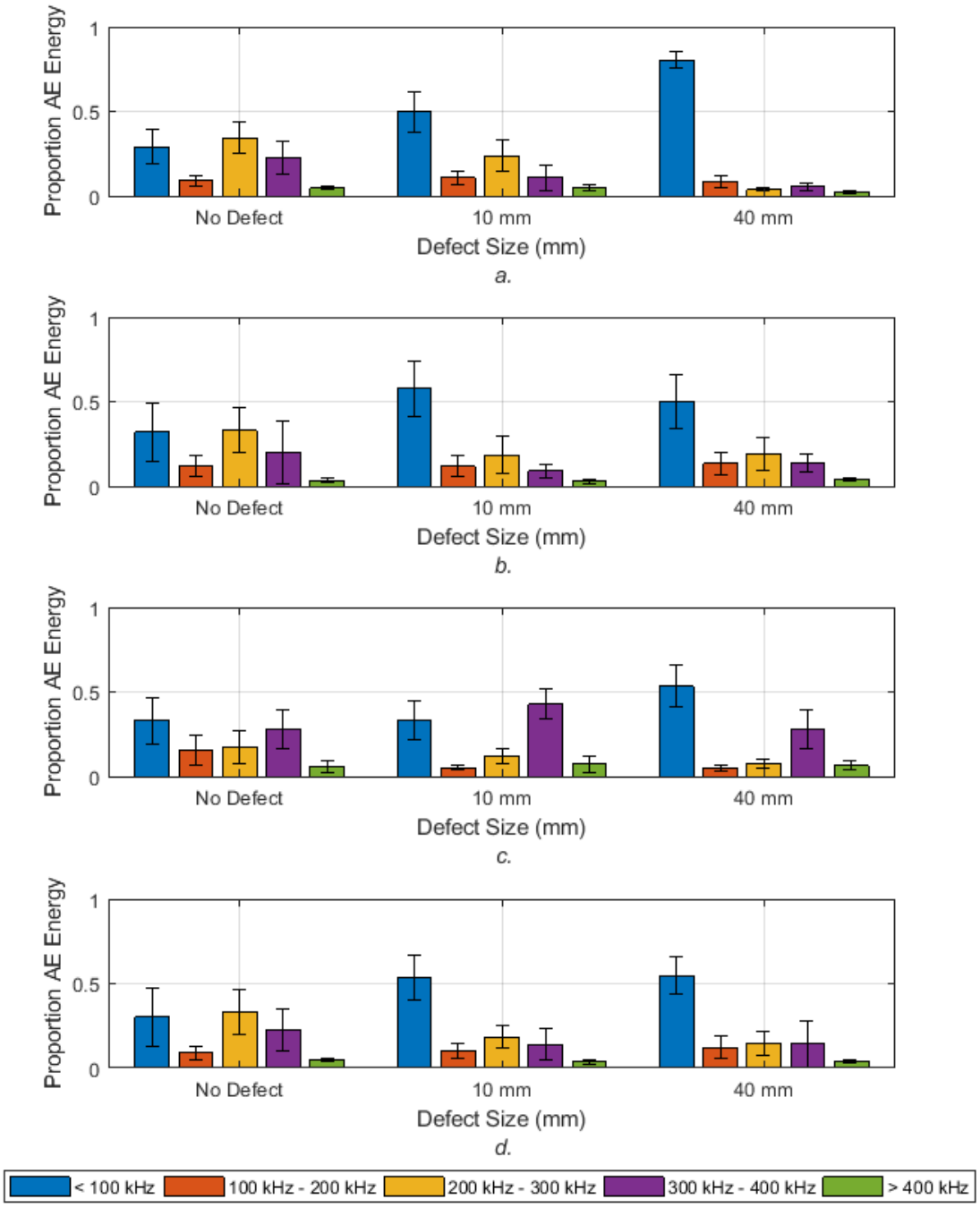

Figure 3.21: Partial power plots for: (a) Configuration A, (b) Configuration B, (c) Configuration C, (d) Configuration D.

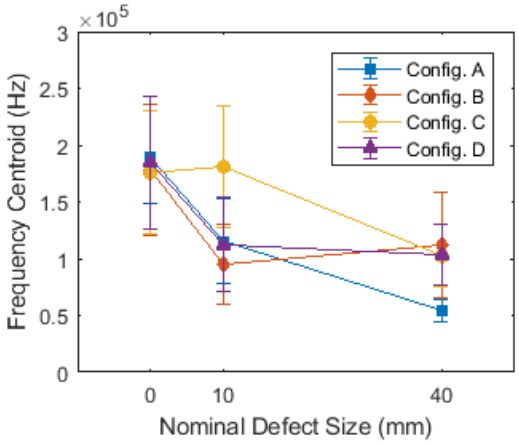

Figure 3.22: Partial power plots for: (a) Configuration A, (b) Configuration B, (c) Configuration C, (d) Configuration D.

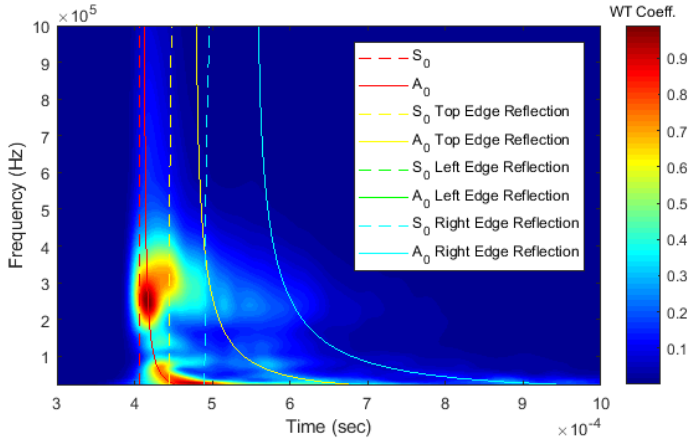

(a)

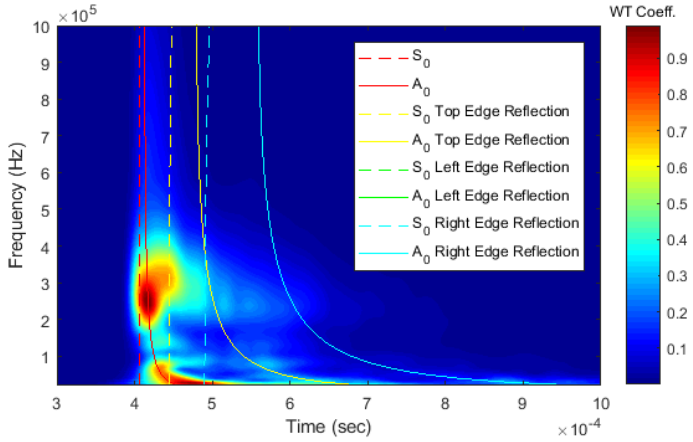

(b)

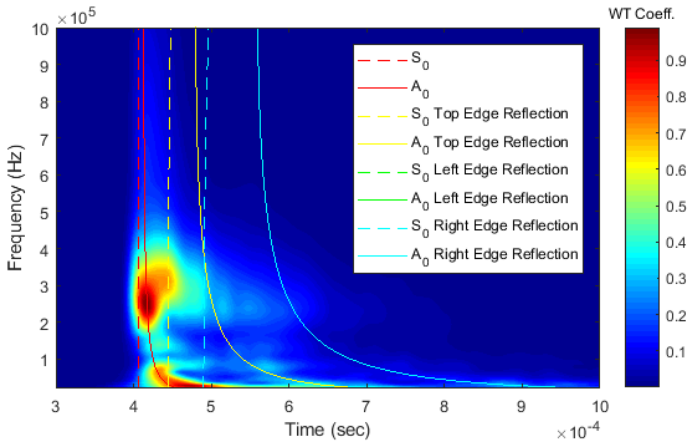

(c)

Figure 3.23: Wavelet-transform plots with overlaid theoretical dispersion-curves for: (a) No Defect, (b) 10 mm Defect (c) 40 mm defect.

3.7.2 Pattern Recognition

The confusion matrices, included in Figure 3.24, show whether or not a signal has been correctly identified by the ANN. The target classes represent the the correct nominal sizes of the defects (class 1 = 0 mm, class 2 = 10 mm, class 3 = 40 mm), and the output class indicates how the ANN has identified the signal. The top number in each cell represents the number of signals classified and the bottom number shows this as a percentage of the total number of signals . For example, the top left cell of the training confusion matrix (Figure 3.24a) indicates that 249 signals which correspond to class 1 defects (0 mm) were correctly identified as such. The zeroes in the cells below this indicate that the none of the class 1 defects were misclassified as class 2 or 3. The zeroes to the right of this indicate that no other classes were misclassified as corresponding to class 1 defects. The right-most column and bottom row of each confusion matrix indicate the percentage of each class correctly and incorrectly identified. Separate confusion matrices are included for the training, validation, testing, and overall whole data-sets. In this case, it can be seen that even when considering all four configurations at once, which includes two different source-sensor distances, as well as varying positions of the source and sensor with regard to the defect, the three nominal defect sizes can be differentiated between using the time-domain information with an accuracy of 100%, with no defects being misidentified as the wrong size. This approach of using an ANN to analyse a section of the signal presents a significant improvement over using any single AE parameter extracted from that same signal, such as energy or duration, which, even when only considering a single optimum configuration, still features some overlap between results which result in misclassification, as previously shown in 3.1.

ANNs were also trained using frequency spectra, time-frequency-domain data, and the full array of time-domain parameters acquired in the previous analyses. Use of the time-frequency-domain data yielded results of similar accuracy at 99.9%, but were significantly more computationally expensive due to both pre-processing of the data, and training and running the ANN on much larger input data-sets. The results from using frequency spectra or multiple time-domain features yielded results only slightly better than those achieved using a single time-domain parameter.

The ability to work successfully with multiple source-sensor configurations, as opposed to cherry-picking an optimum configuration, also provides a significant advantage over the methodology proposed by Prathuru [9], particularly in this case of individual large defects, as opposed to a distribution of small defects; as in a real-world situation only the source-sensor distance will be known, and not the exact location of the defect. It is expected that with the inclusion of a greater number of defect-types and sizes, as would be necessary for real world applications, the level of accuracy would decrease, but would still remain significantly higher than that of other analysis methods.

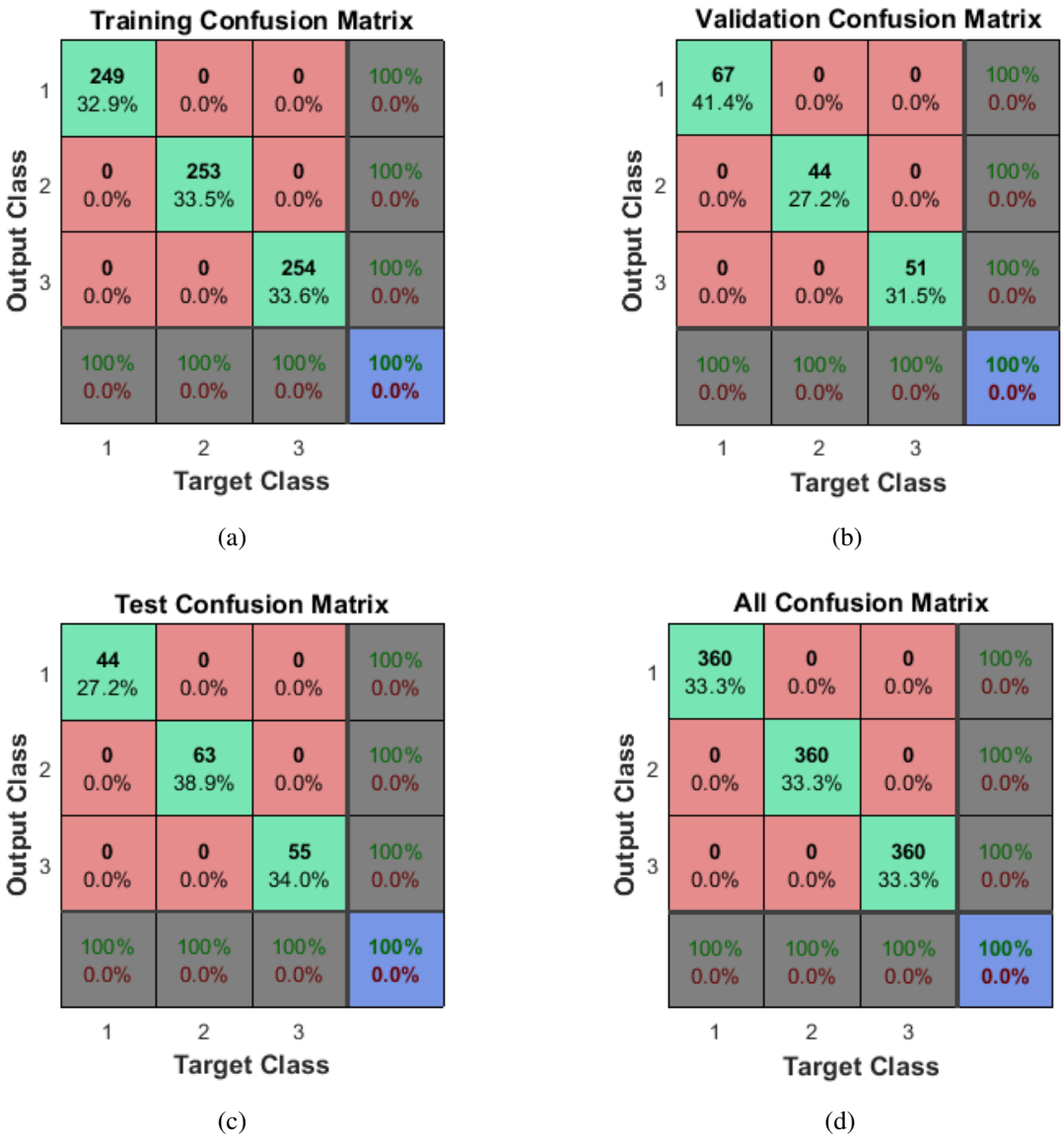

Figure 3.24: Confusion Matrices for defect classification using time-domain data. (a). Training data-set, (b). Validation data-set, (c). Test data-set, (d). All data-sets. (Class 1 = No Defect, Class 2 = 10 mm Void, Class 3 = 40 mm Void)

For real-world applications however, defects will not be of a pre-known size, so a classification-type system will be of little use, unless it is implemented as a pass/fail type classification with a maximum permissible defect size. It is of greater interest to be able to estimate the size of a defect based on the sizes of known training defects. To this end, the second ANN has been created to estimate the defect size based on the training data. The regression plots, included as Figure 3.25 demonstrate the fitting of the data to the model created using the training data, with the known nominal defect size represented by the x-axis position and the defect size predicted by the ANN represented on the y-axis. It can be seen that the model is able to achieve a perfect fit to the training data, giving a positive linear relationship with a correlation coefficient value of R=1. The generalisability of the model is shown to still be strong, though less than perfect, with the validation and test data-sets achieving correlation coefficient values of R=0.95529 and R=0.96379 respectively.

The distribution of defect size estimates is shown in Figure 3.26a, in which the actual nominal size of the defect is denoted by the bar colour, and the height and position of the bars denote the distribution of the estimated defect sizes (a perfect result would be 3 bars, located at $0mm$, $10mm$ and $40mm$, each 360 samples high). It can be seen that the sizes of the majority of defects are estimated with a high level of accuracy, with a small number of results distributed above and below the actual defect sizes. It can also be seen that the distribution of results is very similar between the three nominal defect sizes. Results directly from the ANN are not directly tied to physical properties, and thus some results from the defect-free specimens can predict a negative defect size, which is not physically possible. To correct this issue, all negative results are corrected to zero as this is the closest physically possible value. Following this correction, the mean error of the defect size estimates, as shown in Table 4, was reduced to only 0.562 mm, 0.945 mm and 0.921 mm respectively for defect-free, 10 mm defect and 40 mm defect specimens, giving an overall mean error of 0.921 mm.

Table 3.2: Mean error of defect size estimate

Specimen	Mean Error (ANN only)	Mean Error (ANN with zero-defect correction)
No Defect	0.874 mm	0.562 mm
10 mm Void	0.945 mm	0.945 mm
40 mm Void	1.257 mm	1.257 mm
All Specimens	1.025 mm	0.921 mm

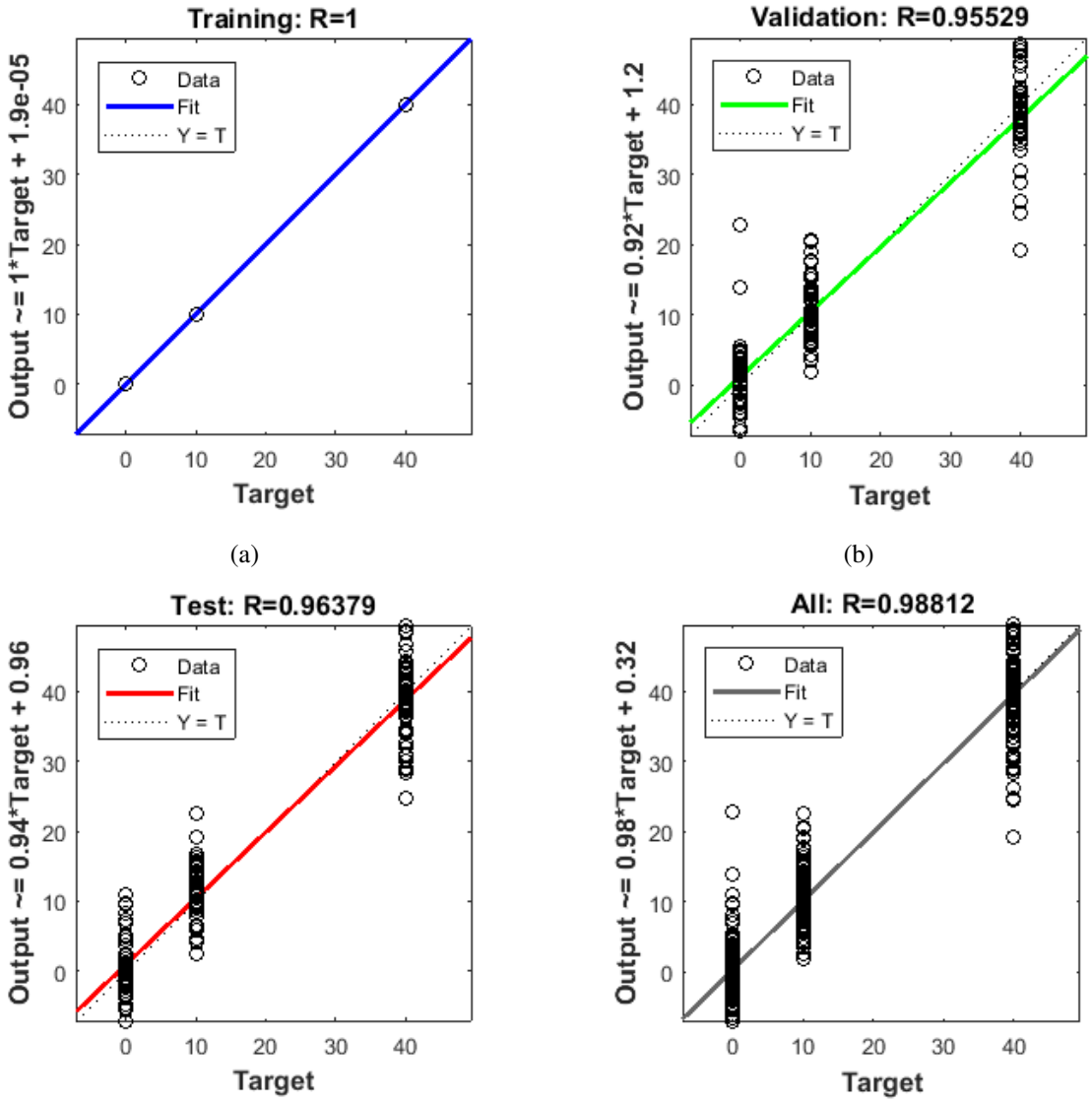

Figure 3.25: Regression plots for defect size estimation using time-domain data, for; (a). Training data-set, (b). Validation data-set, (c). Test data-set, (d). All data-sets. Target is nominal defect size in millimetres.

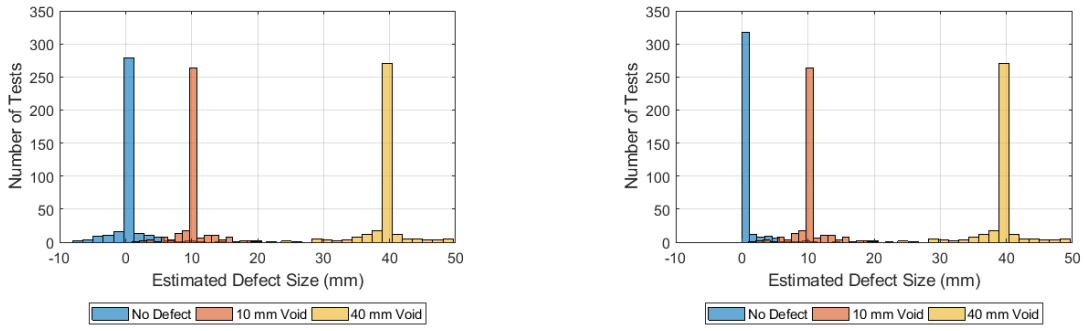

(a) (b)

Figure 3.26: Distribution of defect size estimates (a). Directly from ANN. (b). With correction to remove negative size defects.

3.8 Discussion

3.8.1 Modal Analysis

It has been demonstrated experimentally and analytically, through the generation of group-velocity dispersion-curves, that for the specimens under consideration, and across a frequency-range appropriate to AE testing, the wave-modes recorded in an adhesively-bonded specimen will closely match those recorded in a single adherend. This finding mirrors previous results from studies using ultrasound techniques, as opposed to AE, such as those of Heller et al. [2], who concluded that the modes excited in bonded specimens are identical to the dispersion-curves of a single plate. These findings also fit well with the findings of Seifried et al. [3], whose analytical and FEM investigations based on the work of Heller et al. [2] led to the conclusion that while additional wave-modes are introduced by the presence of the adhesive and the second adherend, only those close to the modes of the single adherend result in significant displacement of the surface of the adherends.

While it is entirely possible, and in many cases practical, to utilise dispersion-curves calculated specifically for the layup of an adhesive joint, the ability to use dispersion-curves of the adherend as a reasonable approximation is greatly advantageous for a variety of practical reasons. First of all, the thickness of an adhesive-bondline may be unknown or may vary along its length, either by design or due to lack of control during manufacture. In these cases it would therefore not be possible to accurately determine dispersion-curves for the entire specimen, but it is most likely that the properties of the adherend will be known and will be much better controlled than those of the bondline, thus allowing the use of dispersion-curves for the adherends. Similarly, the presence of bond defects will change the dispersion characteristics over the localised region of the defect. However if the change in dispersion is negligible, particularly over a small area, the presence of such defects will not have to be accounted for in source-location systems. A change in bond status along the wave-propagation path will also occur with fracture propagation, particularly in laboratory-type fracture tests, such as the DCB tests carried out in subsequent chapters of this work. The ability to approximate the wave dispersion in the bonded region as being the same as in the bare adherends in the pre-crack region greatly simplifies the analysis of test results, particularly with regard to source-location, as a single set of dispersion-curves can be used for the entire specimen, as opposed to having to track the crack-front and apply one set of dispersion-curves for the bonded side of the specimen and a different set for the un-bonded end. An additional consideration for practical application is the accessibility of software capable of producing dispersion-curves for multi-layered structures. As previously mentioned, the commonly-used free software Vallen Dispersion is only capable of handling single layers, while the software ”Dispersion Calculator” from the German Aerospace Centre is capable of handling some multilayered structures, though the current version of Dispersion Calculator is specifically geared towards composites with multiple layers of the same material and could not support the generation of curves for an adhesive joint. Even the MATLAB app ElasticMatrix which was used in this work required some modification to produce the desired group-velocity curves, as in its original form it only generates phase-velocity curves. The ability to use simple dispersion-curves for a single layer adherend, rather than for the whole specimen, therefore opens up which software can actually be used and may simplify the workflow.

While the findings of this experimental and analytical work are in agreement with literature [2, 3], only a single design of joint has been considered. The applicability of these findings to different joint thicknesses and adhesive types will be explored further in Chapter 5, to assess the

generalisability of these findings.

3.8.2 Attenuation

The significant difference in attenuation between the bonded and un-bonded specimens (single- and double-layer), is highly significant for the practical application of AE to bonded structures, and in particular to large structures. The high level of attenuation introduced by the adhesive layer significantly reduces the range over which AE could be effective, and thus, in order to cover the same area as may be possible for other specimen types, a significantly higher number of sensors may be needed. For structures which have localised bonded features, such as stringers in an aircraft, these features will create a discontinuity in the attenuation rate which will need to be accounted for. Likewise, the presence of localised bonding defects within large bond areas will result in lower attenuation and thus higher readings than would otherwise be expected.

In terms of lab-based experimental work, such as fracture tests, this is also significant, as the sensor location in relation to the fracture-plane may impact on results. For example; considering a Double-Cantilever-Beam test, in which sensors are placed on the top and bottom adherends, at the opening end. The test may result in cohesive failure, in which a thinner layer of adhesive will remain attached to each adherend (though not necessarily equal thicknesses on each), or in adhesive failure, in which the adhesive layer will remain bonded to one adherend, while separating entirely from the other. The attenuation along the propagation paths between the crack tip and the two sensors will therefore vary based on the amount of adhesive remaining on each adherend. This is an aspect which is not believed to have been considered in previous works, but which may become a more important consideration as work moves towards a fully quantitative model of AE in adhesives.

3.8.3 Frequency-Domain Analysis

This study has shown that the viscoelastic attenuation induced by the adhesive layer is not uniform across all frequencies, but is much more significant across higher frequencies, thus resulting in not only a significant difference in frequency content between the specimen types, but also variation in frequency with propagation distance in the bonded specimens. Although the frequency-ranges under consideration are different, these findings appear to be in good agreement with those of Heller et al. [2], who reported a loss of the higher-order wave-modes, which exist at high-frequency, in the presence of an adhesive layer.

In AE testing of bonded joints these factors should be considered when selecting sensor placement, as the bond status of the propagation path to the sensor will affect the received spectral content. For example, in a double-cantilever-beam test or similar, the source (the crack front) will be in the central region of the specimen, with an un-bonded section at the opening end and a fully bonded section at the opposite end. Placement of the sensor at the opening end will result in minimal attenuation from source to sensor as the waves propagate through a single adherend, while placement of the sensor at the closed end will result in attenuation of high-frequency components as the AE wave propagates through the bonded region, potentially resulting in significantly different frequency spectra at each sensor. Additionally, as the crack propagates and thus the source moves away from one sensor and closer to the other, the recorded frequency spectra are likely to change, even if the source remains identical. This phenomena was observed in previous work by Droubi et al. [8] but was not explored in any detail.

The variation in frequency spectra with respect to propagation distance does bring into question the use of any frequency-based methods for source-identification when working with adhesively-bonded specimens. In future works it should however be possible to account for this variation by utilising source-location techniques, and then adjusting the recorded frequency spectra to ensure that sources recorded at different locations can be directly compared.

It is however noted that in the small specimens typical of most previous studies, where edge-reflections are prominent, the effect of this may be negligible due to the reflections propagating back and forth across the entire specimen. In large specimens however, where edge-reflections are less significant, the sensor location may have a much greater effect on the recorded spectral content.

3.8.4 The Effects of Void-Type Defects

The aim of including specimens with voids in this study was two-fold. The primary aim was to investigate the effects of voids on wave-propagation and thus the potential impact of voids on typical AE testing. The secondary aim was to establish the effectiveness of the use of a PLB source and AE set-up as a method to detect and size voids.

With regard to the first aim, it can be seen from the results that the presence of voids in the adhesive layer results in significant changes to both time-domain and frequency-domain parameters. Increasing void size leads to increased energy and amplitude, and also increased duration, rise-time, decay-time and number of counts. This aspect can be easily explained by the reduced attenuation over the void region, as established in the previous experiments on bonded and un-bonded defect-free specimens. Based on this, it could also be assumed that there would be an increase in the high-frequency content recorded in the presence of a void, as the frequency-dependent attenuation of the adhesive would not affect the void region. What is observed is however the opposite, with an increase in low-frequency content. While the investigation of adhesive voids by AE and PLB is novel, previous studies such as those by Tanary [136] have applied the Acousto-ultrasonic method.The work by Tanary produced similar findings, demonstrating that the presence of a void results in the appearance of additional low-frequency peaks in the frequency spectra. This appearance of low-frequency content can be attributed to the resonance of the void. The presence of void-type defects within a specimen undergoing AE testing therefore has the potential to produce erroneous results if analysis techniques using these features are utilised but the effects of the defect are not accounted for.

As would be expected based on the findings in Section 3.6.1, as the wave-modes of a bonded or unbonded specimen can both be well approximated by the dispersion curves of a single adherend, the wave-modes appear to remain practically unchanged by the presence of voids. Thus meaning that TDOA-based source-location methods will be minimally affected by the presence of voids. Potential solutions for future work to account for the effects of voids could include ultrasound scanning of the specimen to locate voids prior to AE testing, and then using AE source-location to correlate the AE propagation paths with the void locations. Alternatively, use of a Delta-T-style mapping of the specimen using PLBs would allow the effects of voids and any other localised discontinuities to be assessed and the subsequent AE results to be adjusted accordingly to provide a more accurate representation of the type and magnitude of source.

With regard to the use of AE with a PLB source as a method for defect detection, it has been demonstrated that the use of traditional time- and frequency-domain parameters can give a

reasonable indication of not only the presence of a void, but also its size. The accuracy is, however, limited when relying on a single feature. Even with a large difference between the defect sizes tested, there was still overlap in the ranges of values recorded for all of the parameters. This will be at least in part due to the inherent inconsistency of a PLB source. While efforts can be made to control the source by regulation of lead type, length and application angle, the human aspect will always result in some variation in the application.

The positioning of the source and sensor with regard to the defect was also seen to have a significant impact on the accuracy of this technique, with the most accurate classification of defects being achievable in configuration A, when the defect made up the greatest proportion of the propagation path.

The introduction of analysis by ANN however, resulted in the technique being 100% accurate in its classification for all of the specimens tested in this study, and for all source-sensor configurations. By utilising an ANN for defect-size estimation, as opposed to classification, it was found to be capable of achieving a respectable overall mean error of only 0.921 mm. This level of accuracy, along with the ease of analysis, does provide a significant improvement over previous attempts to utilise an AE system and PLB source for defect detection [9, 49]. It should be noted that this level of accuracy has been achieved using a large amount of training data and a limited variety of defects and source-sensor-defect configurations, it can therefore be expected that this accuracy will drop as more variables are introduced. This is however outside the scope of work for this project and remains an area for investigation in future work.

The use of an ANN for interpretation of data from a HN source test does rely on the generation of a significant set of training data which is time consuming, particularly if considering multiple different defect types and combinations of defects. It would therefore only be appropriate to use in situations where the potential benefits of its use could outweigh the necessary investment of time in producing training data-sets. The use of an ANN does however have the significant advantage that it requires very little user input or interpretation of the results, and requires no prior knowledge of the material properties or AE system characteristics, thus making it a relatively robust and easy-to-use method. The computational requirement for the implementation of an ANN of this scale is relatively low, and implementation through use of an app or toolbox, such as the MATLAB app used in this case, requires very little specialist expertise and can be completed through an easy-to-operate graphical user interface. Development of more advanced network structures may become necessary to achieve optimum results when considering additional parameters such as multiple defect types, and implementation of these would require a more in-depth approach to the development of the network, but for the situation considered in the work thus far, a very simple fully-connected network has proven adequate to provide excellent results.

Based on the limited scope of this initial study, it is not possible to give a full comparison with other NDT techniques, however some general comparisons can be made. In terms of accuracy, the defects tested in this work are at the larger end of the scale of what would be useful for practical application. To be competitive with other techniques, further testing is needed to establish the potential for accuracy in sizing defects below 10 mm, preferably down to in the region of 1 mm. With regards to time taken to test a specimen, this method has the advantage of inspecting a path, as opposed to a point, therefore making inspection faster in a similar way to the use of ultrasonic guided-wave techniques or pitch-and-catch methods as opposed to point-based through-transmission. Attempting to utilise this for time-saving may reduce its accuracy though, as it has been seen that the accuracy is significantly better with a shorter source-sensor distance. Additionally, the need for a set of training data adds to the overall time required if a suitably trained system

is not already available. The requirement for operator experience and knowledge is fairly minimal in comparison to the majority of other techniques as the ANN is capable of providing a simple output which does not require any user interpretation. The process of inspecting a whole specimen would however be more complicated and less intuitive than other methods such as ultrasound c-scans or infrared-thermography, which can produce an image of the specimen and its defects. The use of a Hsu-Nielsen Source and AE sensors has previously [9] been proven to be able to detect distributed kissing-type bonds, which many other methods are unable to detect, and in this work has been demonstrated to be able to detect voids. Further experimental work is required to determine which other types of defects this technique may be effective for, and to fully establish how it compares to other methods.

3.9 Summary

In this chapter, experimental investigation into AE propagation in relatively large-scale bonded joints has been conducted. Un-bonded reference specimens, bonded specimens, and bonded specimens with varying sizes of defect have all been tested. Testing has been conducted using a Pencil Lead Break source to provide a repeatable source which is comparable between specimens. Analysis has been conducted in terms of time-, frequency- and time-frequency-domains, with the effect of adhesive-bond status on many different AE parameters being established. Additionally, methods for the detection and sizing of adhesive defects, using only AE equipment, has been proposed and demonstrated to yield a number of benefits over similar methodologies previously published. The experimental results are discussed and compared with previous findings found in literature. The findings of this chapter have been used to inform the experimental methodology used in the following chapter, and the applicability of the findings expanded on by application of FEA in Chapter 5.

Chapter 4

AE-Instrumented Destructive Tests

This chapter describes AE instrumented Mode-I and -II fracture tests carried out on adhesively-bonded specimens. It describes the materials, equipment, experimental set-up and signal-processing techniques used, and includes discussion of the results obtained.

4.1 Introduction

The relationship between source-orientation and the excited Lamb-modes in plate- and sheet-type specimens is well documented, with Gorman [58] having initially demonstrated the concept with the use of in-plane, out-of-plane and angled PLBs applied to aluminium plates. It was shown that out-of-plane sources create a proportionally larger response in the asymmetric mode, while in-plane sources produced a proportionally larger symmetric mode. This finding has since been verified through simulations by Hamstad et al. [67] amongst others, and has been utilised to great success in subsequent studies to differentiate between failure mechanisms of delamination (out-of-plane), and fibre-breakage and matrix-cracking (in-plane) [62, 63]. It has, however, not been fully investigated whether this methodology could be applied to differentiation between fracture-modes in adhesively-bonded joints. It is anticipated that as the principal stresses in a shear (mode-II) specimen are oriented approximately 45° out-of-plane [137], while the principal stresses of crack-opening (mode-I) are oriented directly out-of-plane, that shear failure should produce a proportionally greater symmetric mode than would arise from crack-opening.

Work by Prathuru [9] makes the assumption that the behaviour of Mode-I and -II fractures of adhesive joints will produce similar results to out-of-plane and in-plane pencil lead breaks conducted on similar specimens, and uses comparison between the fracture signals and those acquired from the PLBs to verify the fracture mode found in four-point-bending and lap-shear tests. The majority of signals found in these tests did correspond most closely to the in-plane PLBs, as may be expected from Mode-II tests, but no Mode-I or mixed-mode tests were carried out for a full comparison. While a variety of features were examined and used in a k-means type clustering algorithm, the feature of greatest discrimination between the in-plane and out-of-plane PLB sources was found to be the ratios of energy contained in the high-frequency and low-frequency bands, as opposed to any factor relating directly to the individual Lamb-modes. It is possible that the difference in energy in these frequency bands was due to different wave-modes being excited, but this was not specifically confirmed, as the frequency bands can contain multiple wave-modes

occurring at different points in time.

Work by Dzenis and Saunders [85] has demonstrated that there is a difference between the signals arising from Mode-I and -II fracture which could be clearly identified by use of statistical pattern-recognition software, but which could not be identified using typical parametric or frequency-spectra analyses. So while variation in the signals was identified, no fundamental reason for the difference was presented.

In this section of work, AE-instrumented Mode-I and -II fracture tests have been carried out with the aim of establishing if there is a relationship between the fracture-mode of an adhesive joint and the prominence of the Lamb-modes in the generated AE signal.

The Mode-I tests conducted were of the double-cantilever-beam type, while the Mode-II tests conducted were single lap-shear tests. These test types were chosen over other tests, such as end-notch-flexure tests, as they could be conducted with relatively thin adherends without risking plastic deformation of the adherends, and also because they would allow a significant uninterrupted section of the specimen between the fracture region and the sensors for AE wave-propagation. This avoids the potential of accidental detection of friction between the specimen and its supports. It is acknowledged that the lap-shear test may not be a completely pure Mode-II test due to the potential for bending of the adherends creating a crack-opening load, but it is predominantly Mode-II, and it has been verified by both Dzenis and Saunders [85] and Prathuru [9] that the AE signals resulting from a lap-shear test are indistinguishable from the results of a pure Mode-II test.

4.2 Materials

Both specimen types used were manufactured from 3.175 mm x 50 mm HE30TF aluminium bar. Adherends were cut to 300 mm long for the DCB test, and 360 mm long for the lap-shear test. While it would typically be preferable to utilise standard test dimensions to allow greater comparability with other studies, the standard specimen dimensions, as per ASTM D5528-01 [138] (DCB test) or ASTM D1002 [139] (lap-shear test), do not lend themselves to the aims of this study, as the narrow 25 mm wide specimens would result in signals dominated by multiple edge reflections, making modal analysis difficult. It was also important to have an adherend thickness that would work for both test types. The adherends were selected to be thicker than recommended for ASTM D1002 (1.62 mm), but at the thin end of the recommended thicknesses for ASTM D5528-01 (3 mm to 5 mm) in order to generate a highly dispersive Lamb wave, while not being so thin as to risk plastic deformation of the adherend. To aid selection of suitable adherends, dispersion-curves were generated in the software Vallen Disperse to ensure appropriate dispersion characteristics. The widths were chosen to be as large as could be practically accommodated in the testing apparatus, in order to minimise the effects of edge-reflections, and thus simplify analysis. For this reason the width used is double that recommended in the ASTM standards. The specimen lengths were chosen to provide significant propagation distance from the fracture region to the sensor location, so that the Lamb-modes would be dispersed far enough upon arrival at the sensor that regions of the time-frequency-domain corresponding to each mode could be clearly identified and separated. While extending them beyond 300 mm long would have been advantageous for increasing dispersion and minimising reflections, it was not practical to do so in the testing apparatus being used, and a longer source-sensor distance would further increase the already significant affects of attenuation.

The adhesive bonding process consisted of surface preparation, adhesive application and cur-

ing. The specimens were initially rinsed with acetone, before being abraded with P400 grade abrasive paper, rinsed with acetone again, and then cleaned with Loctite®SF 7063. Silicone grease was then carefully applied to a 60 mm long region of the DCB specimens to prevent bonding and thus create a pre-crack, as shown in Figure 4.1a. Loctite®EA 3430, a relatively brittle two-part epoxy adhesive, was then applied through a mixer-nozzle to the bond areas of one adherend for each of the specimens. The bond area for the DCB specimens covered the entire specimen, aside from the pre-crack, while the bond area for the shear specimens was a 50 mm x 50 mm square, located 70 mm from the ends of the adherends, as shown in Figure 4.1b. Small 0.5 mm thick aluminium shims were then added into the adhesive to maintain a uniform bond thickness as the other adherends were placed on top. Once assembled, weights totalling 4 kg were added on top of each specimen and they were left to cure for a minimum of five days, at an average temperature of 19C and humidity of approximately 20%.

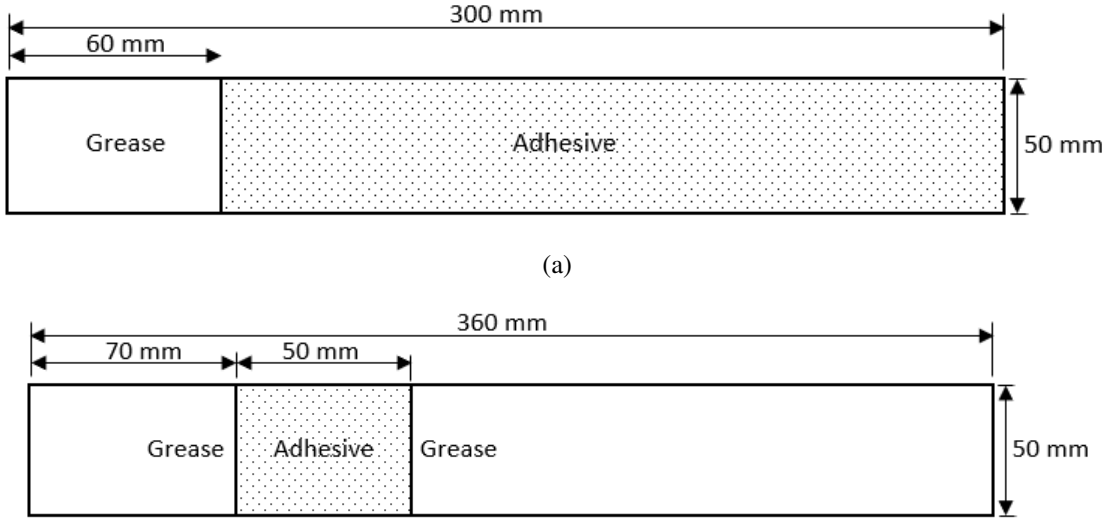

Figure 4.1: Areas of adhesive application on each adherend for (a). DCB test specimens, (b). Lap-shear test specimens

The lap-shear specimens were fitted with tabs at the clamping areas at each end of the specimen to prevent misalignment and bending, which would introduce Mode-II loads. The tabs were cut from the same 3.175 mm x 50 mm HE30TF aluminium bar, and measured 60 mm long. These tabs were bonded to the specimens using the same procedure as described above. The DCB specimens were fitted with mounting blocks, to allow the specimens to be mounted in the yokes of the tensile-test machine. The blocks were the full width of the specimens and 20 mm long. The hole for the connecting pin to attach the specimens to the yoke was located 20 mm from the top of the specimens. These blocks were bonded to the specimens using the same procedure as described above, but using the stronger LOCTITE EA 9461 adhesive, to ensure that the blocks did not fail before the intended fracture zone did.

4.3 Experimental Procedure

Both types of specimen were tested using an Instron 3382 universal testing machine (UTM), controlled through BlueHill 3 software. The DCB specimens were mounted using the previously described loading blocks, which were secured into the loading yokes of the machine. The lap-shear specimens were clamped into the machine using 50 mm mechanical jaws. The loading rates used were 0.5 mm/min, based on ASTM D5528 01 [139], and 1.3 mm/min, based on ASTM D1002-10 [138], for the DCB and lap-shear specimens respectively. DCB tests were run up to a crosshead displacement of 10 mm, while lap-shear tests were run until complete failure was achieved. Each test was conducted four times to ensure repeatability.

The AE equipment used in this work was the same set-up as previously described in Section 3.3. The two sensor locations used were both on the same adherend of the specimens. On the DCB specimens, as indicated in Figure 4.2, one sensor was located at the end of the pre-crack, and the other 10 mm from the end of the specimen. On the lap-shear specimens, illustrated in Figure 4.3, the sensors were located either side of the bond area, at distances of 90 mm and 200 mm away from the centre of the bond area. These locations were chosen for the following reasons: the sensors needed to be located on either side of the bond area to allow a linear TDOA-type source-location scheme, as described in Section 2.2.9 to be used. At least one sensor should be at a significant propagation distance from the source, so as to allow dispersion of the symmetric and asymmetric modes before reaching the sensor. Sensors should not be located so close to the ends of the specimens that the reflections of the higher-velocity waves from the ends of the specimen will overlap with the slower waves and interfere with the signal analysis. The sensors were coupled to the specimens with a layer of silicone grease to avoid the inclusion of any air-gap, and secured to the specimens using aluminium adhesive tape. Photographs of the experimental set-ups are shown in Figures 4.4 and 4.5. An NI LabVIEW VI was used to record the AE data in .TDMS format. The AE data was recorded continuously throughout the experiments, with recording being started and stopped manually, as opposed to only recording data from hits, due to the limitations of the available equipment. While this was incredibly inefficient, and resulted in the generation of a vast quantity of meaningless data, it did mean that the definition of suitable threshold values could be optimised based on the results during post-processing. A sampling rate of 2.5 MHz was used for the tests, and amplification on the pre-amplifiers and signal conditioning unit were set to +60 dB and +12 dB. As in the previous chapter, the sampling rate was chosen to be more than double the maximum frequency of interest (1 MHz) thus ensuring that the Nyquist sampling criteria [126] was satisfied and the signal would not be subject to aliasing. The amplification levels were chosen to give the best signal resolution for the relatively low-amplitude signals, while avoiding the risk of data-loss which can occur from over-saturation of the system if too high a level of amplification is used [140]. This amplification was removed during post-processing in MATLAB.

For the DCB tests, a video camera positioned on a tripod in front of the test set-up was used to record crack propagation. To aid this, the edges of the specimens were painted with white correction-fluid to make the appearance of any cracks more prominent, and distance markers were added along the length of the specimen. This can be seen in Figure 4.4 While this approach is of limited accuracy due to the frame-rate and resolution of the camera, and due to the assumption of a uniform crack-front throughout the specimen width, it does provide a useful approximation with which the AE source-locations can be compared. This approach could not be used effectively for the lap-shear specimens due to the nature of their failure being sudden and complete.

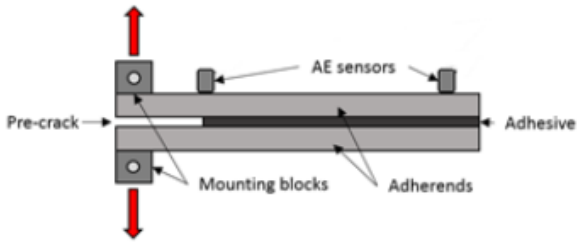

Figure 4.2: Double Cantilever Beam (Mode-I) experimental schematic (not to scale)

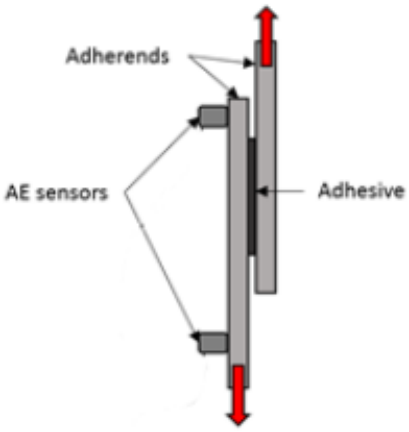

Figure 4.3: Lap-shear (Mode-II) experimental schematic (not to scale)

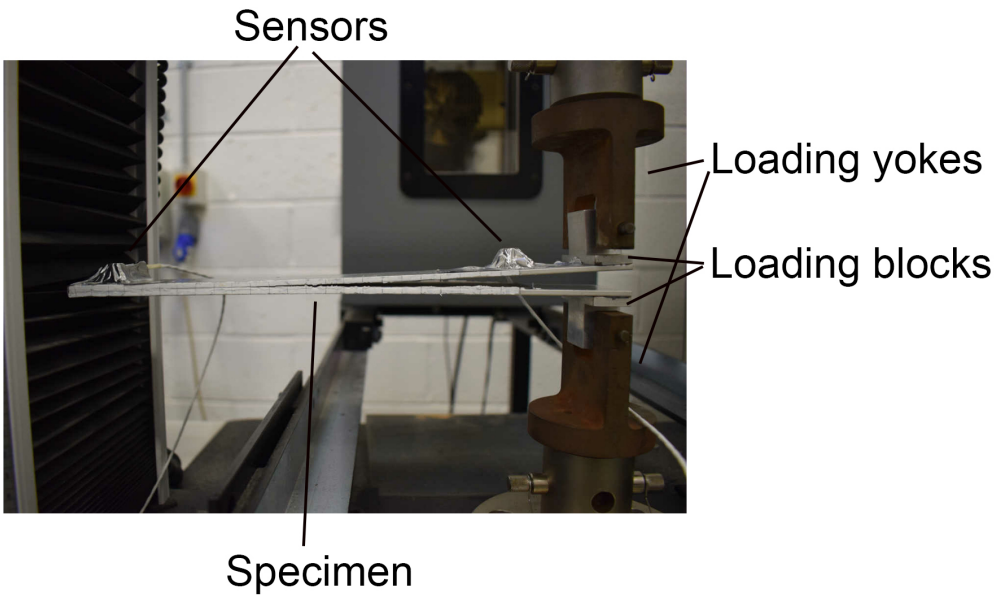

Figure 4.4: DCB experimental set-up as seen from the video camera

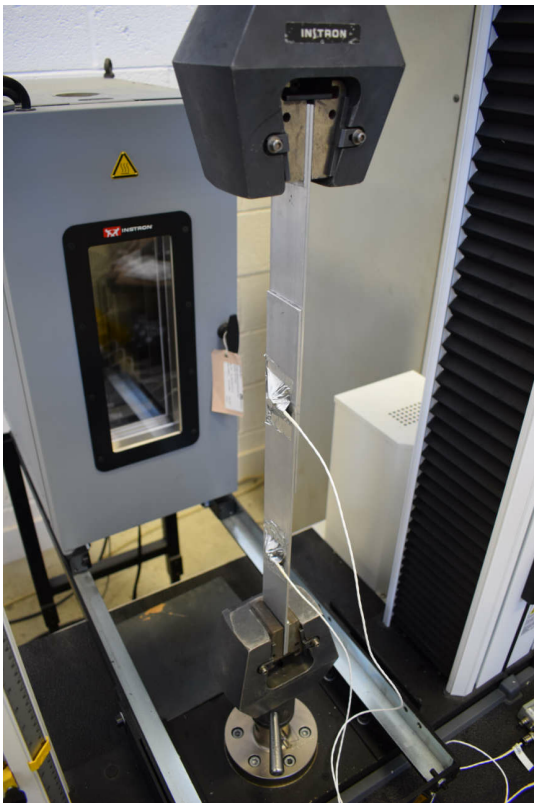

Figure 4.5: Lap Shear experimental set-up

4.4 AE Signal-Processing Techniques

As the system was recording continuously, the initial step was to isolate hits for further analysis and to discard the noise. The signal was rectified and smoothed by averaging the RMS value of the signal using an averaging window of 200 data points (80 μs). Two thresholds were then used. The higher threshold of $0.15V$ was used to identify hits of significant amplitude. The lower threshold of $0.05V$ was then used to identify the start and end of these hits. The use of this double-threshold technique is advantageous for this study, as the higher threshold avoided the inclusion of any low amplitude hits which only just exceeded the background noise. This was important as if the dominant A_0 mode only just exceeds the threshold then accurate detection of the lower amplitude S_0 mode will be difficult. The use of the lower threshold, in conjunction with the higher one, ensures that the entire duration of the signal, including the low amplitude S_0 mode, is included in the analysis. The threshold values were chosen experimentally, based on the level of background noise.

The peak amplitude and energy for each hit was calculated using the methods previously described in Section 2.2, as were the frequency spectra.

The identified hits were transformed into the time-frequency-domain by continuous wavelet-transform. In this case the Gabor wavelet was used, as this provides the best combination of time and frequency resolution. An example of this transformation from time- to time-frequency-domain is illustrated in the upper panels of Figure 4.6. Arrival times, corresponding to the A_0 mode at

300 kHz, were determined as the first peak in the 300 kHz band of the wavelet-transform to exceed 70% of the maximum WT coefficient. These arrival times, and the separation distance between the sensors, were used to estimate the linear source-location of each hit, and therefore the propagation distance from the source to each of the sensors. The A_0 velocity of 3065 m/s used in the source-location calculations was taken from dispersion-curves calculated for the adherends using Vallen Dispersion. Hits located as occurring from outside the potential bond-regions of the specimens were excluded from further analysis.

Based on the identified propagation distances, the arrival times of both the S_0 and A_0 wave-modes are calculated using the theoretical dispersion-curves for the adherends (generated by Vallen Dispersion software). The central panel of Figure 4.6 shows these dispersion-curves, modified by the propagation distance, overlaid on the wavelet-transform plot of the signal. This allows certain peaks in the wavelet-transform plot to be attributed to these wave-modes. This process was automated in MATLAB, though with all hits being manually verified to ensure accuracy and avoid confusion due to issues such as overlapping hits. The S_0 and A_0 modes of the adherends were selected for analysis as these modes will propagate throughout the unbonded sections of the specimen, while the modes propagating through the bonded region will be very similar and can be well approximated by these modes. This is illustrated by the theoretical dispersion-curves shown in Figure 4.7, in which it can be seen that while nine different modes may theoretically exist, they generally follow the modes of a single adherend, and as previously discussed in Chapter 3, it is the regions of the modes closest to those of the adherends which are typically recorded as having the highest amplitude [3].

To allow quantitative analysis of the contributions of each wave-mode, the corresponding peaks within a certain frequency band were extracted. The frequency band around 300 kHz was chosen as it is close to the resonant peak of the sensor and contains significant content from both wave-modes. There is also significant enough dispersion at this frequency to differentiate between the wave-modes in the time-domain. The lower panel of Figure 4.6 shows the WT coefficients in the 300 kHz band with the S_0 and A_0 peaks marked. The ratio between the amplitudes of these peaks was then used to investigate the difference between the fracture-modes. This technique of modal AE analysis based on WT-coefficients has been well proven in previous works, most prominently those by Hamstad et al. [57, 59, 61, 67, 141]. In a small number of hits, the wave-modes could not be clearly identified or separated due to factors such as overlapping of hits, or poor signal-to-noise ratio. In such cases the hits were excluded from further analysis.

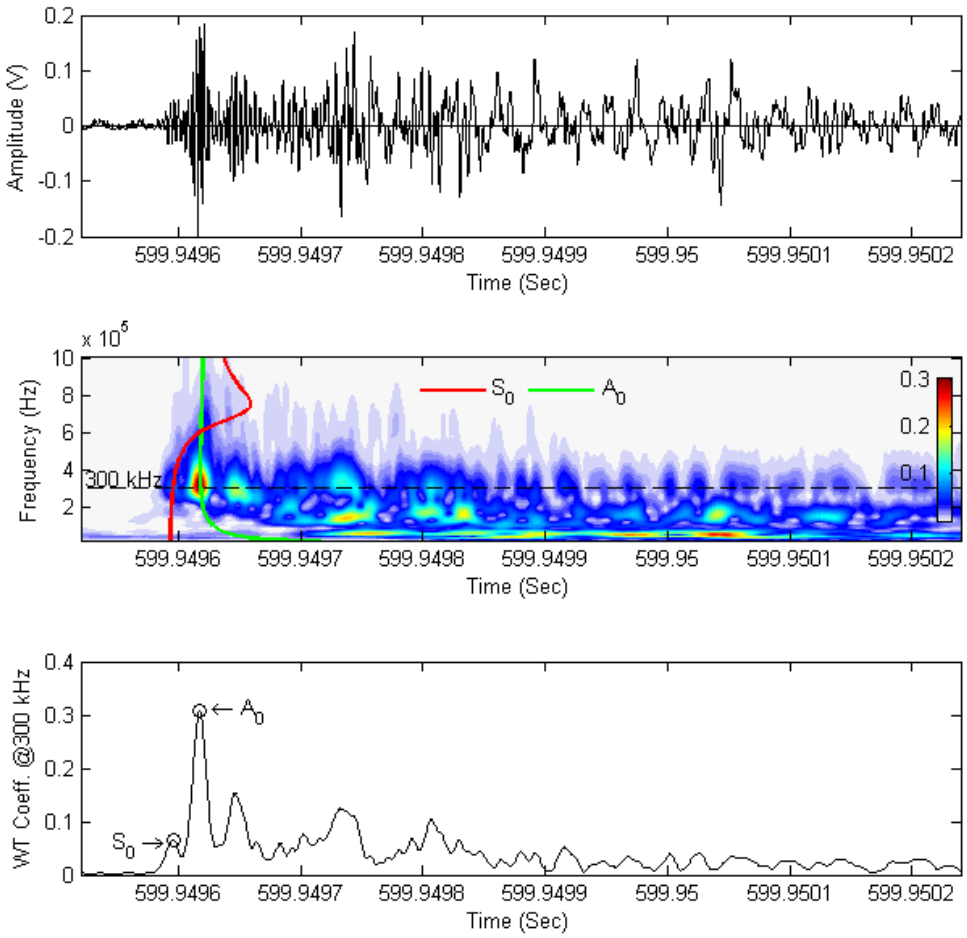

Figure 4.6: Example of signal-processing method. Top: Original AE signal. Middle: Wavelet-transform plot with overlaid dispersion-curves indicating symmetric (S_0) and asymmetric (A_0) wave-modes. Bottom: Wavelet-transform coefficients for 300 kHz frequency band, with S_0 and A_0 peaks marked.

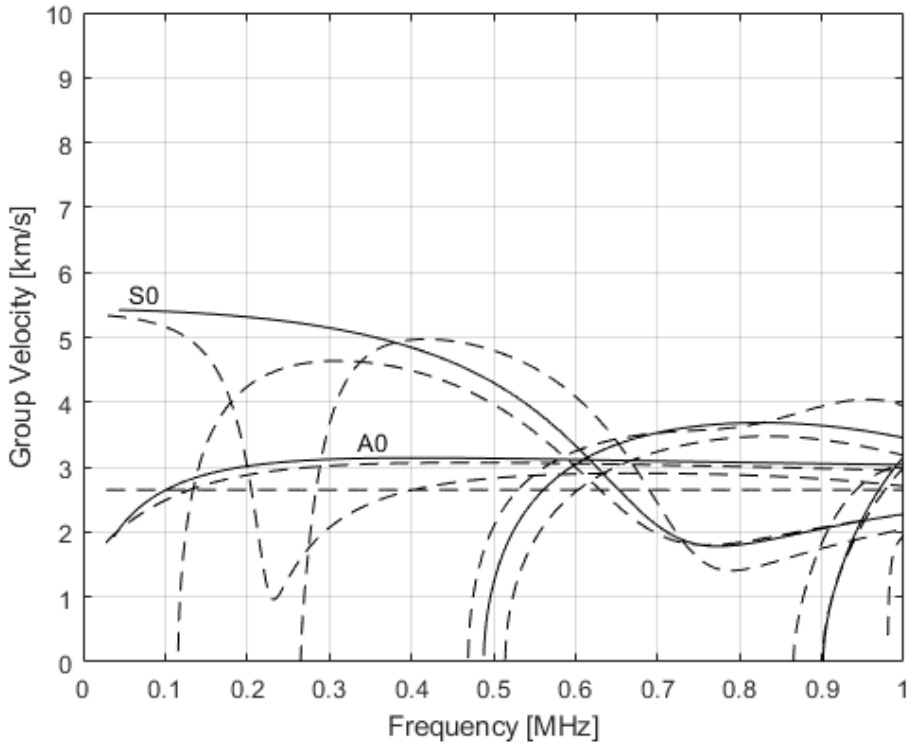

Figure 4.7: Comparison of group-velocity dispersion-curves for a single 3.175 mm aluminium sheet (solid lines) and an adhesively-bonded specimen with 3.175 mm thick aluminium adherends and a 0.5 mm epoxy adhesive layer (dashed lines).

4.5 Results of Destructive Tests

4.5.1 Load/Displacement Results

The loading curves acquired from the tensile-test machine are presented in Figures 4.8a and 4.8b, for the DCB and Lap-shear tests respectively. It is noted that the first two DCB tests exhibited highly typical behaviour, featuring an approximately linear increase in load as the adherends deflect elastically in the pre-crack region until the maximum load is reached. This is followed by multiple small drops in load as the adhesive fails in sections, and small rises in load between these, as the adherends elastically deform again. The third and fourth specimens, however, exhibited slightly less typical behaviour, with the load increasing again significantly after fracture initiation. This is believed to be indicative of significantly weaker bonding in the region closest to the pre-crack, which has failed at a much lower stress than the rest of the bond. This is particularly prominent in the fourth specimen. It is possible that contamination in the region close to the pre-crack occurred due to the use of grease on the pre-crack region as an adhesion inhibitor. There is also significant variation in both the initial fracture-load and the maximum load sustained by the specimens, with initial fracture occurring between 10 N and 50 N, and the maximum loads varying from 20 N to 55 N. The most likely cause of this variation is thought to be contamination of the adherends due to other processes taking place in the workshop during specimen preparation, though other factors such as improper mixing may also have contributed. While such variation in specimen strength would typically be cause for concern, for the purposes of this study the variation in bond strength between specimens is of little consequence, as this bond strength is not a factor being investigated. The lap-shear tests all exhibit typical behaviour, with an approximately linear region of elastic deformation up to their maximum load, followed by sudden and complete failure in which the adherends completely separate. The maximum loads withstood by the lap-shear specimens varied from 1200 N to 2000 N. The disparity in maximum load between the two specimen configurations highlights the importance of loading orientation for adhesively-bonded joints, and thus the importance in potentially being able to differentiate between fracture-modes.

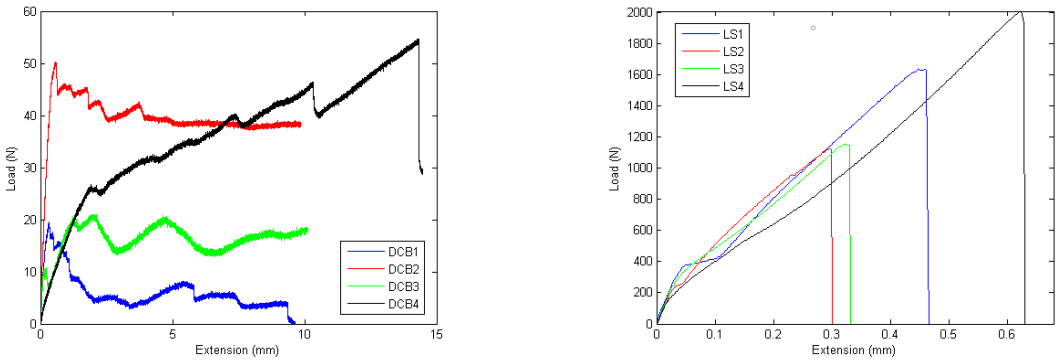

(a) (b)

Figure 4.8: Loading curves for: (a) DCB test. (b) Lap-shear test.

4.5.2 Failure Mechanisms

The main failure mechanism observed in all specimens was adhesive failure, with the adhesive layer separating from one adherend as the bond between adhesive layer and adherend failed, while remaining bonded to the other adherend. In the DCB specimens, and to a lesser extent in two of the lap-shear specimens, some adhesive cracking was also found. In some regions of these specimens the adhesive failure would occur at the interface with the upper adherend, and in other regions it would occur at the lower adherend, the result being that the adhesive layer cracked between these regions, allowing sections of the adhesive to remain attached to either adherend. Figure 4.9 shows annotated examples of the failure mechanisms present in both types of specimen. Assuming that both adhesive-failure and adhesive-cracking generated AE, it can be assumed that a minimum of two different AE source-types were therefore present in the tests. With the test set-up used, it was not possible to identify which hits occurred from each failure type. Further investigation of this poses a potential future research topic.

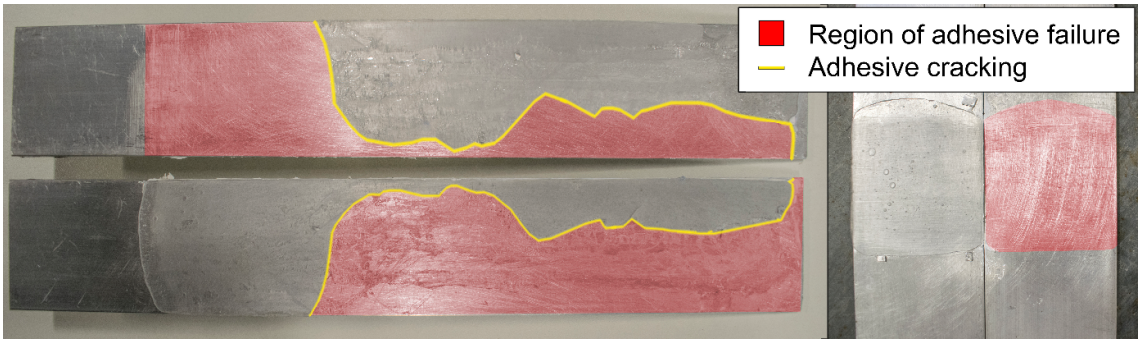

Figure 4.9: Example of failure mechanisms observed. Left: DCB specimen showing adhesive failure and cracking of the adhesive layer. Right: Lap-shear specimen showing only adhesive failure.

4.5.3 Relationship between AE and Loading

As can be seen in Figures 4.10 to 4.13, the relationship between AE and load is as would be expected from previous studies, with AE events generally corresponding to significant drops in load. In the DCB specimens the first hits slightly pre-empt the initial load-drop, and then occur throughout the rest of the test as the crack propagates from one end of the specimen to the other. In the lap-shear specimens, the first hits occur within the linear portion of the loading curve, between approximately a third and half of the maximum load. Events then increase in frequency up until final failure. The final failure of the specimen results in a very high level of AE activity over a very short time-span, starting just before the visible drop in load.

4.5.4 AE Source-Location

The AE source-locations identified in the DCB tests generally correspond well with the visually observed crack-front recorded with the video-camera, with the hits initially being located at the sensor at the tip of the 60 mm pre-crack and then progressing further along the specimens as the crack opens. While the AE source-location results generally correspond well, there is some

variation and scatter which is believed to be due to a combination of factors. The crack-front will not be uniform due to the inhomogeneous bond quality, so the location of the crack-front recorded at one side will not necessarily be accurate through the entire specimen width. This can be clearly seen in Figure 4.9. The use of a linear source-location method, as opposed to 2D or 3D, may also introduce a small level of error, as not all hits will occur directly between the sensors. In the lap-shear specimens hits are mainly concentrated within the bond area, as would be expected, although some hits were identified as occurring outside the bond area. This may again be due to the limitations of linear source-location but may also be due in some cases to the incorrect identification of arrival times due to interference between overlapping hits; this is a problem which can also occur in the DCB specimens but is much more prominent in the lap-shear tests due to the limited time in which the hits all occur. Additionally, once the adherends have separated there is no mechanism to prevent them coming into contact again and potentially causing further AE events due to their contact. To isolate events potentially occurring from sources other than adhesive, events located as occurring outside of the adhesive region have been isolated from further analysis.

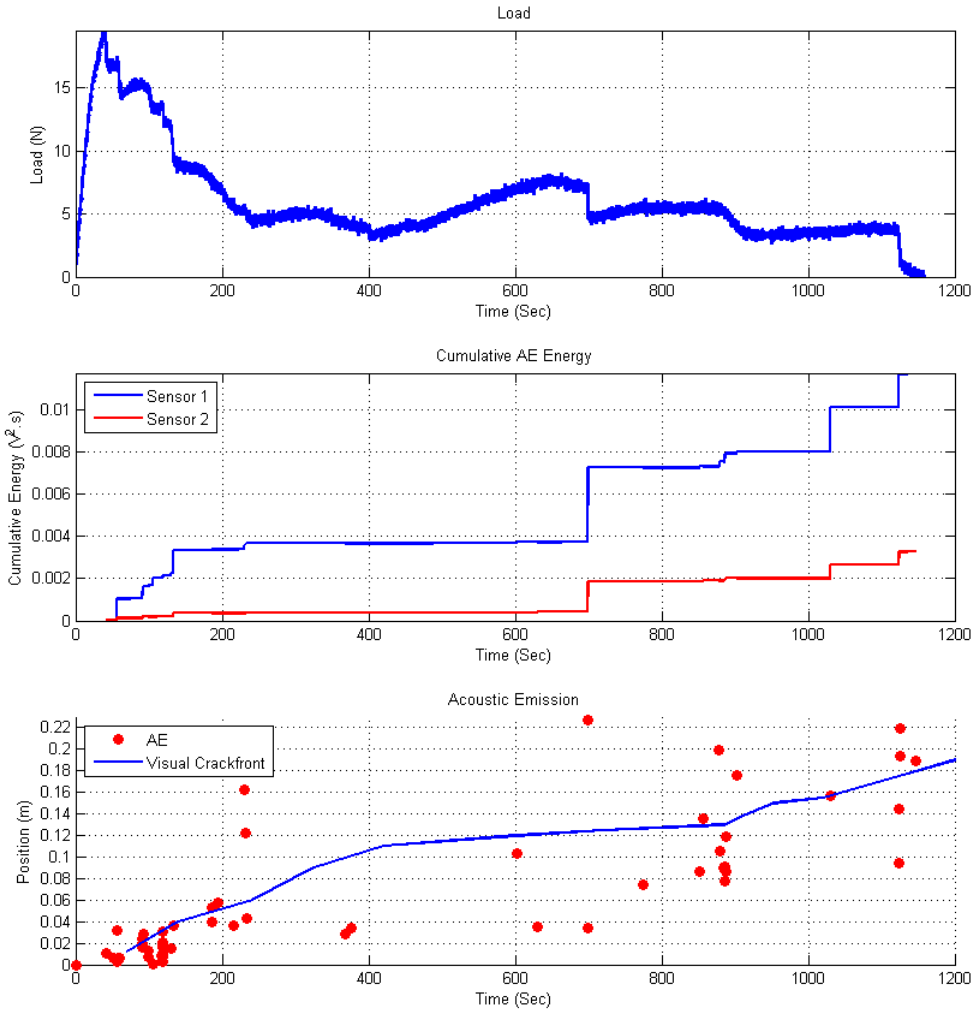

Figure 4.10: Loading and AE relationship for DCB specimen 1. Top: Loading curve. Middle: Cumulative AE energy at sensor 1 and sensor 2. Bottom: AE source-location and visually-identified (video-camera) crack-length

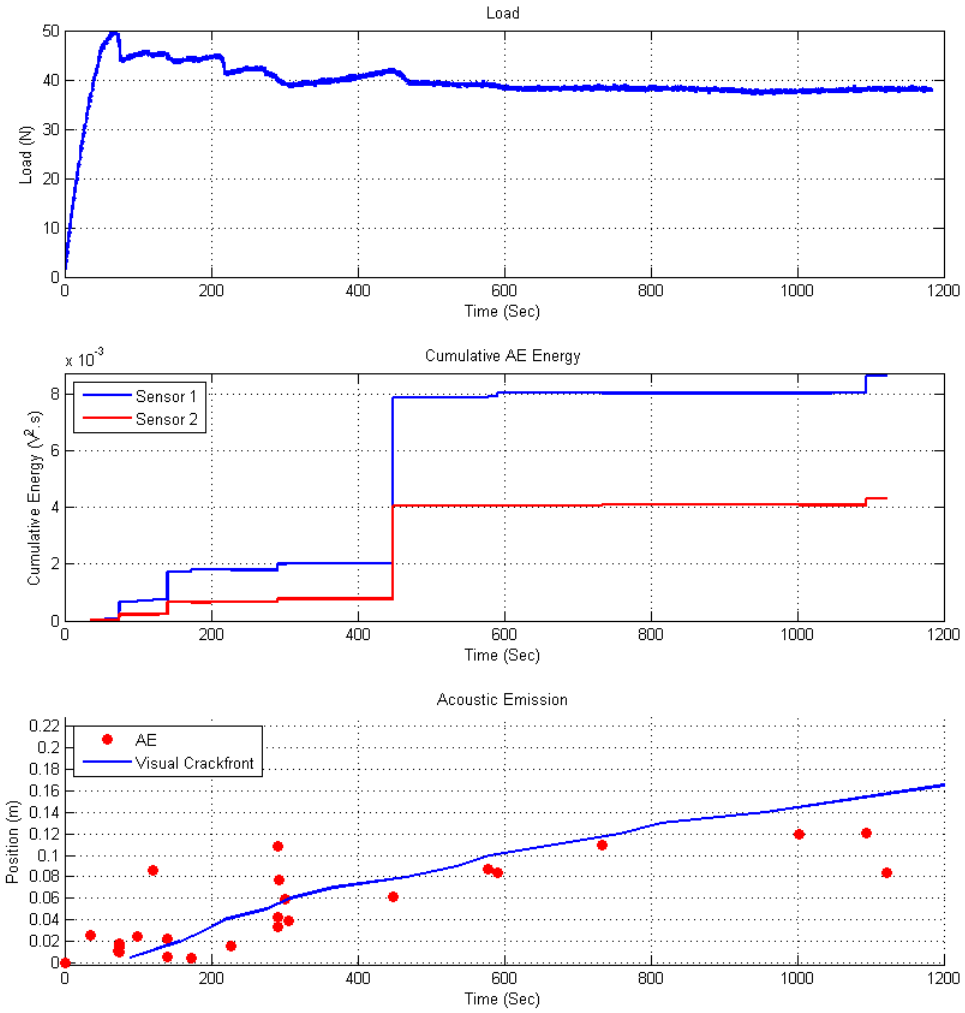

Figure 4.11: Loading and AE relationship for DCB specimen 2. Top: Loading curve. Middle: Cumulative AE energy at sensor 1 and sensor 2. Bottom: AE source-location and visually-identified crack-length

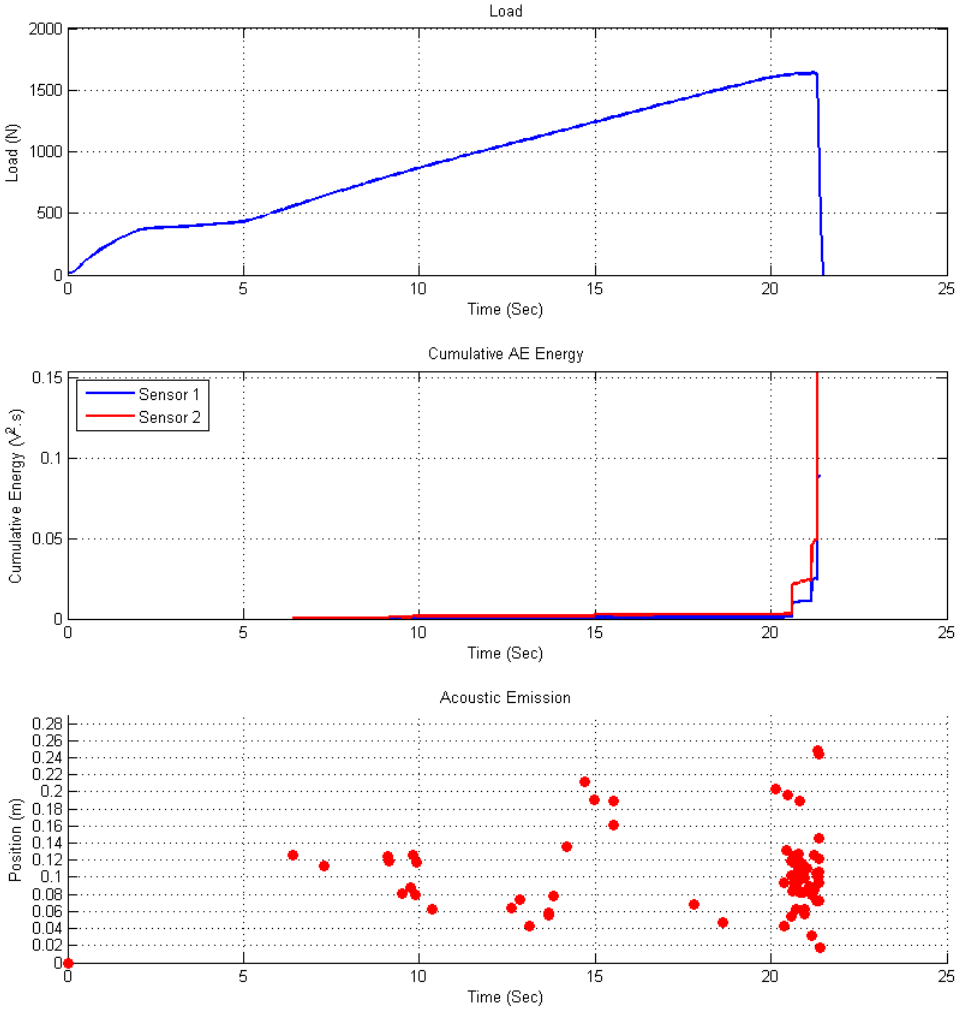

Figure 4.12: Loading and AE relationship for LS specimen 1. Top: Loading curve. Middle: Cumulative AE energy at sensor 1 and sensor 2. Bottom: AE source-location

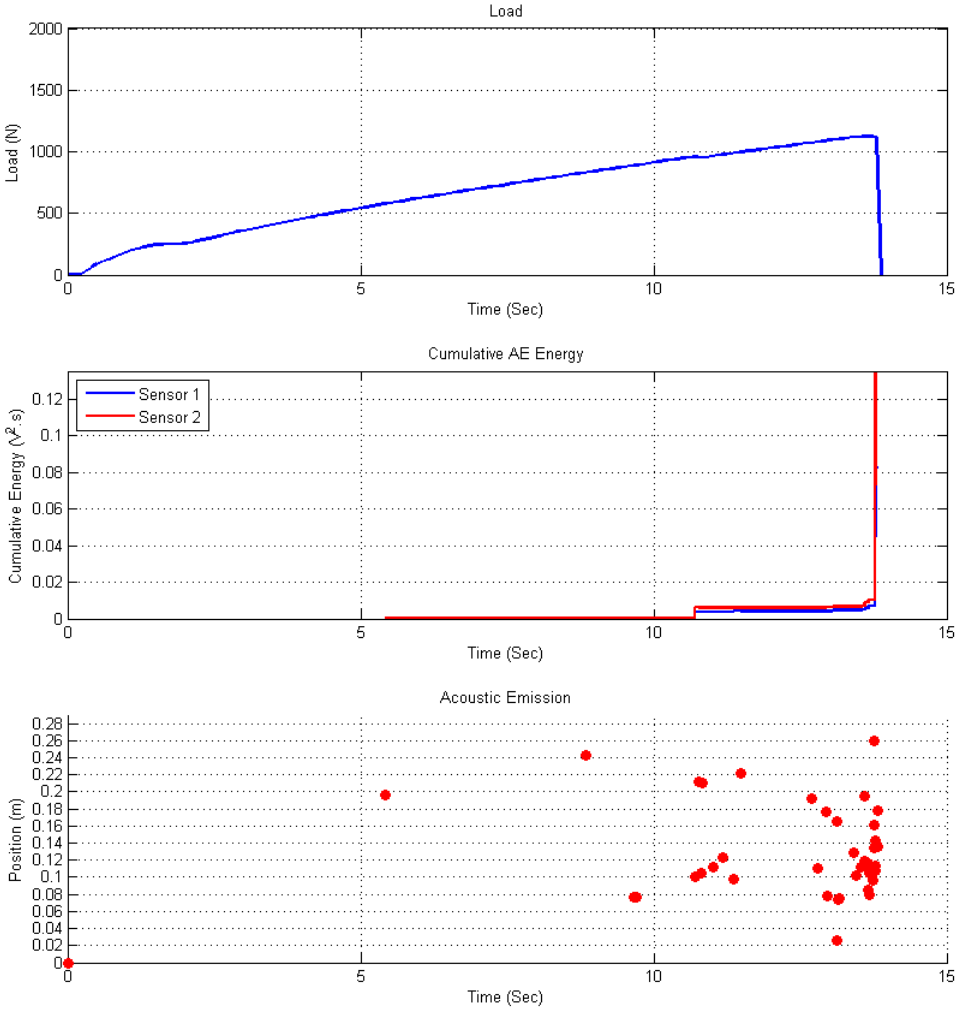

Figure 4.13: Loading and AE relationship for LS specimen 2. Top: Loading curve. Middle: Cumulative AE energy at sensor 1 and sensor 2. Bottom: AE source-location

4.5.5 Parametric Analysis

While the aim of this work is to investigate the use of modal analysis to differentiate between fracture-modes, energy and frequency parameters have also been investigated for the sake of comparison as potential methods of differentiation. The AE energy of each hit (Calculated as per Section 2.2.5) is plotted against time of occurrence for each of the specimens tested in Figure 4.14. For all of the specimens tested, the energy of the majority of hits varied over a range between $10e^{-5}V^2.s$ and $10e^{-2}V^2.s$, with most hits being in the lower end of this range between $10e^{-5}V^2.s$ and $10e^{-3}V^2.s$. The highest energy hits occurred in the lap-shear specimens during the sudden final fracture. As the two fracture-modes both exhibit a similar wide range of hit energies, it can be concluded that energy is not a suitable parameter for differentiating between fracture-modes.

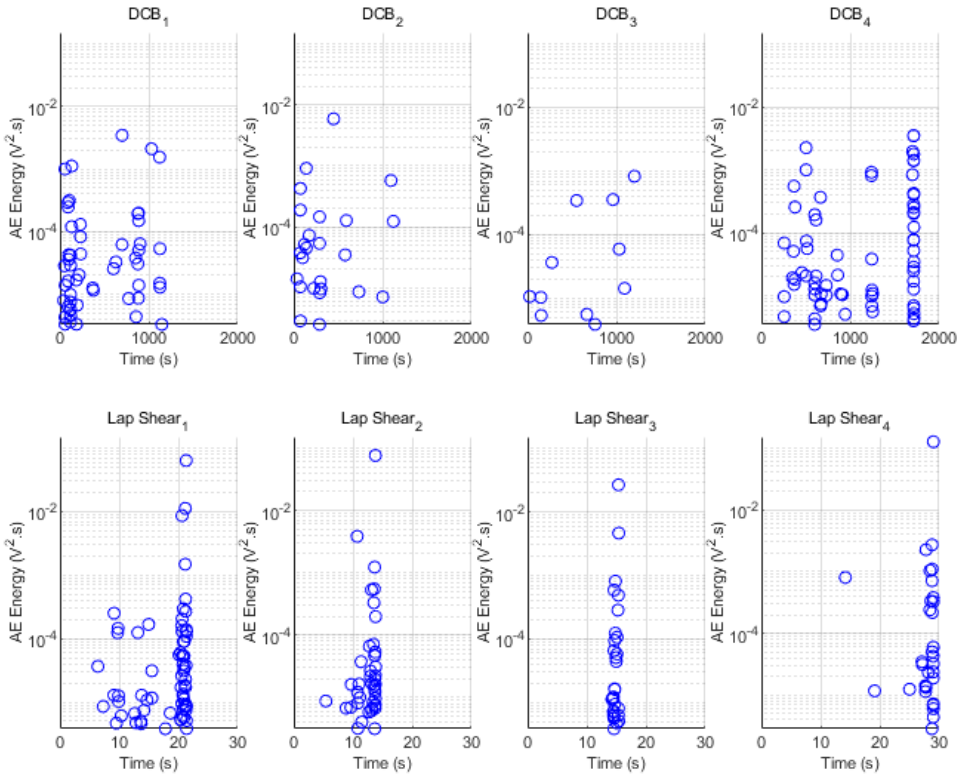

Figure 4.14: AE energy vs time for all tests

Peak frequencies, frequency spectra and the ratio between high- and low-frequency energy have all been investigated. Figure 4.15 shows the peak frequency of each of the hits recorded, plotted against their time of occurrence. The peak frequencies vary in all of the specimens from a minimum of around 20 kHz, which is the cut-off frequency of the pre-amplifier, up to 350 kHz, just above the peak frequency of the sensor response. The peak frequencies generally fall into three regions. The most frequently occurring is the region around 300 kHz to 350 kHz, in close proximity to the peak of the sensor response. A second region of peaks is found between 20 kHz and 50 kHz, this region may occur from sources which do actually have peak frequencies in this region, or may be the result of significantly lower-frequency sources which have then been

filtered. While the majority of the peak frequencies fall into the two regions described, a still significant number of hits fall into the region in between. Comparison between the DCB and lap-shear tests shows that both tests produce a broad range of peak frequencies, which fall into all of these regions, thus implying that, in this case, peak frequency cannot be used as a discriminating feature.

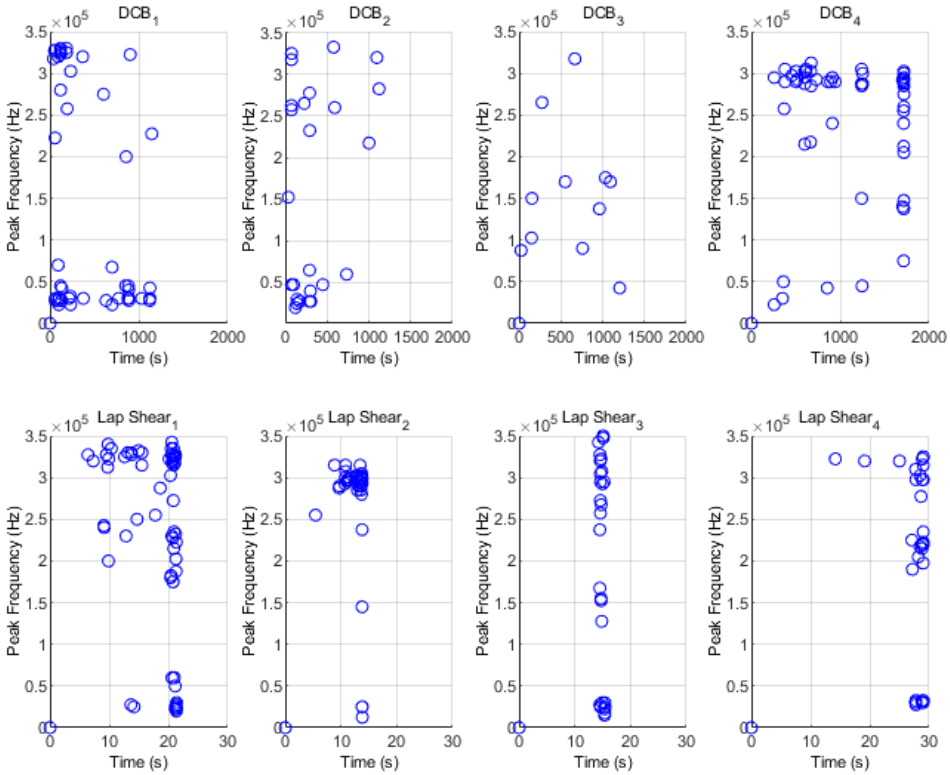

Figure 4.15: Peak Frequency vs time for all tests

To investigate the full frequency-range, as opposed to just the peaks, the mean FFTs for each test have been calculated and are presented in Figures 4.16 and 4.17, for the DCB and lap-shear tests respectively. While the use of a mean FFT for each test, as opposed to an FFT for each hit, does result in the loss of data, it does allow the variation in frequency spectra between tests to be easily summarised. In order to establish the mean frequency spectra for each test, the frequency spectra for each hit have been normalised to a maximum value of 1, to ensure that all hits have a similar contribution to the mean, rather than the spectra being dominated by a single high-energy hit. The mean values of these normalised frequency spectra have then been calculated for each test.

Investigation of the frequency spectra shows that almost all of the activity is concentrated under 400 kHz. As indicated in the peak frequency analysis, the main peaks exist in the regions of 20 kHz to 50 kHz, and 300 kHz to 350 kHz, with peaks also existing in the 150 kHz to 250 kHz region in some tests. The amplitude and breadth of these peaks does vary significantly between specimens. The peak relating to the peak frequency of the sensor, at 300 kHz to 350 kHz, is present in all specimens. The lowest frequency peak is also of a similar amplitude in most

specimens, but is of a very low amplitude in specimens DCB 4 and LS 2. The middle frequency peak varies significantly, being of high amplitude in DCB 2, DCB 3, LS 3 and LS 4, but relatively low amplitude in the other tests. Due in part to the significant variation between specimens within each test type, it is difficult to draw any significant comparisons between the frequency spectra of Mode-I and Mode-II fracture. Frequency content has previously been proposed as a potential method for differentiating between fracture-modes by Prathuru [9], with it being suggested that the ratio between energy in a low-frequency band and a high-frequency band could be used as a possible discriminator. To investigate this further, the energy in the low-frequency and high-frequency bands of each hit was calculated by low-pass or high-pass filtering of the signal, prior to energy being calculated as previously described. A cut-off between low and high-frequency in this case was chosen as 150 kHz, as this was felt to be a natural divide, with most frequency-spectra featuring a local minima in this region. The resulting ratios of low-frequency energy to high-frequency energy are presented in Figure 4.18, on the basis of each hit, mean and standard deviation for each specimen, and mean and standard deviation for each fracture mode. As with previously discussed frequency parameters, the results show significant scatter, spanning over a range from 0 to 1 for both specimen types. Overall, the Mode-I DCB specimens do feature a greater proportion of low-frequency energy than the Mode-II lap-shear specimens, as was suggested by Prathuru, with overall mean values of 0.3680 and 0.2961 for the DCB and lap-shear tests respectively. The difference between the means is, however, minimal, particularly when compared to the standard deviations of 0.2826 and 0.2961, meaning that, in this case, the ratio between high and low-frequency content does not provide an adequate method to reliably differentiate between fracture-modes.

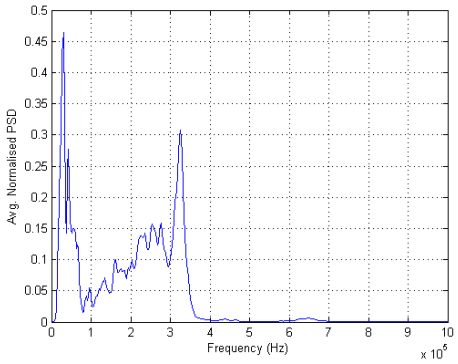

(a) DCB 1

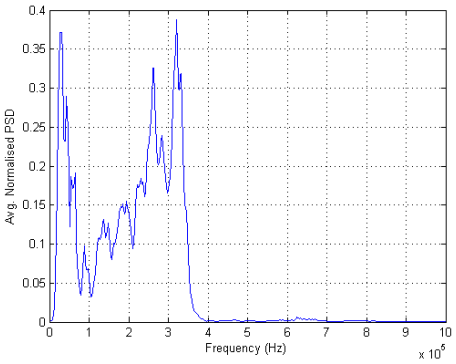

(b) DCB 2

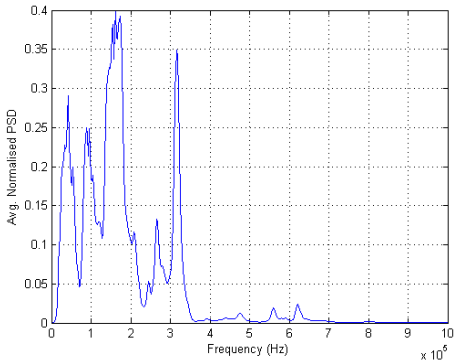

(c) DCB 3

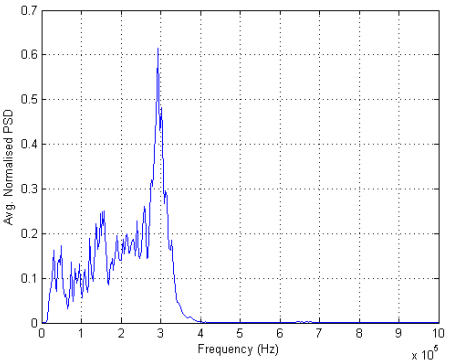

(d) DCB 4

Figure 4.16: Mean normalised FFT of DCB tests

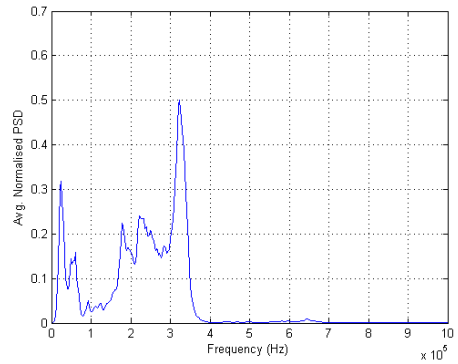

(a) LS 1

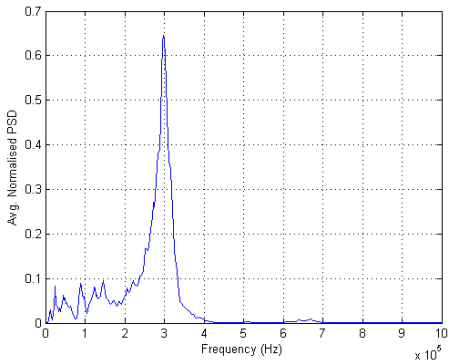

(b) LS 2

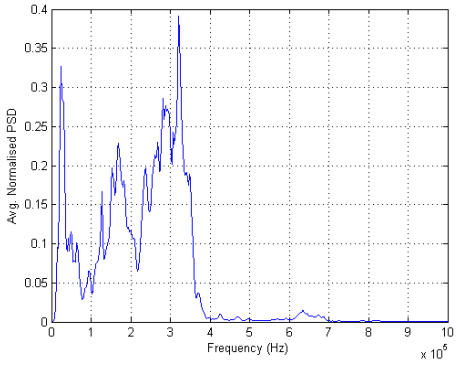

(c) LS 3

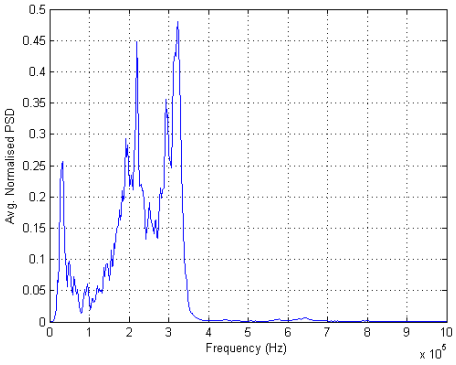

(d) LS 4

Figure 4.17: Mean normalised FFT of of Lap-shear tests

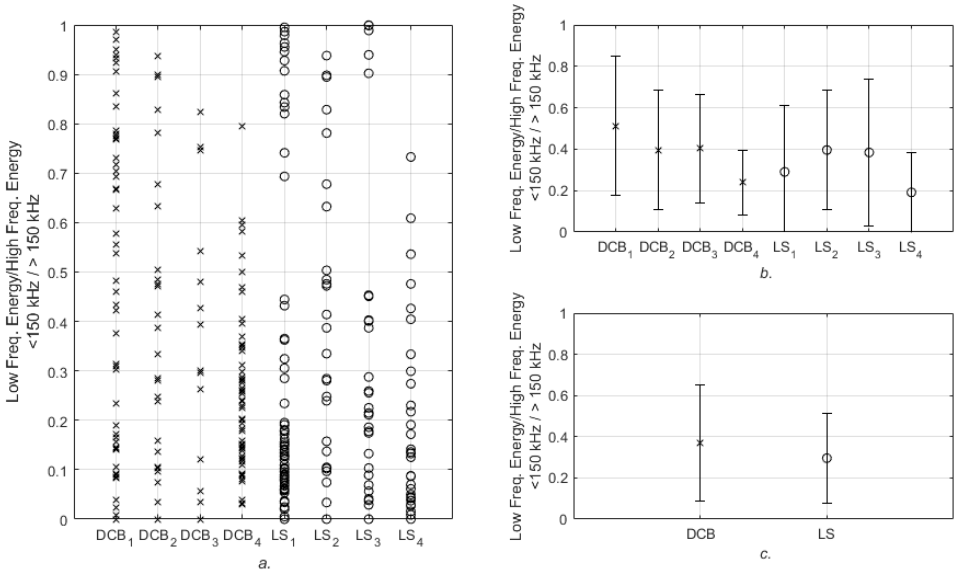

Figure 4.18: Ratio of energy in low-frequency band ($< 150\ kHz$) to high-frequency ($> 150\ kHz$) band, for (a). Each hit, (b). Mean and std. deviation for each specimen, (c). Mean and std. deviation for each test type

4.5.6 Modal AE Results

The resulting ratios of the peak wavelet-transform coefficients corresponding to the S_0 and A_0 wave-modes are presented in Figure 4.19. Both fracture-modes can result in a wide range of S_0/A_0 ratios being generated. For the DCB tests, values range from 0.0169 to 0.4178 with an overall mean and standard deviation of 0.085 and 0.0848 respectively. Lap-shear tests produced values ranging from 0.0616 to 0.7197 and with an overall mean and standard deviation of 0.1902 and 0.1425.

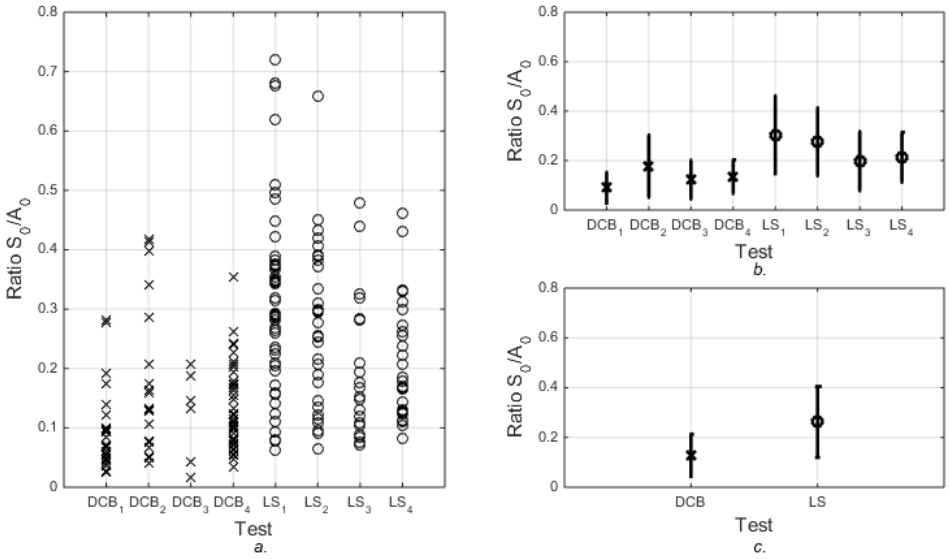

Figure 4.19: Results of Modal AE analysis. (a). S_0/A_0 ratio of each hit. (b). Mean and std.deviation of S_0/A_0 ratio for each specimen. (b). Mean and std.deviation of S_0/A_0 ratio for each test type

4.6 Discussion

It has been seen that, in this case, the fracture mode has had minimal impact on the frequency content of the resultant acoustic emission. This means that frequency-based parameters do not pose a suitable method for reliable discrimination between fracture-modes. It does, however, mean that frequency-based parameters can be utilised for other purposes, such as discrimination between failure mechanisms, regardless of the specimen loading orientation. While this may currently be of little use in the analysis of metal-to-metal adhesive joints, it is potentially significant for the analysis of composite joints in which frequency-based parameters are used to differentiate between failure modes such as fibre-breakage and matrix-cracking [48].

The WT-coefficient peak-ratios show that in both tests the A_0 mode is dominant and that there is significant overlap between the sets of results. There is also a clear trend indicating that the S_0 mode is generally greater in the Mode-II lap-shear tests than in the Mode-I DCB tests. This result appears to be in line with previous work, as Mode-I failure creates a clear out-of-plane source, very

similar to the delamination of composites, which has previously been shown to create a dominant A_0 component. The dominance of the A_0 mode in the lap-shear tests, despite the loading being applied in-plane, can be explained by two factors: Firstly, the principal stresses induced in the adhesive layer due to shear will not be directly in-plane, they will be located at approximately 45° to the plane, thus creating wave-modes which would be somewhere between those expected from in-plane and out-of-plane sources. Additionally, any failure occurring at the interface with the adhesive is occurring at the surface of the adherend rather than near the mid-plane, as can be the case for other in-plane sources previously investigated, such as fibre-failure or matrix cracking in composites. It has been previously demonstrated by Hamstad et al. [59] that while a signal generated by an in-plane source located on the mid-plane will be dominated by the symmetric mode, the same source, applied away from the mid-plane, can create a signal dominated by the asymmetric mode. This provides some explanation as to why both fracture-modes result in signals dominated by the asymmetric mode, despite the loading orientation. Additionally, a lap-shear test is technically not a pure Mode-II test. While the loading is predominantly in shear, bending of the adherends can result in a small Mode-I crack-opening component, making it Mixed-mode, and potentially contributing further to the generation of the A_0 mode.

As both fracture-modes have a significantly higher amplitude A_0 than S_0 mode, a suitably-chosen threshold can be used to consistently select the arrival time of the A_0 mode, without risk of accidental selection of the S_0 arrival time. If the Mode-II tests had resulted in a greater S_0 component, then a more sophisticated method would be necessary to select arrival times and calculate source-locations.

The results presented by Dzenis and Saunders [85], analysed using Vallen VisualClass, do clearly demonstrated the possibility of differentiation between fracture-modes using AE, but they provide little insight into the fundamental differences in the signals which allowed this differentiation. The results presented in this thesis indicate that it is likely that the difference in wave-modes excited during their tests will have been one of the significant factors contributing to the differentiation which was achieved, while other differences may have also occurred from features such as the specimen geometries causing variation in attenuation and reflections. An increased understanding of these factors which allow differentiation will be beneficial if attempts are made to utilise these techniques on full-scale structures, rather than small laboratory specimens, as any method used will need to suitably account for the dispersion, attenuation and reflection which will be present in larger structures with potentially irregular geometries.

The use of the WT peak ratio as a classifier to differentiate between fracture-modes may be feasible when considering multiple hits (i.e. an entire test), but due to significant variation between hits, and the overlap between tests, it would not be possible in most cases to identify fracture-mode based on a single hit. Future work should therefore consider either other variations of modal analysis which may yield clearer discrimination, or, combining this parameter with others to form a more robust method of discrimination. Differentiation between hits occurring from the adhesive failure and the cracking of the adhesive layer has not been attempted within this study, and it is recognised that results for each test may include hits from both of these failure mechanisms, which may exhibit different characteristics. Future work should address this issue by conducting tests capable of isolating each of these failure mechanisms to identify their defining AE characteristics.

4.7 Summary

In this chapter, Mode-I and Mode-II fracture tests of adhesive joints are conducted and the abilities of modal AE analysis to differentiate between the fracture-modes is investigated, along with some additional parameters. Geometrically-similar test specimens are prepared for double-cantilever-beam and lap-shear tests, and the tests are conducted with AE sensors fitted to the adherends. A signal-processing methodology is developed in which 1D time-difference-of-arrival type source-location (based on theA_0 mode) is used to estimate the source-locations and thus the propagation distances for each hit. The theoretical dispersion-curves for the adherends are then used to identify the S_0 and A_0 modes in the time-frequency-domain. The wavelet-transform coefficients corresponding to these two fundamental modes are then extracted, and the ratio between them assessed as a classifier of fracture-mode. The results are discussed and compared with other previously published methods of determining fracture-mode and other uses of modal AE analysis. The findings of this chapter are expanded on in Chapter 6 by the use of FEA to further investigate the relationship between fracture-mode and wave-mode.

Chapter 5

FEA of PLB tests

This chapter describes dynamic finite element simulations of PLB tests conducted on adhesively-bonded specimens. It details the development of the model, including geometry, materials, and boundary conditions, validation of the model against experimental results and theory, and the results of the simulation are presented and discussed.

5.1 Introduction

FEA modelling of AE provides a number of advantages over experimental work for certain types of investigation. Assuming a suitably accurate model can be developed, it offers the ability to isolate the effects of varying certain parameters, while holding others entirely constant in a manner not always possible in experiments. It also allows a much greater number of values for each variable to be investigated, without the associated cost of fabricating multiple test-specimens. Simulations were conducted in COMSOL Multiphysics ®, and the simulated AE results then exported to MATLAB for post-processing and analysis. While the majority of commercial FEA packages could have been used, COMSOL Multiphysics ® was chosen for this project based on a combination of availability and proven track-record within the field of AE modelling, having been used extensively by Sause et al. [109, 110, 112, 114, 116] amongst others [111].

In this section of work, a variety of different simulations have been carried out to further validate and augment the findings of the experimental work previously described. The first simulation carried out was a validation test, to ensure that the modelling process was providing results in suitable agreement with both the obtained experimental results and the theory. This was conducted as a simple PLB test on a small section of aluminium bar, allowing validation of the source and sensor models, and of the simulated wave-propagation.

PLB tests were then simulated on bonded specimens. In the experimental work it was established that the Lamb wave behaviour of the adherends of a bonded specimen approximately matched that of a single un-bonded adherend, but only one adhesive type and one adhesive thickness was tested. To provide further validation of this conclusion, and to ascertain the wider applicability of it, PLB tests have been simulated on specimens with varying adhesive Young's modulus and adhesive-layer thickness.

PLB tests on specimens featuring adhesive voids of varying sizes have also been conducted in an attempt to further explain the behaviour observed in the experimental work. The use of

simulations has allowed a much greater number of void sizes to be investigated and has allowed far greater control over the void size and shape, which can be difficult top control in experimental work.

5.2 Geometry

Simulated PLB tests have been conducted on 3D geometries which have been set up to simulate the behaviour of infinitely large sheets, i.e. removing the effects of edge-reflections, and thus simplifying analysis, while using the smallest model possible to reduce computational time. 3D simulations, as opposed to more computationally efficient 2D simulations, were chosen as they allow the source and sensor geometries to be modelled in a more realistic manner as finite 2D regions of the top adherend's upper surface, as opposed to simply points or lines of infinite depth. Use of a 3D simulation also allows for spreading of the wave-front in three dimensions, which, for a finite-area source like a PLB, forms a critical part of the signal's attenuation.

The specimens modelled consisted of two 1 mm thick rectangular aluminium sheets, separated by a 0.5 mm (unless otherwise stated) adhesive layer. The length of the specimens modelled is 120 mm, chosen to allow 100 mm source-sensor propagation distance, while maintaining some clearance between the sensor locations and the end of the specimen. The specimen width is 5 mm, chosen to fit the 4 mm radius of the chosen sensors, with 1 mm clearance from the edge. Symmetry has been applied to both the end and the side which the source is located on, giving quarter-symmetry. The opposing end and side utilise low-reflecting boundaries, thus removing edge-reflections and approximating the behaviour of an infinitely large sheet. Cylindrical (Semi-cylindrical) domains passing through the entire specimen thickness have been defined to give surfaces for application of the source and sensors. 10 sensor regions were utilised, evenly spaced from 10 mm to 100 mm from the source. The sensor regions had a diameter of 8 mm (corresponding to the contact area of a PAC Micro-80D sensor), and the source region a diameter of 0.5 mm (the diameter of a pencil lead). The geometry used for the majority of the tests is shown in Figure 5.1, with the dimensions illustrated in Figure 5.2. A simplified single-adherend model with a single sensor was also used for early stage validation tests; aside from only being a single 1 mm aluminium layer, all other dimensions and parameters used were the same as described.

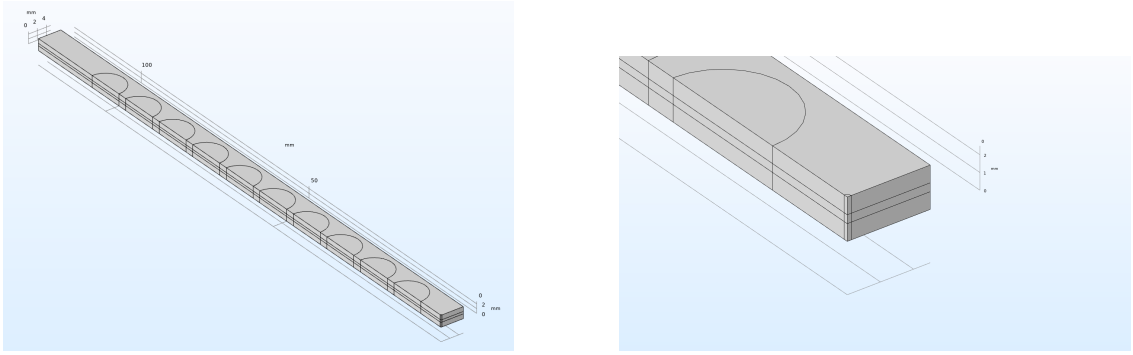

(a) (b)

Figure 5.1: Geometry used for PLB simulation (a) Whole geometry (b) Source

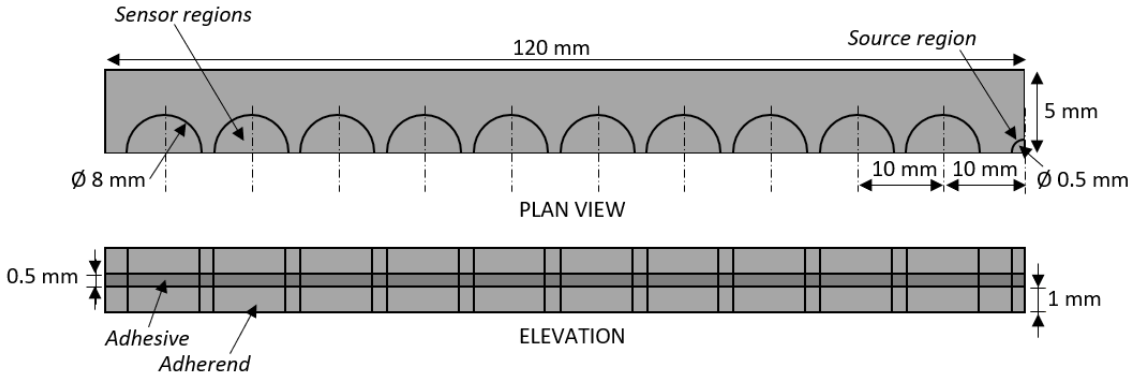

Figure 5.2: PLB Model Dimensions (Not to scale)

5.3 Materials

The material properties used for the simulations (unless otherwise specified) are summarised in Table 5.1 below, and correspond to 1050A H14 Aluminium for the adherends and Loctite® EA3430 for the adhesive. While Young's modulus, density and Poisson's Ratio are readily available from supplier data-sheets, the viscoelastic properties of adhesives are not readily available. As the process of determining them experimentally is time consuming and of significant complexity [142], it was deemed to be outwith the scope of this project. The approach chosen was therefore to select values used in literature for similar materials, and then to adjust these to match the simulation results to the experimental results as closely as possible. The values used therefore do not give a fully-accurate representation of the adhesives' viscoelastic behaviour, but do provide a usable approximation of their characteristics.

Table 5.1: Simulation Material Properties

	Adherends	Adhesive [143]
Young's modulus	69 GPa	3.21 GPa
Density	2700 kg/m^3	1140 kg/m^3
Poisson's Ratio	0.33	0.3

Table 5.2: Adhesive Material Viscoelastic Properties

	Shear modulus	Relaxation Time
Generalised Maxwell Model - Branch 1	2 GPa	50 s
Generalised Maxwell Model - Branch 2	2 GPa	$2e^{-9}s$

5.4 Boundary Conditions and Load Steps

The PLB simulations utilise a three-step approach to simulation. The first step is a static simulation, in which the maximum load of the PLB is applied. This is equivalent to the relatively slow loading of the pencil lead, leading up to the break. During this step the lower surface of the specimen is fixed, analogous to support from the work surface on which experiments were conducted.

The second step is a dynamic simulation in which the load of the PLB is rapidly released over 1 μs, resulting in the propagation of elastic waves. Throughout this short step the lower surface of the specimen remains fixed, to prevent rigid-body motion.

In the third step, from 1 μs to 100 μs, the constraint on the lower surface is removed and the specimen is free for wave-propagation to occur. Interaction between the specimens and the surface on which they are placed has been excluded from the simulation as the use of a contact model in this type of simulation would be computationally expensive to the point of being prohibitive.

As previously mentioned, the bottom surface of the specimens was fixed throughout the application of the static and dynamic PLB loads, and was then free for the remainder of the simulation to allow wave-propagation. The upper surface of the specimens was free throughout all stages of the simulation, with the exception of the source area, to which the source load was applied in the first two steps. For all specimens, half-symmetry was used, meaning that symmetry was applied to the edge representing the specimen centre-line. In the case of quarter-symmetry being used, symmetry conditions were also applied to the end of the specimen at which the source was applied. The two sides furthest from the source used low-reflecting boundaries to remove edge-reflections and provide the behaviour of a semi-infinite specimen.

Time steps of 0.01 μs were utilised throughout the dynamic steps, chosen to ensure that the Courant-Friedrichs-Lewy (CFL) stability condition is met. This condition requires the time steps to be shorter than the time taken for the highest velocity wave to cross an element.

Table 5.3: Boundary Conditions and Load Steps

	Step 1	Step 2	Step 3
Type	Static	Dynamic	Dynamic
Time	N/A	0 s to 1 μs	1 μs to 100 μs
Time Step Size	N/A	0.01 μs	0.01 μs
Source	Static Load -3 N (see 5.5)	Dynamic Load -3 N to 0 N (see 5.5)	Free
Top Surface	Free	Free	Free
Bottom Surface	Fixed	Fixed	Free
End (Source)	Symmetry	Symmetry	Symmetry
End (Far)	Symmetry	Symmetry	Symmetry
Side (Source)	Low-Reflecting	Low-Reflecting	Low-Reflecting
Side (Far)	Low-Reflecting	Low-Reflecting	Low-Reflecting
Sensors	Free	Free	Free

5.5 Source

As previously mentioned, the out-of-plane PLB source is applied over two steps; a static step of maximum load and a dynamic unloading step. It should be noted that a variety of previous articles [104–106] have applied the PLB as a sudden application of load, when it is in fact a slow application of load and then a sudden release of load. The properties of the source are based on the findings of Sause's experimental investigation of PLBs as AE sources [112]. Based on these findings, a maximum load of 3 N has been selected (-3 N due to downward direction), with an unloading time of 1μs, following the temporal dependency illustrated below in Figure 5.3. The

load is applied to a circular area of diameter 0.5 mm, corresponding to the diameter of the pencil lead. Due to the use of symmetry only a semi-circle or quarter-circle is actually modelled and the load amplitude is divided accordingly. It is noted that the use of a circle of the same diameter as the pencil lead is a simplifying assumption, as the profile of the pencil lead tip will vary depending on the nature of the previous break, the angle of application and any deformation of the lead tip prior to fracture.

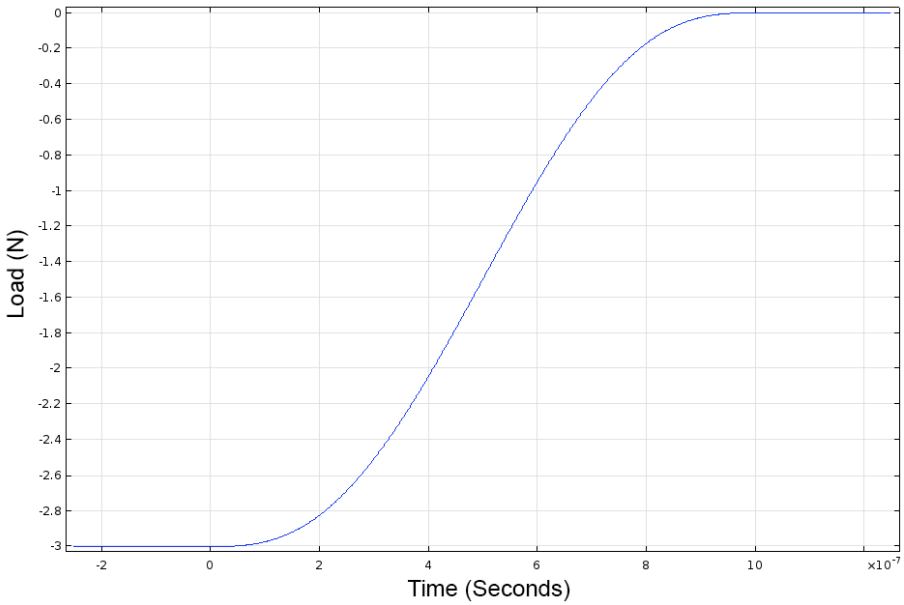

Figure 5.3: PLB source unloading curve

5.6 Sensor

Sensors have been implemented as circular (semi-circular due to symmetry) regions on the surfaces of the adherends which have been assigned as Boundary Probes, recording the mean normal-velocity (out-of-plane) over the probe area. It should be noted that some previous studies [104–106, 111] have utilised displacement, rather than velocity, as the output of their simulations, but it is indicated by Ono et al. [125] that many sensors respond primarily to velocity, rather than displacement. Velocity has been used in some previous simulation work such as that by Sause et al. [109] and Ghouri et al. [119]. The probe areas are 8 mm in diameter, corresponding to the contact area of a Physical Acoustics Micro-80D sensor, as used in the experimental work, and are located every 10 mm from 10 mm to 100 mm from the source-end of the specimen. Perfect contact between the sensor and the adherend is assumed, with the effects of the grease couplant being neglected. Any effect of the mass of the sensor has also been neglected from the simulation. To account for the limited frequency response of the real sensors and the filtering provided by the pre-amplifiers, the signals were post-processed in MATLAB, as described in a subsequent section.

5.7 Mesh

The mesh utilised for all simulations was a free triangular mesh on the upper surface of the specimens, swept through the depth of the specimens to create prism-type elements, as illustrated in Figure 5.4. The default Quadratic-Serendipity (2nd Order) type discretisation was used. The use of a second-order method provides improved accuracy over first order methods, as second-order elements feature mid-side nodes, as well as the corner nodes seen in first order elements, allowing them to better represent deformation and curvature. The use of Serendipity elements, which do not feature a central node, over Lagrangian elements, which do, provides a more computationally-efficient solution with comparable accuracy [144]. Mesh sizing was chosen based on the minimum wavelength of interest, and by use of a mesh-convergence study. The shortest wavelength of interest has been calculated as 4.97 mm, resulting from propagation of the S_0 mode at a frequency of 1 MHz. Thus to capture all wave-modes and frequencies of interest the largest element-size used must be less than 4.97 mm. A mesh-convergence study was used to identify a suitable element-size. The parameters considered for convergence were the AE parameters of energy, amplitude, arrival-time, peak frequency, frequency centroid and weighted peak frequency. Mesh-convergence was investigated in a single 1 mm adherend and over a reduced time-frame of 80 μs for the sake of computational efficiency due to the long run time. The mesh sizes used, and the corresponding number of elements for a single adherend model are shown in 5.4. While the 5 mm mesh was known to be inappropriate, it was included to establish the potential effects of inadequate meshing. The results of the convergence study are illustrated in Figure 5.5.The peak frequency remains constant throughout all element-sizes, while frequency centroid and weighted peak frequency increase with refinement of the mesh, converging at an element-size of 1 mm. The arrival time of the A_0 mode increases with mesh refinement and converges with the theoretical arrival time by an element-size of 0.75 mm. Peak amplitude and energy also both increase with refinement of the mesh, with peak amplitude converging at 0.75 mm and energy at 1 mm. A maximum element-size of 0.75 mm was selected, with elements decreasing in size towards the source. A minimum of four elements was maintained through the thickness of each section of the specimens when the adhesive thickness was varied. The selected mesh size is in a similar region to the sizes used in previous similar studies, such as the 0.5 mm maximum mesh size used by Sause & Horn [109] or 0.4 mm mesh used by Le Gall et al. [60].

Table 5.4: Mesh sizes used in convergence study. Corresponding No. of elements listed for a single adherend

Max. Mesh Size	No. of Elements
5 mm	177
2.5 mm	351
1 mm	3,144
0.75 mm	8,151
0.5 mm	23696

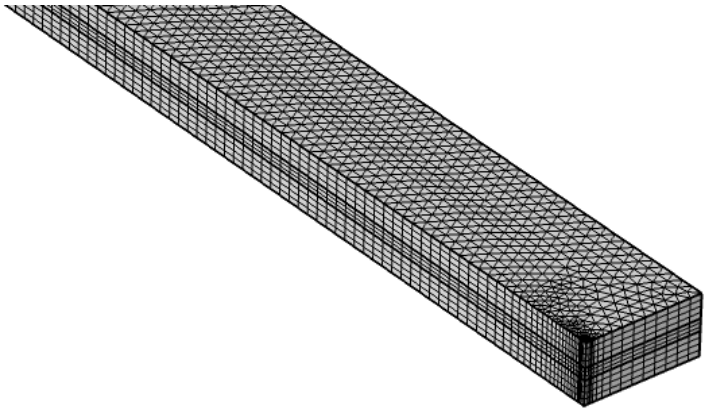

Figure 5.4: Swept triangular mesh

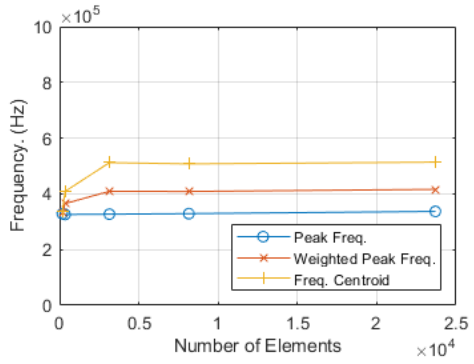

(a) Peak, Weighted Peak & Frequency Centroid convergence

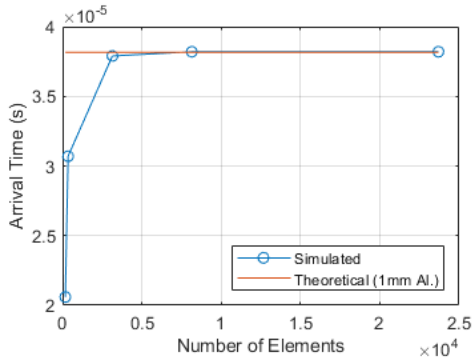

(b) A_0 Arrival Time convergence (Calculated at 325 kHz)

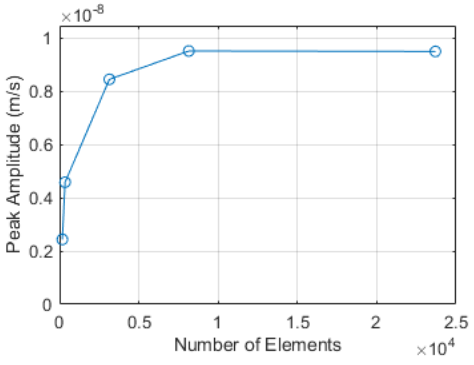

(c) Peak Amplitude convergence

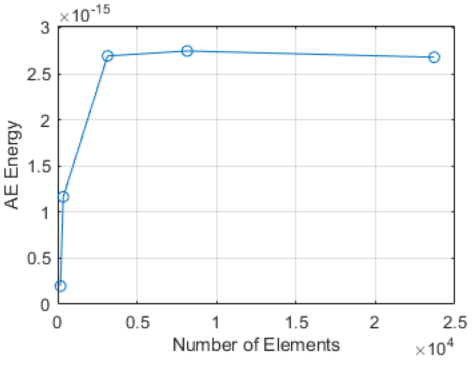

(d) AE Energy convergence

Figure 5.5: Mesh Convergence in terms of (a) Peak Frequency and Weighted Peak Frequency (b) Arrival Time of the A_0 mode at 325 kHz (c) Peak Amplitude (d) AE Energy

5.8 Solver

All of the simulation steps, both static and dynamic, were computed using COMSOL's default MUMPS (MUltifrontal Massively Parallel Sparse) type direct solver. The use of a direct solver, over an iterative solver, provides a more robust solution for a well-conditioned model, though is more memory intensive. The MUMPS solver is particularly advantageous over some other direct-type solvers due to its ability to utilise out-of-core memory, essentially offloading RAM requirements onto the hard-drive in order to solve models which would otherwise be unsolvable with the available RAM.

5.9 Post-processing

Simulated AE signals were recorded throughout the simulation using surface-domain probes, which averaged the z-direction (normal) velocity over the sensor-surface area. The effective sampling rate of these probes is the same as the rate of time-steps taken in the simulation, the time-steps of $1e^{-8}$ s therefore giving an effective sampling rate of 100 MHz. The simulated signals were re-sampled in MATLAB to 10 MHz to improve computational efficiency. This also brings the sampling rate into the range of what is possible with most AE systems. It should however be noted that this is still higher than the sampling rates of 2 MHz or 2.5 MHz which were used in the experimental work throughout this project. The simulated signals were then filtered using an arbitrary-magnitude filter which was designed to replicate the frequency sensitivity of the PAC Micro-80D sensors used in the experimental work. The sensitivity plot for the AE sensor used (taken from the calibration certificate) and the magnitude response of the arbitrary-magnitude filter are both shown below in Figure 5.6. An additional 20 kHz high-pass filter was then used to replicate the high-pass filter included within the pre-amplifier in the experimental set-up. While these adjustments to the simulated results do not include all factors contributing to the recorded signal, such as sensor coupling, electrical noise etc, they do account for the most significant modifiers of the recorded signal and serve to bring the simulated signal much closer to what is recorded experimentally.

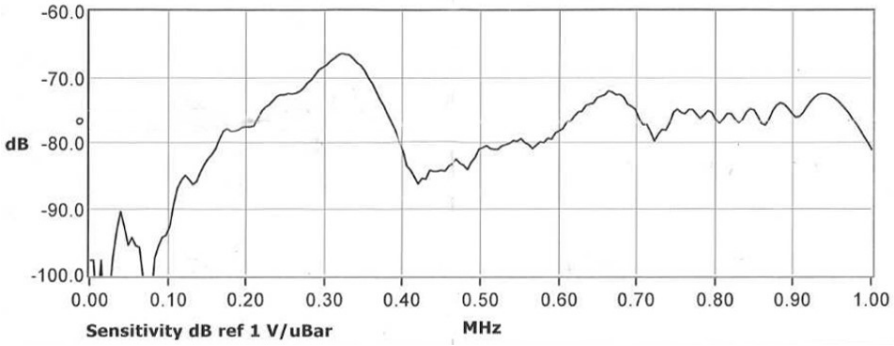

(a) Physical Acoustics Micro 80-D AE sensor response

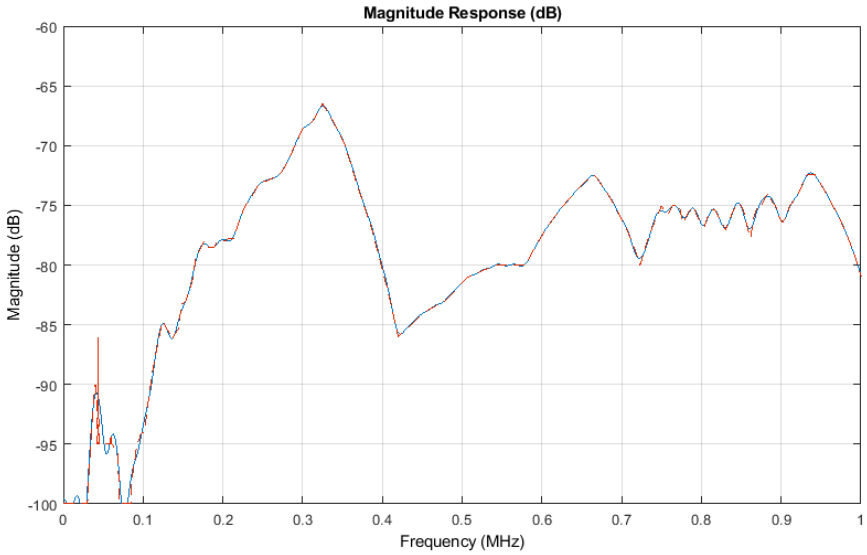

(b) Arbitrary-magnitude filter response

Figure 5.6: Comparison of (a) Physical Acoustics Micro 80-D AE sensor response (from calibration certificate) and (b) magnitude response of implemented arbitrary-magnitude filter

5.10 Effects of Adhesive Properties

From the experimental work conducted in this project using PLBs on adhesively-bonded specimens, some conclusions have been drawn about the effects of adhesive layers on the transmission of AE. For reasons of practicality, the range of adhesive properties and adhesive thicknesses were restricted. The following simulations have therefore been conducted to establish the potential effects of the adhesive properties on these findings and thus verify the generalisability or limitations of the experimental findings.

5.10.1 Effects of Adhesive Young's Modulus

In the experimental work conducted in this project, Loctite® EA9461 2-Part Epoxy Adhesive was used for the PLB test specimens. There are however a large variety of different adhesive types that can be used. To establish whether the findings of the experimental work are applicable to other types of adhesive, and to study the differences that may be induced by the use of other types of adhesive, the effects of varying the Young's modulus of the adhesive layer has been studied. Five adhesives, which span a significant range of potential Young's moduli, have been chosen for investigation and their properties (as per manufacturers data-sheet) are shown in Table 5.5. While there is also some variation in the density of the selected adhesives, it was chosen to keep density consistent for all simulations and only vary Young's modulus, as the variation in Young's modulus between adhesives is highly significant, while variation in densities is minimal. As well as providing an understanding of the effects of different adhesives, the variation in Young's modulus is also representative of variation in curing.

Table 5.5: Adhesive Young's Moduli Simulated

Young's modulus (E)	Comments
4.4 GPa	E value for Loctite® EA9480 2-Part Epoxy Adhesive [145]
3.21 GPa	E value for Loctite® EA3430 2-Part Epoxy Adhesive [143]
2.757 GPa	E value for Loctite® EA9461 2-Part Epoxy Adhesive [145]
1.87 GPa	E value for Loctite® 3090 Cyanoacrylate Adhesive [6]
0.515 GPa	E value for Loctite® 3090 Cyanoacrylate Adhesive [6]

5.10.2 Effects of Adhesive Thickness

Adhesive thickness will vary based on the application, the adhesive used, and the control of the bonding process. In some cases, the exact adhesive thickness will be uncontrolled and the thickness may vary. It is therefore important to establish the effects of adhesive thickness on AE propagation and whether measures need to be taken to account for variation in adhesive thickness during AE testing. Adhesive thicknesses of 0.2 mm, 0.5 mm, 0.75 mm, 1 mm, 1.5 mm and 2 mm have been simulated. This range is sufficient to identify the general effects of variation in adhesive thickness, but is by no means the full range of potential adhesive thicknesses in real life. The range simulated was limited by the following factors. Thicknesses over 2 mm were not simulated due to the increased computational expense and the lack of RAM available to complete the simulations. Thicknesses under 0.2 mm were not considered, as adequate meshing of the thin bond-line, without the generation of poor quality high-aspect-ratio elements, would also be too computationally expensive for the available computer.

5.11 Effects of Adhesive Defects

It was demonstrated in Chapter 3 that void-type adhesive defects will affect AE propagation, and can be detected, and their size estimated, by use of an AE system with a PLB source. However, due to the arduous process of specimen preparation only 2 defect sizes and defect-free reference specimens were tested. In this section, the tests carried out have been simulated, and a number of

further defect sizes have also been investigated. The defect sizes simulated are: 0 mm (defect-free reference), 0.1 mm, 1 mm, 2.5 mm, 5 mm, 7.5 mm, 10 mm, 20 mm, 30 mm, 40 mm. The defects were modelled as rectangular voids the full depth of the adhesive layer and the full thickness of the specimen. This differs from the voids which were investigated experimentally, as these were of finite width. The experimental results were therefore subject to edge-reflections which did not pass through the defect region. These unaffected reflections will not exist in the simulated results. It should be noted that the simulated voids are perfectly rectangular, which is not truly representative of the nature of real-life voids. Real voids, typically existing due to inadequate adhesive volume or to trapped air, are likely to feature filleted edges, based on the nature of the surface wetting of the adhesive. The model may therefore not provide an accurate representation of the local wave interaction at the ends of the voids, and thus for small defects, but should provide a reasonable approximation of the global behaviour for larger defects.

5.12 FEA Results

5.12.1 Model Validation

In order to validate the main features of the model, such as the source, sensor and boundary conditions, an initial model of a single 1 mm thick aluminium adherend was created, and the simulated results were compared with experimentally-obtained data. Initial validation using a single adherend, as opposed to a bonded joint, was chosen for the following reasons; reduced computational expense due to smaller size, no dependency on the approximated values for the viscoelastic properties of the adhesive, and direct comparison with theoretical dispersion-curves is possible. The experimental results come from a sensor placed at the middle of a 500 mm x 500 mm sheet, with a source located 100 mm from the sensor. The simulated results are designed to approximate the effects of a sheet of infinite dimensions by the use of symmetry and low-reflecting boundaries.

Figures 5.7 and 5.8 illustrate the propagation of the waves throughout the specimen, in terms of out-of-plane velocity. These plots can be utilised to confirm the correct function of the boundary conditions. It can be seen that the application of the PLB source results in a quarter-circle wave-front propagating away from the source. The quarter-circle profile, free from distortion, confirms the function of the symmetry conditions applied to the two edges of the specimen adjacent to the source. It can also be seen in Figure 5.7b, 5.7c and 5.7d, that upon reaching the edge of the modelled specimen, there are no reflections propagating back across the modelled region. The lack of reflections thus makes the small modelled volume analogous to a sheet of infinite width. Inspection of the later times illustrated in Figure 5.8 also reveals the same behaviour from the low-reflecting boundary at the end of the specimen, making it analogous to a specimen of infinite length. It is noted, however, that the use of a low-reflecting boundary does cause a slight reduction in amplitude close to the boundary, which is not physically realistic for an infinite specimen. The effect of this has been minimised by ensuring the sensors are not located along this edge of the specimen, and are thus less affected. While this feature may be a disadvantage to the use of low-reflecting boundaries, the ability to avoid the interference of edge-reflections and to approximate the behaviour of a large specimen without having to model the entire specimen, or resort to a 2D model, make this a worthwhile compromise for this study.

The time, frequency and time-frequency-domain results are presented in Figure 5.9 for the ex-

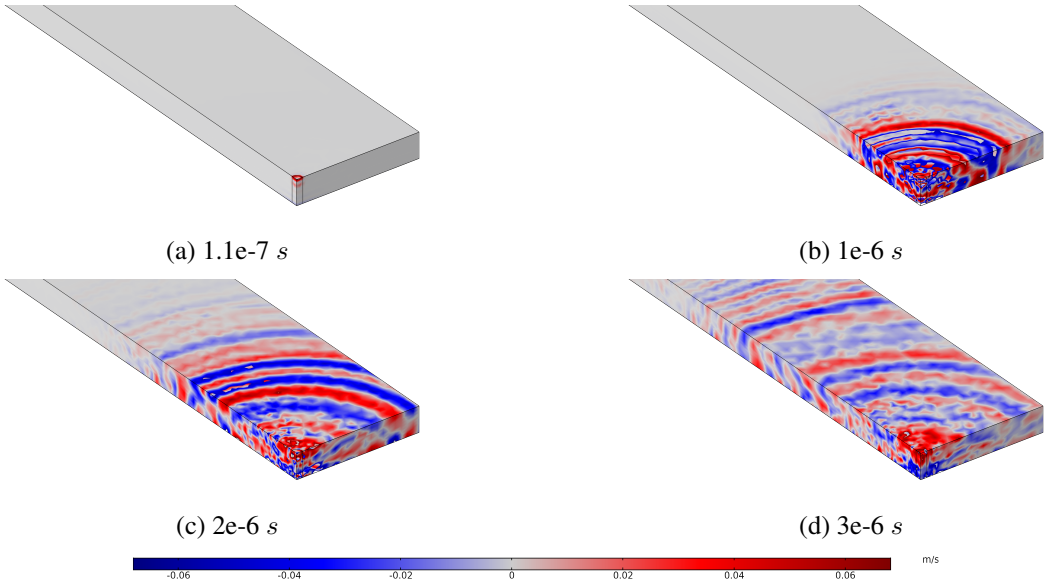

(a) 1.1e-7 s (b) 1e-6 s

(c) 2e-6 s (d) 3e-6 s

Figure 5.7: Early stages of wave-propagation in the source vicinity in a single $1mm$ aluminium adherend from an out-of-plane PLB source

perimental and simulated results. Figure 5.9a shows the experimental results, Figure 5.9b shows the simulated results subjected to re-sampling to 10 MHz, but without any frequency filtering. Figure 5.9c illustrates the simulated results after the application of a 20 kHz high-pass filter, representative of the pre-amplifier, and an arbitrary-response filter constructed to match the frequency response of the sensor, as described in Section 5.9. The WT plots for each result have been overlaid with the theoretical Lamb wave dispersion-curves for a 1 mm thick aluminium sheet, allowing the results to be validated against theory, as well as against the experimental results.

In terms of the wave-modes excited by the source, and their dispersion, the simulation gives a very good representation of both the theory and the experimental data. There is a clear arrival of the low amplitude S_0 mode, seen in the time-domain, which aligns perfectly with the theoretical arrival time indicated by the dispersion-curves. There is then a high amplitude A_0 mode, which can be seen in both the time- and time-frequency-domain plots. The arrival time of the A_0 mode is in line with the theoretical dispersion-curve across the full frequency-range for which the mode is present. Detailed inspection of the unfiltered time-domain signal, as shown in Figure 5.10 confirms the nature of the modes present. It can be seen that in Figure 5.10a, the top and bottom surface velocities at the sensor are 180° out-of-phase, implying expansion and contraction of the specimen thickness, as is expected in the S_0 mode. Figure 5.10b illustrates a later section of the signal in which it can be observed that the surface velocities are in-phase, indicating a flexural mode, as would be expected for the A_0 mode. It can therefore be concluded that the model is capable of simulating the dispersion of Lamb waves with reasonable accuracy. Subsequent to the arrival of the A_0 mode there is a continued period of activity in the 200 kHz to 400 kHz band seen in the experimental result. While this is captured to some extent in the simulations, visible in the form of a low-amplitude peak in the filtered results, it is to a much lower extent.

In terms of frequency content, the unfiltered simulated signal is dominated by very low frequency content which is below the usable range of the sensor and the pre-amplifier. In the mid to high frequency region there is a relatively uniform level of content, whereas in the experimental

signal, the higher frequency content is limited due again to the frequency response of the sensor, and potentially by other additional factors. The introduction of high-pass and arbitrary-magnitude filters results in a simulated signal much more similar to that seen experimentally. In both cases, the frequency response is dominated by the peak frequency of the sensor at around 307 kHz. The simulated signal features a higher level of high frequency content than the experimental signal, featuring a peak at around 700 kHz, whereas the frequency spectra of the experimental signal decays smoothly with increasing frequency. Below the peak frequency, both the experimental and simulated signals feature another peak; however, the simulation underestimates the level of low-frequency content when compared to the experiment. Overall, the filtered simulation results present the correct peak frequency but slightly underestimate the low frequency content and slightly overestimate the high frequency content. As the filters used have been designed to match the characteristics of the pre-amplifier and the sensor used in the experiment as closely as possible, it is expected that the differences may occur due to factors which have not been accounted for in the model. While further investigation would be needed to confirm these suggestions, it is proposed that the layer of silicone grease, used as a couplant for the sensor, may result in some loss of high frequency content. Additionally, the mass of the sensor and the tape used to secure it will result in some level of resonance which is not included in the model, but may contribute to the increased level low-frequency content.

While the results of the model are not perfectly comparable with experimental data, the model does provide a good approximation of the AE behaviour and is deemed to be suitable for a comparative study of the effects of the variables described in the prior section.

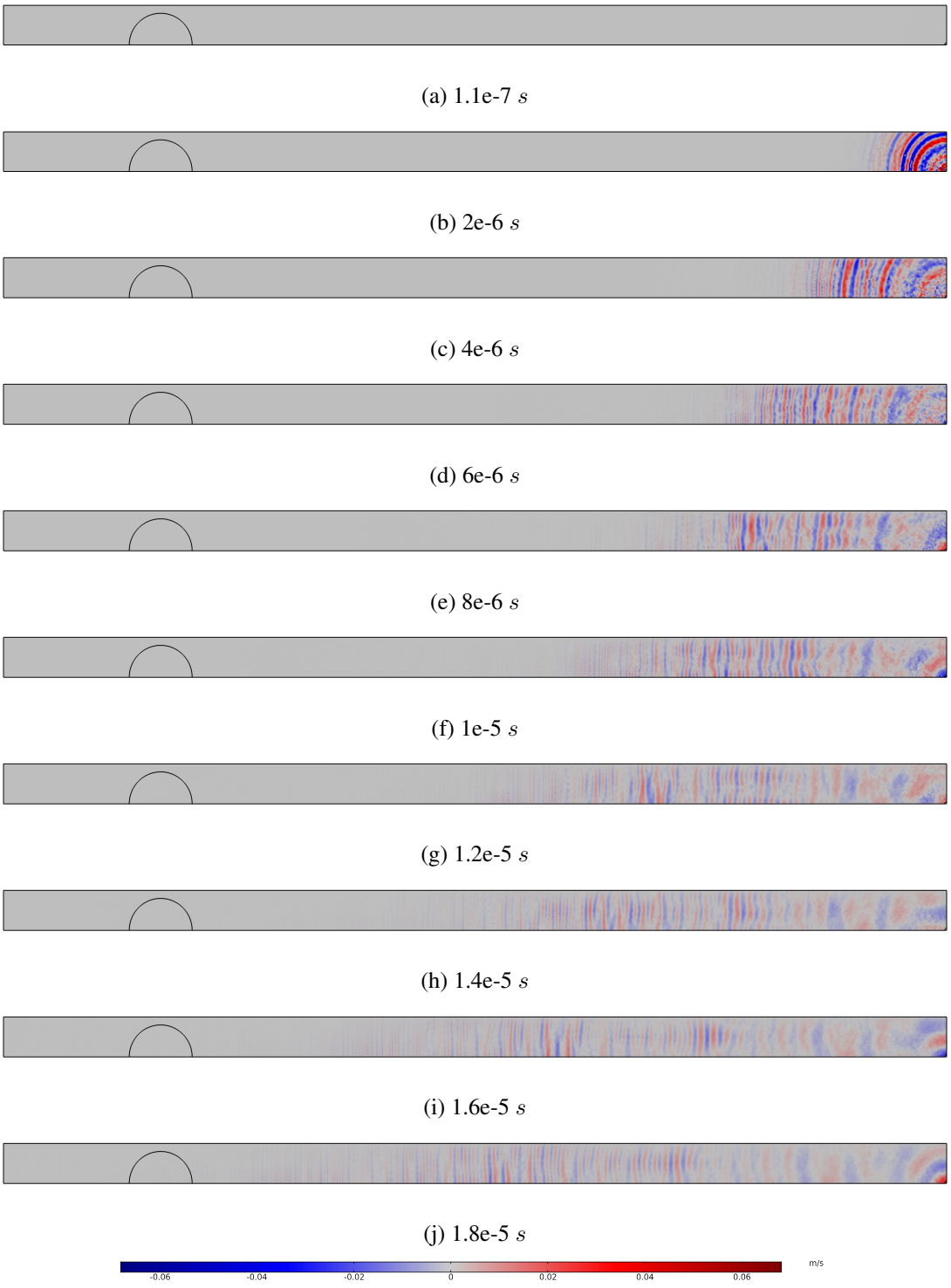

(a) 1.1e-7 s

(b) 2e-6 s

(c) 4e-6 s

(d) 6e-6 s

(e) 8e-6 s

(f) 1e-5 s

(g) 1.2e-5 s

(h) 1.4e-5 s

(i) 1.6e-5 s

(j) 1.8e-5 s

Figure 5.8: wave-propagation in a single $1mm$ aluminium adherend from an out-of-plane PLB source

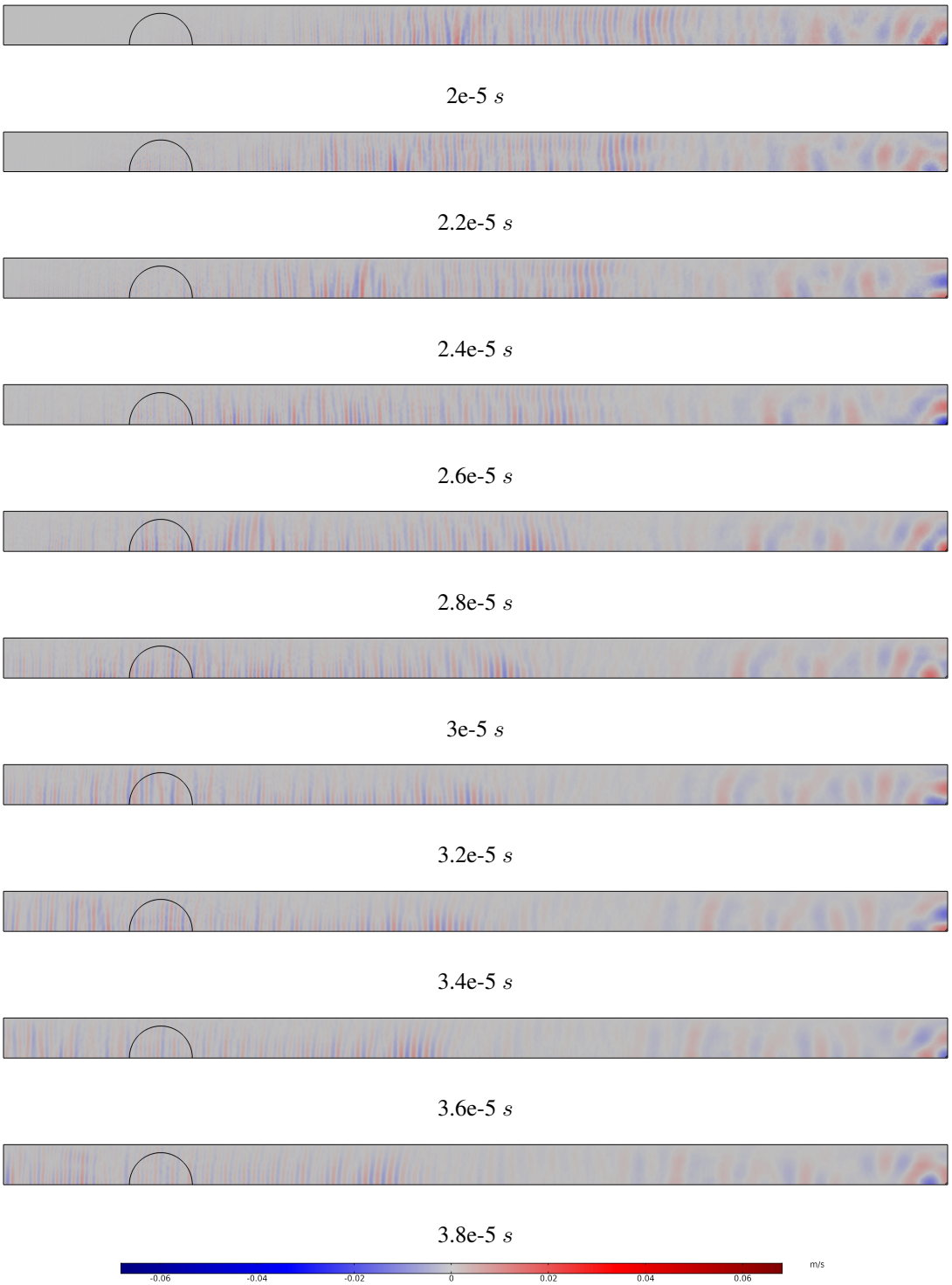

Figure 5.8: (contd.) Wave-propagation in a single $1mm$ aluminium adherend from an out-of-plane PLB source

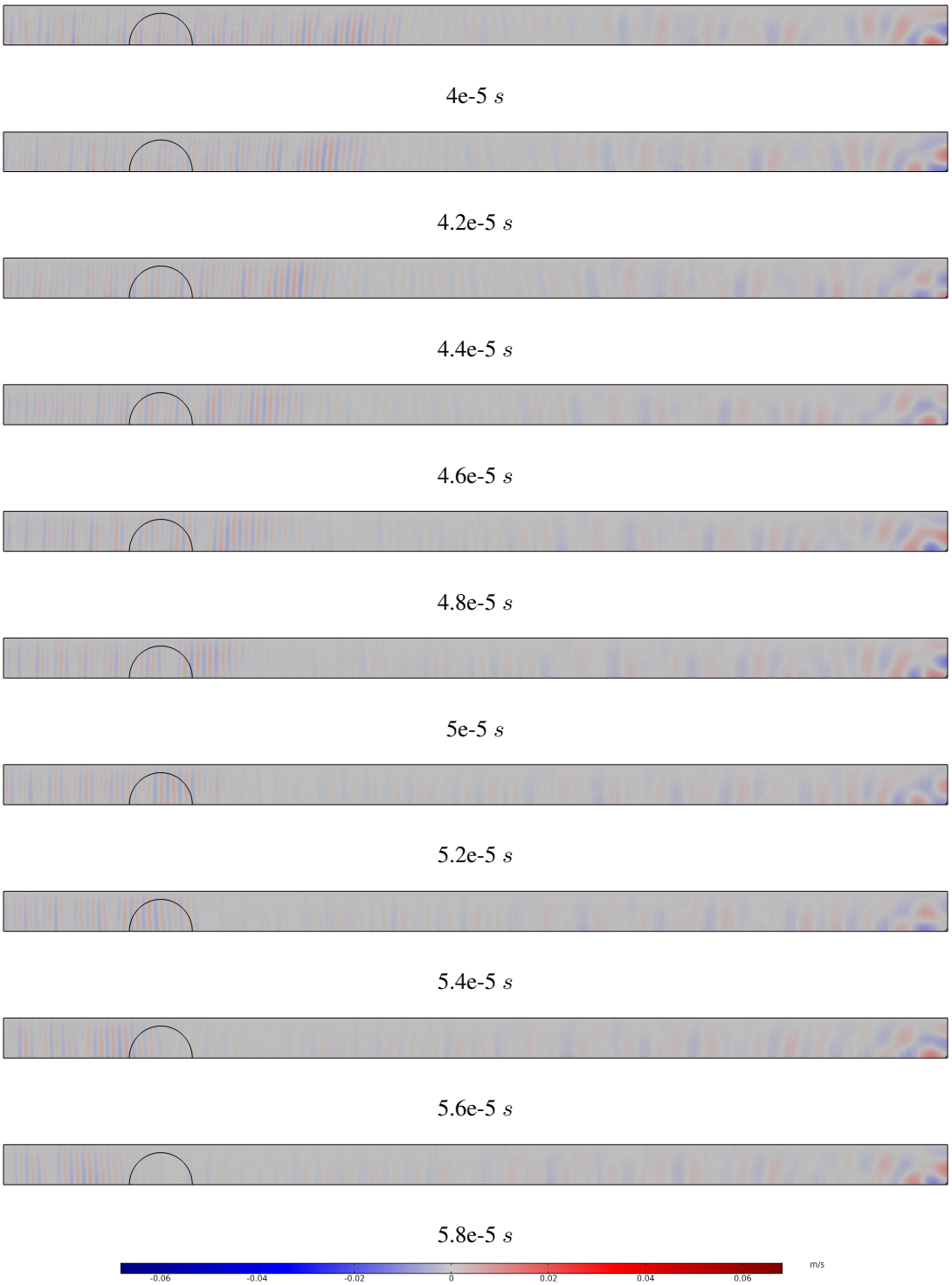

Figure 5.8: (contd.) Wave-propagation in a single $1mm$ aluminium adherend from an out-of-plane PLB source

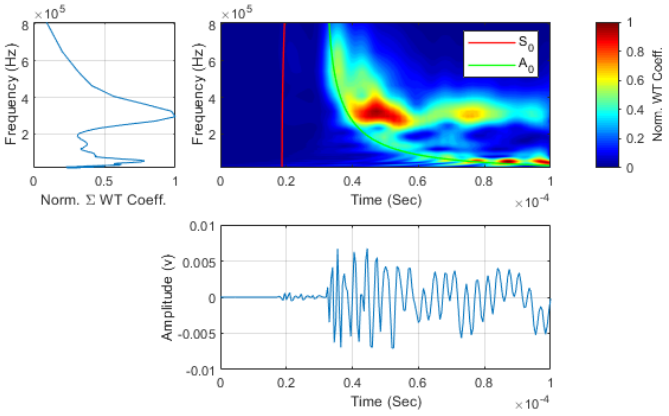

(a) Experimental result

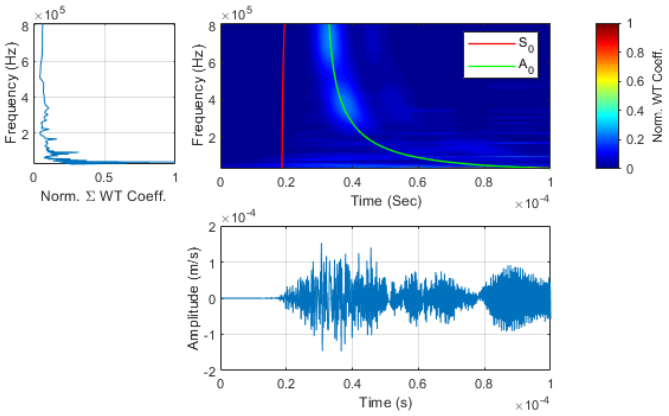

(b) Simulated result (Unfiltered)

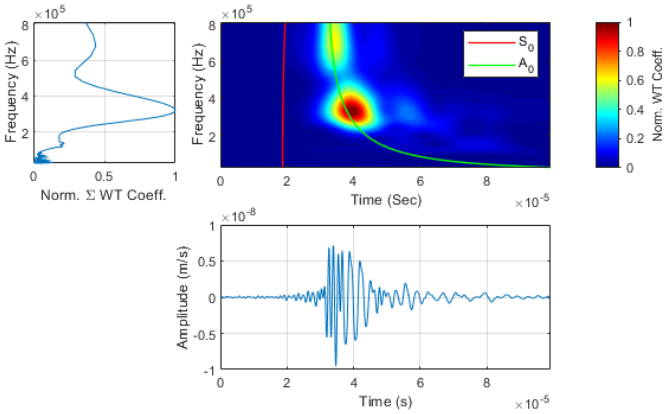

(c) Simulated result (Filtered)

Figure 5.9: Comparison between an experimentally-obtained signal and simulated signals in Time-Domain, Frequency-Domain and Time-Frequency-Domain. Out-of-plane source on a single 1 mm adherend, 100 mm source-sensor distance

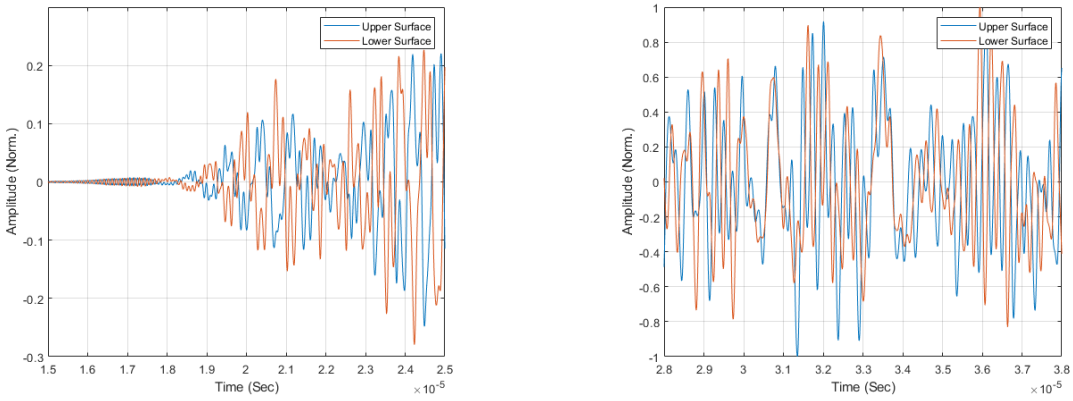

(a) S_0 mode dominant region

(b) A_0 mode dominant region

Figure 5.10: Detail views of unfiltered time-domain signal for an out-of-plane source on a single $1mm$ adherend. 100 mm source-sensor distance. (a) Detail of S_0 mode dominant region (b) Detail of A_0 mode dominant region

5.12.2 Effects of Adhesive Young's Modulus

Variation in the Young's modulus of the adhesive has been investigated, as this can be representative of the differences between different adhesives which may be used, and may also be representative of different stages of adhesive cure. The range of values simulated between 0.515 GPa and 4.4 GPa correspond to published properties for various 2-Part Epoxy and Cyanoacrylate adhesives. In all instances the adhesive density has been kept constant at 1140 Kg/m^3.

Figure 5.11 contains the WT plots and associated time- and frequency-domain plots for the sensor located on the upper surface (source-side) 100 mm from the source. It can be observed that, as would be expected for an out-of-plane source, the energy is largely carried in the primary A_0 wave in all cases. The arrival times of the A_0 wave are relatively close to those predicted theoretically for a single 1 mm adherend, but do vary with varying Young's moduli. Figure 5.12c illustrates the arrival times of the A_0 wave, taken at a frequency of 325 kHz. It can be seen that the significantly lower Young's moduli of the adhesive, compared to the adherends, results in a lower wave-velocity in the bonded specimen than would be found in a single adherend. The slowest wave-propagation is found in the adhesive of the lowest Young's moduli, with properties based on Loctite® 3090 Cyanoacrylate adhesive. This results in a wave-velocity 7.4% slower than predicted for a single adherend. The fastest-propagating wave occurs in the Loctite® EA9480 2-part epoxy adhesive, with the resultant wave-propagation in the bonded specimen only 4.8% slower than that predicted for a single adherend.

The simulated signals span a broad frequency-range, much like those acquired experimentally, with a high energy region in the 300 kHz to 500 kHz range in most signals, corresponding to the peak frequency of the simulated sensor. With increasing Young's modulus there is a significant reduction in low-to-mid frequency content, that below approximately 500 kHz, and an increase in high-frequency content. This can be seen in the WT and frequency plots in Figure 5.11, and is also summarised in the plots of PSD, peak, weighted peak and frequency centroid, included as Figures 5.12a and 5.12b. Investigation of the peak, weighted peak and frequency centroid reveals that over the range of moduli simulated, the peak frequency increases slightly from 332 kHz to 342 kHz, representing a change of around 3% over this range. Frequency centroid however better reflects the loss of low frequency content, increasing from 334 kHz to 446 kHz, an increase of 33%. Weighted Peak Frequency, being a product of both peak frequency and frequency centroid, also shows an increase, from 333 kHz to 392 kHz, an increase of around 15%.

As illustrated in Figure 5.12d the Peak Amplitude shows an approximately linear decay with increasing Young's moduli, reducing from $3e^{-8}$ m/s to $2.1e^{-8}$ m/s over the range of moduli simulated, a reduction of 30%. AE Energy follows an exponential decay, with respect to increasing Young's moduli, from a maximum of $3.87e^{-14}$ down to $1.33e^{-14}$, a reduction of approximately 66%. The signal attenuation has also been investigated and is plotted for both Peak Amplitude and Energy in Figure 5.13. Both parameters exhibit logarithmic decay, as would be expected for attenuation curves, from a propagation distance of 20 mm onwards. Prior to this, between 10 mm and 20 mm, there is some variation in the trend with some simulations exhibiting increases in amplitude and energy, while others exhibit decreases. This behaviour can be attributed to this being the early stages of wave-propagation, in which the wave field is not yet established. Considering the region from 20 mm onwards, it can be seen that the level of attenuation is dependent on the Young's moduli of the adhesive, with specimens with the lowest Young's moduli exhibiting the steepest attenuation.

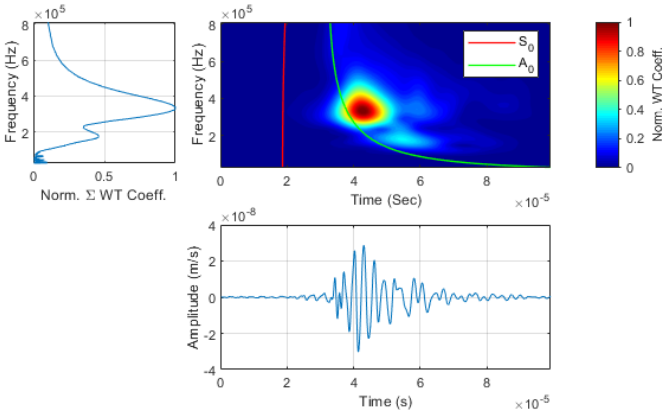

(a) 0.515 GPa Adhesive Young's modulus

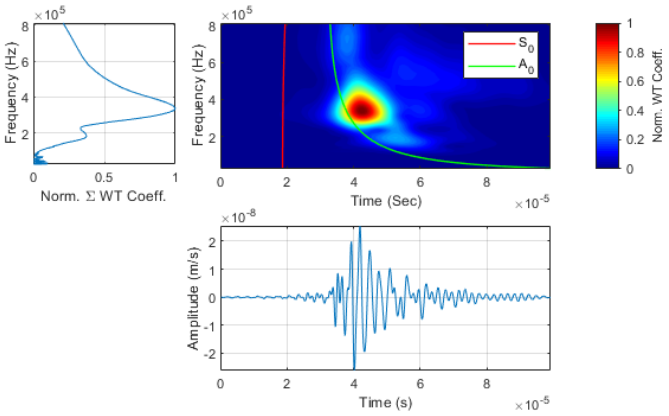

(b) 1.87 GPa Adhesive Young's modulus

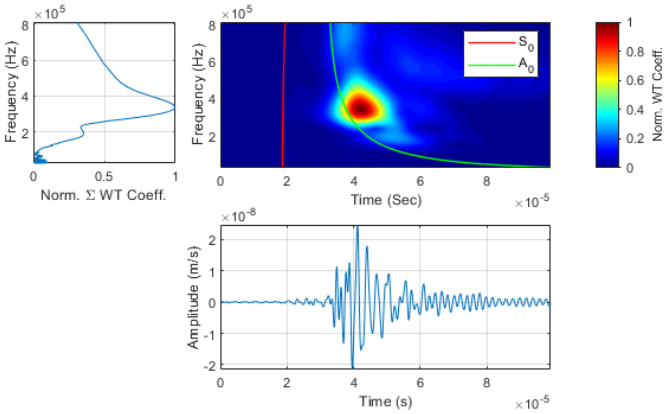

(c) 2.757 GPa Adhesive Young's modulus

Figure 5.11: Time-Domain, Frequency-Domain and Time-Frequency-Domain plots for results of an out-of-plane source on a bonded specimen of 1 mm adherend thickness, 0.5 mm adhesive thickness, 100 mm source-sensor distance, with adhesive Young's modulus values of (a) 0.515 GPa, (b) 1.87 GPa, (c) 2.757 GPa, (d) 3.21 GPa, (e) 4.4 GPa.

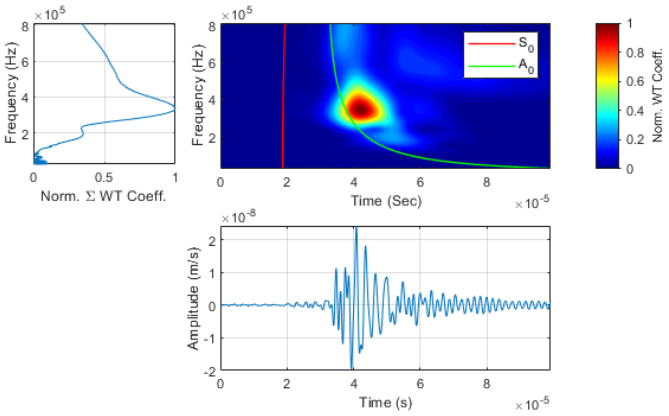

(d) 3.21 GPa Adhesive Young's modulus

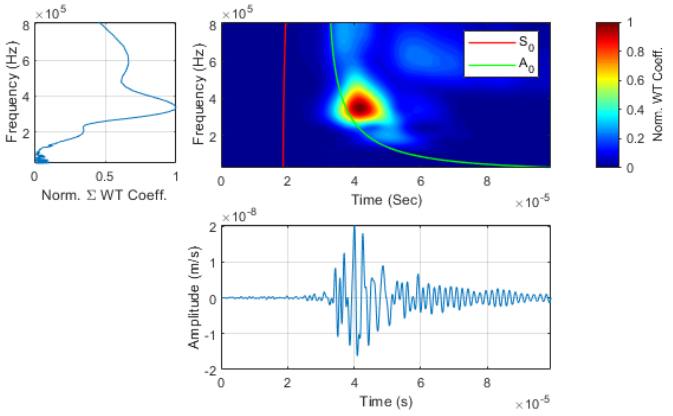

(e) 4.4 GPa Adhesive Young's modulus

Figure 5.11: Time-Domain, Frequency-Domain and Time-Frequency-Domain plots for results of an out-of-plane source on a bonded specimen of 1 mm adherend thickness, 0.5 mm adhesive thickness, 100 mm source-sensor distance, with adhesive Young's modulus values of (a) 0.515 GPa, (b) 1.87 GPa, (c) 2.757 GPa, (d) 3.21 GPa, (e) 4.4 GPa.

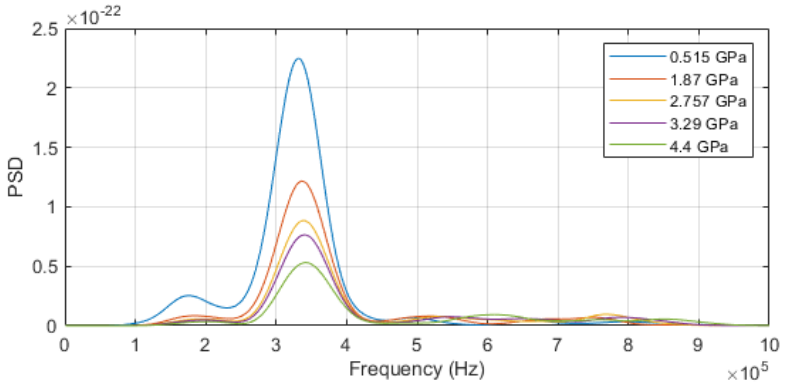

(a) PSD

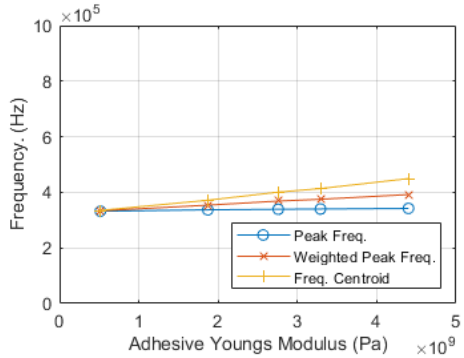

(b) Peak & Weighted Peak Frequency

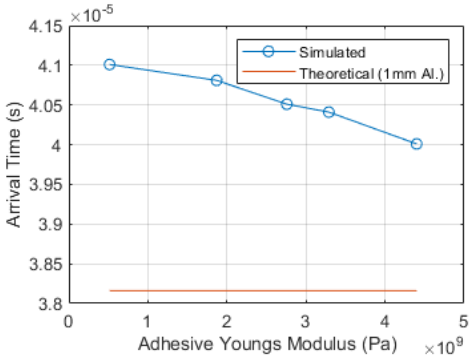

(c) A_0 Arrival Times (325 kHz)

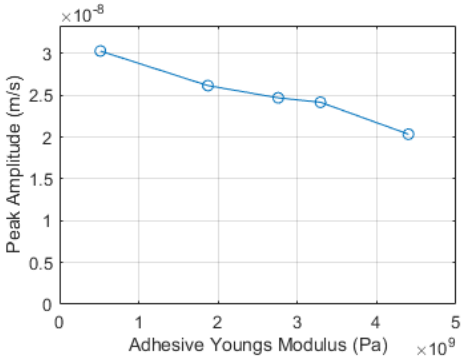

(d) Peak Amplitudes

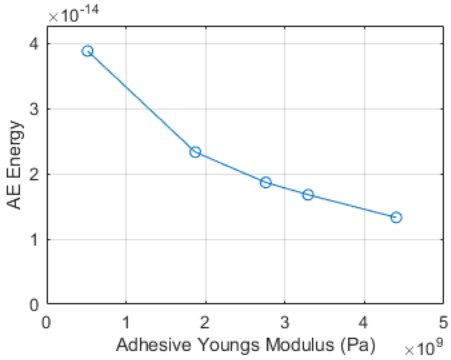

(e) AE Energy

Figure 5.12: Effects of Adhesive Young's modulus in terms of (a) Power Spectral Density (b) Peak Frequency and Weighted Peak Frequency (c) Arrival Time of the A_0 mode at 325 kHz (d) Peak Amplitude (e) AE Energy

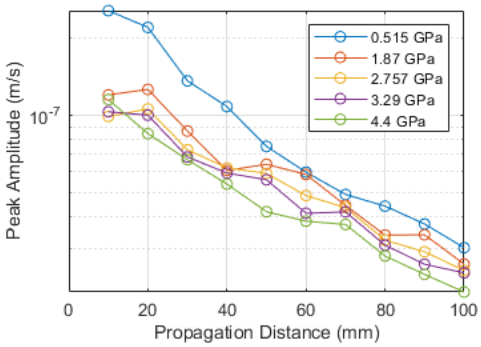

(a) Variation in Peak Amplitude with Propagation Distance

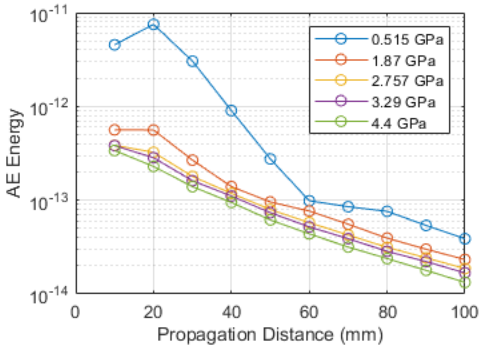

(b) Variation in AE Energy with Propagation Distance

Figure 5.13: Effects of Adhesive Young's modulus at varying Propagation Distances (a) Peak Amplitude (b) AE Energy

5.12.3 Effects of Adhesive Thickness

The effects of adhesive-layer thickness have been investigated as this is a feature which will vary between applications, but can also vary within a single joint, either due to deliberate design or due to lack of control of the bonding process. It is therefore valuable to gain an understanding of how variations in adhesive thickness can affect AE propagation.

Inspection of the WT, time-domain and frequency-domain plots included in Figure 5.14 reveals that throughout the range of thicknesses tested (0.2 mm to 2 mm), the majority of the energy is carried in the primary A_0 wave-mode, and shows a relatively close fit to the theoretical A_0 mode of a single adherend. Closer inspection of the wave arrival times, as per Figure 5.15c, indicates that while the arrival times can be roughly approximated as those of a single adherend, the presence of an adhesive layer and second adherend does reduce the effective wave-velocity. Increasing thickness of the adhesive layer leads to logarithmic increase in the recorded A_0 arrival time over the range of thicknesses simulated. At an adhesive thickness of 0.2 mm the arrival time is 1.17% later than that predicted for a single adherend. This increases up to 10% for an adhesive thickness of 1.5 mm, but shows no further increase for an adhesive thickness of 2 mm. Due to computational limitations, greater thicknesses could not be simulated. Based on the observed trend, it is expected that further increases in thickness would yield little change to the wave velocities and arrival times. The reduction in propagation velocity with increasing overall thickness is contrary to what would be expected of a solid linear-elastic specimen, so the reduced velocity can therefore be attributed to the material properties of the adhesive. Due to the significantly lower Young's modulus, wave-propagation in the adhesive (when considered as a standalone component) will be much slower than in the aluminium adherends.

The peak amplitude and AE energy both exhibit initial increases with increasing adhesive thickness, up to 1 mm, followed by a reduction with any further increases in thickness. The decreasing amplitude and energy for higher thicknesses can be attributed to the increased volume of the specimens, and therefore the increased geometric attenuation due to spreading of the wave-front. The initial increase in energy and amplitude is due to the nature of the PLB source which has been simulated. The source has been defined as a set force, as would be required to break a pencil lead. Increasing the thickness of the adhesive layer has the effect of also increasing the initial displacement achieved where the source is applied. This then translates to higher peak amplitude and and higher energy, despite the increased attenuation. The steeper attenuation in the thicker adhesive layers is illustrated in Figure 5.16, which illustrates the variation of both peak amplitude and energy with respect to the propagation distance.

Increasing adhesive thickness is also seen to affect the frequency spectra. The frequency spectra are illustrated individually for each simulated thickness in Figure 5.14 a-f, and cumulatively in 5.15a. The frequency parameters of peak frequency, frequency centroid and weighted peak frequency are shown in 5.15b. It can be observed that the viscoelastic nature of the adhesive results in higher attenuation of high-frequency components than of lower-frequency components. Increased adhesive thickness therefore leads to decreased high-frequency content. This is well summarised by the frequency centroid and weighted peak frequency plots which shown an exponential decay towards the peak frequency, which remains essentially constant throughout all thicknesses simulated. The constant peak frequency is partly due to the parameters of the source and specimen, but is largely determined by the frequency response of the sensor, which has been included in the post-processing of the simulated results.

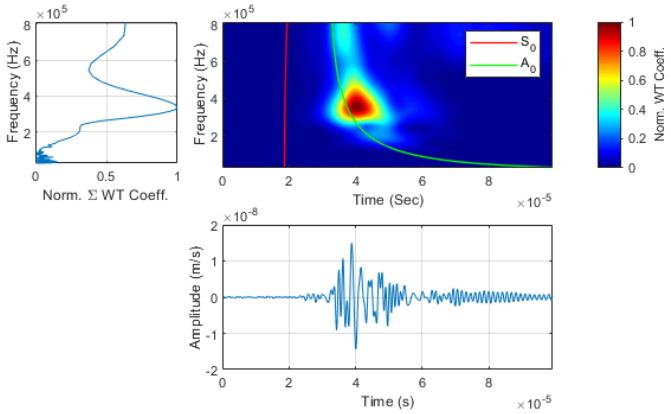

(a) 0.2 mm Adhesive Thickness

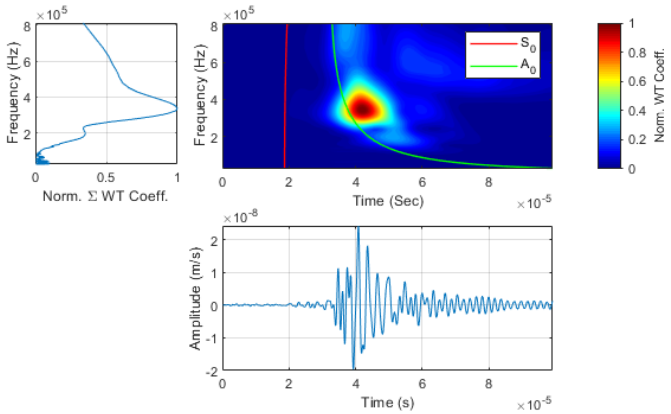

(b) 0.5 mm Adhesive Thickness

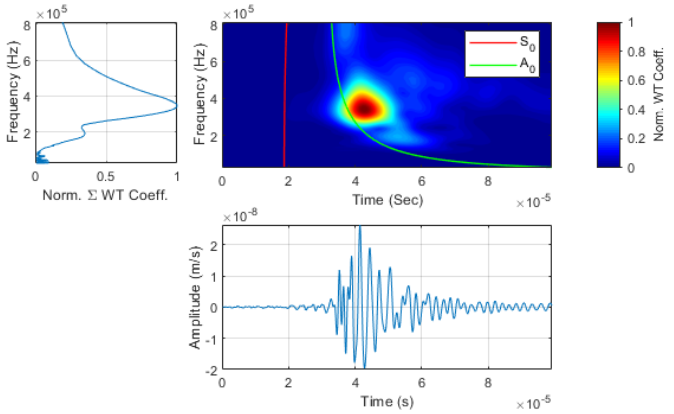

(c) 0.75 mm Adhesive Thickness

Figure 5.14: Time-Domain, Frequency-Domain and Time-Frequency-Domain plots for results of an out-of-plane source on a bonded specimen of 1 mm adherend thickness, 100 mm source-sensor distance, with adhesive thicknesses of (a) 0.2 mm, (b) 0.5 mm, (c) 0.75 mm, (d) 1 mm, (e) 1.5 mm, (f) 2 mm

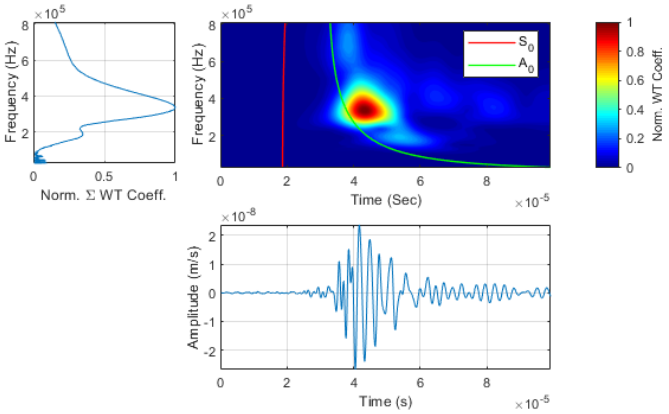

(d) 1 mm Adhesive Thickness

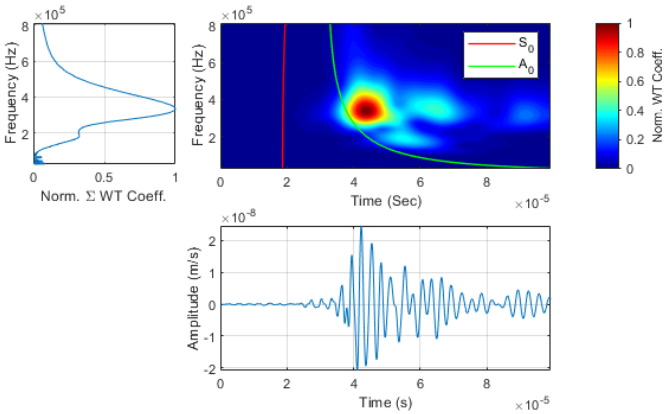

(e) 1.5 mm Adhesive Thickness

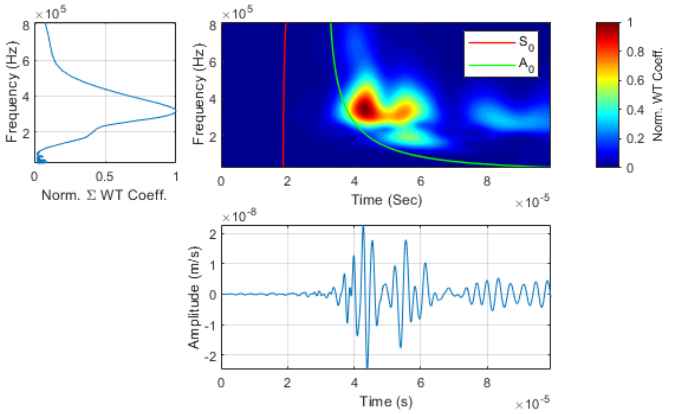

(f) 2 mm Adhesive Thickness

Figure 5.14: (contd.) Time-Domain, Frequency-Domain and Time-Frequency-Domain plots for results of an out-of-plane source on a bonded specimen of 1 mm adherend thickness, 100 mm source-sensor distance, with adhesive thicknesses of (a) 0.2 mm, (b) 0.5 mm, (c) 0.75 mm, (d) 1 mm, (e) 1.5 mm, (f) 2 mm

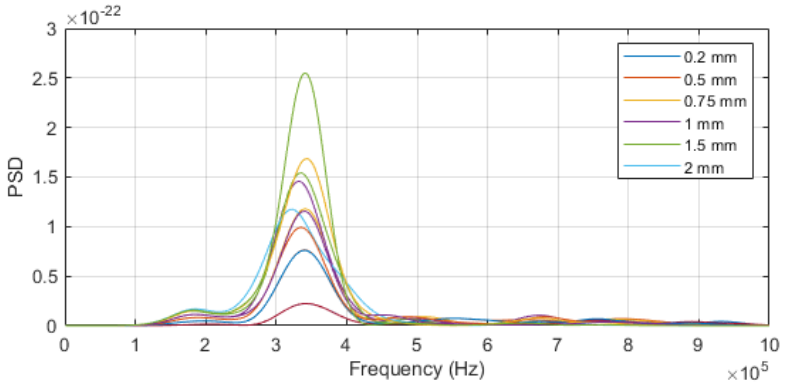

(a) PSD

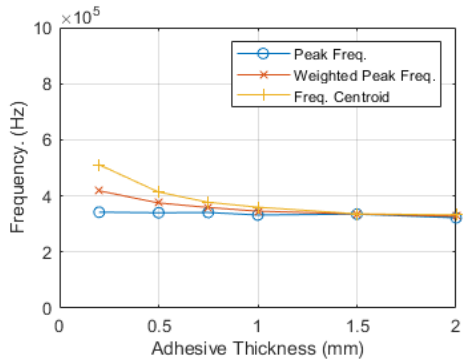

(b) Peak, Weighted Peak & Frequency Centroid

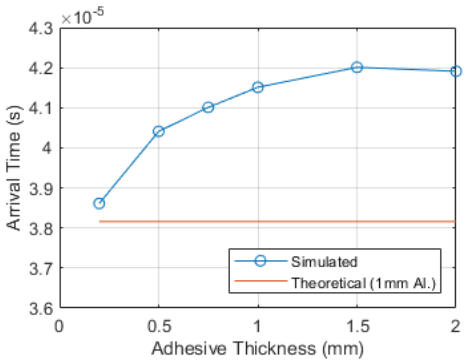

(c) A_0 Arrival Times (325 kHz)

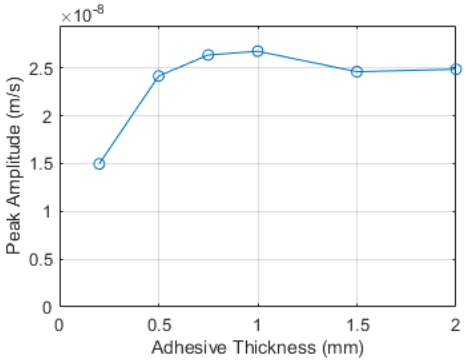

(d) Peak Amplitudes

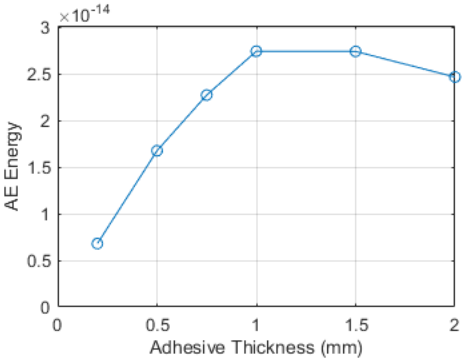

(e) AE Energy

Figure 5.15: Effects of Adhesive Thickness in terms of (a) Power Spectral Density (b) Peak Frequency, Weighted Peak Frequency and Frequency Centroid (c) Arrival Time of the A_0 mode at 325 kHz (d) Peak Amplitude (e) AE Energy

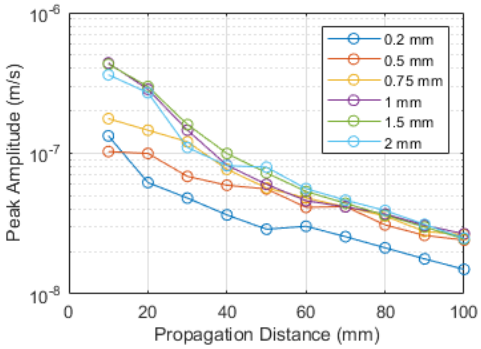

(a) Variation in Peak Amplitude with Propagation Distance

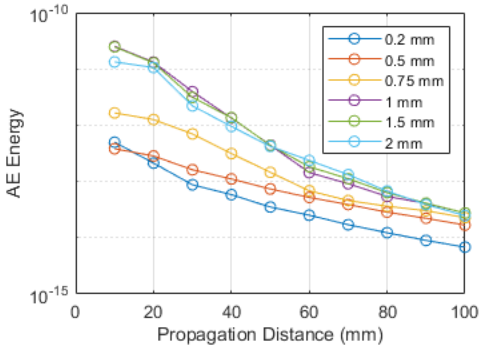

(b) Variation in AE Energy with Propagation Distance

Figure 5.16: Effects of Adhesive Thickness at varying Propagation Distances (a) Peak Amplitude (b) AE Energy

5.12.4 Effects of Adhesive Defects

The effects of the inclusion of void-type defects of different sizes has been simulated, and results compared with a defect-free specimen.

Investigation of the time- and time-frequency-domain plots, presented as Figure 5.17, illustrates that, as would be expected with an out-of-plane source applied to a sheet-type specimen, the signal is dominated by the A_0 mode, with a low amplitude S_0 appearing beforehand. The dispersion of the waves matches well with the theoretical predictions for a single aluminium adherend, as illustrated by the correspondence to the overlaid dispersion-curves in the WT plots. The introduction of void-type defects appears to have little effect on the wave-modes propagating, with no sign of the introduction or loss of any modes. Investigation of the arrival times of the A_0 component at 325 kHz, as illustrated in Figure 5.18c, reveals that as previously noted in Section 5.12.3 the presence of the adhesive layer does reduce the velocity of the A_0 wave compared to that of an un-bonded adherend (illustrated as the theoretical arrival time in Figure 5.18c). In general, increasing the void size, and thus the proportion of the wave-propagation path which is a single un-bonded adherend, results in an arrival time tending closer to that of a single adherend, implying that the wave-velocity across the defect area is higher than that in the bonded section of the specimen. While this is the clear trend across the defect sizes from 7.5 mm to 40 mm, there is some deviation from this between the 0 mm (defect-free) specimen and the 7.5 mm specimen, with a local minima at 2.5 mm. Currently the reason for this local anomaly is unknown, and further investigation is necessary.

In terms of frequency content, there is very little difference induced by the presence of the defects. The experimental results described in Chapter 3 illustrated an increase in low frequency content with increasing void size. This, however, is not observed in the results of the simulation, with the peak, weighted peak, and frequency centroid all remaining approximately constant across all void sizes, as shown in Figure 5.18b. Investigation of the PSD plot (Figure 5.18a) also shows little difference in the frequency spectra induced by the voids.

In terms of energy and peak amplitude, there is a general trend of increasing amplitude and energy with increasing void size, particularly over the larger void sizes. There is, however, an initial drop in both parameters as the void size increases up to 2.5 mm, followed by a localised peak at 7.5 mm. The overall increasing trend, seen in the larger void sizes, is in line with the experimental findings and can be easily explained by the reduced attenuation across the void region due to the lack of adhesive. For large defects this is expected to be the dominant factor in any variation in AE energy. The other mechanism which is expected to cause variation in these factors is reflection or diffraction of the wave at the start of the void. Based on this mechanism, it could be expected that the presence of a void of any length would result in an increase in energy on the source-side of the defect, as the wave is reflected back, and a corresponding decrease in energy on the opposite side of the void. The assumption of this type of behaviour would explain an initial decrease in energy between the defect-free specimen and the smallest void (0.1 mm), but does not fully explain the further decrease in energy seen in the two subsequent void sizes. It also does not explain the increase in energy then seen in the 5 mm and 7.5 mm voids. The reflection and diffraction of the waves in the adhesive layer at the ends of the void is supported by the analysis of the AE energy over the whole length of the specimen. Figure 5.19b illustrates the AE energy at sensors spaced every 10 mm from the source, for all void sizes. The defect-free specimen follows a typical trend of exponential decay, as would be expected due to geometric and material-based attenuation. The specimens featuring voids all follow the same basic trend, with some deviation in

energy over their length, but more interestingly with localised peaks which align with the ends of the voids. That is to say that the sensors located over the ends of the void register higher levels of energy than the sensors on either side of them. This is particularly clear in the 20 mm and 40 mm void specimens, where the sensors at 40 mm and 60 mm, and 30 mm and 70 mm respectively, are centred on the ends of the voids. In the cases in which the end of the void does not align directly under a sensor, the sensors either side of the void see a relative increase in energy, but to a much lower level than that which is seen when the sensors are aligned over the ends of the void. It is therefore proposed that the reflection, refraction and wave-interference occurring at either end of the void results in a localised increase in AE energy. It is noted that this may not be fully representative of real adhesive specimens. The simulation models the ends of the voids as perfect, flat, right-angled faces. The reality is however that the faces of the void are likely to be concave, if the void is formed by bubbles/trapped air, or convex, if it is caused by insufficient quantities of adhesive. Additionally, the surfaces are not likely be uniform or symmetrical. It is likely that including these effects may produce significantly different results in terms of localised wave behaviour around the edges of the voids. Capturing the effects of void shape is outwith the scope of this study, and is likely to be outwith the capabilities of the available equipment, as a significant mesh refinement would be needed around the defects to accurately capture the void shape, and an accompanying reduction in time-step would also be necessary to satisfy the CFL stability condition.

It is concluded that the current model provides a reasonable approximation of the global behaviour of a specimen with large defects, and is capable of capturing the reduced attenuation which was observed experimentally, but may be insufficient to accurately capture the wave interaction with the ends of the void region and may thus be insufficient for the investigation of small defects where geometric and material-based attenuation are not of highest concern.

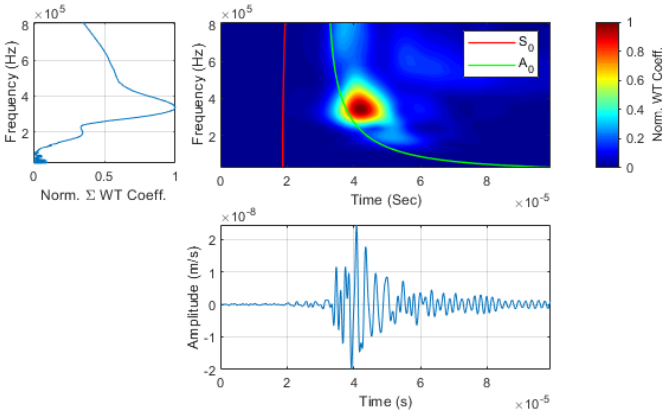

(a) No Void

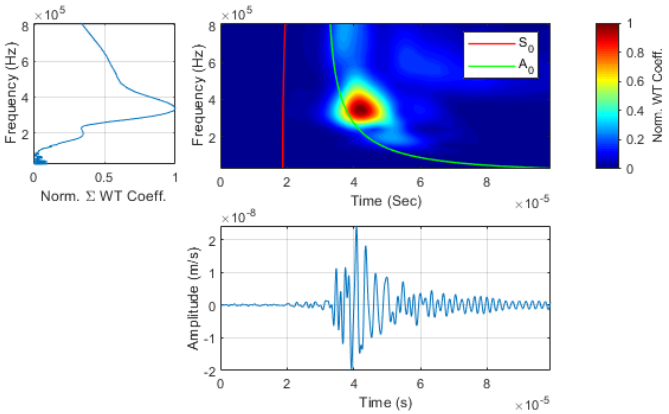

(b) 0.1 mm Void

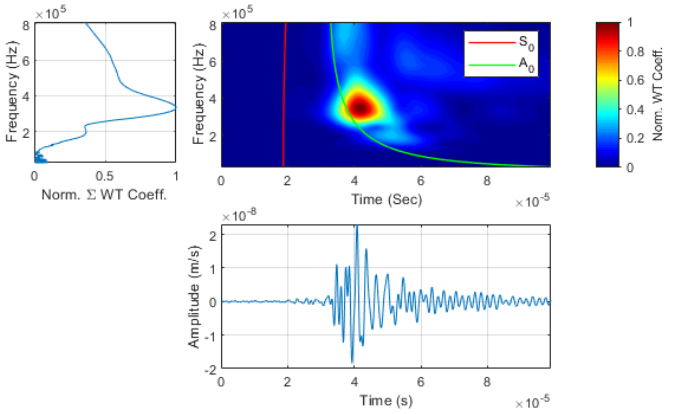

(c) 1 mm Void

Figure 5.17: Time-Domain, Frequency-Domain and Time-Frequency-Domain plots for results of an out-of-plane source on a bonded specimen of 1 mm adherend thickness, 0.5 mm adhesive thickness and 100 mm source-sensor distance, with adhesive void sizes of (a) No Void, (b) 0.1 mm, (c) 1 mm, (d) 2.5 mm, (e) 5 mm, (f) 7.5 mm, (g) 10 mm, (h) 20 mm, (i) 30 mm, (j) 40 mm

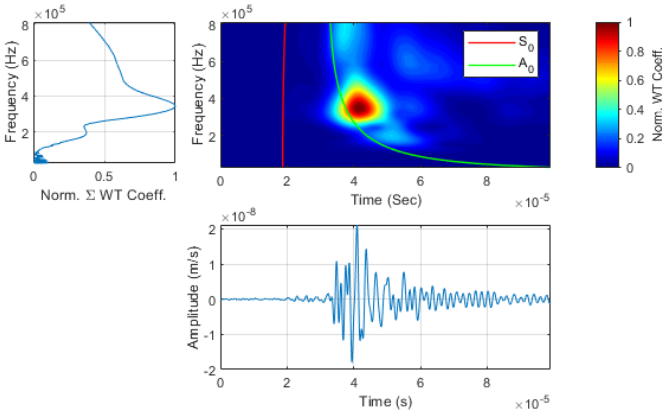

(d) 2.5 mm Void

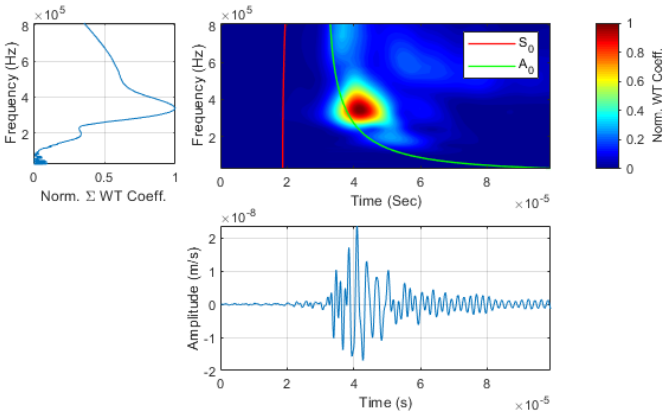

(e) 5 mm Void

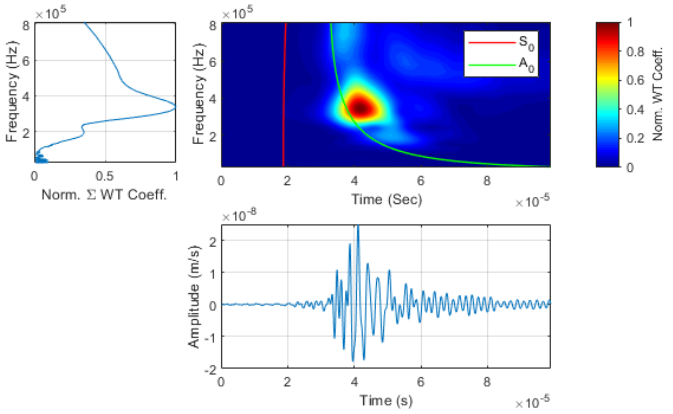

(f) 7.5 mm Void

Figure 5.17: (contd.)Time-Domain, Frequency-Domain and Time-Frequency-Domain plots for results of an out-of-plane source on a bonded specimen of 1 mm adherend thickness, 0.5 mm adhesive thickness and 100 mm source-sensor distance, with adhesive void sizes of (a) No Void, (b) 0.1 mm, (c) 1 mm, (d) 2.5 mm, (e) 5 mm, (f) 7.5 mm, (g) 10 mm, (h) 20 mm, (i) 30 mm, (j) 40 mm

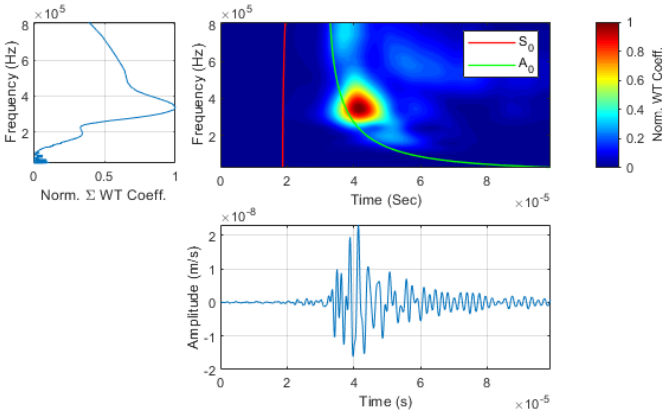

(g) 10 mm Void

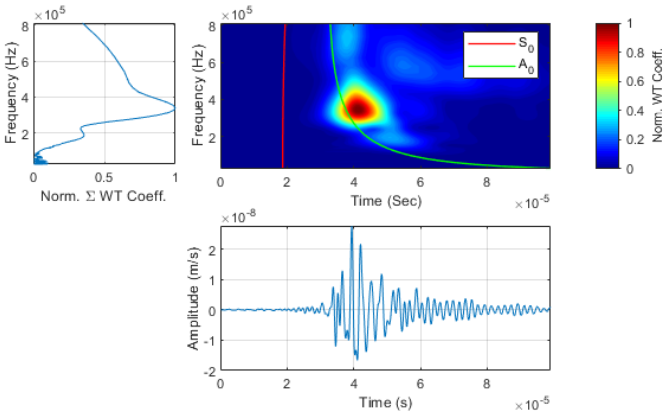

(h) 20 mm Void

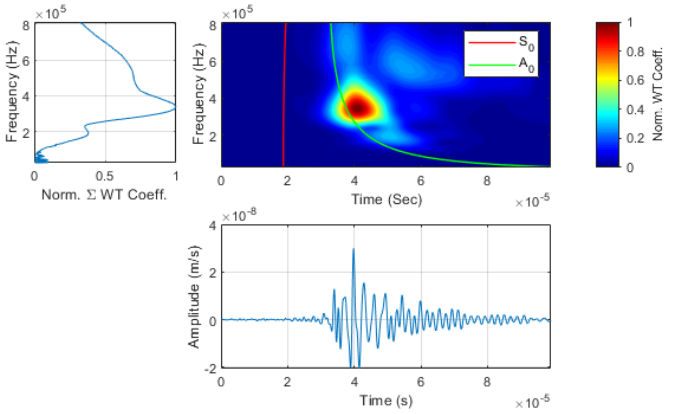

(i) 30 mm Void

Figure 5.17: (contd.) Time-Domain, Frequency-Domain and Time-Frequency-Domain plots for results of an out-of-plane source on a bonded specimen of 1 mm adherend thickness, 0.5 mm adhesive thickness and 100 mm source-sensor distance, with adhesive void sizes of (a) No Void, (b) 0.1 mm, (c) 1 mm, (d) 2.5 mm, (e) 5 mm, (f) 7.5 mm, (g) 10 mm, (h) 20 mm, (i) 30 mm, (j) 40 mm

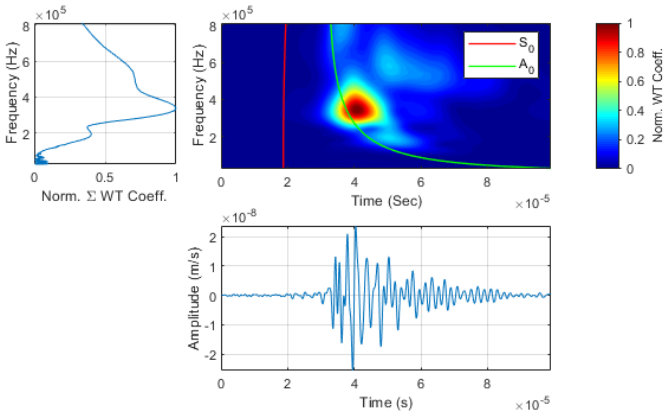

(j) 40 mm Void

Figure 5.17: (contd.) Time-Domain, Frequency-Domain and Time-Frequency-Domain plots for results of an out-of-plane source on a bonded specimen of 1 mm adherend thickness, 0.5 mm adhesive thickness and 100 mm source-sensor distance, with adhesive void sizes of (a) No Void, (b) 0.1 mm, (c) 1 mm, (d) 2.5 mm, (e) 5 mm, (f) 7.5 mm, (g) 10 mm, (h) 20 mm, (i) 30 mm, (j) 40 mm

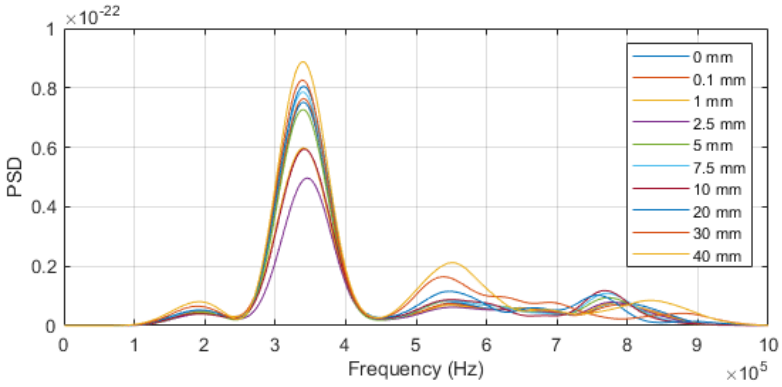

(a) PSD

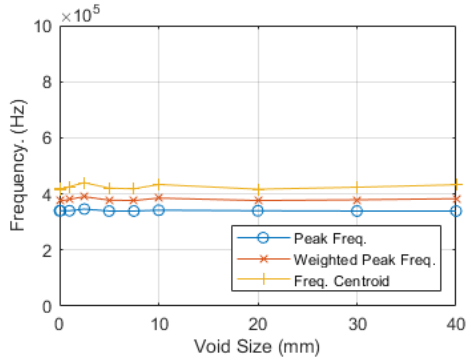

(b) Peak & Weighted Peak Frequency

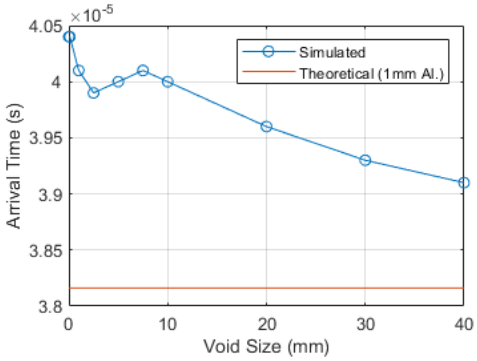

(c) A_0 Arrival Times (325 kHz)

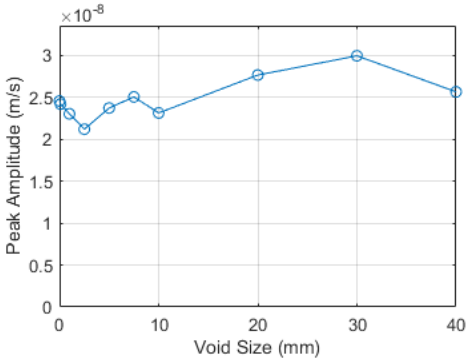

(d) Peak Amplitudes

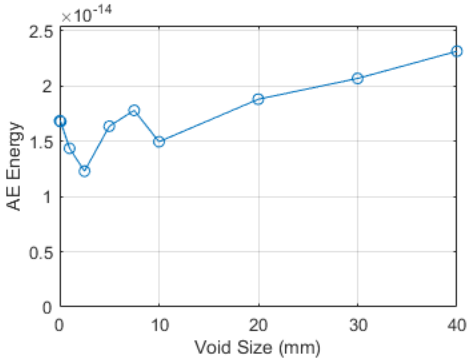

(e) AE Energy

Figure 5.18: Effects of adhesive void size in terms of (a) Power Spectral Density (b) Peak Frequency and Weighted Peak Frequency (c) Arrival Time of the A_0 mode at 325 kHz (d) Peak Amplitude (e) AE Energy

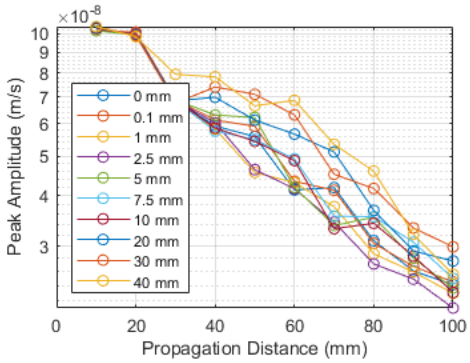

(a) Variation in Peak Amplitude with Propagation Distance

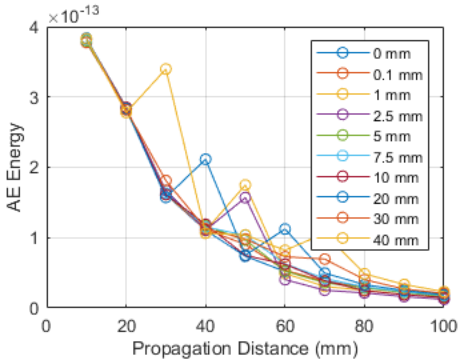

(b) Variation in AE Energy with Propagation Distance

Figure 5.19: Effects of adhesive void size at varying propagation distances (a) Peak Amplitude (b) AE Energy

5.13 Discussion

The results of the simulations are largely in good agreement with the experimental work conducted in this project, and with findings within literature, but do illustrate a variety of additional points of interest.

In previous works, Heller et al. [2] have demonstrated experimentally, through use of laser-based ultrasound, that the Lamb wave propagation in an adhesively-bonded aluminium specimen shows good correspondence to the dispersion-curves of a single adherend. Seifried et al. [3] have subsequently conducted analytical and FEA investigation of the results presented by Heller et al. They have concluded from their analytical study that the presence of additional layers does introduce a number of additional wave-modes, however, the dispersion-curves for many of these wave-modes follow, or at least partly follow, the dispersion-curves of the adherends. The use of an FEA study by Seifried et al. [3] then demonstrated that the highest out-of-plane displacements of the adherends surfaces (the feature which would be recorded by AE or ultrasound techniques), corresponded to the modes which followed the dispersion-curves of the adherends, thus supporting the observations of Heller et al.. The results of the simulations carried out in this work reflect the observations of both Heller et al. [2] and Seified et al. [3], with the generated wave-modes showing good correspondence to the theoretical dispersion-curves of the adherends, for all specimen properties tested. Further to this however, this work has demonstrated that the accuracy with which the generated wave-modes correspond to the theoretical curves for the adherends is dependent on the properties of the adhesive layer, namely adhesive thickness and Young's modulus. This finding is validated by comparison with the analytical solutions for the group velocity dispersion-curves of adhesive bonds of varying thicknesses shown in Figure 5.20, in which a decrease in velocity with increasing thickness can be seen in the modes closely following both the S_0 and A_0 modes. It can also be seen from these figures that the accuracy of the approximation is also highly dependent of the frequency at which analysis is conducted. The real-world implication of this is that in situations where an approximation of wave-velocity is sufficient, and where exact source location isn't critical, the easiest and quickest approach is to assume the relevant wave-velocities based on the adherends. However, in situations in which accurate velocities are required, it will be necessary to evaluate the wave-velocity on a case-by-case basis, taking into account the properties and geometry of both the adherends and the adhesive layer. Additionally, any changes in specification of a joint in terms of adhesive used, curing cycle, or adhesive-layer thickness, will require appropriate adjustment to account for the changes which may be induced. Specimens featuring variation in bond thicknesses, either by design or due to lack of process control, will also require special consideration as the wave-velocity will vary throughout the specimen.

The application of frequency-, energy- or amplitude-based techniques for signal classification will also be affected by any changes in the specification of the adhesive layer. Care should therefore be taken when attempting to transfer techniques from one type of specimen to another. This could potentially be an issue in attempts to move from laboratory specimens to industrial applications if the specimens are not suitably matched to the application, or if suitable adjustments are not made to the analysis methods.

The presence of voids within the adhesive-layer has been shown to have a significant effect on the recorded AE parameters, the implications of which are two-fold. In terms of AE testing, it implies that the presence of voids, particularly large voids, in the propagation path between the source and sensor may significantly alter the recorded signals, and thus lead to erroneous classification or location of sources. It does, however, illustrate that the use of a PLB AE source with

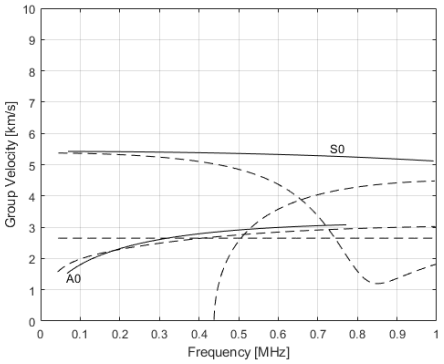

(a) 0.2 mm adhesive layer

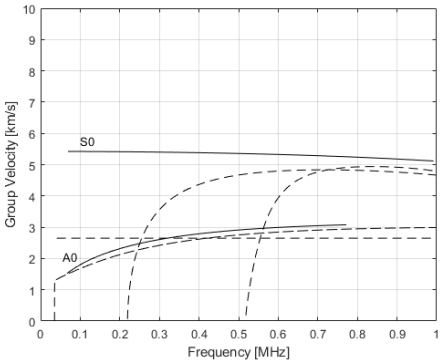

(b) 0.5 mm adhesive layer

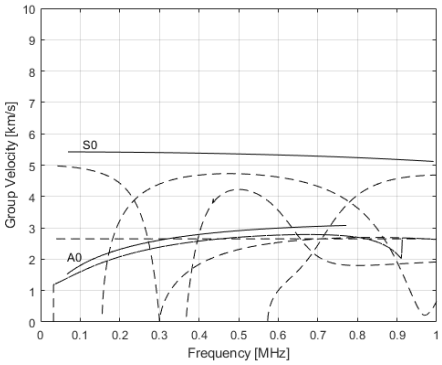

(c) 1 mm adhesive layer

Figure 5.20: Comparison of group-velocity dispersion-curves for a single 1 mm aluminium sheet with those for adhesively-bonded specimens with 1 mm thick aluminium adherends and adhesive layer thicknesses of (a). 0.2 mm, (b). 0.5 mm and (c). 1 mm. (Single adherend curves shown as solid lines, multi-layered specimen curves shown as dashed lines)

an AE system may provide an adequate method for detection and sizing of void-type defects, as was demonstrated in Chapter 3. It is therefore recommended that whenever possible or practical, specimens are inspected with suitable NDT methods to identify potential defects and their effects before commencing AE testing. For laboratory research specimens this should not pose a significant challenge, assuming suitable equipment is available. For industrial applications this could be more challenging, but application of appropriate NDT techniques during the initial inspection and commissioning stages of a structure could provide adequate data for accurate AE testing throughout the service-life of the structure.

5.14 Summary

In this chapter, a 3D dynamic FEA model has been developed of the AE generation, propagation and detection occurring from the application of a Pencil Lead Break source applied to an adhesively-bonded specimen. The AE generation and propagation has been simulated in COMSOL Multiphysics ®, while the effects of the sensing equipment has been accounted for by post-processing of the results in MATLAB. The model has been validated against both experimental

work and theoretical results. The model has been used to investigate the effects of varying the material properties of the adhesive, the adhesive-layer thickness and the effects of void-type defects within the adhesive-layer. The effects of these parameters have been considered in terms of modal analysis and of classical AE time-domain and frequency-domain features. The results have been discussed and compared with the results of the experimental work described in Chapter 3, as well as with those of pertinent literature. Many features of the model developed in this chapter have been used as a basis for development of the model in the following chapter.

Chapter 6

FEA of Destructive Tests

This chapter describes dynamic finite element simulations of Mixed-Mode Bending tests of adhesively-bonded specimens, conducted to investigate the relationship between fracture-mode and the generated wave-modes. It details the development of the model, including materials, geometry and physics set-up, and presents and discusses the results obtained, making comparisons with the experimental work conducted and with literature.

6.1 Introduction

It has been hypothesised, and demonstrated experimentally, that the fracture-mode of an adhesively-bonded specimen undergoing failure will alter the relative prominence of the resulting Lamb wave modes propagating from the failure. Experimental work was conducted using the Double-Cantilever-Beam (Mode-I) and Lap-Shear (Mode-II) tests, chosen to give as close to pure Mode-I and Mode-II failure as possible, therefore increasing the chance of any difference in wave-mode being observable. The disadvantage of this approach, however, is the use of two different specimen geometries, which may affect the results. To allow investigation of multiple mode-mixities, without change to the specimen geometry, a Mixed-Mode Bending (MMB) test has been simulated.

6.2 Geometry

The MMB test has been modelled in 2D, as opposed to 3D. The foremost reason for this is the necessary specimen size. The analysis methods being investigated require the Lamb wave modes to be dispersed far enough that they can be separated in the time and time-frequency-domains. This requires a much greater propagation distance than was utilised in the PLB simulations previously described. Additionally, the adherend thickness simulated was chosen to match that used experimentally (3.175 mm), as opposed to the thinner (1 mm) adherends utilised in the PLB tests. This increased physical size resulted in a model too large to realistically compute in 3D with the available resources.

The specimen modelled consists of two adherends with thicknesses of 3.175 mm and total lengths of 300 mm. These are separated by a full-length adhesive layer 0.5 mm thick. Each of

these is split into four sections along their length. The first 40 mm section contains the pre-crack. The next 0.5 mm long section contains the section of adhesive which will be debond and act as the source. The final split between sections is at the centre of the specimen where the bending load is applied. This geometry is illustrated in Figure 6.1.

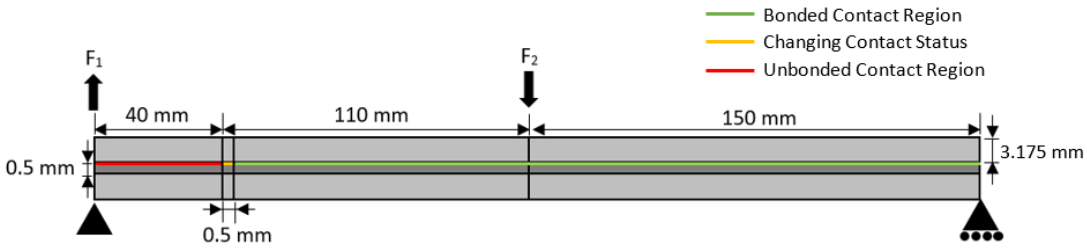

Figure 6.1: Schematic of MMB model geometry (not to scale)

6.3 Mesh

A mapped quadrilateral mesh was applied to the specimen, with an area of refinement, which has a refinement factor of 1, applied around the source, spanning the entire specimen thickness and 5 mm either side of the source. As before, mesh sizing was chosen based on a combination of lowest wavelength of interest, and a mesh-convergence study based on AE parameters. The minimum wavelength of interest was determined to arise from the S_0 mode at a frequency of 1 MHz and was calculated to be 2.27 mm. The mesh sizes and corresponding number of elements used in the convergence study are included as Table 6.1. The mesh-convergence study indicated that convergence of frequency, A_0 arrival time, peak amplitude and AE energy were suitably converged using a maximum element-size of 0.75 mm. It was, however, decided to use a maximum element-size of 0.45 mm to ensure a larger number of elements across the source region, as recommended by previous studies. Due to the 2D nature of the simulation, the computational expense of the additional refinement of the mesh was minimal. A maximum element growth rate of 1.3 was used.

Table 6.1: Mesh sizes used in convergence study. Corresponding number of elements listed for a single adherend

Max. Mesh Size	No. of Elements
2 mm	846
1 mm	3,009
0.75 mm	4,862
0.45 mm	13,320
0.25 mm	37,016

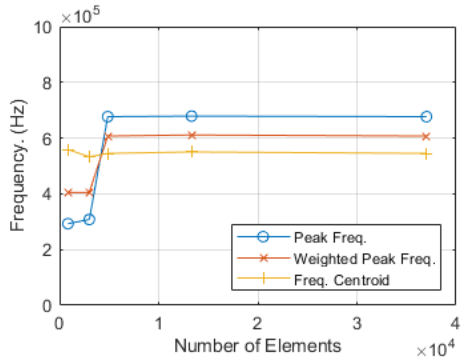

(a) Peak, Weighted Peak & Frequency centroid convergence

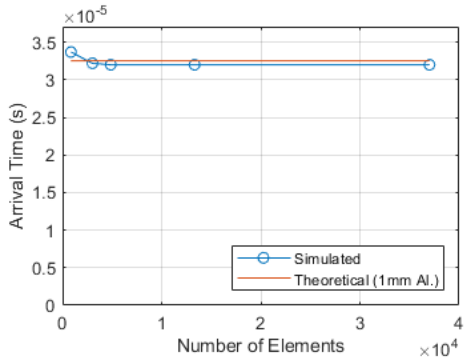

(b) A_0 Arrival Time convergence (Calculated at 325 kHz)

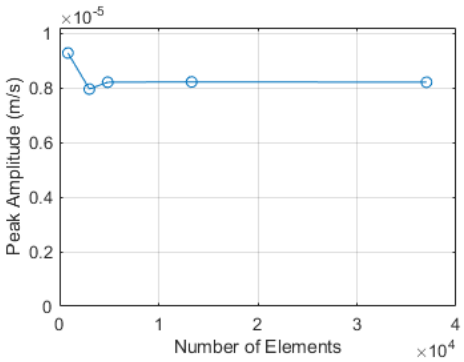

(c) Peak Amplitude convergence

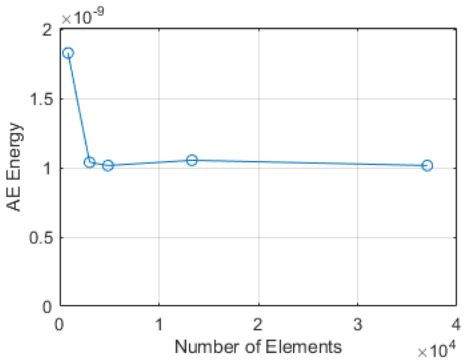

(d) AE Energy convergence

Figure 6.2: Mesh Convergence in terms of (a) Peak Frequency and Weighted Peak Frequency (b) Arrival Time of the A_0 mode at 325 kHz (c) Peak Amplitude (d) AE Energy

6.4 Materials

The adherends were modelled as 1050A H14 Aluminium, and the adhesive as Loctite® EA3430, as used in the experimental work described in Chapter 4. The material properties utilised are the same as those listed in Section 5.3.

6.5 Boundary Conditions and Load Steps

The simulation of the DCB test was conducted in two steps, as illustrated in Figure 6.3 . The first step is a static loading of the specimen, as illustrated in Figure 6.3a,c and d, in which the specimen deforms (Figure 6.3a), and stresses are accumulated at the crack-tip (Figure 6.3c) but the source area of the adhesive remains bonded. The second stage is a dynamic simulation, in which the bond ”fails”. Due to the highly localised nature of the failure, and the short time-frame of the simulation, the global displacement and global stress-field remain largely unchanged, as seen in Figures 6.3)b and d. The localised redistribution of stress results in the propagation of elastic waves, as can seen in Figure 6.3f, which propagate through the specimen and are recorded as AE.

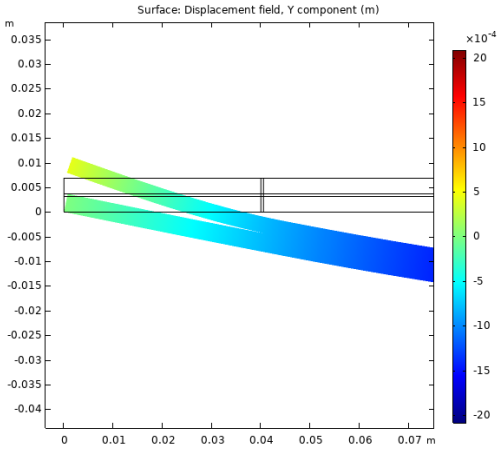

(a) Static Y-Displacement

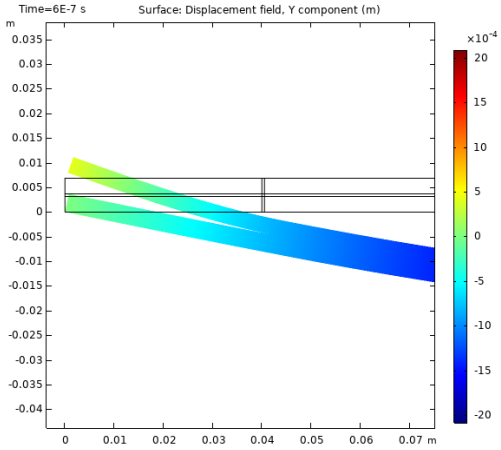

(b) Dynamic Y-Displacement

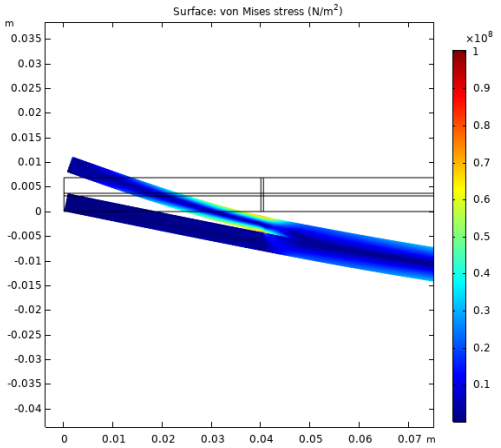

(c) Static Von-Mises Stress

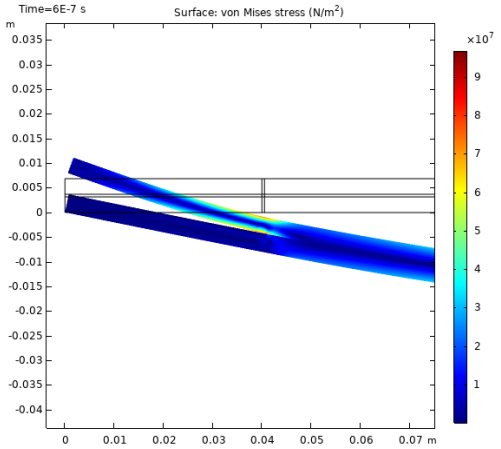

(d) Dynamic Von-Mises Stress

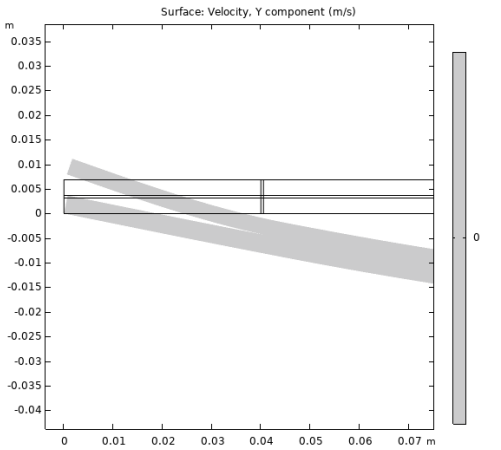

(e) Static Y-Velocity

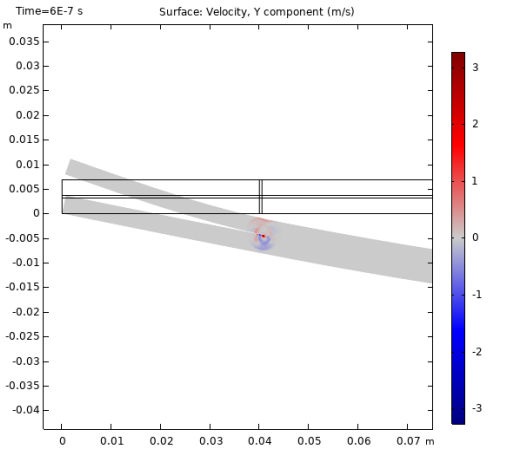

(f) Dynamic Y-Velocity

Figure 6.3: Y-Displacement, Von-Mises Stress and Y-Velocity fields for static and dynamic steps (Time shown= 0.6 μs). Deformation scaled x10. Un-deformed Wire-frame shown.

Prescribed displacements of 0 mm were applied to the bottom corners of the specimen to act as supports. At the crack-opening end, the displacement was fixed in both x- and y-directions. At the opposite end, the displacement was fixed only in the y-direction, allowing free movement in x. Vertical loads were applied upwards at the top corner at the crack-opening end, and downwards at the mid-point of the specimen. The magnitudes of these were dependent on the mode-mixity and are summarised in Table 6.3 below. The top and bottom surfaces of the specimen remained free throughout the simulation. The ends of the adherends and the adhesive layer have low-reflecting boundaries applied to minimise the effects of edge-reflections, and thus simplify analysis of the generated AE signals.The lower adherend and the adhesive layer were formed as one part, and the upper adherend as a second separate part. Throughout all stages of the simulation, the interface between the upper and lower parts in the pre-crack region are free, and thus able to separate. Throughout the initial static step, the rest of the interface between top and bottom parts is bonded, allowing no separation or penetration to occur. In the dynamic step, the bonded condition is removed from the source area of the interface and replaced with a free condition, allowing the adhesive layer to separate from the upper adherend.

The loading apparatus for the MMB test (See Figure 6.4) was not modelled, but the necessary loading values were calculated to achieve the desired mode-mixities. Equation 6.1 was used to determine the effective lever length c.

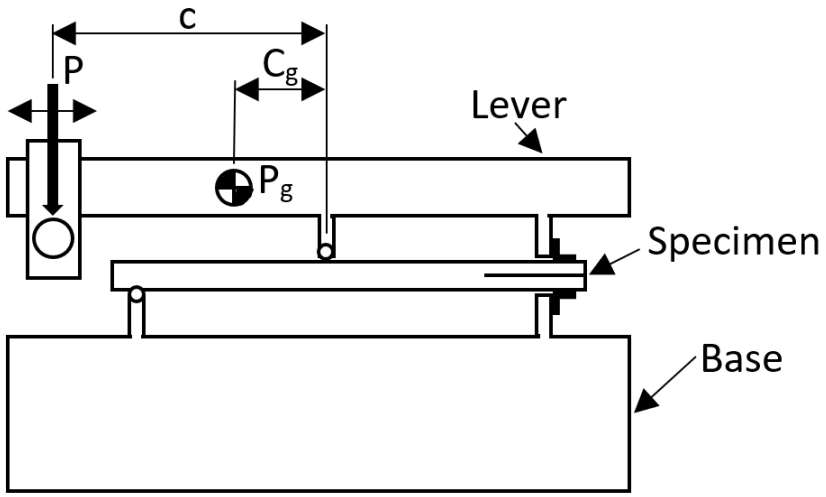

Figure 6.4: Mixed-Mode-Bending apparatus as per ASTM D6671 [146]

$$\frac{G_1}{G_2} = \frac{4}{3}\left[\frac{(3c-L)}{(c+L)}\right]^2 \tag{6.1}$$

Where:

$\frac{G_1}{G_2}$: Mode-Mixity

c : Lever length

L : Half the specimen length

The principle of moments was then used to calculate the ratio of applied loads at the crack-opening end (F_1) and on the mid-span (F_2), assuming small deflections. To ensure as consistent

an approach as possible across all mode-mixities, loads were chosen to give the same total strain-energy in the specimen for each mode-mixity. This means that as the loading-arm length increases to increase the mode-mixity, the loading-arm load is decreased in order to maintain the same strain-energy. A loading-arm force of 5 kN was selected for the first simulation ($\frac{G_1}{G_2} = 0.25$), and then loads for the following tests were chosen to provide the same strain-energy. The point loads which have actually been applied to the model are shown in Table 6.3. This approach does not account for the variation in failure-load with respect to fracture-mode that would exist in a real-world scenario. The use of a consistent strain-energy across all mode-mixities has been chosen to minimise the number of variables changing between simulations, and thus simplify comparison of results in terms of comparing wave-modes and fracture-modes. For comparison of other features, and for closer relation to real-world applications, other approaches to the selection of loads, such as utilising failure-loads from experimental data, would be more appropriate.

$$F_1 = \frac{Pc}{L} \qquad F_2 = F_1 + P \tag{6.2}$$

Where:

F_1 : Vertical load at crack-opening end

F_2 : Vertical load at mid-span

P : Load applied to the end of the loading arm

c : Lever length

L : Half the specimen length

Table 6.2: Mixed-Mode-Bending test boundary conditions and load steps

	Step 1	Step 2
Type	Static	Dynamic
Time	N/A	0 s to 100 μs
Time-step size	N/A	0.01 μs
Top surface	Free	Free
Bottom surface	Free	Free
Side (crack-opening)	Low-Reflecting	Low-Reflecting
Side (car)	Low-Reflecting	Low-Reflecting
Bottom corner (Crack-opening)	Prescribed Displacement x = 0 , y = 0	Prescribed Displacement x = 0 , y = 0
Bottom corner (far)	Prescribed Displacement x = Free , y = 0	Prescribed Displacement x = Free , y = 0
Top corner (Crack-opening)	See Table 6.1	See Table 6.1
Mid-span	See Table 6.1	See Table 6.1
Pre-crack interface region	Free	Free
Debonding interface region	Bonded	Free
Bonded interface region	Bonded	Bonded

Table 6.3: Loading values for Mixed-Mode-Bending Test

Mode Mixity	Loading-arm Load P	Crack-Opening End Load F_1	Midpoint Load F_2	Total Strain-Energy
$G_1/G_2 = 0.25$	5000 N	2791 N	-7791 N	8.767 J
$G_1/G_2 = 0.5$	4626.75 N	3124 N	-7751N	8.767 J
$G_1/G_2 = 1$	4094 N	3580 N	-7674 N	8.767 J
$G_1/G_2 = 2$	3337.75 N	4183 N	-7521N	8.767 J
$G_1/G_2 = 4$	2297 N	4950 N	-7247 N	8.767 J

6.6 Source

The AE source in the DCB model is the redistribution of stress occurring when a small section of the adhesive layer is no longer bonded to the upper adherend. In this simulation, the debonding over this small region is approximated as being instantaneous, with the contact condition between the adhesive and the adherend being switched from ”bonded” to ”free” between the initial static loading of the specimen and the subsequent dynamic step. This behaviour is a significant simplification of real-world debonding behaviour, but it is believed to be a reasonable approximation when considering a very localised region of debonding. The use of a 2D simulation means that the 0.5 mm long section of interface which is debonding in 2D is equivalent to a rectangular section with a side length of 0.5 mm and a depth which could be considered to be infinite, or in more physical terms it is representative of uniform debonding across the entire specimen width. For a perfectly uniform specimen, with a perfectly distributed load, this is a reasonable representation. It is noted that in a real specimen featuring loading eccentricity and potentially random variation in bond quality, it is unlikely that the specimen will fail uniformly across the entirety of its width. Conversely, the sudden failure of a small section is more representative of a real bonded specimen than of a theoretically perfect specimen. A perfectly uniform specimen would debond in a smooth manner with the crack length increasing smoothly as the loading is increased, with no sudden re-distributions of stress which could be recorded as acoustic emissions. Fracture of a real specimen, however, is more stop-start, with localised sections failing rapidly and generating acoustic emissions. The use of instantaneous debonding over a very small area is therefore felt to be a reasonable approximation of the highly localised debonding behaviour responsible for the generation of acoustic emissions, while other models, such as the various cohesive-zone models available, would be more suitable for modelling of debonding on a global scale.

With this method it should be noted that the source does not have a specified rise-time or duration, which is necessary with other modelling methods such as the typical buried dipole which has been used in many works [59, 67, 108–111, 113–115]. The rise-time of the source is defined by the properties of the material. In this case, due to the source occurring from the separation of the adhesive layer and adherend, the source essentially has two rise-times, a faster rise-time in the aluminium layer and a slower rise-time in the epoxy layer.

6.7 Sensor

Point probes recording y-direction velocity were used as sensors in these simulations, and were located on the top edge of the upper adherend at 10 mm intervals from 10 mm to 200 mm from

the source. Area-type probes, as previously used, could not be used to represent the sensors due to the 2D nature of the simulation. While the use of point probes will not capture the effects of sensor size or shape, they have been used in the majority of previous studies [55, 59, 60, 67, 104–108, 110, 117, 141] and are adequate for the investigation of the parameters under consideration in this study, namely identification of the wave-modes generated by fracture of the specimen.

6.8 Post-processing

The post-processing routine previously described in Section 5.9 has also been applied to the results of the MMB test. Results presented in Chapter 5 include both unfiltered results, to give a clear picture of what is happening on the specimen surface, and frequency-filtered results, to illustrate what is likely to actually be detectable in an experimental set-up.

6.9 Results

Mixed-Mode-Bending tests have been simulated with five different mode-mixity ratios, 0.25, 0.5 1, 2 and 4. The primary aim of the simulations is to observe the variation in the generation of Lamb wave modes due to the variation in fracture-modes. Figures 6.5 and 6.6 present the time-, frequency- and time-frequency-domain results for all five mode-mixities, as recorded by a point sensor located on the upper surface of the upper adherend at a distance of 200 mm from the source. Figure 6.5 presents the results prior to any frequency filtering, and thus gives a better representation of what is actually happening on the specimen surface or what would be recorded by a broadband sensor with a perfectly flat frequency-response. Figure 6.6 presents the results following frequency filtering, to better represent what would be recorded with a real-world AE system, in this case a Physical Acoustics Micro 80-D sensor with a 20 kHz high-pass preamplifier. Overlaid on the WT plots for each result are the dispersion-curves relating to the theoretical arrival-times of the S_0 and A_0 Lamb-modes for the upper adherend, and also the multiple theoretical dispersion-curves calculated for entire three-layered geometry, labelled as B_n and referred to from hereon as the 'multi-layer modes'.

Investigation of the unfiltered results in the time-frequency-domain show that the A_0 mode is dominant across all frequencies for all mode-mixities, with the mid-to-high frequency region arriving at around 65μs, and the highly dispersive low-frequency components arriving after this. The S_0 mode is also clearly visible in the mid-frequency range from 200 kHz to 600 kHz, and is responsible for the earliest activity seen in the time-domain plot, arriving at around 65μs. It can also be seen that other additional modes, related to the multilayered structure of the bond are also present. Two of these modes feature an early arrival time, appearing in the mid-frequency range just after the S_0 mode, but are highly dispersive at both higher and lower frequencies. These modes are visible in the region in which they are close to, and can be roughly approximated by, the S_0 mode, but are of relatively low amplitude even in this region. Two additional wave-modes also appear in the high-frequency region, just before the first arrival of the A_0 mode. These modes both follow a similar trend of increasing dispersion with decreasing frequency, similar to the A_0 mode, but only exist in the frequency region above 500 kHz. These modes both produce a significant medium energy region prior to the arrival of the A_0 mode, but do not appear after it. Another similar wave-mode also exists, which arrives just after the A_0 mode, and existing at frequencies above 300 kHz. This mode is clearly visible in the WT plots across the entire frequency-range

for which it exists. One critical feature of this wave-mode in particular, is that its amplitude varies significantly with respect to mode-mixity. At a low mode-mixity of only 0.25, this mode is of similar amplitude to the S_0 mode. However, as the mode mixity increases, the amplitude of this mode increases, to the extent that with a mode-mixity of 4, this mode has a higher amplitude than even the A_0 mode.

Comparison between mode-mixities reveals a shift in frequency content in the unfiltered results, with an increase in mid- to high-frequency content with increasing mode-mixity, as can be observed in terms of PSD and frequency-based parameters in Figures 6.7a and 6.7b. In the time-frequency-domain this increase can be seen to occur in all of the modes previously discussed. In the filtered results, the frequency response is dominated by the sensor response, and so the shift in frequency is much less prominent, as illustrated in Figures 6.8a and 6.8b. It can also be observed that the increase in mode-mixity leads to increases in both peak-amplitude (occurring at the arrival of the A_0 mode), and AE energy, as illustrated in Figures 6.7c, 6.7d, 6.8c and 6.8d.

In order to visualise the variation in wave-modes more clearly, the WT coefficients for a single frequency-band have been plotted in Figure 6.9. A frequency of 325 kHz has been selected for examination due to it being close to the peak-frequency of the sensor, containing significant activity relating to both the S_0, A_0 and multi-layer modes, and due to the dispersion characteristics of the specimen giving significant separation between these modes in the time-domain, thus allowing separate peaks to be clearly identified. In Figure 6.9a there are three clearly identifiable regions, relating to the S_0 and A_0 modes, and the additional multi-layer mode. The relative amplitude of the S_0 peak is seen to reduce slightly with increasing mode-mixity, while the A_0 peak increases slightly. The subsequent peak relating to the multi-layer mode also sees a very significant increase with increasing mode-mixity.

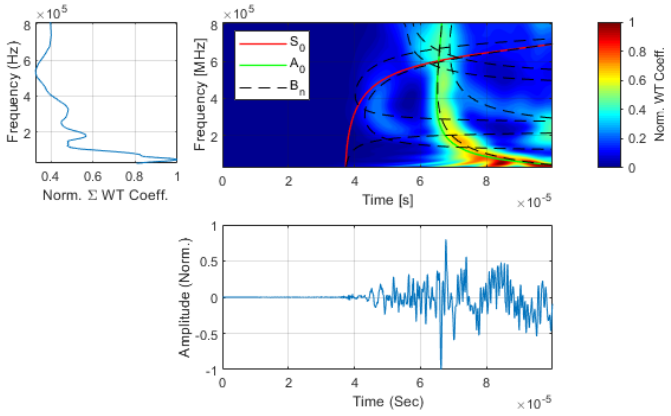

(a) $G_1/G_2 = 0.25$

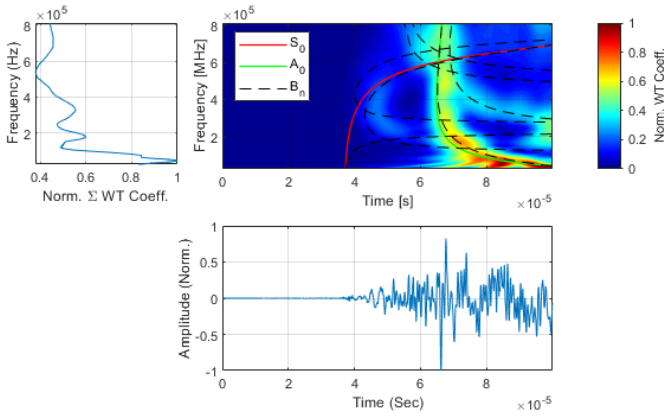

(b) $G_1/G_2 = 0.5$

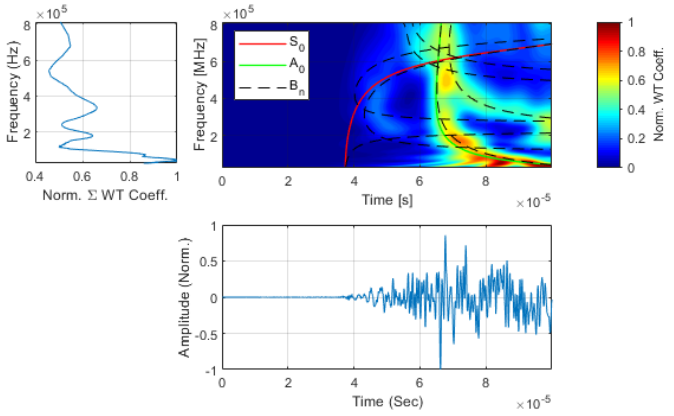

(c) $G_1/G_2 = 1$

Figure 6.5: Unfiltered Time-Domain, Frequency-Domain and Time-Frequency-Domain plots for results of a mixed-mode bending test, with specimens of 3.175 mm adherend thickness, 0.5 mm adhesive thickness and 200 mm source-sensor distance, with mode-mixities (G_1/G_2) of (a) 0.25, (b) 0.5, (c) 1, (d) 2, (e) 4

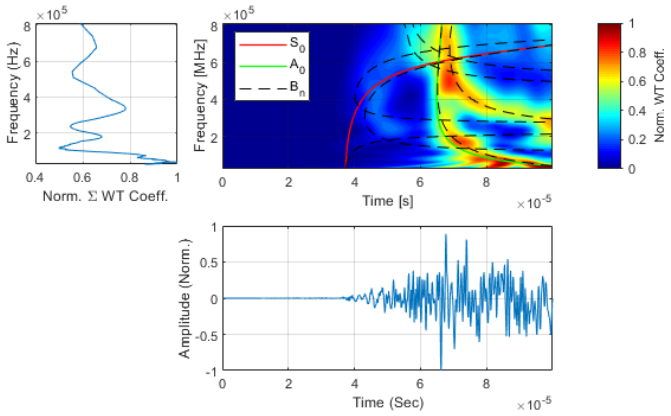

(d) $G_1/G_2 = 2$

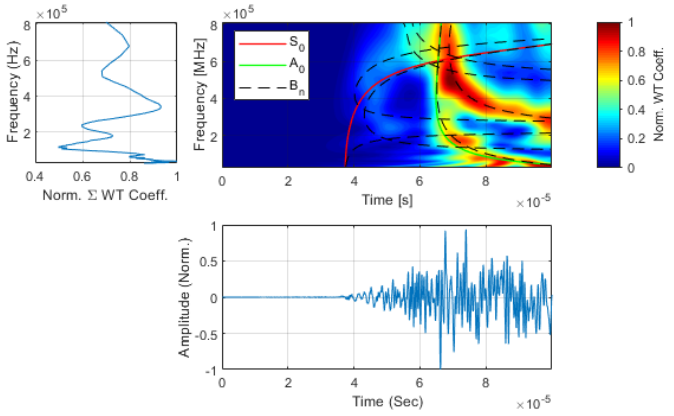

(e) $G_1/G_2 = 4$

Figure 6.5: Unfiltered Time-Domain, Frequency-Domain and Time-Frequency-Domain plots for results of a mixed-mode bending test, with specimens of 3.175 mm adherend thickness, 0.5 mm adhesive thickness and 200 mm source-sensor distance, with mode-mixities (G_1/G_2) of (a) 0.25, (b) 0.5, (c) 1, (d) 2, (e) 4 (contd.)

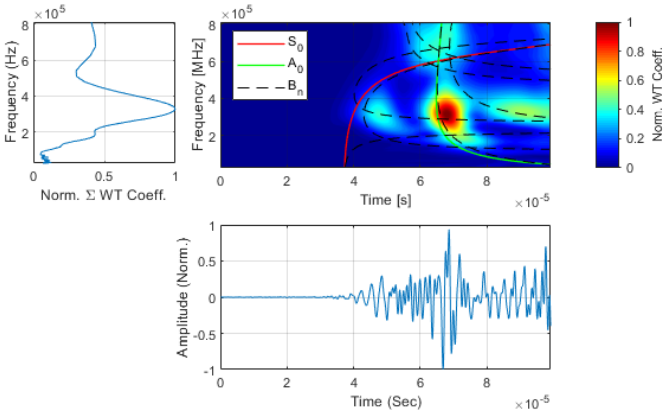

(a) $G_1/G_2 = 0.25$

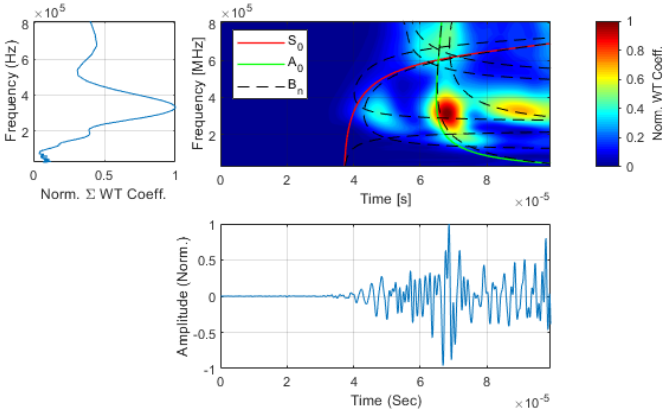

(b) $G_1/G_2 = 0.5$

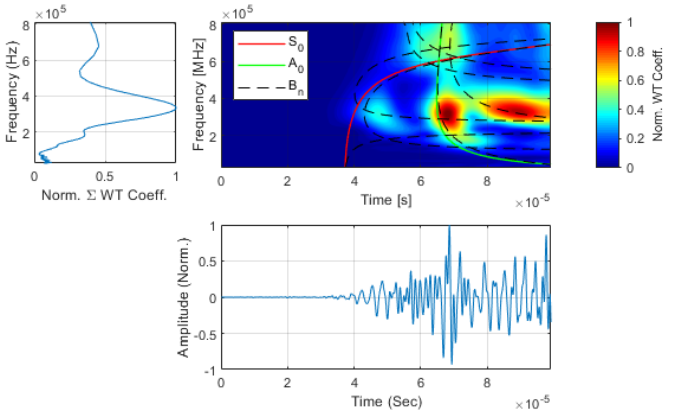

(c) $G_1/G_2 = 1$

Figure 6.6: Time-Domain, Frequency-Domain and Time-Frequency-Domain plots for results of a mixed-mode bending test, with specimens of 3.175 mm adherend thickness, 0.5 mm adhesive thickness and 200 mm source-sensor distance, with mode-mixities (G_1/G_2) of (a) 0.25, (b) 0.5, (c) 1, (d) 2, (e) 4. (Results filtered to frequency response of Micro 80-D AE Sensor).

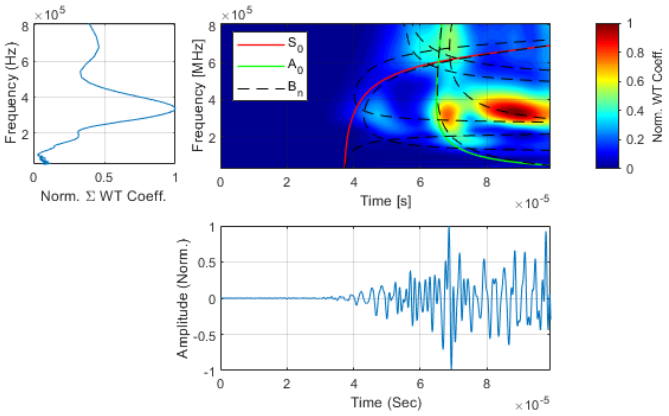

(d) $G_1/G_2 = 2$

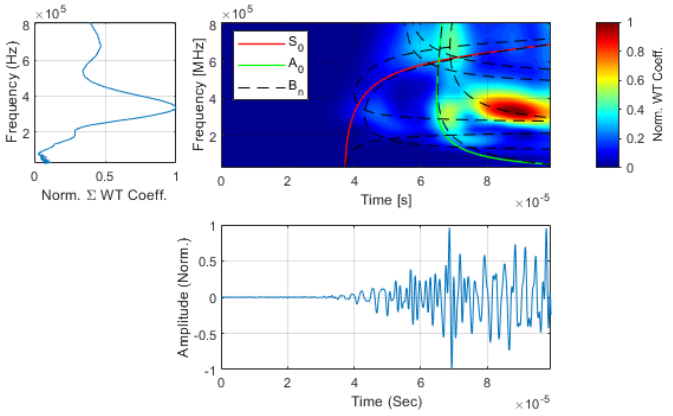

(e) $G_1/G_2 = 4$

Figure 6.6: (contd.) Time-Domain, Frequency-Domain and Time-Frequency-Domain plots for results of a mixed-mode bending test, with specimens of 3.175 mm adherend thickness, 0.5 mm adhesive thickness and 200 mm source-sensor distance, with mode-mixities (G_1/G_2) of (a) 0.25, (b) 0.5, (c) 1, (d) 2, (e) 4 (Results filtered to frequency response of Micro 80-D AE Sensor)

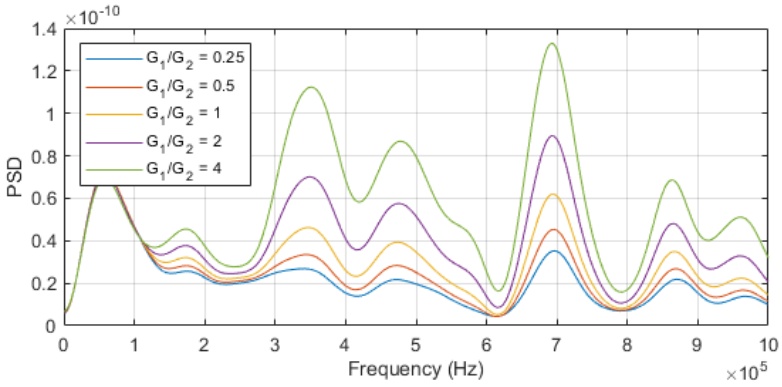

(a) PSD

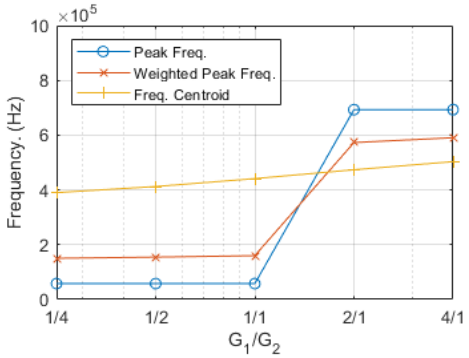

(b) Peak, Weighted Peak & Frequency Centroid

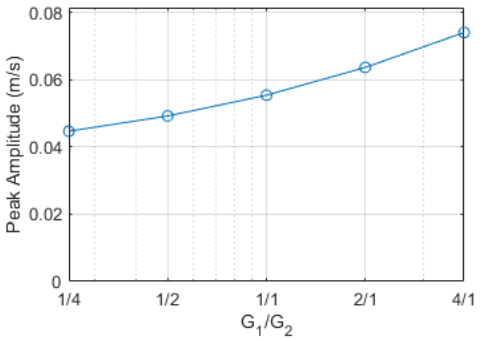

(c) Peak Amplitudes

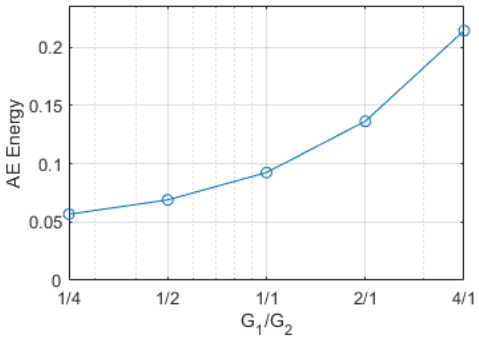

(d) AE Energy

Figure 6.7: Effects of Mode-Mixity in terms of (a) Power Spectral Density (b) Peak Frequency, Weighted Peak Frequency and Frequency Centroid (c) Peak Amplitude (d) AE Energy (Unfiltered results)

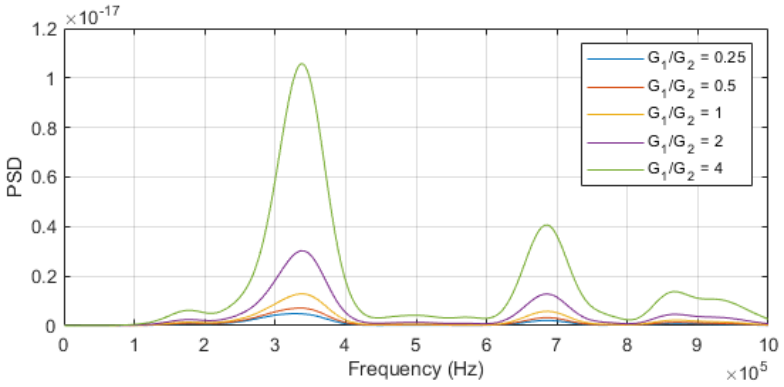

(a) PSD

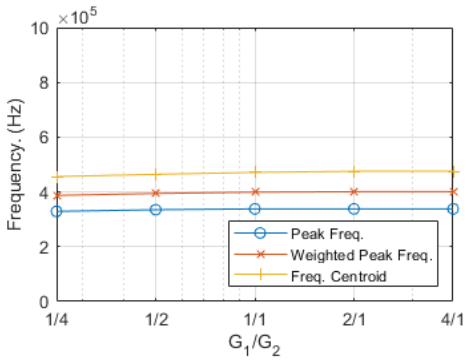

(b) Peak, Weighted Peak & Frequency Centroid

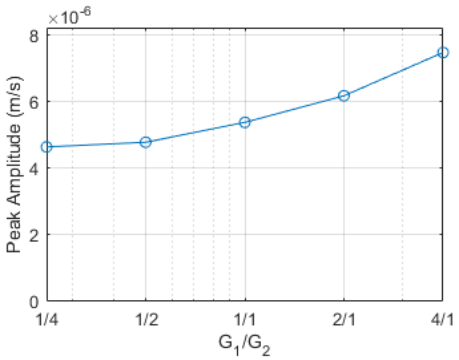

(c) Peak Amplitudes

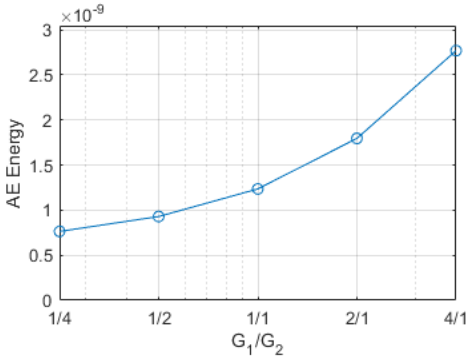

(d) AE Energy

Figure 6.8: Effects of Mode-Mixity in terms of (a) Power Spectral Density (b) Peak Frequency, Weighted Peak Frequency and Frequency Centroid (c) Peak Amplitude (d) AE Energy (Frequency-filtered results)

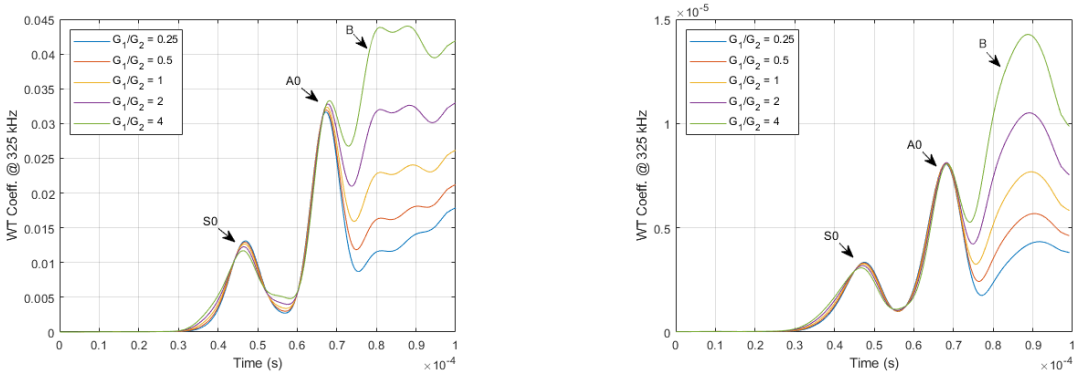

(a) Unfiltered (b) Filtered

Figure 6.9: Normalised wavelet-transform coefficients at 325 kHz, showing S_0, A_0 and multi-layer mode (B) peaks. (a) Unfiltered result (b) Filtered to match Micro-80D AE sensor response

As demonstrated in the prior experimental work, the ratio between the peak WT coefficients for the S_0 and A_0 modes has been investigated as a potential indicator of fracture-mode. The resulting plots of peak-ratio are presented as Figures 6.10a and 6.10b for the unfiltered and filtered results respectively. In both cases a clear relationship can be seen between mode-mixity and WT coefficient peak-ratio, with the ratio decreasing with increasing mode-mixity. The ratio, calculated from the unfiltered results, reduces from 0.4141 to 0.3516 over the range of mode-mixities from 0.25 to 4. The frequency-filtered results illustrate the same trend, though with lower variation, from 0.4148 to 0.3817. This relationship corroborates that which has been identified experimentally. While the values from the simulation are significantly higher than the mean values identified experimentally (DCB = 0.085, LS 0.1902), they do fall within the wide range of values recorded experimentally (DCB = 0.0169 to 0.4178, LS = 0.0616 to 0.7197). This variation between simulation and experiment can be attributed to a number of uncontrollable variables within the experimental set-up, which are responsible for the high level of variation within the experimental results, and also the simplifying assumptions made within the simulation.

While the experimental work conducted has focused on only the S_0 and A_0 modes, this simulation-based work has highlighted that the greatest potential for differentiation by modal analysis may actually lie in the use of the multi-layer modes. A similar approach as taken to the S_0 and A_0 modes has therefore also been applied to the A_0 and multi-layer modes. The result of this is illustrated for both the filtered and unfiltered signals in Figure 6.11, in which the multi-layer modes are denoted as "B". It can be seen that, for the unfiltered results, the WT peak-ratio varies from 2.7 down to 0.75 over the range of mode-mixities from 0.25 to 4. The filtered results range from 1.9 down to 0.55 over the same range. This demonstrates that the the selected multi-layer mode has a much greater sensitivity to mode-mixity than the fundamental modes of the adherends.

An additional method to investigate the relationship between mode-mixity and wave-mode has also been utilised. Sections of the time-domain signal relating to the S_0 and A_0 modes have been extracted, and the signal energy calculated in each section. The ratio of energy in each of these sections has then been used as a parameter for investigation. The S_0 section of the time-domain ranges from 35μs to 55μs, while the A_0 region ranges from 55μs to 70μs. The results of this method, as illustrated in Figure 6.12, also show a clear relationship between mode-mixity and wave-mode, with increasing mode-mixity leading to decreasing energy-ratio.

These results indicate that mode-mixity of fracture of an adhesive joint does have a signifi-

cant effect on the generated wave-modes, when considering a constant loading (in terms of global strain-energy prior to fracture), area of debonding, specimen geometry and source-sensor propagation distance. While this in itself is a novel finding, it may be of limited use unless it can be utilised in experimental work. For this to be possible it is important to acknowledge other mechanisms which may have similar effects, and to try to identify methods to differentiate between variations in wave-mode generated by varying mode-mixity, and variations in wave-mode caused by other factors. To this end, the area of debonding has been varied, with fracture lengths of 0.25 mm, 0.5 mm (as previously presented), and 1 mm. The results in terms of S_0/A_0 WT peak-ratios, and S_0/A_0 energy ratios, are presented in Figures 6.13 and 6.14. In both the WT peak-ratio analysis and energy-ratio analysis it can be seen that, for all three debonding areas tested, the same trend of decreasing S_0/A_0 ratio exists. The size of debonding area , however, does affect the ratio, with smaller debond areas resulting in a relative decrease in the A_0 mode and larger debond areas resulting in a relative increase. The difference in WT peak-ratio due to debond size is greatest at high mode-mixity values, while the difference in energy-ratios is highest at low ratios of mode-mixity.

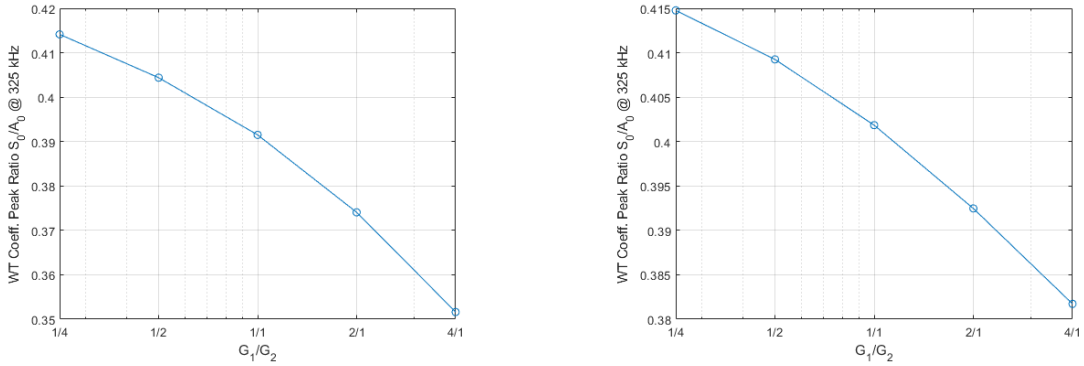

(a) Unfiltered (b) Filtered

Figure 6.10: S_0/A_0 WT peak-ratio vs. mode-mixity G_1/G_2. (a) Unfiltered result (b) Filtered to match Micro-80D AE sensor response

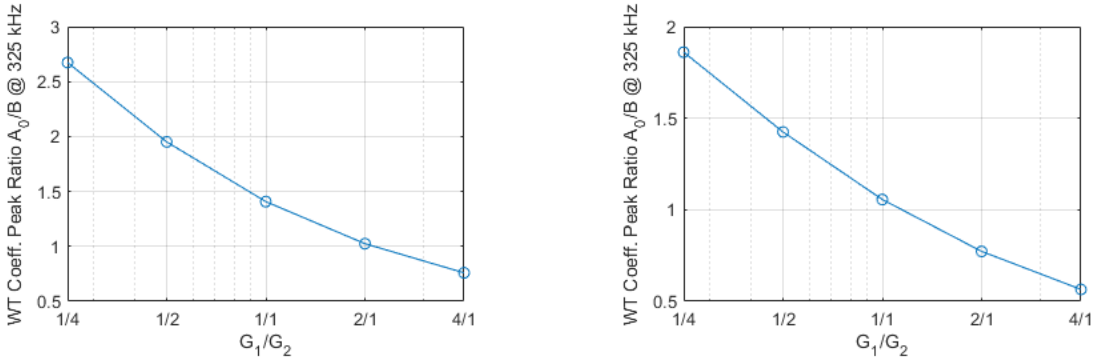

(a) Unfiltered (b) Filtered

Figure 6.11: A_0/B WT peak-ratio vs. mode-mixity G_1/G_2. (a) Unfiltered result (b) Filtered to match Micro-80D AE sensor response

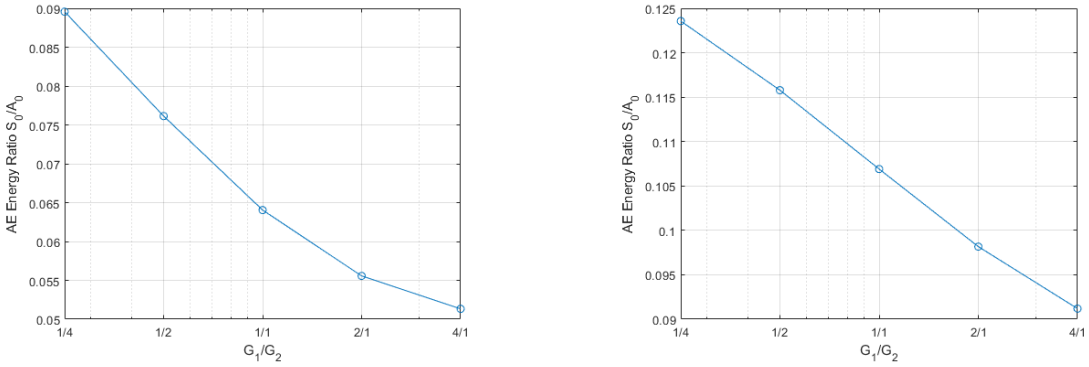

(a) Unfiltered (b) Filtered

Figure 6.12: S_0/A_0 AE energy-ratio vs. mode-mixity G_1/G_2. (a) Unfiltered result (b) Filtered to match Micro-80D AE sensor response

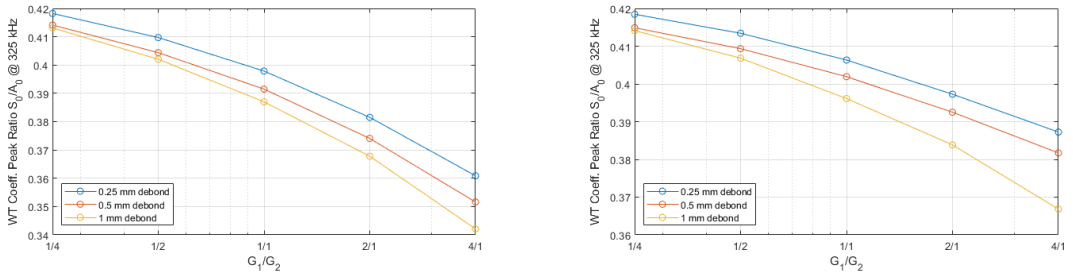

(a) Unfiltered (b) Filtered

Figure 6.13: S_0/A_0 WT peak-ratio vs. mode-mixity G_1/G_2 for debond lengths of 0.25 mm, 0.5 mm and 1 mm. (a) Unfiltered result (b) Filtered to match Micro-80D AE sensor response

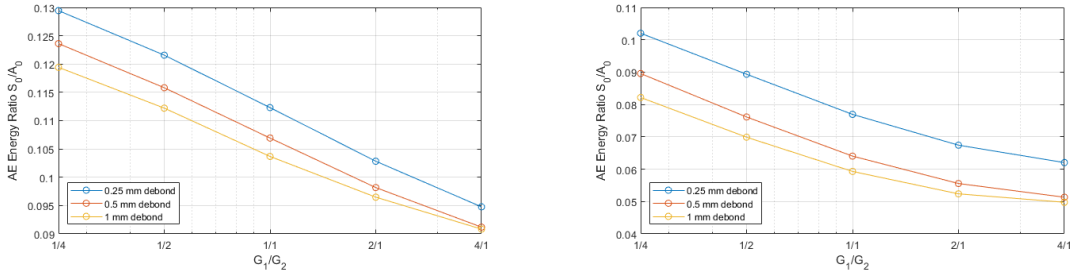

(a) Unfiltered (b) Filtered

Figure 6.14: S_0/A_0 AE energy-ratio vs. mode-mixity G_1/G_2 for debond lengths of 0.25 mm, 0.5 mm and 1 mm. (a) Unfiltered result (b) Filtered to match Micro-80D AE sensor response

6.10 Discussion

The simulation work conducted has confirmed the general hypothesis that an increased Mode-I fracture component produces a relative increase in the dominance of the A_0 wave-mode, while an increased Mode-II component produces a relative increase in the S_0 component. This finding is in line with the findings of the experimental work conducted as part of this project and detailed in Chapter 4. While the values for the S_0/A_0 ratio differ from those in the experimental work, and seemingly overestimate the contribution of the S_0 mode, the results do point towards the same trend. The experimental results feature a high level of variation within each test, due to factors which could not be fully controlled experimentally. The simulations have highlighted that one factor contributing to the variation may be the size of the region debonding during each AE event, as it has been shown that this will also affect the wave-modes generated. This is only one of many potential sources of variation which could be investigated in future work.

In addition, this simulation work has highlighted the fact that the multi-layer modes which propagate within the joint may actually be a greater indicator of fracture-mode than the fundamental modes of the adherends. The experiments conducted in Chapter 4 were designed based on the assumption that the fundamental modes of the adherends would be the dominant modes which would exist in both the bonded region and the cracked region of the specimens. The sensor placement on the adherends in the un-bonded regions was therefore considered to be appropriate. The simulation results do, however, suggest that better differentiation may have been achieved by use of sensors located in the bonded region, with the multi-layer modes being utilised. This approach would, however, face the disadvantage of higher attenuation, thus reducing the ability to accurately capture these modes.

In terms of comparison with other works, the results of this study are in line with what would be expected from the results of previous investigations into the relationship between source angle and wave-mode, such as that by Gorman [58]. While results have been presented thus far in terms of mode-mixity, they may also be considered in terms of source angle. To establish the effective source angle, the mean principal-stress direction has been calculated within the region of the adhesive layer which is subject to debonding. The principal stress orientations are included in Table 6.4 and plotted against mode-mixity in Figure 6.15. The range of mode-mixities investigated, 0.25 to 4, relate to effective source orientations ranging from 58.92° to 71.06°. At this point it should be recognised that the range of potential source orientations for adhesive failure is significantly more limited than for other applications for which modal AE analysis has previously been utilised. PLB sources can be applied at any angle, while use to differentiate between failure-modes in composites considers sources which can be entirely in-plane (fibre-breakage) or entirely out-of-plane (delamination). The principal stresses in an adhesive bond will vary from being out-of-plane (under Mode-I loading), to being only 45° out-of-plane (under pure Mode-II loading), as opposed to being entirely in-plane as was previously implied by Prathuru [9]. The observable difference in the excited wave-modes can therefore be expected to be significantly reduced, compared to what may be seen in other applications of modal AE analysis. This does unfortunately somewhat reduce the potential for application of modal analysis to identifying fracture-modes of adhesive joints, as the results will be more susceptible to the effects of noise and other confounding factors.

Considering the applicability of the demonstrated modal analysis methods to real-world experimental work, it has been illustrated in Chapter 4 that the method may be useable when considering the mean of the peak-ratios over the full duration of a test, rather than just considering individual hits. The simulations have, however, demonstrated that while there is a clear relationship between

Table 6.4: Mean principal stress directions in adhesive fracture region

Mode Mixity	Principal stress orientation (° from horizontal)
0.25	58.92
0.5	61.20
1	64.07
2	67.46
4	71.06

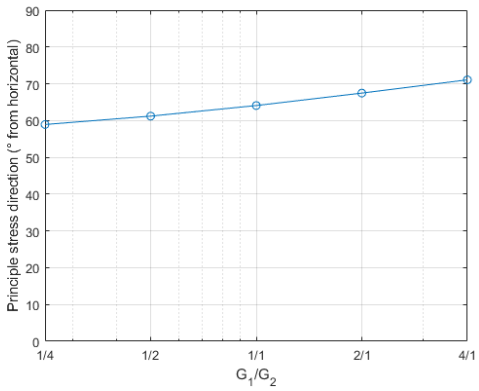

Figure 6.15: Effects of mode-mixity G_1/G_2 on principle stress directions in the debond region of the adhesive

wave-modes and fracture-mode, the peak-ratios or energy ratios do not provide a unique classifier for the mode-mixity, when other parameters such as the area of debonding are variable. For example, considering the peak-ratios for the filtered results illustrated in Figure 6.13, a peak-ratio of 0.41 may relate to a mode-mixity of either 0.7, 0.5 or 0.4, depending on whether the length of the debonding region is 1 mm, 0.5 mm or 0.25 mm respectively. It may be possible to use the modal parameters in combination with other AE parameters, such as energy, to uniquely identify the fracture mode/mode-mixity. It will first need to be established which parameters will affect the excited wave-modes. In the this work, mode-mixity and debond length have been verified as causing variation in the modes excited. Hamstad et al. [59] demonstrated that the depth of a buried dipole beneath the specimen's surface also determined the proportions of the excited wave-modes. It is therefore anticipated that, in the case of adhesive failure, which adherend the adhesive layer breaks away from (and thus the effective source depth), will also affect the generated wave-modes. Further simulation and experimentation is therefore needed to fully establish the effects of all of the potential variables if this approach is to be utilised and a full understanding of the relationship between the source and signals is to be gained.

In terms of practical application, the approach of using statistical pattern-recognition, as demonstrated by Dzenis and Saunders [85], may remain the most feasible, as it allows differentiation between fracture-modes without any prior understanding of the fundamental differences in the signals. The work presented in this chapter does, however, provide a greater understanding of signal-features which are likely to have allowed the pattern-recognition software to achieve that differentiation.

6.11 Summary

In this chapter, a 2D Dynamic FEA model has been developed to model AE generation, propagation and detection occurring from localised adhesive failure within an adhesively-bonded mixed-mode-bending test specimen. Modelling of the source and propagation medium has been conducted in COMSOL Multiphysics ®, while the effects of the sensing equipment have been applied to the results in a post-processing step using MATLAB. This model has been used to investigate the effects of mode-mixity on the Lamb-modes generated in the specimen. Modal AE analysis has been conducted by use of wavelet-transforms, which were used to investigate the recorded signals in the time-frequency-domain, combined with theoretically-calculated dispersion-curves, which were utilised to aid in identifying the wave-modes recorded. The wavelet-transform coefficients corresponding to the fundamental symmetric and asymmetric modes of the adherends, and the multi-layer modes, have been extracted at peak-frequency. The ratio between these coefficients has been compared with the mode-mixity of the test to demonstrate the relationship between these features. The results of this chapter have also been compared with the experimental work conducted in Chapter 4 and with the findings of pertinent literature.

Chapter 7

Conclusions

The overall aim of this project was to further the current understanding of acoustic emission generation from, and propagation through, adhesively-bonded joints, with the intention that the findings could be utilised to improve the accuracy and abilities of acoustic emission methods, used in both research, and industrial applications. The simulated source tests, conducted on specimens of differing bond and defect status, have allowed exploration of the effects of adhesive bonds on AE wave propagation, and have highlighted a number of critical features which should considered when developing AE methodologies for adhesively bonded joints in future works. This increased understanding of AE propagation has also formed a foundation for the rest of the experimental work conducted in this project.

The introduction of ANNs to analyse PLB based AE data for the detection and sizing of adhesive defects builds on the work conducted by other authors in previous studies. While this technique is not currently at a stage of readiness to be rolled out for industrial applications, and a significant amount of further testing and development is necessary, the addition of ANNs to the process simplifies the workflow and currently appears to yield significantly better results than the analysis techniques used in the previous studies.

The novel identification of a relationship between fracture-modes of adhesive joints and the generated wave-modes has the potential to be beneficial to further research and may also find use in industrial applications. In a research setting, it will be useful for researchers to understand the effects of fracture-mode on the generated AE signals so that this effect can be differentiated from the effects of other variables which may be under test. This may be of particular interest in the testing of composite joints, where different loading orientations may be introduced to initiate different failure types within the composite adherends. In an industrial setting, this finding may be useful for health diagnostics of bonded joints, as it could be possible to identify dangerous unexpected loadings, such as a peel load occurring in a joint designed to only see shear loading, as could happen due to causes such as structural damage or environmental effects, such as temperature change.

The development of FEA models of both the simulated source tests and the destructive tests has allowed the applicability and generalisability of the experimental findings to be assessed against a larger range of parameters than would have been practical experimentally, and has allowed the effect of certain parameters to be isolated in a more controlled manner than would have been achievable experimentally. This has led to greater confidence in the experimental results presented. Additionally this work has added a novel application to the relatively young, but rapidly

growing field of AE simulation and has helped to demonstrate its potential effectiveness. The main conclusions from each of the sections of work conducted in this project are outlined below, as are a number of areas identified for potential future work.

7.1 Simulated-Source Tests

This research presents, for the first time, a systematic investigation of AE wave-propagation in large metal-to-metal adhesively-bonded joints. Wave-propagation has been investigated in three specimens; a single aluminium sheet, two aluminium sheets placed together without adhesive, and an adhesively-bonded specimen; both in-plane and out-of-plane sources were applied at varying distances from the sensor. Analysis in the time-frequency-domain by use of wavelet-transforms with overlaid dispersion-curves, and analysis in the frequency-domain by use of FFT and partial power techniques, allows the following general conclusions to be made:

- For the large specimens tested, the use of wavelet-transforms with modified dispersion-curves allows positive identification of reflections corresponding to each edge of the specimens, as well as Lamb-modes contained in the initial wave, while using only a single transducer and simple PLB source.
- It has been demonstrated that while the presence of an adhesive layer does cause the generation of additional wave types and slight variation in the dispersion characteristics of the fundamental symmetric and asymmetric waves, the experimentally identified wave-modes propagating in the specimens correspond well to the Lamb-modes of a single adherend, and appear to be largely insensitive to bond status. Standard Rayleigh-Lamb equations for the adherends can therefore be used to provide a reasonable approximation of wave-velocities in bonded specimens regardless of bond status or quality.
- The presence of an adhesive layer vastly increases the attenuation in a sheet-type specimen. In practical applications with large bond areas, the adhesive will greatly reduce the effective range of AE transmission, and the use of additional sensors may therefore be required.
- The presence of additional layers in the specimen results in significant changes in frequency-spectra recorded from application of the same source. Care must therefore be taken in the use of frequency-based methods of source characterisation, as the bond status of the AE propagation path may lead to erroneous identification of failure-mechanisms.
- The viscoelastic nature of the adhesive results in attenuation of high-frequency content in the adhesively-bonded specimen, leading to spectral content varying with propagation distance. This may be critical in AE testing of large specimens, as similar sources at different locations will produce vastly different signals, again potentially leading to erroneous identification of failure mechanisms.

7.2 Simulated-Source Void Tests

This work presents an initial investigation into the effects of the presence of void-type adhesive-bonding defects on AE propagation, and also investigates the use of a simulated AE source to

detect and size these defects, building on the work of previous authors' use of the technique to investigate distributed kissing-bond type adhesive defects. Tests have been conducted on defect-free reference specimens, and specimens with 10 mm x 10 mm and 40 mm x 40 mm defects. An investigation of typical time-domain, frequency-domain and time-frequency-domain parameters has been conducted to asses the effects of void-type features on these parameters, and to identify suitable parameters to use for defect identification. Artificial neural networks have also been developed, and shown to have much greater ability than typical AE parameters both to differentiate between known defect sizes and to predict defect sizes based on a set of training data. The conclusions which can be drawn from this study are as follows:

- The presence of void-type defects has a significant effect on AE propagation in an adhesively-bonded joint, causing significant variation in time-domain- and frequency-domain-based parameters. The presence of undetected defects within an adhesively-bonded specimen therefore has the potential to produce erroneous results if these parameters are used.
- The use of a simulated AE source offers huge potential to detect and size void-type defects in adhesive bonds, and therefore to assess the integrity of a bonded structure.
- Source-sensor configuration was seen to be critical when attempting defect detection. The best differentiation could be achieved in the configuration in which the defect made up the greatest proportion of the direct source-sensor propagation path.
- Out of the time-domain parameters examined in this study, AE energy provided the best discrimination between defects when a single configuration was considered. However when all configurations were considered, signal duration was found to be a more suitable parameter.
- Frequency content was also demonstrated to be sensitive to the presence of voids. Investigation of frequency spectra, partial powers and frequency centroids showed a general shift towards low-frequency content with increasing defect-size. Variation within the data and between configurations does, however, prevent any of these parameters from being a reliable classifier of defect size.
- Investigation of the time-frequency-domain reveals that the significant content of the signals is contained in the initial A_0 mode, with edge-reflections contributing minimal energy and only at low frequencies. Visual differentiation between defect types in the time-frequency-domain was not found to be possible, although subtle differences are present.
- The use of ANNs trained on raw time-domain data has been demonstrated to provide 100% accurate differentiation between the three defect types tested and has been able to predict nominal defect size with a mean error of only 0.921 mm. The addition of ANNs to the analysis methods previously utilised for defect detection by PLB source can yield a significant improvement in accuracy, as well as a major simplification of the analysis process, making it a much more viable technique.
- The use of ANNs trained using other parameters can also be successful, but is significantly more computationally expensive with no improvement in accuracy for the defects under consideration in this work.

7.3 Destructive Tests

The aim of this study was to investigate, for the first time, the AE wave-modes generated by Mode-I and Mode-II fracture of adhesively-bonded joints (aluminium metal-to-metal) and to identify whether modal analysis has the potential to discriminate between fracture-modes in a similar manner to which it has been used to discriminate between failure mechanisms of composites. Differentiation between fracture-modes is particularly important in adhesive joints due to the vast disparity in strength between joints in Mode-I and Mode-II loading. Assessment of loading conditions through AE could therefore provide a very useful tool for structural health monitoring. Understanding of the wave-modes generated by different fracture-modes is also important for accurate source-location. Due to the differing propagation velocities of the modes, it is critical that the velocity used in source-location calculations corresponds to the wave-mode for which arrival times have been detected. From the work conducted, the following has been concluded:

- Use of linear source-location to identify propagation-distances and theoretical dispersion-curves to identify arrival times has successfully identified regions of the time-frequency-domain corresponding to the fundamental S_0 and A_0 modes.
- Modal analysis, based on investigation of the amplitude-ratio of peaks in the continuous wavelet-transform corresponding to the S_0 and A_0 modes, has revealed clear differences between Mode-I and Mode-II/Mixed-mode fracture. While signals from both fracture-modes are dominated by the A_0 mode, the S_0 mode is generally greater in the Mode-II tests than in the Mode-I.
- As the amplitude of the A_0 mode is consistently higher than that of the S_0 mode, a suitably-chosen threshold can be used as a reliable method to select the arrival time of the A_0 mode for the purposes of source-location.
- Analysis of the amplitude-ratio of wavelet-transform peaks corresponding to the wave-modes has been demonstrated to reveal differences between the fracture-modes when considering the mean values over each test. However, due to the variation between hits within each test, and the overlap between results from the two test types, it is generally not possible to distinguish between fracture-modes based on a single hit. Future work should therefore focus on utilising the wavelet peak-ratio in combination with other parameters to provide a more robust classifier.

7.4 FEA of PLB Tests

A 3D dynamic finite element model has been developed to allow simulation of PLB tests conducted in extremely large (semi-infinite), multi-layer sheet-type specimens. The model has been validated against theory, with the generated AE signals being found to correspond well to the Lamb wave dispersion-curves calculated, both for the adherends and for the full structure. The model has also been validated against experimental results. It has been shown that the model can suitably approximate many aspects of the specimen behaviour, but is limited in its ability to accurately replicate the frequency-spectra recorded experimentally, in part due to the simplified representation of the sensor and in part due to the greatly simplified and approximated visco-elastic behaviour of the adhesive layer. The use of the simulations allowed the following conclusions to be made:

- It has been found that variation of the adhesive Young's moduli, representative of variation in the adhesive type or stage of cure, induces significant changes in the AE parameters. This has been demonstrated by simulating tests with adhesive Young's moduli corresponding to five commercially available adhesives.
  - It has been observed that while, for all of the specimens tested, the theoretical dispersion-curves for a single adherend do provide a good approximation of the wave arrival-times, the presence of an adhesive layer does reduce the wave-velocity somewhat. It has been shown that the difference in wave-velocity varies with the Young's moduli of the adhesive. For the adhesive Young's moduli tested, the wave-velocity in a bonded specimen was found to be reduced from that of a single aluminium adherend by between 4.8% and 7.4%.
  - Peak amplitude and AE energy have also both been demonstrated to be significantly affected by the Young's modulus of the adhesive, with higher Young's modulus resulting in lower amplitude and energy. The range of values tested resulted in variations of 30% and 66% for peak amplitude and energy respectively.
  - The frequency content is also seen to be affected by the Young's moduli of the adhesive. Increasing Young's moduli results in increasing peak-frequency, frequency centroid, and thus weighted peak frequency, with these features seeing increases of 3%, 33% and 15% respectively.

  It can therefore be concluded that any change in the adhesive used can have a significant effect on the result of any AE analyses using frequency-, energy-, amplitude- or even modal-analysis-based methods. Testing and analysis methods therefore cannot be simply transferred from one application to another without significant consideration being given to the properties of the specific adhesive being used in each case.
- The thickness of the adhesive layer has also been demonstrated to have significant effects on AE propagation. Simulations have been conducted with adhesive thicknesses ranging from 0.25 mm to 2 mm.
  - As previously mentioned, the wave-velocity in a bonded specimen is reduced compared to that of a single adherend. Over the thickness-range tested, it was found that the wave-velocity decreases with increasing adhesive thickness, with the difference between the bonded specimens and a single adherend ranging from only 1.17% to 10%. The relationship is, however, logarithmic, meaning that it appears that increasing adhesive thickness beyond a certain limit will produce no further change in wave-velocity. In the case of the simulations conducted this limit was found to be around 1.5 mm. The behaviour of particularly thin adhesive layers of less than 0.25 mm has not been explored, but remains a topic of interest for future work.
  - The frequency content is also affected by adhesive thickness, with increases in thickness reducing the level of high frequency content. Considering the parameters of peak-frequency, frequency-centroid and weighted-peak-frequency, this also appears to be an logarithmic relationship with little variation as the adhesive thickness increases past 1.5 mm. The variation over lower thicknesses is however significant, with the frequency-centroid reducing by around 30% and weighted-peak-frequency reducing by around 15%. Peak-frequency has remained unaffected across all thicknesses tested.

  - Increasing thickness of the adhesive layer results in steeper attenuation, in terms of energy and peak amplitudes, due to the increased overall volume for geometric attenuation and the increased volume of viscoelastic material, which features a high level of material-based attenuation.
  - Increased thickness of the adhesive layer results in an increased initial surface displacement under the force of a PLB source, thus resulting in increased peak amplitude and energy in the near-field, before the effects of the increased attenuation take effect. This factor should be taken into account in any future works in which a PLB source may be used for assessment of an adhesive specimen.

- Specimens containing void-type defects of different sizes have been simulated. It is concluded that the model developed is capable of simulating the global behaviour of large defects 10+ (mm), but may not have sufficient resolution to resolve defects significantly smaller than this. The following conclusions can however be drawn:

  - The wave-modes present in a specimen containing void-type defects such as those modelled remain the same as in a defect-free specimen, with no sign of mode-conversion or generation of additional modes. The wave velocities remain reduced from those of a single adherend, but the larger the defect, the closer the effective velocity becomes to that of a single adherend, as the wave-velocity will increase over the defect region.
  - Large defects ($> 10\ mm$) result in increased AE energy and peak-amplitude due to the reduced attenuation over the defect region.
  - Small defects may result in reduced amplitude and AE energy due to reflections of the waves propagating in the adhesive layer. Further investigation of this effect is however required to confirm this hypothesis.
  - The presence of a void results in increased peak amplitudes being recorded on sensors placed over the void region.
  - The presence of a void results in increased energy being recorded by the sensors placed over the ends of the void region. This effect is assumed to be due to the effects of wave reflection, refraction and interference, but further investigation of this effect is still required.

7.5 FEA of Destructive Tests

A 2D dynamic finite element model has been developed to simulate AE generation and propagation from localised adhesive failure in a mixed-mode-bending test. A range of mode-mixities have been tested to examine the relationship between fracture-mode and the excited wave-modes. It has been concluded that:

- For the range of mode-mixities tested, the A_0 mode of the adherends remains the dominant fundamental mode in all cases. It is anticipated that it will remain the dominant fundamental mode for any adhesive failure, regardless of fracture-mode.

- The multi-layer modes which propagate in the bonded region of the specimens can also be clearly identified, and have been shown to be highly sensitive to mode-mixity. One of these modes actually increases to an amplitude exceeding that of the fundamental A_0 mode of the adherends at high mode-mixity.

- The relative contributions of the S_0 and A_0 modes vary dependent on the mode-mixity. Increasing the Mode-I loading component increases the relative amplitude of the A_0 mode, while increasing the Mode-II loading component results in relative increases in the S_0 mode. This has been observed from examination of the time-frequency-domain, and quantified by the use of wavelet-transform peak-amplitude ratios and by use of time-windowed energy-ratios relating to the S_0 and A_0 modes. Either of these techniques provides a unique classifier for the mode-mixity, assuming all other variables remain fixed.
- The relative contributions of the multi-layer modes also vary dependent on the mode-mixity, with some modes exhibiting much greater variation than is seen in the fundamental modes of the adherends. These modes may therefore provide a much more usable classifier of fracture-mode, but are limited in their use, as these modes only propagate within the bond region, unlike the fundamental modes of the adherends which will continue to propagate beyond the boundaries of the bonded region.
- It has been demonstrated that other variables are also capable of inducing changes in the wave-modes recorded. The size of the localised debond region has been shown to affect the modes excited, with increasing debonding area leading to a relative increase in the A_0 mode. While this is the only other variable to be investigated in this study, it is expected based on findings in literature, that a number of other variables will also induce changes to the excited wave-modes. It is therefore proposed that modal analysis will need to be used in combination with other features to allow reliable classification in an experimental situation in which other parameters may vary.

7.6 Future Work

While this study has successfully drawn a number of conclusions relating to various aspects of AE testing of adhesively-bonded specimens, it has highlighted a number of areas which are worthy of further investigation in future work.

- This study has added to the previously conducted work [9] investigating the use of a PLB source with an AE system for detection and characterisation of adhesive bonding defects by investigating voids as an additional defect-type, and by introducing analysis by artificial neural network. There are also multiple other defect types, specimen materials and geometries which are worth investigation using this technique. The ultimate aim would be to develop methods to differentiate between multiple different defect types and sizes, a task which will become progressively more challenging as the variety of defects included in studies increases.
- The simulations conducted in this study have implemented a Generalised Maxwell type viscoelastic model to include the viscoelastic behaviour of the adhesive, which leads to frequency-dependent attenuation. While this theoretically allows a much more accurate simulation than the use of other methods such as Rayleigh damping, the difficulty in finding suitable values for the materials used significantly restricts the improvement that this actually offers in practice. If simulation of AE or ultrasound techniques for inspection of adhesive bonding is to become a more mainstream approach, it would be beneficial for a database to be constructed with the viscoelastic properties of materials recorded over a suitable frequency-range. Ultimately, such a database could be integrated into the commercial

finite element packages in the same way that other material properties for common materials are included.

- Further investigation is needed into the interaction of AE waves with adhesive defects, particularly with regard to wave-reflection, -refraction and -interference at the ends/edges of the defects, as the model used in this study used a simplified geometry and did not have sufficient resolution to accurately resolve the wave-propagation in these regions.

- The simulations of adhesive failure during mixed-mode-testing conducted in this study have used a simplified source-model which assumes perfect instantaneous debonding across a highly-localised region, with debonding occurring at an arbitrarily specified load which is not directly derived from the properties of a real adhesive. While this provides a step up from a dipole source as used in many previous studies, further investigation of AE occurring from adhesive failure should focus on implementing a more realistic source-model. This could be achieved by implementation of a cohesive-zone model at the fracture plane, as has been demonstrated by Sause et al. [116].

- Future work using FEA to investigate adhesive-bond failure should aim towards determining the effects of all potential variables and identifying methods to differentiate between them. So far, mode-mixity and debond size have been investigated. Further investigations could include source depth (adhesive failure from top adherend or bottom adherend), source type (adhesive or cohesive failure),and adhesive and adherend geometries and material properties. With use of a 3D model it would also be possible to investigate variations in the geometry of the fracture region, which is of significance as real adhesive failure is rarely completely uniform.

Appendices

Appendix A

Sensor Calibration Certificates

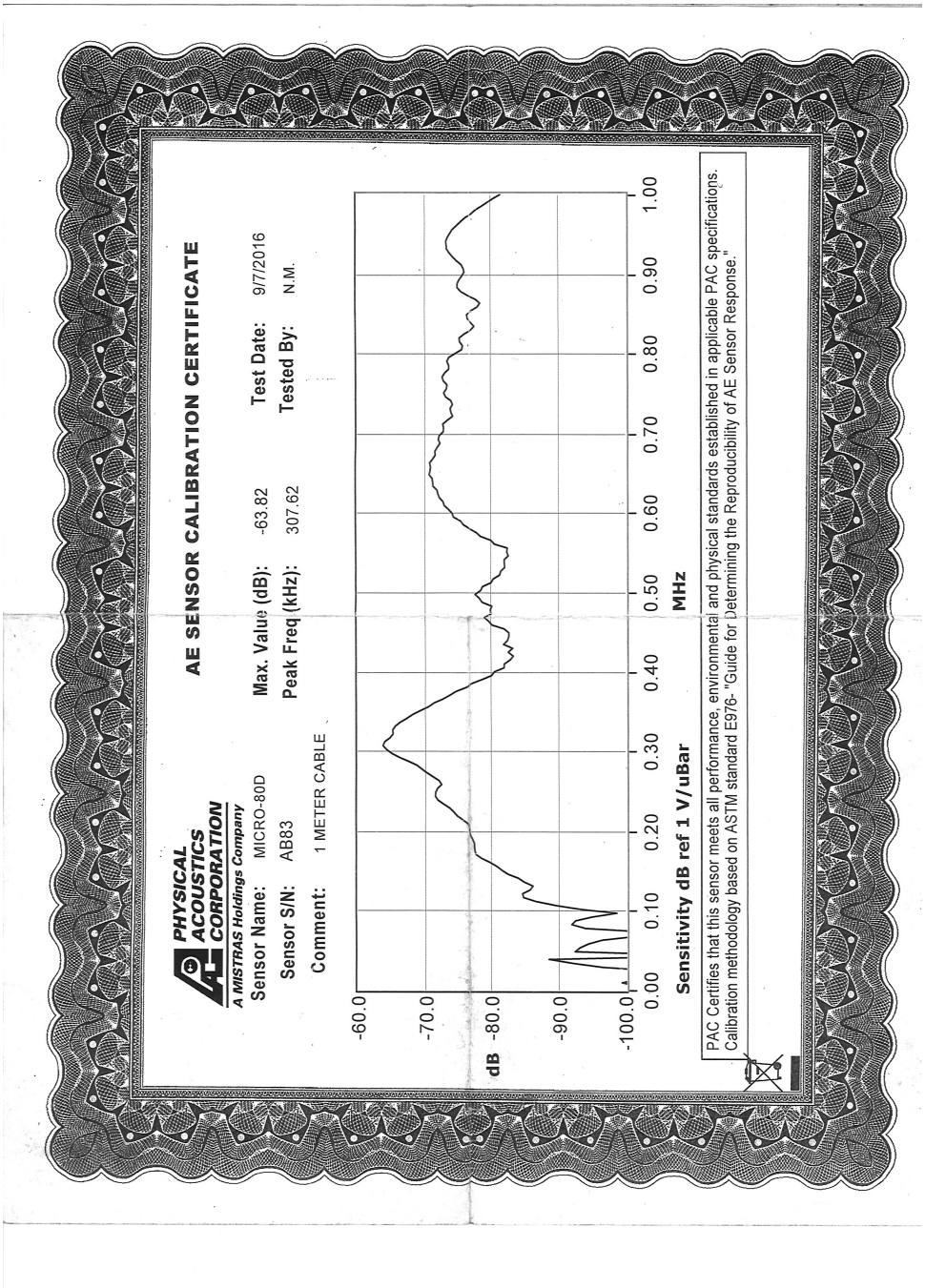
PHYSICAL ACOUSTICS CORPORATION
A MISTRAS Holdings Company
AE SENSOR CALIBRATION CERTIFICATE
Sensor Name: MICRO-80D
Sensor S/N: AB83
Comment: 1 METER CABLE
Max. Value (dB): -63.82
Peak Freq (kHz): 307.62
Test Date: 9/7/2016
Tested By: N.M.
-60.0
-70.0
-80.0
-90.0
-100.0
dB
0.00 0.10 0.20 0.30 0.40 0.50 0.60 0.70 0.80 0.90 1.00
Sensitivity dB ref 1 V/uBar
MHz
PAC Certifies that this sensor meets all performance, environmental and physical standards established in applicable PAC specifications.
Calibration methodology based on ASTM standard E976- "Guide for Determining the Reproducibility of AE Sensor Response."

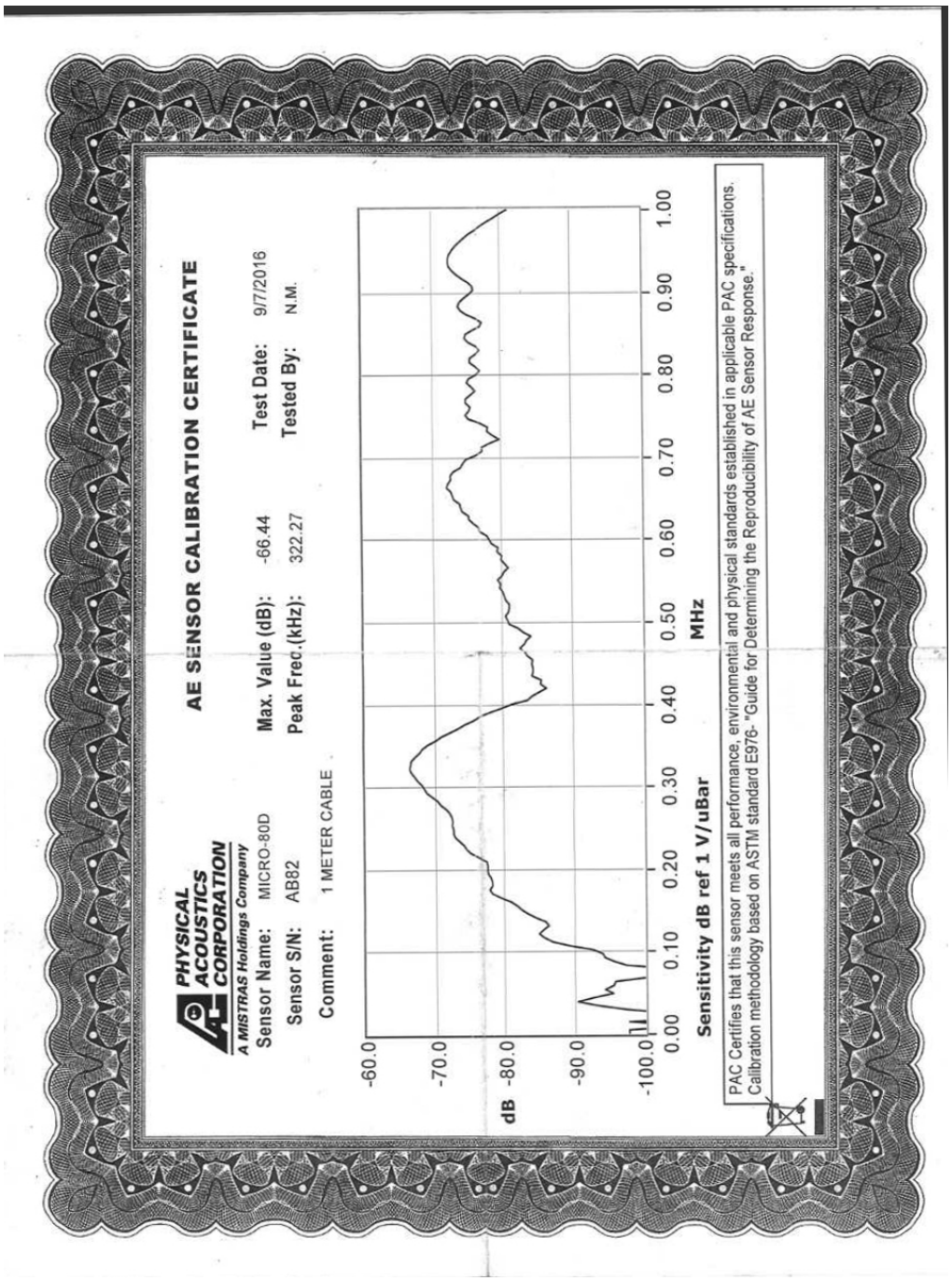
PHYSICAL ACOUSTICS CORPORATION
A MISTRAS Holdings Company
AE SENSOR CALIBRATION CERTIFICATE
Sensor Name: MICRO-80D
Sensor S/N: AB82
Comment: 1 METER CABLE
Max. Value (dB): -66.44
Peak Freq.(kHz): 322.27
Test Date: 9/7/2016
Tested By: N.M.
dB
-60.0
-70.0
-80.0
-90.0
-100.0
0.00 0.10 0.20 0.30 0.40 0.50 0.60 0.70 0.80 0.90 1.00
MHz
Sensitivity dB ref 1 V/uBar
PAC Certifies that this sensor meets all performance, environmental and physical standards established in applicable PAC specifications.
Calibration methodology based on ASTM standard E976- "Guide for Determining the Reproducibility of AE Sensor Response."

References

[1] B. Wong, "Non-destructive evaluation (NDE) of composites: detecting delamination defects using mechanical impedance, ultrasonic and infrared thermographic techniques," in *Non-Destructive Evaluation (NDE) of Polymer Matrix Composites*. Elsevier, 2013, pp. 279–308e.

[2] K. Heller, L. Jacobs, and J. Qu, "Characterization of adhesive bond properties using Lamb waves," *NDT & E International*, vol. 33, no. 8, pp. 555–563, 2000.

[3] R. Seifried, L. J. Jacobs, and J. Qu, "Propagation of guided waves in adhesive bonded components," *NDT & E International*, vol. 35, no. 5, pp. 317–328, 2002.

[4] L. F. Da Silva, A. Öchsner, and R. D. Adams, *Handbook of adhesion technology*. Springer Science & Business Media, 2011.

[5] W. Broughton and R. Mera, "Environmental degradation of adhesive joints: accelerated testing." *Project PAJ3 - Combined Cyclic Loading and Hostile Environments 1996-1999*, vol. 7, 1999.

[6] Loctite, "Loctite EA3090 technical data sheet," *Henkel*, 2014.

[7] K. Subrahmanian and F. Dubouloz, "Adhesives for bonding wind turbine blades," *Reinforced Plastics*, 2009.

[8] M. G. Droubi, A. Stuart, J. Mowat, C. Noble, A. K. Prathuru, and N. H. Faisal, "Acoustic emission method to study fracture (mode-I, II) and residual strength characteristics in composite-to-metal and metal-to-metal adhesively bonded joints," *The Journal of Adhesion*, vol. 94, no. 5, pp. 347–386, 2018.

[9] A. Prathuru, "Structural and residual strength analysis of metal-to-metal adhesively bonded joints," Ph.D. dissertation, School of Engineering, Robert Gordon University, 2019.

[10] R. Marks, A. Clarke, C. Featherston, C. Paget, and R. Pullin, "Lamb wave interaction with adhesively bonded stiffeners and disbonds using 3d vibrometry," *Applied Sciences*, vol. 6, no. 1, p. 12, 2016.

[11] ASTM, "976," standard guide for determining the reproducibility of acoustic emission sensor response," *ASTM Book of Standards*, pp. 03–03, 1993.

[12] L. F. Da Silva, A. Öchsner, and R. D. Adams, "Introduction to adhesive bonding technology," *Handbook of adhesion technology*, pp. 1–7, 2018.

[13] L. J. Hart-Smith, "Adhesively bonded joints in aircraft structures," in *Handbook of adhesion technology*, 2011.

[14] C. Désagulier, "Aerospace industry," in *Handbook of adhesion technology*, 2011.

[15] Y. Suzuki, "Railway industry," in *Handbook of Adhesion Technology*, 2011.

[16] B. Burchardt, "Automotive industry," in *Handbook of Adhesion Technology*, 2011.

[17] P. Davies, "Marine industry," in *Handbook of Adhesion Technology*, 2011.

[18] E. Papon, "14 adhesive families," *Handbook of Adhesion Technology*, p. 315, 2011.

[19] A. V. Pocius and D. A. Dillard, *Adhesion science and engineering: surfaces, chemistry and applications*. Elsevier, 2002.

[20] W. H. Carothers, "Polymers and polyfunctionality," *Transactions of the Faraday Society*, vol. 32, pp. 39–49, 1936.

[21] M. Peschka, "Equipment for adhesive bonding," in *Handbook of Adhesion Technology*.

[22] A. Lutz, "Preparation for bonding," in *Handbook of Adhesion Technology*.

[23] NTSB, "Aircraft accident report, aloha airlines, flight 243, boeing 737-200, n73711, near maui, hawaii," 2088.

[24] E. Karachalios, R. Adams, and L. F. da Silva, "The behaviour of single lap joints under bending loading," *Journal of Adhesion Science and Technology*, vol. 27, no. 16, pp. 1811–1827, 2013.

[25] H. Nayeb-Hashemi and J. Rossettos, "Nondestructive evaluation of adhesively bonded joints by acousto-ultrasonic technique and acoustic emission," *Journal of Acoustic Emission*, vol. 12, no. 1–2, pp. 1–14, 1994.

[26] R. Adams and N. Peppiatt, "Stress analysis of adhesive bonded tubular lap joints," *The Journal of Adhesion*, vol. 9, no. 1, pp. 1–18, 1977.

[27] L. F. Silva, "Design rules and methods to improve joint strength," in *Handbook of adhesion technology*, 2011.

[28] M. Blanch and A. Dutton, "Acoustic emission monitoring of field tests of an operating wind turbine," in *Key Engineering Materials*, vol. 245. Trans Tech Publ, 2003, pp. 475–482.

[29] A. Huerta Herraiz, A. Pliego Marugan, F. P. Garcia Marquez, I. Segovia Ramirez, and M. Papaelias, "A novel walking robot based system for non-destructive testing in wind turbines," 2019.

[30]

[31] T. G. Álvarez-Arenas and J. Camacho, "Air-coupled and resonant pulse-echo ultrasonic technique," *Sensors*, vol. 19, no. 10, p. 2221, 2019.

[32] N. Perez, "Linear-elastic fracture mechanics," in *Fracture Mechanics*. Springer, 2017, pp. 79–130.

[33] K. Ono, "Acoustic emission," in *Springer Handbook of Acoustics*. Springer, 2014, pp. 1209–1229.

[34] C. U. Grosse and M. Ohtsu, *Acoustic emission testing*. Springer Science & Business Media, 2008.

[35] S. Heverdine, "Use of acoustic emission in inspection investigations wtthtn tct."

[36] W. Demtröder, "Mechanical oscillations and waves," in *Mechanics and Thermodynamics*. Springer, 2017, pp. 321–379.

[37] H. Kolsky, "Stress waves in solids," 1953.

[38] K. Miller and E. Hill, "Nondestructive testing handbook, acoustic emission testing," vol. 6, 2005.

[39] T. Holroyd, "The acoustic emission and ultrasonic monitoring handbook," 2000.

[40] Z. Su and L. Ye, "Fundamentals and analysis of Lamb waves," in *Identification of Damage Using Lamb Waves*. Springer, 2009, pp. 15–58.

[41] C. J. Hellier, *Handbook of nondestructive evaluation*. McGraw-Hill Education, 2013.

[42] M. N. El-Shaib *et al.*, "Predicting acoustic emission attenuation in solids using ray-tracing within a 3d solid model," Ph.D. dissertation, Heriot-Watt University UK, 2013.

[43] P. Kelly, *Solid mechanics part I: An introduction to solid mechanics. Solid mechanics lecture notes*, 2013 (accessed June 30, 2020). [Online]. Available: http://homepages.engineering.auckland.ac.nz/~pkel015/SolidMechanicsBooks/Part_I/BookSM_Part_I/10_Viscoelasticity/10_Viscoelasticity_Complete.pdf

[44] M. G. Sause, *In situ monitoring of fiber-reinforced composites: theory, basic concepts, methods, and applications*. Springer, 2016, vol. 242.

[45] E. Njuhovic, M. Bräu, F. Wolff-Fabris, K. Starzynski, and V. Altstädt, "Identification of interface failure mechanisms of metallized glass fibre reinforced composites using acoustic emission analysis," *Composites Part B: Engineering*, vol. 66, pp. 443–452, 2014.

[46] E. Njuhovic, M. Bräu, F. Wolff-Fabris, K. Starzynski, and V. Altstädt, "Identification of failure mechanisms of metallised glass fibre reinforced composites under tensile loading using acoustic emission analysis," *Composites Part B: Engineering*, vol. 81, pp. 1–13, 2015.

[47] M. Kempf, O. Skrabala, and V. Altstädt, "Acoustic emission analysis for characterisation of damage mechanisms in fibre reinforced thermosetting polyurethane and epoxy," *Composites Part B: Engineering*, vol. 56, pp. 477–483, 2014.

[48] K. M. Bak and K. Kalaichelvan, "Evaluation of failure modes of pure resin and single layer of adhesively bonded lap joints using acoustic emission data," *Transactions of the Indian Institute of Metals*, vol. 68, no. 1, pp. 73–82, 2015.

[49] M. G. Droubi, N. H. Faisal, F. Orr, J. A. Steel, and M. El-Shaib, "Acoustic emission method for defect detection and identification in carbon steel welded joints," *Journal of constructional steel research*, vol. 134, pp. 28–37, 2017.

[50] H. Suzuki, T. Kinjo, Y. Hayashi, M. Takemoto, K. Ono, and Y. Hayashi, "Wavelet transform of acoustic emission signals," *Journal of acoustic emission*, vol. 14, pp. 69–84, 1996.

[51] D. Gabor, "Theory of communication. part 1: The analysis of information," *Journal of the Institution of Electrical Engineers-Part III: Radio and Communication Engineering*, vol. 93, no. 26, pp. 429–441, 1946.

[52] G. Kaiser, *A friendly guide to wavelets*. Springer Science & Business Media, 2010.

[53] J. Vallen, "Vallen wavelet software, version r2005. 1121," *Vallen-Systeme GmbH, Munich, Germany. Available as http: // www. valleh. de / wavelet / index. html*, 2015.

[54] A. Majkowski, M. Kołodziej, and R. J. Rak, "Joint time-frequency and wavelet analysis-an introduction," *Metrology and Measurement Systems*, vol. 21, no. 4, 2014.

[55] B. Burks and M. A. Hamstad, "On the anisotropic attenuation behavior of the flexure mode of carbon fiber composites," in *19th International Conference on Composite Materials*, 2013, pp. 1–9.

[56] B. Burks and M. Hamstad, "The impact of solid–fluid interaction on transient stress wave propagation due to acoustic emissions in multi-layer plate structures," *Composite Structures*, vol. 117, pp. 411–422, 2014.

[57] M. A. Hamstad, "Comparison of wavelet transform and Choi-Williams distribution to determine group velocities for different acoustic emission sensors," *J. Acoust. Emiss*, vol. 26, pp. 40–59, 2008.

[58] M. R. Gorman and W. H. Prosser, "AE source orientation by plate wave analysis," *NASA Technical Report*, 1991.

[59] M. A. Hamstad, A. O'Gallagher, and J. M. Gary, "Examination of the application of a wavelet transformation to acoustic emission signals: part 1. source identification," *Journal of Acoustic Emission*, vol. 20, no. Journal of Acoustic Emission, 2002.

[60] T. Le Gall, T. Monnier, C. Fusco, N. Godin, and S.-E. Hebaz, "Towards quantitative acoustic emission by finite element modelling: Contribution of modal analysis and identification of pertinent descriptors," *Applied Sciences*, vol. 8, no. 12, p. 2557, 2018.

[61] X. Zhang, N. Feng, Y. Wang, and Y. Shen, "An analysis of the simulated acoustic emission sources with different propagation distances, types and depths for rail defect detection," *Applied Acoustics*, vol. 86, pp. 80–88, 2014.

[62] M. Surgeon and M. Wevers, "Modal analysis of acoustic emission signals from CFRP laminates," *Ndt & e International*, vol. 32, no. 6, pp. 311–322, 1999.

[63] J. Martínez-Jequier, A. Gallego, E. Suárez, F. J. Juanes, and Á. Valea, "Real-time damage mechanisms assessment in CFRP samples via acoustic emission Lamb wave modal analysis," *Composites Part B: Engineering*, vol. 68, pp. 317–326, 2015.

[64] A. Ebrahimkhanlou and S. Salamone, "Acoustic emission source localization in thin metallic plates: A single-sensor approach based on multimodal edge reflections," *Ultrasonics*, vol. 78, pp. 134–145, 2017.

[65] A. Ebrahimkhanlou and S. Salamone, "Single-sensor acoustic emission source localization in plate-like structures using deep learning," *Aerospace*, vol. 5, no. 2, p. 50, 2018.

[66] M. T. I. Khan, "Structural health monitoring by acoustic emission," *Structural Health Monitoring from Sensing to Processing*, p. 23, 2018.

[67] M. A. Hamstad and J. Gary, "A wavelet transform applied to acoustic emission signals: part 2: source location," in *Journal of Acoustic Emission*. Citeseer, 2002.

[68] M. G. Baxter, R. Pullin, K. M. Holford, and S. L. Evans, "Delta T source location for acoustic emission," *Mechanical systems and signal processing*, vol. 21, no. 3, pp. 1512–1520, 2007.

[69] M. Surgeon and M. Wevers, "One sensor linear location of acoustic emission events using plate wave theories," *Materials Science and Engineering: A*, vol. 265, no. 1-2, pp. 254–261, 1999.

[70] K. M. Holford and D. Carter, "Acoustic emission source location," in *Key Engineering Materials*, vol. 167. Trans Tech Publ, 1999, pp. 162–171.

[71] F. Pashmforoush, R. Khamedi, M. Fotouhi, M. Hajikhani, and M. Ahmadi, "Damage classification of sandwich composites using acoustic emission technique and k-means genetic algorithm," *Journal of Nondestructive Evaluation*, vol. 33, no. 4, pp. 481–492, 2014.

[72] R. Gutkin, C. Green, S. Vangrattanachai, S. Pinho, P. Robinson, and P. Curtis, "On acoustic emission for failure investigation in CFRP: Pattern recognition and peak frequency analyses," *Mechanical systems and signal processing*, vol. 25, no. 4, pp. 1393–1407, 2011.

[73] N. Godin, S. Huguet, R. Gaertner, and L. Salmon, "Clustering of acoustic emission signals collected during tensile tests on unidirectional glass/polyester composite using supervised and unsupervised classifiers," *Ndt & E International*, vol. 37, no. 4, pp. 253–264, 2004.

[74] F. Pashmforoush, M. Fotouhi, and M. Ahmadi, "Damage characterization of glass/epoxy composite under three-point bending test using acoustic emission technique," *Journal of materials engineering and performance*, vol. 21, no. 7, pp. 1380–1390, 2012.

[75] T. Bohmann, M. Schlamp, and I. Ehrlich, "Acoustic emission of material damages in glass fibre-reinforced plastics," *Composites Part B: Engineering*, vol. 155, pp. 444–451, 2018.

[76] J. Destouesse, M. Diakhate, C. Badulescu, D. Thévenet, M. Stackler, W. Albouy, and N. Carrere, "Cluster analysis of acoustic emission data to investigate the damage evolution in modified scarf joint under bi-axial loading," *The Journal of Adhesion*, pp. 1–19, 2018.

[77] R. De Oliveira and A. Marques, "Health monitoring of FRP using acoustic emission and artificial neural networks," *Computers & structures*, vol. 86, no. 3-5, pp. 367–373, 2008.

[78] C. S. Kumar, V. Arumugam, R. Sengottuvelusamy, S. Srinivasan, and H. Dhakal, "Failure strength prediction of glass/epoxy composite laminates from acoustic emission parameters using artificial neural network," *Applied Acoustics*, vol. 115, pp. 32–41, 2017.

[79] S. Kalafat and M. G. Sause, "Acoustic emission source localization by artificial neural networks," *Structural Health Monitoring*, vol. 14, no. 6, pp. 633–647, 2015.

[80] G. Caprino, V. Lopresto, C. Leone, and I. Papa, "Acoustic emission source location in unidirectional carbon-fiber-reinforced plastic plates with virtually trained artificial neural networks," *Journal of Applied Polymer Science*, vol. 122, no. 6, pp. 3506–3513, 2011.

[81] Z. Wang, P. Willett, P. R. DeAguiar, and J. Webster, "Neural network detection of grinding burn from acoustic emission," *International Journal of Machine Tools and Manufacture*, vol. 41, no. 2, pp. 283–309, 2001.

[82] J.-S. Kwak and M.-K. Ha, "Neural network approach for diagnosis of grinding operation by acoustic emission and power signals," *Journal of Materials Processing Technology*, vol. 147, no. 1, pp. 65–71, 2004.

[83] K. Jemielniak, L. Kwiatkowski, and P. Wrzosek, "Diagnosis of tool wear based on cutting forces and acoustic emission measures as inputs to a neural network," *Journal of Intelligent Manufacturing*, vol. 9, no. 5, pp. 447–455, 1998.

[84] T. Boczar, S. Borucki, A. Cichon, and D. Zmarzly, "Application possibilities of artificial neural networks for recognizing partial discharges measured by the acoustic emission method," *IEEE Transactions on Dielectrics and Electrical Insulation*, vol. 16, no. 1, pp. 214–223, 2009.

[85] Y. A. Dzenis and I. Saunders, "On the possibility of discrimination of mixed mode fatigue fracture mechanisms in adhesive composite joints by advanced acoustic emission analysis," *International journal of fracture*, vol. 117, no. 4, pp. 23–28, 2002.

[86] S. Tanary, Y. Haddad, A. Fahr, and S. Lee, "Nondestructive evaluation of adhesively bonded joints in graphite/epoxy composites using acousto-ultrasonics," *Journal of Pressure Vessel Technology*, 1992.

[87] A. J. Brunner, G. P. Terrasi, T. Vallée, and T. Keller, "Acoustic emission analysis and acousto-ultrasonics for damage detection in GFRP adhesive joints," in *Proceedings 28th European conference on acoustic emission, European working group on acoustic emission*, 2008, p. 100e105.

[88] L. Michalcová and M. Kadlec, "Carbon/epoxy composite delamination analysis by acoustic emission method under various environmental conditions," *Engineering Failure Analysis*, vol. 69, pp. 88–96, 2016.

[89] Z. Chen, D. Li, Y. Li, and Q. Feng, "Damage analysis of FRP/steel composite plates using acoustic emission," *Pacific Science Review*, vol. 16, no. 3, pp. 193–200, 2014.

[90] A. Magalhaes and M. De Moura, "Application of acoustic emission to study creep behaviour of composite bonded lap shear joints," *NDT & E International*, vol. 38, no. 1, pp. 45–52, 2005.

[91] J. J. Andrew, V. Arumugam, D. Bull, and H. N. Dhakal, "Residual strength and damage characterization of repaired glass/epoxy composite laminates using AE and DIC," *Composite Structures*, vol. 152, pp. 124–139, 2016.

[92] F. Ducept, P. Davies, and D. Gamby, "Mixed mode failure criteria for a glass/epoxy composite and an adhesively bonded composite/composite joint," *International Journal of Adhesion and Adhesives*, vol. 20, no. 3, pp. 233–244, 2000.

[93] K. M. Bak, K. Kalaichelvan, G. Vijayaraghavan, M. Dinesh, and V. Arumugam, "Study on the effect of adhesive thickness of single lap joints using acoustic emission and fea," *Insight-Non-Destructive Testing and Condition Monitoring*, vol. 55, no. 1, pp. 35–41, 2013.

[94] K. M. Bak, K. KalaiChelvan, G. Vijayaraghavan, and B. Sridhar, "Acoustic emission wavelet transform on adhesively bonded single-lap joints of composite laminate during tensile test," *Journal of Reinforced Plastics and Composites*, vol. 32, no. 2, pp. 87–95, 2013.

[95] D. Croccolo and R. Cuppini, "A methodology to estimate the adhesive bonding defects and the final releasing moments in conical joints based on the acoustic emissions technique," *International journal of adhesion and adhesives*, vol. 26, no. 7, pp. 490–497, 2006.

[96] D. Croccolo and R. Cuppini, "Adhesive defect density estimation applying the acoustic emission technique," *International journal of adhesion and adhesives*, vol. 29, no. 3, pp. 234–239, 2009.

[97] G. Curtis, "Acoustic emission energy relates to bond strength," *Non-Destructive Testing*, vol. 8, no. 5, pp. 249–257, 1975.

[98] M. G. Droubi, J. Mcafee, R. C. Horne, S. Walker, C. Klaassen, A. Crawford, A. K. Prathuru, and N. H. Faisal, "Mixed-mode fracture characteristics of metal-to-metal adhesively bonded joints: experimental and simulation methods," *Procedia Structural Integrity*, vol. 5, pp. 40–47, 2017.

[99] J. Galy, J. Moysan, A. El Mahi, N. Ylla, and N. Massacret, "Controlled reduced-strength epoxy-aluminium joints validated by ultrasonic and mechanical measurements," *International Journal of Adhesion and Adhesives*, vol. 72, pp. 139–146, 2017.

[100] K. Senthil, A. Arockiarajan, and R. Palaninathan, "Experimental determination of fracture toughness for adhesively bonded composite joints," *Engineering Fracture Mechanics*, vol. 154, pp. 24–42, 2016.

[101] J. Manterola, M. Aguirre, J. Zurbitu, J. Renart, A. Turon, and I. Urresti, "Using acoustic emissions (AE) to monitor mode I crack growth in bonded joints," *Engineering Fracture Mechanics*, vol. 224, p. 106778, 2020. [Online]. Available: http://www.sciencedirect.com/science/article/pii/S0013794419309002

[102] R. Liu, G.-T. Shen, P.-f. Zhang, and W. Zhou, "Acoustic emission response and progressive failure behaviors of composite adhesively bonded joints loaded by mode I and II," *Materials Research Express*, vol. 7, no. 1, p. 015307, 2019.

[103] C. Santulli and A. Lucia, "Relation between acoustic emission analysis during cure cycle and bonded joints performances," *Ndt & E International*, vol. 32, no. 6, pp. 333–341, 1999.

[104] J. Gary and M. A. Hamstad, "On the far-field structure of waves generated by a pencil lead break on a thin plate," *Journal of acoustic emission*, vol. 12, no. 3-4, pp. 157–170, 1994.

[105] M. Hamstad, J. Gary, and A. O'GALLAGHER, "Far-field acoustic emission waves by three-dimensional finite element modeling of pencil-lead breaks on a thick plate," *Journal of acoustic emission*, vol. 14, no. 2, pp. 103–114, 1996.

[106] W. Prosser, M. Hamstad, J. Gary, and A. O'Gallagher, "Finite element and plate theory modeling of acoustic emission waveforms," *Journal of Nondestructive Evaluation*, vol. 18, no. 3, pp. 83–90, 1999.

[107] W. Prosser, M. A. Hamstad, J. Gary, and A. OGallagher, "Reflections of AE waves in finite plates: finite element modeling and experimental measurements," *Journal of Acoustic Emission*, vol. 17, no. 1-2, pp. 37–47, 1999.

[108] M. A. Hamstad, "On Lamb modes as a function of acoustic emission source rise time." *Journal of Acoustic Emission*, vol. 28, 2010.

[109] M. Sause and S. Horn, "Simulation of acoustic emission in planar carbon fiber reinforced plastic specimens," *Journal of Nondestructive Evaluation*, vol. 29, no. 2, pp. 123–142, 2010.

[110] M. G. Sause and S. Horn, "Simulation of Lamb wave excitation for different elastic properties and acoustic emission source geometries." *Journal of Acoustic Emission*, vol. 28, 2010.

[111] P. Hora and O. Červená, "Acoustic emission source modeling," *Applied and Computational Mechanics*, vol. 4, no. 1, 2010.

[112] M. G. Sause, "Investigation of pencil-lead breaks as acoustic emission sources." *Journal of acoustic emission*, vol. 29, 2011.

[113] M. G. Sause, "Influence of internal discontinuities on ultrasonic signal propagation in carbon fiber reinforced plastics," in *30th European Conference on Acoustic Emission Testing & 7th International Conference on Acoustic Emission*, 2012.

[114] M. Sause, "Acoustic emission signal propagation in damaged composite structures," *Journal of Acoustic Emission*, vol. 31, no. 1, pp. 1–18, 2013.

[115] M. G. Sause, M. A. Hamstad, and S. Horn, "Finite element modeling of Lamb wave propagation in anisotropic hybrid materials," *Composites Part B: Engineering*, vol. 53, pp. 249–257, 2013.

[116] M. G. Sause and S. Richler, "Finite element modelling of cracks as acoustic emission sources," *Journal of nondestructive evaluation*, vol. 34, no. 1, p. 4, 2015.

[117] M. A. Hamstad, "Modeled transverse surface AE signals from buried dipole sources in a polymer rod." *Journal of Acoustic Emission*, vol. 33, 2016.

[118] S. Sikdar, W. Ostachowicz, and J. Pal, "Damage-induced acoustic emission source identification in an advanced sandwich composite structure," *Composite Structures*, vol. 202, pp. 860–866, 2018.

[119] A. Ghouri, Y. Alajlani, N. Ahmadi, D. Hutson, and K. Kirk, "Investigation of Lamb wave modes using broadband thin-film transducers and finite element modelling," *International Journal of Condition Monitoring*, vol. 8, no. 4, pp. 95–99, 2018.

[120] R. Blake and L. Bond, "Rayleigh wave scattering from surface features: wedges and downsteps," *Ultrasonics*, vol. 28, no. 4, pp. 214–228, 1990.

[121] M. A. Hamstad, A. O'Gallagher, and J. M. Gary, "Modeling of buried monopole and dipole sources of acoustic emission with a finite element technique," *Journal of acoustic emission*, vol. 17, no. Journal of Acoustic Emission, 1999.

[122] C. Scruby, H. Wadley, and J. Hill, "Dynamic elastic displacements at the surface of an elastic half-space due to defect sources," *Journal of Physics D: Applied Physics*, vol. 16, no. 6, p. 1069, 1983.

[123] Y.-H. Pao, R. R. Gajewski, and A. N. Ceranoglu, "Acoustic emission and transient waves in an elastic plate," *The Journal of the Acoustical Society of America*, vol. 65, no. 1, pp. 96–105, 1979.

[124] N. N. Hsu and N. N. Hsu, *Dynamic Green's functions of an infinite plate-A computer program*. National Bureau of Standards, 1985.

[125] K. Ono, H. Cho, T. Matsuo, *et al.*, "Transfer functions of acoustic emission sensors," *J. Acoust. Emiss*, vol. 26, pp. 72–90, 2008.

[126] H. Nyquist, "Certain topics in telegraph transmission theory," *Transactions of the American Institute of Electrical Engineers*, vol. 47, no. 2, pp. 617–644, 1928.

[127] N. Hsu and B. FR, "Characterization and calibration of acoustic emission sensors," *Materials Evaluation*, vol. 39, pp. 60–68, 1981.

[128] J. Vallen, "Vallen dispersion software, version r2005. 1121," *Vallen-Systeme GmbH, Munich, Germany. Available as http: // www. valleh. de / wavelet / index. html*, 2015.

[129] D. R. Ramasawmy, B. T. Cox, and B. E. Treeby, "Elasticmatrix: A matlab toolbox for anisotropic elastic wave propagation in layered media," *SoftwareX*, vol. 11, p. 100397, 2020.

[130] S. Shanmuganathan, "Artificial neural network modelling: An introduction," in *Artificial Neural Network Modelling*. Springer, 2016, pp. 1–14.

[131] N. Kumar, "Sigmoid neuron building block of deep neural networks," *Towards Data Science*, 2019.

[132] S. Saxena, "Introduction to softmax for neural network," *Analytics Vidhya*, 2021.

[133] Mathworks, "Linear neural networks," *Mathworks Help Center. Available as http: // https://uk.mathworks.com/help/deeplearning/ug/linear-neural-networks.html*, 2021.

[134] M. Droubi, R. Reuben, and G. White, "Statistical distribution models for monitoring acoustic emission (AE) energy of abrasive particle impacts on carbon steel," *Mechanical Systems and Signal Processing*, vol. 30, pp. 356–372, 2012.

[135] A. Crawford, M. G. Droubi, and N. H. Faisal, "Analysis of acoustic emission propagation in metal-to-metal adhesively bonded joints," *Journal of Nondestructive Evaluation*, vol. 37, no. 2, p. 33, 2018.

[136] S. Tanary, "Characterization of adhesively bonded joints using acousto-ultrasonics," Ph.D. dissertation, University of Ottawa (Canada), 1988.

[137] R. Adams and N. Peppiatt, "Stress analysis of adhesive-bonded lap joints," *Journal of strain analysis*, vol. 9, no. 3, pp. 185–196, 1974.

[138] ASTM, "D5528-01 standard test method for mode-I interlaminar fracture toughness of unidirectional fiber-reinforced polymer matrix composites," *ASTM International*, 2007.

[139] ASTM, "D1002-10 standard test method for apparent shear strength of single-lap-joint adhesively bonded metal specimens by tension loading (metal-to-metal)." *ASTM International*, 2010.

[140] V. Systeme, "Acoustic emission preamplifiers, specification," 2017.

[141] M. Hamstad, "Acoustic emission source location in a thick steel plate by Lamb modes," *Journal of acoustic emission*, vol. 25, pp. 194–214, 2007.

[142] W. Ong, N. Rajic, W. Chiu, and C. Rosalie, "Adhesive material property evaluation for improved Lamb wave simulation," *International Journal of Adhesion and Adhesives*, vol. 71, pp. 28 – 38, 2016. [Online]. Available: http://www.sciencedirect.com/science/article/pii/S0143749616301701

[143] Loctite, "Loctite EA3430 technical data sheet," *Henkel*, 2014.

[144] COMSOL, *Understanding, and changing, the element order*, (accessed March 07, 2020). [Online]. Available: https://uk.comsol.com/support/knowledgebase/1270

[145] Loctite, "Loctite EA9461 technical data sheet," *Henkel*, 2014.

[146] ASTM, "D6671/d6671m standard test method for mixed mode I-mode II interlaminar fracture toughness of unidirectional fiber reinforced polymer matrix composites," *ASTM International*, 2006.

[147] P. Welch, "The use of fast fourier transform for the estimation of power spectra: a method based on time averaging over short, modified periodograms," *IEEE Transactions on audio and electroacoustics*, vol. 15, no. 2, pp. 70–73, 1967.

[148] M. Giordano, L. Condelli, and L. Nicolais, "Acoustic emission wave propagation in a viscoelastic plate," *Composites Science and Technology*, vol. 59, no. 11, pp. 1735 – 1743, 1999. [Online]. Available: http://www.sciencedirect.com/science/article/pii/S0266353899000354

[149] P. Nivesrangsan, "Multi-source, multi-sensor approaches to diesel engine monitoring using acoustic emission," Ph.D. dissertation, Heriot-Watt University, 2004.

[150] J. Zhang, R. Perez, and E. Lavernia, "Documentation of damping capacity of metallic, ceramic and metal-matrix composite materials," *Journal of Materials Science*, vol. 28, no. 9, pp. 2395–2404, 1993.

[151] P. Feraboli and K. Kedward, "Four-point bend interlaminar shear testing of uni- and multi-directional carbon/epoxy composite systems," *Composites: Part A,*, vol. 34, pp. 1265–1271, 2003.

[152] K. Vine, P. Cawley, and A. Kinloch, "Comparison of normal and oblique incidence ultrasonic measurements for the detection of environmental degradation of adhesive joints," *NDT & E International*, vol. 35, no. 4, pp. 241–253, 2002.

[153] S. Rokhlin, L. Wang, B. Xie, V. Yakovlev, and L. Adler, "Modulated angle beam ultrasonic spectroscopy for evaluation of imperfect interfaces and adhesive bonds," *Ultrasonics*, vol. 42, no. 1-9, pp. 1037–1047, 2004.

[154] P. Mylavarapu and E. Woldesenbet, "Non-destructive characterization of bondlines in composite adhesive joints," *Journal of adhesion science and technology*, vol. 20, no. 7, pp. 647–660, 2006.

[155] W. Wang and S. Rokhlin, "Evaluation of interfacial properties in adhesive joints of aluminum alloys using angle-beam ultrasonic spectroscopy," *Journal of Adhesion Science and Technology*, vol. 5, no. 8, pp. 647–666, 1991.

[156] S.-C. Her and Y.-C. Lin, "Assessment of adhesive bond strength using the ultrasonic technique," *The Journal of Adhesion*, vol. 90, no. 5-6, pp. 545–554, 2014.

[157] R. V. Kumar, M. Bhat, and C. Murthy, "Evaluation of kissing bond in composite adhesive lap joints using digital image correlation: Preliminary studies," *International Journal of Adhesion and Adhesives*, vol. 42, pp. 60–68, 2013.

[158] X. Ma, K. Bian, J.-y. Lu, and K. Xiong, "Experimental research on detection for interface debond of CFRP T-joints under tensile load," *Composite Structures*, vol. 158, pp. 359–368, 2016.

[159] R. V. Kumar, M. Bhat, and C. Murthy, "Some studies on evaluation of degradation in composite adhesive joints using ultrasonic techniques," *Ultrasonics*, vol. 53, no. 6, pp. 1150–1162, 2013.

[160] R. C. Tighe, J. M. Dulieu-Barton, and S. Quinn, "Identification of kissing defects in adhesive bonds using infrared thermography," *International Journal of Adhesion and Adhesives*, vol. 64, pp. 168–178, 2016.

[161] M. Santos and J. Perdigao, "Leaky Lamb waves for the detection and sizing of defects in bonded aluminium lap joints," *NDT & e International*, vol. 38, no. 7, pp. 561–568, 2005.

[162] R. Tamborrino, D. Palumbo, U. Galietti, P. Aversa, S. Chiozzi, and V. A. M. Luprano, "Assessment of the effect of defects on mechanical properties of adhesive bonded joints by using non destructive methods," *Composites Part B: Engineering*, vol. 91, pp. 337–345, 2016.

[163] S. Mustapha, L. Ye, X. Dong, and M. M. Alamdari, "Evaluation of barely visible indentation damage (BVID) in CF/EP sandwich composites using guided wave signals," *Mechanical Systems and Signal Processing*, vol. 76, pp. 497–517, 2016.

[164] S. Goutianos, "Acoustic emission characteristics of unidirectional glass/epoxy composites under mixed-mode fracture," *SN Applied Sciences*, vol. 1, no. 5, p. 474, 2019.

[165] N. R. Center, *AE Source Location Techniques*, 2014 (accessed Sept 03, 2020). [Online]. Available: https://www.nde-ed.org

[166] German Aerospace Centre (DLR), "Dispersion calculator software,," *German Aerospace Centre (DLR). Available as https://www.dlr.de/zlp/en/desktopdefault.aspx/tabid-14332/24874*$_read - 61142/$, 2020.

[167] Loctite, "Loctite EA9480 technical data sheet," *Henkel*, 2014.